COUPLING SOURCE TERM, MINERAL REACTIVITY AND FLOW IN RADIONUCLIDE TRANSPORT

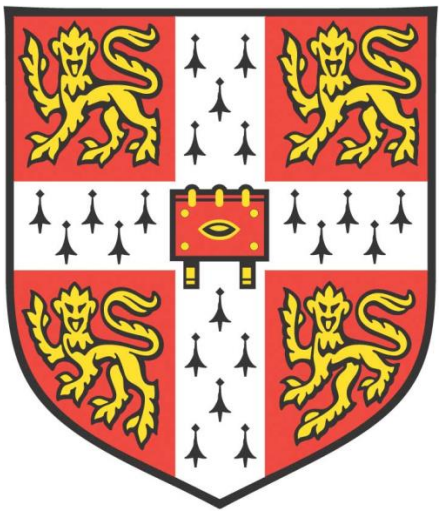

Tajudeen M. Iwalewa

Darwin College

Department of Earth Sciences, University of Cambridge

A thesis submitted for the degree of

Doctor of Philosophy

May 2017

To my mother

DECLARATION

This dissertation is the result of my own work and includes nothing which is the outcome of work done in collaboration except where specifically indicated in the text.

Tajudeen M. Iwalewa, May 2017.

ABSTRACT

The focus of this work is to investigate the dissolution of MW25, a non-radioactive simulant of UK high-level nuclear waste borosilicate glass, and to predict its performance in the near field of a geological repository. A single-pass flow-through (SPFT) experimental system was used to measure the forward dissolution rates of MW25. Experiments were conducted in two parts, resulting in a total of 432 experiments. Experiment Part 1 considers the dissolution of the waste glass in deionised water at 40 and 90 ^{o}C and circum-neutral pH. Experiment Part 2 considers the dissolution of the waste glass in simulant groundwaters, with similar compositions to groundwaters of Callovo-Oxfordian clay (lower-strength sedimentary rock (LSSR)) and Borrowdale Volcanic Group rocks (higher-strength rock (HSR)), at 40 ^{o}C and pH 7. Experiments in both parts were conducted at flow rates ranging from ~10 mL d^{-1} to 250 mL d^{-1}. The wide range in flow rates, together with adjustments to the sample surface area, were used to produce a range of ratios of flow rate to surface area (q/S) values.

The forward dissolution rate measured in deionised water was found to be approximately one order of magnitude higher at 90 ^{o}C than at 40 ^{o}C. A similar release was observed for Si, Mg and Al at 40 ^{o}C and 90 ^{o}C, whereas the B, Cs, Na, Li and Mo showed an order of magnitude increase when the temperature was increased from 40 to 90 ^{o}C for low q/S values. The temperature dependence of the dissolution rates was determined using the Arrhenius rate law, and the resultant activation energy (E_a) shows that the dissolution process is a surface phenomenon. At 90 ^{o}C the net effect of the processes governing MW25 dissolution led to the preferential release of boron and alkali metals relative to the release of Si during the transient dissolution stage, accompanied by an increase in the concentration of silicic acid. This suggests that the solution activity of silicic acid at a higher temperature has a weak influence on the release of the mobile elements.

The forward dissolution rate measured in LSSR simulant groundwater was found to be slightly higher than that measured in HSR simulant groundwater. The dissolution behaviour of MW25 in both groundwaters is consistent with its behaviour in deionised water at 40 ^{o}C, with the dissolution rates of elements increasing as q/S values were increased. However, forward dissolution rates measured in the simulant groundwaters were lower than the forward dissolution rates measured in deionised water under these experimental conditions. This is attributable to the interaction of the components of the

simulant groundwaters with the glass, as revealed by post-reaction surface analyses, and a consequential lower alkalinity of the leachates collected in the experiments with simulant groundwater than in deionised water.

Reactive chemical transport simulations of waste glass dissolution and radionuclide release in a hypothetical near field were conducted over a time span of a million years with GoldSim. Model parameterisation was accomplished by coupling direct laboratory measurements and literature data with transport processes. Time and spatial dependence of radionuclide flux on waste glass were evaluated under four different scenarios. The results showed that Scenario 4, which assumes enclosing the waste glass in a steel canister covered by a copper canister and emplacing the waste package in a granite host rock, is optimal for the long-term isolation of the radionuclides. The waste glass was found to play a significant role in the overall performance of the near field.

This study features a new method for estimating the surface area of reacted glass powder more accurately than the geometric surface area estimate, which is the preferred standard method among researchers.

ACKNOWLEDGEMENTS

This work was made possible with the financial support of an IDB-Cambridge International Scholarship through the Cambridge Trust and the Islamic Development Bank (IDB).

I am tremendously indebted to my supervisor, Ian Farnan, for his forethought regarding the direction in which to take this research, and for his guidance, encouragement and patience, which made possible the large-scale experimental work presented in this thesis. I appreciate Ian's knowledge and skill in several areas of science. Completing a PhD that draws upon research questions from many disciplines – geochemistry, hydrogeology, mineral science and mathematics – would not have been possible without his breadth of knowledge in many disciplines. Ian has taught me, both consciously and unconsciously, how good experimental research is conducted. I appreciate all his contributions in terms of time, ideas and funding to make my PhD experience both productive and stimulating. I am especially grateful to Ian for always going out of his way to provide pastoral support whenever the need arises. I doubt that I will ever be able to convey my appreciation fully, but I owe him my eternal gratitude.

The direction of this work was helped greatly by the early advice of my academic friend, Andy Woods, who encouraged me to think about which lines of research are most effective. In particular, Andy's advice provided the insight into a new surface area method that I designed and applied in estimating the evolving surface area of nuclear waste glass during reaction with solution.

A very special thanks goes to Jason Day for providing ICP-MS analyses. Jason's expertise and practical help were instrumental in the preparation of the simulant groundwaters used in this study. I would like to thank Giulio Lampronti and Iris Buisman for their assistance with SEM/EDX and XRD analyses; they also provided excellent training in the analytical techniques. I am thankful to Chris Parish, Martin Walker (Department of Earth Sciences, University of Cambridge) and Richard Nightingale (Department of Chemistry, University of Cambridge) for their technical assistance with the experimental apparatus, and Wayne Skelton-Hough (Department of Materials Science and Metallurgy, University of Cambridge) for his help with BET and particle-size analyses.

I would like to thank William Ebert of Argonne National Laboratory, USA, for his continuous discussion on this study. I wish to thank James Schofield of Amec Foster Wheeler for supplying the nuclear waste glass used in this study. I also wish to acknowledge Mike Harrison of the National Nuclear Laboratory, UK, and Steve Swanton of Amec Foster Wheeler for providing useful information about UK nuclear waste glass.

I must acknowledge Darwin College, University of Cambridge, and Cambridge Philosophical Society for providing significant support during my three and a half years at Cambridge. My special appreciation also goes to Leo Howe (former Dean of Darwin College, University of Cambridge) and Duncan Needham (current Dean of Darwin College, University of Cambridge) for their invaluable support.

I thank Andy Buckley (Department Administrator), Simon Redfern (Head of Department) and all members of the Department of Earth Sciences, University of Cambridge, for their hospitality and support.

The members of the Ian Farnan group have contributed immensely to my personal and professional time at Cambridge. Appreciation goes to my colleagues, Frederick Lord, Huixing Zhang, Aleksej Popel, Karishma Patel, Rui Gui, Tingyu Qu, Tom Gout, Giles Rought Whitta, Rana Dhan-sham, and the numerous summer and rotation students who have come through the lab, for their stimulating discussions, good advice and camaraderie.

My time at Cambridge was made enjoyable in large part thanks to the many friends that have become part of my life. My appreciation goes to the families of Abdulhakeem and Kifayah Oladejo, and Nurudeen and Basirat Afinowi for their friendship and support. I must thank my friend, Bashir Kasim, who always gracefully trims my hair whenever it is getting bushy. And to Amanda George, who has always helped me to read my writing, I say thank you.

Special thanks to my friends, Saheed Hussein, Lateef Adedigba, Abdulafeez Adebiyi, Tosin Okeyemi, Afeez Babatunde, Moshood Kazeem, Hakeem Babatunde, Rasheed Balogun and Taiwo Odedairo, for their camaraderie and support. And I would like to thank my late friend, Nasir Alabidun, for his moral support.

To my late father, who raised me despite many difficulties and supported me in all my pursuits, I say thank you. I would like to thank Luqmon Iwalewa, Tunde Kareem and all the members of my extended family for their love and encouragement. I thank my

parents-in-law, Tajudeen and Fausat Lawal, for their encouragement. And I am grateful to Lateef Kareem, Rahman Ayinde Mogaji and Rasaq Ayinde Sanni for their solid support.

Last but in no way least, my special thanks goes to my wife, Airat Omobolanle, whose love, patience, encouragement and faithful support have been my driving force. And many thanks to my children, Hanifah and Tajudeen Jnr, whose love has been a means of hope and encouragement.

CONTENTS

LIST OF TABLES

LIST OF FIGURES

1 INTRODUCTION

1.1 Nuclear Waste Disposal Status

With renewed interest in nuclear energy and the dismantling of nuclear weapons, the safe disposal of nuclear waste is a growing concern. With the push to decarbonise electricity, a nuclear revival seems increasingly likely. In Europe and North America interest has been reignited, and elsewhere initiated, in replacing old nuclear plants with new ones (Grimes and Nuttal, 2010). This renewed interest brings concerns about the fate of nuclear waste. Nuclear waste presents a potential hazard to the environment, ecosystem services and human health. Because of the harm that they can potentially cause, radioactive materials must be contained and isolated from the accessible environment for sufficiently long periods of time, so that the radiological impact of disposed waste is reduced to an acceptable level.

The currently preferred option for the safe disposal of high-level waste (HLW) arising from the aqueous reprocessing of spent nuclear fuel is to immobilise radioactive materials within a chemically durable borosilicate matrix (Jantzen *et al.,* 2010; Gin *et al.,* 2013). An internationally supported strategy is for the vitrified HLW to be disposed of in a deep geological repository for thousands, or even millions, of years (IAEA, 2011). The presence of groundwater in the vicinity of a geological repository is inevitable, raising challenging scientific questions regarding dissolution rate should groundwater come into contact with the waste package. Efforts to elucidate the feasibility of geological repositories have led to an appreciation of the safety function of borosilicate glass; accordingly, a proliferation of studies have focused on quantifying dissolution kinetics through laboratory experiments to provide source terms for key contaminants and to predict the performance of nuclear waste glasses in geological

repository systems (Lasaga, 1981; Grambow, 1985; Grambow, 1987; Bourcier, 1994; McGrail *et al.*, 1997a; Abraitis *et al.*, 2000 a,b,c; Gin *et al.*, 2001; Ebert, 2005; Curti *et al.*, 2006; Pierce *et al.*, 2008 a,b; Icenhower *et al.*, 2008; Jollivet *et al.*, 2012; Corkhill *et al.*, 2013; Gin *et al.*, 2015).

Experimental investigations have typically centred on determining waste glass dissolution rates as a function of glass composition, solution chemistry, temperature and pH (McGrail *et al.*, 1997a; Abraitis *et al.*, 2000 a,b,c). Today, many aspects of the waste glass dissolution mechanisms and kinetics seem to have been understood. However, given the long time frame required by a geologic repository to isolate radionuclides and the unavoidable dissolution of waste glass by repository groundwater, long-term safety needs to take credit from additional engineered and natural existing barriers, including canisters, buffer material and host rock. Depending on the durability of the waste glass and the effectiveness of the other barriers, the contribution of waste glass to overall safety will either be large or small. The challenging task is therefore to predict the long-term glass performance in combination with other engineered and natural barriers.

1.2 Vitrification of Nuclear Waste Borosilicate Glass

Radionuclides are immobilised in glasses by a process called vitrification (Ojovan and Lee, 2007; Donald, 2010). The development of vitrification has progressed over the last five decades. Currently this technology has become industrially robust, such that a number of countries, including Belgium, France, Germany, Japan, the UK and USA, have vitrification facilities in operation for the treatment of high-level or intermediate-level waste. With the exception of alumina-phosphate glass in Russia, borosilicate glass has been selected in many countries as an HLW glass (Gin *et al.* 2013). This is a result of the properties of borosilicate glasses, which include (NRC, 1995):

- its ability to incorporate a wide variety of fission products and actinides, around thirty oxides that constitute the calcined wastes;
- its reasonably low formation temperature, below 1200 ^{o}C;
- its ability to incorporate a high proportion of waste, up to 40 wt% depending upon the composition;
- its tolerance for reasonably wide variability in the waste composition;
- its resistance to radiation-induced degradation;

- its ability to be produced remotely with a simple and reliable process requiring minimum maintenance; and
- its low susceptibility to leaching in an aqueous environment.

The general data related to nuclear waste amounts and HLW synthesis of some of the countries with operational vitrification facilities is presented in Table 1.1. There is a wide variation in the number of existing HLW glasses among the countries, and the total activity confined ranged between 10^{18} and 10^{20} Bq. In addition, the percentage of spent nuclear fuel that is reprocessed varies among countries. The focus of the present study, however, is the UK HLW borosilicate glass, which is discussed in more detail in the subsequent section.

Table 1.1: General data related to nuclear waste amounts and HLW glass synthesis in countries with vitrification facilities (modified after Gin *et al.*, 2013).

Key Figures	UK	USA	Japan	France	Belgium	Germany
Currently operating reactors	16	104	50	58	7	9
Existing HLW glass, 2012 (tons)	2200	6700	700	7700	650	2300
Total activity confined (Bq)	2.4×10^{19}	2.6×10^{18}	3.2×10^{19}	2.8×10^{20}	6.3×10^{18}	2.4×10^{19}
Origin	Spent fuel from NPPs	By activity - 30% NPP, 70% defence. By mass - 7% NPP, 93% defence	Spent fuel from NPPs	Spent fuel from NPPs, few from defence	Spent fuel from NPPs	Spent fuel from NPPs
Glass/SNF (% of SNF reprocessed)	> 90%	< 1% NPP, ~99% defence	~30%	> 90%	~13% (if no further reprocessing)	~47.9%
Vitrification Facilities	Sellafield (1990 →)	WVDP (1996 -2002), DWPF (1996 →), WTP (est. 2019 - 2047)	TVF (Tokai 1995 →), KA facility (currently in active testing)	R7T7 (La Hague 1989 →), AVM (Marcoule 1978 -2012)	Eurochemic (Dessel, Belgium)	Karlsruhe (until 2010)

1.3 Vitrification of Nuclear Waste Borosilicate Glass

The key stages in the development of HLW vitrification in the UK are listed in Table 1.2. In the UK spent fuel from the UK's civil nuclear power stations is reprocessed using the PUREX (Plutonium URanium EXtraction) process to recover the uranium and

plutonium. The PUREX process is based on liquid–liquid (solvent) extraction using tributyl phosphate (TBP), which gives rise to a nitric-acid-based liquid waste stream containing the fission products and residual actinides from the spent fuel (Harrison, 2014a). This highly active liquor (HAL) is concentrated by evaporation and stored in tanks prior to being converted into a borosilicate glass at the Sellafield waste vitrification plant (WVP). The vitrification process yields a stable and durable waste glass that is suitable for long-term storage and subsequent disposal.

Table 1.2: Key stages in the development of HLW vitrification in the UK (Harrison, 2014a).

Research into vitrification of radioactive waste started	1950s
FINGAL developed at the UK Atomic Energy Authority (AEA) laboratories, Harwell	1960 -1962
FINGAL operations (72 glass-making runs)	1962 - 1966
Development suspended	1966 - 1972
Review decision to continue vitrification development for HARVEST process	1972
Detailed comparison of HARVEST and French AVM process	1979 - 1980
Decision to implement the AVM process for HLW vitrification in the UK	1980
Full scale inactive facility (FSIF) replica of AVM process built	1981 - 1983
Decision that WVP should use the AVH process	1982
FSIF operational	1983 - 1991
Commissioning of WVP Lines 1 and 2	1989 -1990
WVP Lines 1 and 2 operational	1990 - Present
Commissioning of WVP Line 3	1998 - 2002
WVP Line 3 operational	2002 - Present
Vitrification Test Rig (VTR) constructed	2002 - 2004
VTR operational	2004 - Present

Two separate reprocessing facilities that have been operational at Sellafield since 1994 include (Harrison, 2014a):

- The Magnox plant for the reprocessing of natural uranium-metal-based fuel from the UK's first-generation Magnox reactors; and
- THORP (thermal oxide reprocessing plant) for enriched uranium oxide fuels from AGRs (advanced gas cooled reactor) and LWR (light water reactors) (operational).

Magnox and THORP (or Oxide) HAL have distinct chemical compositions. Magnox HAL contains high concentrations of magnesium and aluminium from residual cladding material, whereas Oxide HAL contains no Mg or Al, but has elevated fission product and actinide content, as well as the presence of gadolinium, which is used as a neutron poison in the process.

The waste vitrification plant (WVP) fabricates two main products from these separate HAL feeds (Harrison, 2014b):

- 'Magnox' glass from feeds containing > 90% Magnox HAL; and
- 'Blend' glass from feeds containing typically a mix of 75% Oxide and 25% Magnox (75o:25m) HAL.

The waste incorporation for both Magnox and Blend glasses has historically been targeted at 25 wt% on an oxide basis. However, recent vitrification campaigns have increased this to 32 wt% and 28 wt%, respectively. In addition to the compositional variations arising from the different types of HAL feed and waste incorporation, other differences occur as a result of different burn-up and cooling times of the spent fuel, as well as the way it has been reprocessed (Harrison, 2014b). Importantly, the interest of the present study is on Magnox glass, which is produced from Magnox HAL.

1.3.1 Sellafield WVP Process Description

The design of WVP is based on the continuous two-stage design of the French AVH (Atelier de Vitrification de la Hague) process, which is shown schematically in Figure 1.1. HAL is transferred from the storage tanks to one of four WVP feed tanks, where it is combined with a sugar solution (to reduce ruthenium volatilisation and enhance de-nitration) and fed to an electrically heated rotary calciner. The calciner evaporates and partially de-nitrates the HAL, producing a dry powder. This 'calcine' material is discharged by gravity, along with a metered quantity of base glass frit, directly into an induction-heated melter crucible and heated to ~1050 ^{o}C. The calcine reacts with the molten base glass and the resulting homogeneous melt is then periodically poured into product containers. Once filled, the product containers are allowed to cool for at least 24 hours before having a lid welded in place. They are then decontaminated, checked for any activity on the outer surface through swabbing, and then transferred to an interim storage facility called the vitrified product store (VPS) (Harrison, 2014a).

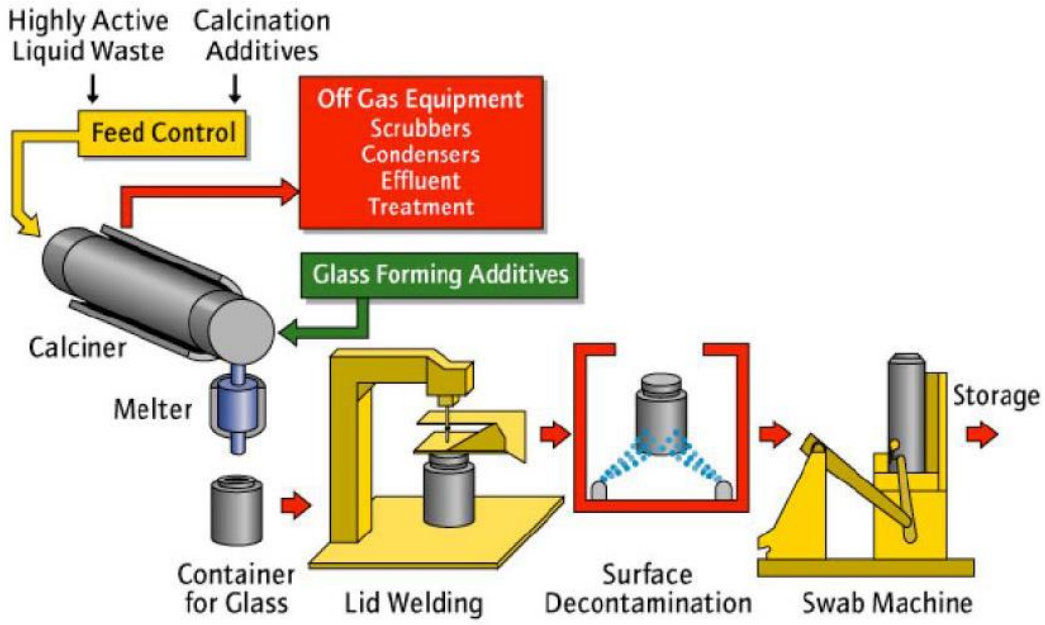

Figure 1.1: Schematic of the HLW vitrification process on the Sellafield site (Harrison, 2014a).

The WVP will continue operation until the existing inventory of HAL is immobilised following the planned completion of reprocessing at Sellafield. It is currently estimated that the WVP will produce ~8,620 containers during its operational lifetime, of which ~1,850 will be returned to overseas Magnox reactors at Latina in Italy and Tokai Mura in Japan (NDA, 2010). This will result in ~6,770 packages containing ~2,200 tons of HLW glass for disposal in the UK.

1.3.2 Development of the Base Glass used in WVP

The decision to implement the two-stage AVH vitrification process in the UK resulted in the selection of the 'MW' (Mixture Windscale) composition, which is shown in Table 1.3. An equimolar amount of Li and Na in the composition was found to optimise the properties of the MW base glass. However, the strategy of dosing the HAL with $LiNO_3$ was found to suppress the formation of refractive oxides, leading to improvement in the reactivity of the calcine (Harrison, 2014a,b). The optimum proportions to get the targeted lithia (Li_2O) in 'standard' 25 wt% waste incorporation vitrified product was a 50:50 split between the HAL feed and the base glass. Hence, the MW glass was reformulated with half of the Li removed (i.e. 'MW-½Li' in Table 1.3), which became the standard base glass feedstock (Harrison, 2014a). However, variations in the amount of Li dosing has led to deviations from the targeted 1:1 Li:Na ratio in the glass product (Harrison, 2014b).

Table 1.3: Composition of base glasses used for the vitrification of HLW in the UK (Harrison, 2014a).

Base Glass Type	SiO_2	B_2O_2	Na_2O	Li_2O
MW	61.75	21.88	11.05	5.33
MW-1/2Li	63.42	22.5	11.35	2.74

Despite these variations, a large number of the laboratory and full-scale vitrification development programmes have used standard representative compositions with ideal Li_2O concentrations. For example, the current reference non-active simulant compositions for Magnox and 75:25 Blend glasses are known as 'WRW17' and 'WRW16', respectively (Harrison, 2014b). A comparison of the concentrations of key glass durability elements in WRW17- and WRW16-based glasses with the calculated compositions of recent Magnox (x3) and Blend (x2) WVP campaigns is presented in Table 1.4.

Table 1.4: Comparison of recent WVP campaigns with the reference Magnox (WRW17) and Blend (WRW16) simulant compositions (Harrison, 2014b).

Waste Oxide (wt%)	Magnox 1	Magnox 2	Magnox 3	WRW17	Blend 1	Blend 2	WRW16
Al_2O_3	6.67	6.08	5.02	5.18	1.59	1.43	2.00
Gd_2O_3	0.58	0.49	0.78	0.78	2.77	2.30	4.50
Li_2O	4.45	3.93	3.76	3.90	4.23	4.07	3.90
MgO	6.02	5.48	4.52	5.49	1.41	1.33	1.76
Waste loading	30.9	28.3	27.3	28.0	26.7	27.3	28.0

1.3.3 Calcination

An image of the calciner used on the full-scale non-active vitrification test rig (VTR) is shown in Figure 1.2. The calciner consists of a tube (4 m long, 300 mm diameter) inclined at 1.73^{o} (2%) to the horizontal, rotating (20–30 rpm) inside a four-zone electrical resistance furnace heated at 600–840 ℃. As the HAL flows down the calciner, it is dried and de-nitrated; the first two heating zones evaporate the HAL to dryness, forming solid waste nitrates, and the second two partially de-nitrate the solids, forming a waste oxide calcine (Harrison, 2014a).

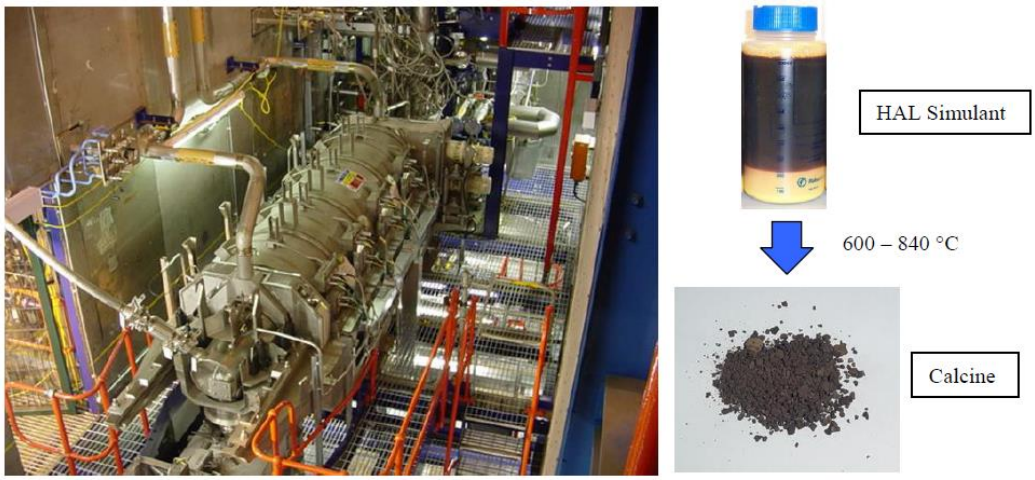

Figure 1.2: Full-scale calciner on the non-active vitrification test rig (VTR) showing conversion of HAL simulant to calcine material (Harrison, 2014a).

1.3.4 Melting and Pouring

The melting stage of the WVP process is designed to produce a homogenous and reproducible glass product. This is achieved by heating a mixture of MW-½Li base glass frit and calcine in an elliptical Nicrofer® 6025 HT alloy melter crucible (working volume ~100 litres) using electrical induction. Frit and calcine are fed over an eight-hour period, with mixing provided by four argon or air sparge tubes. The glass is then poured into the product container once the temperature has reached > 1000 ^{o}C (typically 1050 ℃) through an induction-heated freeze valve. Each pour is ~200 kg glass, with ~70 kg remaining in the crucible as a heel. The vitrification product container (VPC) is a 169-litre-capacity cylindrical 309 stainless steel vessel. This is sufficient for two ~200 kg pours, giving a total of ~400 kg glass per container (Harrison, 2014a).

1.4 Borosilicate Glass Structure and Dissolution Mechanism

Borosilicate glasses are thermodynamically metastable, with a tendency to transform into more stable compounds during reaction with water (Jantzen *et al.*, 2010; Gin, 2014). In silicate glasses, the tetrahedral hybridisation of Si generates a three-dimensional polymeric network of –Si-O-Si= bonds, where the bond lengths and bond angles are constrained in individual tetrahedra, but long-range order is not maintained (Ebert and Mazer, 1993). Other elements may be incorporated into the silicate network, but will be disruptive to the silicate network as a result of their different ionic sizes and charges. The size and valence of elements added to the glass determines, in part, how they will be incorporated into the glass network. The addition of monovalent and

divalent components terminates the network structure, while tetravalent elements may be incorporated as network-forming groups. The addition of trivalent components may maintain the network structure, but requires charge compensation by the presence of an alkali metal to maintain electric neutrality. Most components have limited solubility in the glass, and the precipitation of phases containing elements not incorporated into the glass structure, such as noble metals and insoluble spinel phases, may occur within the glass (Scales, 2011).

Although this model of the glass structure has proven helpful in understanding glass dissolution, it cannot account for some commonly observed aspects of dissolution behaviour. In particular, boron is typically released from borosilicate glasses at a rate similar to the alkali metals (Scholze *et al.,* 1982), which occupy terminal sites, while boron is modelled to occupy tetrahedral sites.

The description of the glass structure provides insights into the breakdown of glass in the presence of water. The release of alkali metals (M) from network terminal sites occurs through ion exchange with protons from water to produce silanol groups and free alkali. The ion exchange reaction can be written as (Ebert and Mazer, 1993):

$$\equiv \boldsymbol{SiO - M + H^+ = \equiv SiO - H + M^+} \quad \textbf{(1.1)}$$

$$\equiv \boldsymbol{SiO - M + H_3O^+ = \equiv SiO - H + M^+ + H_2O} \quad \textbf{(1.2)}$$

$$\equiv \boldsymbol{SiO - M + H_2O = \equiv SiO - H + M^+ + OH^-} \quad \textbf{(1.3)}$$

where ≡SiO-H is the silanol group, and M^+ is an alkali metal ion.

While Eq. (l.1) gives the basic reaction, a non-hydrolysed proton is unlikely to be stable in either solution or glass. Different authors have expressed the reaction as Eqs. (l.2) and (1.3), which are simply related through the ionisation of water; the reaction in Eq. (1.3) is a hydrolysis reaction. Continued alkali release requires the proton-bearing species to diffuse into the glass to access other alkali metals. The diffusion of water into the glass is usually not accounted for specifically in reaction models, and alkali release is sometimes discussed in terms of the ‘interdiffusion’ of hydronium and alkali metal ions (Gin, 2014). Other evidence supports the diffusion of molecular water into glass (Smeta and Lommen, 1983). Some have pointed to the observation that the measured proton-to-alkali exchange ratio is often near three to support the alkali for hydronium exchange in Eq. (l.2) (Schnatter *et al.,* 1988), although exchange according to Eq. (1.3)

followed by sorption of a second water molecule would give the same result. Silanol is known to strongly sorb water (Ebert and Bates, 1991).

Hydrolysis reactions are thought to be responsible for the degradation and dissolution of the silicate network. Hydrolysis of ≡SiO-H≡ linkages is modelled to occur through nucleophilic attack on a Si atom by either molecular water or hydroxide. Hydrolysis of internal ≡SiO-H≡ linkages may occur to break the network as (Ebert and Mazer, 1993):

$$\equiv SiO - Si + H_2O = \equiv SiOH + HO - Si \equiv \quad \textbf{(1.4)}$$

$$\equiv SiO - Si + OH^- = \equiv SiO^- + HO - Si \equiv \quad \textbf{(1.5)}$$

Hydrolysis of terminal –$Si(OH)_3$ groups leads to dissolution of the glass as:

$$\equiv SiO - Si(OH)_3 + H_2O = SiOH + H_4SiO_4\,(aq) \quad \textbf{(1.6)}$$

$$\equiv SiO - Si(OH)_3 + OH^- = SiO^- + H_4SiO_4\,(aq) \quad \textbf{(1.7)}$$

The forward reactions in Eqs. (1.4) and (1.5) are referred to as network hydrolysis reactions, and the forward reactions in Eqs. (1.6) and (1.7) are referred to as network dissolution reactions. The reverse reactions are referred to as condensation reactions. The ≡SiO^- groups generated in Eqs. (1.5) and (1.7) may become protonated by interacting with another water molecule. The experimentally observed pH effects on the rate of Si release suggest that Eqs. (1.5) and (1.7) better represent the hydrolysis reactions under neutral and alkaline conditions (Ebert and Mazer, 1993). Similar reactions can be written for the hydrolysis of other terminal metal-oxygen bonds, such as for boron:

$$\equiv SiO - B(OH)_2 + OH^- = SiO^- + B(OH)_3 \quad \textbf{(1.8)}$$

1.4.1 Description of Glass Dissolution

Initial contact between the glass and water results in both ion exchange and hydrolysis reactions at the glass surface, such that the surface of the glass is dissolved (Ebert and Mazer, 1993). These processes are interrelated through the solution chemistry and alteration of the glass structure; for example, hydroxide produced during the release of alkali metals assists in the hydrolysis of nearby metal–oxygen bonds (Doremus, 1975; Rebiscoul *et al.,* 2007). The exchange of alkali in the glass for protons and the hydrolysis of network bonds will enhance water diffusion into the glass, and larger amounts of water in the glass will enhance the ion exchange reactions. Water subsequently diffuses into the glass and undergoes ion exchange with the alkali metal ions that are encountered. Because ion exchange reactions occur at higher rates than the

hydrolysis reactions in dilute, near-neutral solutions, an alkali-depleted region develops at the glass surface (McGrail *et al.,* 2001). The release of alkali metals via ion exchange generates hydroxide, which then catalyses the hydrolysis reactions.

The solution chemistry, particularly the increased pH, alkali metal concentrations and silicic acid concentrations, affects the kinetics of the ion exchange and hydrolysis reactions (McGrail *et al.,* 2001). The build-up of alkali and hydroxide in solution slows the ion exchange, while hydrolysis is slowed by high silicic acid concentrations but accelerated by high pH (Grambow, 1985; Grambow, 1987; Pierce *et al.,* 2008a). Therefore, the pH increase accompanying alkali release slows the reactions to release alkali, but accelerates the hydrolysis reactions. The slowing of the alkali release may also slow the diffusion of water into the glass. Therefore, ion exchange will dominate the dissolution process until the pH and alkali content of the solution become sufficiently high that the alkali release slows to the same rate as the hydrolysis reactions (Ebert and Mazer, 1993). Alkali metals are commonly observed to be initially released from the glass at a higher rate than Si, but at longer times the alkali metals and Si are released at similar rates (Figure 1.3) (Abraitis *et al.,* 2000a). The preferential release of the alkali metals during the early stages of dissolution results in an alkali-depleted layer at the surface of the glass. It is likely that, while the alkali metals and Si are being released into solution at the same rate at later reaction times, they are released from different regions of the reacting glass: the alkalis are released from beneath the depletion layer, and Si is probably released primarily from the outer surface of the depletion layer (Abraitis *et al.,* 2000c). Because the releases of both the alkali metals and Si are controlled by the solution chemistry, their release remains nearly stoichiometric. The effects of alkali release are usually considered to be transient and important only during the initial stages of glass dissolution, and are not normally accounted for in reaction models (Ebert and Mazer, 1993).

1.4.2 Glass Dissolution Kinetics Regimes

The interrelated processes that take place during the glass dissolution reaction have been linked to three main stages of kinetic dissolution: initial rate (Stage I), residual rate (Stage II) and rate resumption (Stage III) (Figure 1.4) (Poinssot and Gin, 2012). The coupled mechanisms that occur at these stages have been reviewed by a wide variety of authors, the most recent being Gin *et al.* (2013). Briefly, when water comes into contact

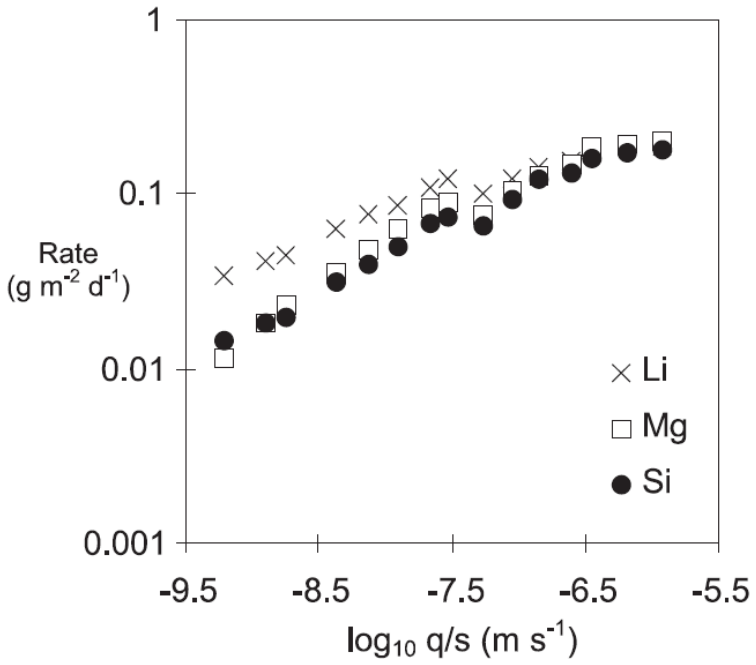

Figure 1.3: Plot of rate against $\log_{10}$(q/S) showing preferential release of Li relative to Si (and Mg) initially (at low flow rates). All the elements were released at similar rates when the flow rates were increased (Abraitis *et al.*, 2000a).

with glass, an expeditious diffusion-controlled reaction is initiated, such that H^+ in solution is exchanged for alkali cation contained in glass through an ion exchange reaction. This is followed by hydrolysis of silica network bonds, which controls the initial dissolution rate. A transitional stage, known as rate drop, occurs between the initial and the residual stage. The rate drop is accompanied by a progressive increase in the concentration of dissolved silica in the solution (Grambow, 1985) and the formation of various surface layers (e.g. gel layer) that could impact the rate of matrix dissolution (Bunker, 1988; Bourcier, 1991). Secondary crystalline phases enriched in hydrolysable elements, including phyllosilicates and zeolites, may precipitate on top of the gel, depending on the glass composition and dissolution conditions (Grambow, 2006; Frugier *et al.*, 2008). The decrease in matrix dissolution that occurs during Stage II (i.e. residual rate) is attributed to the common ion effect; in other words, as the solution becomes more concentrated in the same ions that will be released (or precipitated) from the glass, the chemical potential difference between the glass and aqueous phase decreases, resulting in a decrease in the dissolution rate (Pierce *et al.*, 2008a). The residual rate can be orders of magnitude lower than the initial rate; Grambow (1992) suggests the residual rate at a value lower than 1/1,000 of the initial rate. Importantly,

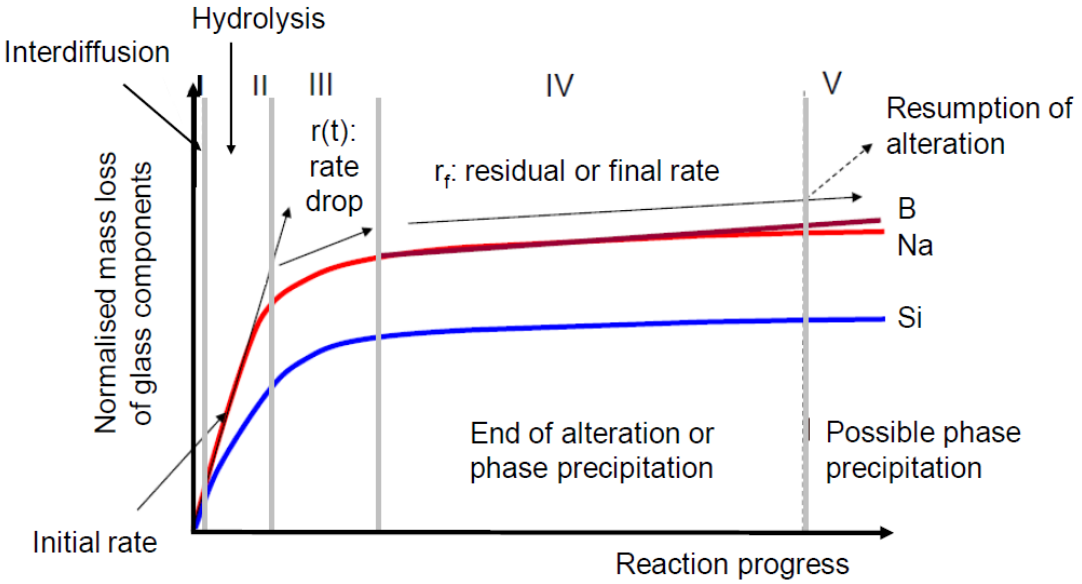

Figure 1.4: Glass dissolution stages and related rate-limiting mechanisms.

the residual stage is considered to be the most important in the geological repository disposal of nuclear waste (Van Iseghem *et al.*, 2009). Depending on the combined effects of glass composition and environmental variables, particularly temperature and pH, relatively rapid dissolution (i.e. rate resumption) may be triggered afterwards (Abraitis *et al.*, 2000c).

The relative significance of solution feedback and mass transport limitations imposed by alteration layers is still very controversial. The generally accepted glass dissolution model is grounded in the mechanisms described above, which assume that the rate-limiting reaction is the hydrolysis of siloxane bonds (Grambow, 1985). A recent study (Gin *et al.*, 2015) combining dissolution experiments and analytical techniques makes a case for *in situ* repolymerisation of the silicate network. Most importantly, it was found that the release rate of the mobile elements (B, Na and Ca) decreased by ~3.7 orders of magnitude from the first hour of the dissolution to 363 d; meanwhile, the network-forming cations (Si, Al and Zr) remained almost undissolved, which was interpreted as an indication of the independent behaviour of the mobile elements. Although the study by Gin *et al.* (2015) also supports dissolution control, it challenges the model proposed by Grambow (1985), which attributes the drop in dissolution rate of the mobile elements to increasing activity of the dissolved silica. This presents a significant dichotomy that requires careful investigation in order to reach an adequate understanding of the mechanisms involved.

1.5 Geological Repository for Nuclear Waste Disposal

More than thirty nations with nuclear power plants are currently engaged, at various stages, in exploring the feasibility, conducting site selection, characterisation and design programmes, and/or licensing of geological repositories (Witherspoon and Bodvarsson, 2006). There are also programmes exploring the possibility of international repositories (IAEA, 2004). While interesting options involving advanced fuel cycle transmutation, reprocessing and even extended storage are also being evaluated in some countries (NEA, 2002), it has become a well-accepted consensus that these options require geological disposal as part of the overall solution for safe management and long-term disposal of radioactive wastes (IAEA, 2011).

While much progress has been made in the scientific and engineering community, the disposal of nuclear waste in a geological repository is still recognised as a contentious issue. Discussions include scientific points, such as long-term safety confirmation given the presence of groundwater in the repository, associated uncertainties (MacFarlane and Ewing, 2006), as well as social points, such as equity between generations and also between the repository-host community and the rest of the country (DECC, 2014). There have been active discussions on the regulatory side and these discussions have affected, and been affected by, site-selection processes and the development of

Table 1.5: Geological disposal options under consideration in different countries (Gin *et al.*, 2013).

	UK	USA	Japan	France	Belgium	Germany
Host Rock Consideration	Not yet defined (clay and granite are being considered)	Not yet defined	Not yet defined	Clay	Poorly indurated clay	Salt dome (clay in future)
Selection method	Municipality volunteers		Municipality volunteers			
URL in operation	Not currently available	Yucca Mountain	Mizunami, Horonobe	Bure	HADES in Mol	Not currently available
Disposal concept	Not yet defined	Not yet defined	Glass, metal overpack, buffer material	Glass, carbon steel overpack	Supercontainer design (concrete buffer)	Not yet defined
Milestones	2040: operating for ILW, 2075: operating for HLW	Not yet defined	Around 2025: licensing, around 2035: operating	2015: licensing, 2025: operating	Pending for policy decision	2030: operating for HLW

repository concepts in each country, as summarised in Table 1.5. Note that the information presented in Table 1.5 is incomplete, as Finland and Sweden are missing from the table. In November 2016, Posiva Oy was granted a licence to operate a geological repository for HLW at Onkalo in Finland. The first such repository (i.e. Waste Isolation Pilot Plant in New Mexico) is for intermediate level defence wastes. Sweden is not far behind in completing licensing for its repository at Forsmark.

1.6 Multi-barrier Concept and the Near Field

The isolation of HLW from the accessible environment (i.e. far field) is obtained by means of multi-barrier concept, involving a combination of both engineered and natural barriers. The waste glass, metal canisters and buffer material constitute the engineered barriers, while host rock is the natural barrier (Nirex, 2005a,b). These barriers will be located within the near field – the deepest part of the repository at a depth of between 300 and 1,000 m below ground surface (Figure 1.5). For HLW, the function of the canister is to isolate the source term and prevent any radionuclide release. The objective is notably to benefit from the decay of short-half-life radionuclides (^{90}Sr, ^{137}Cs, ^{241}Am), which are the most radioactive (Poinssot *et al.,* 2010). The primary function of other barriers is to limit the rate of release and to delay radionuclide migration. This is the role, in particular, of the waste glass when the canister is no longer capable of ensuring its safety function, and of the buffer material and host rock when radionuclides begin to be released from the waste package.

The most obvious, and arguably the most important, constraints on radionuclide concentration in the near field arise when groundwater makes initial contact with waste glass at the time of canister failure. Waste glass dissolution is driven by the fact that groundwater is under-saturated with respect to the waste glass components. The dissolution of the waste glass leads to an increase in the concentration of radioactive and non-radioactive components in the groundwater contacting the waste glass surface, as shown in Figure 1.6 (Apted and Ahn, 2010). As has long been established in natural geochemical and diagenic systems (Berner, 1978), as well as in chemical engineering systems (Chambre *et al.,* 1982), when dissolved components in a closed system are immediately transported away from the surface of a dissolving waste glass, the dissolution rate remains constant (i.e. point A in Figure 1.6). In a closed system, the

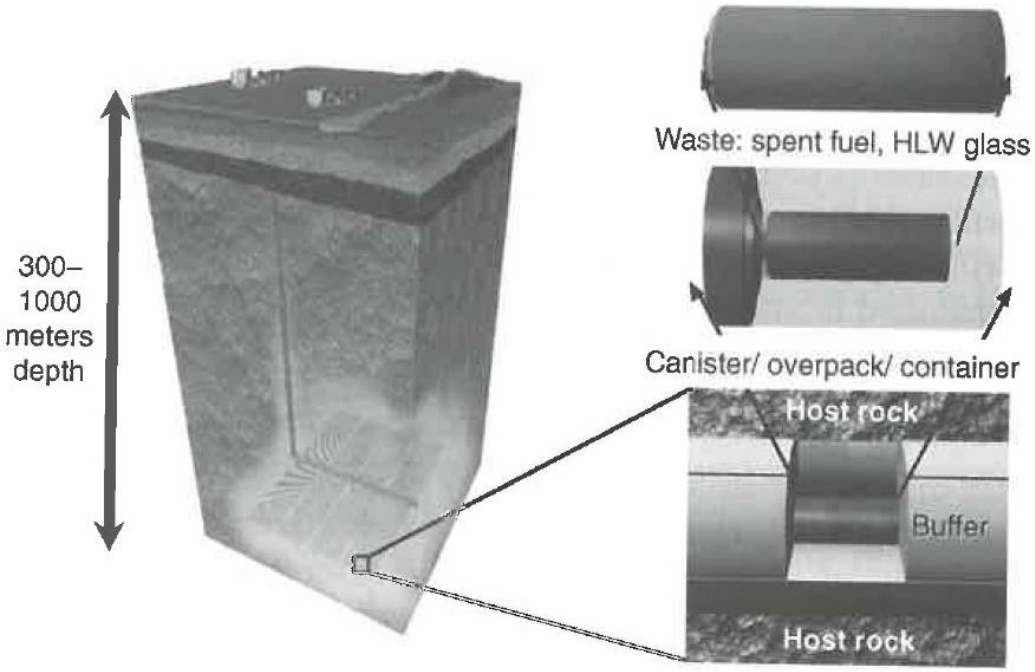

Figure 1.5: Representative illustration of a deep-geological repository design with multiple barriers that include (moving from the inside of the outside) a waste glass, a combination of metal canisters, an encompassing buffer and the host rock, which constitute the near field.

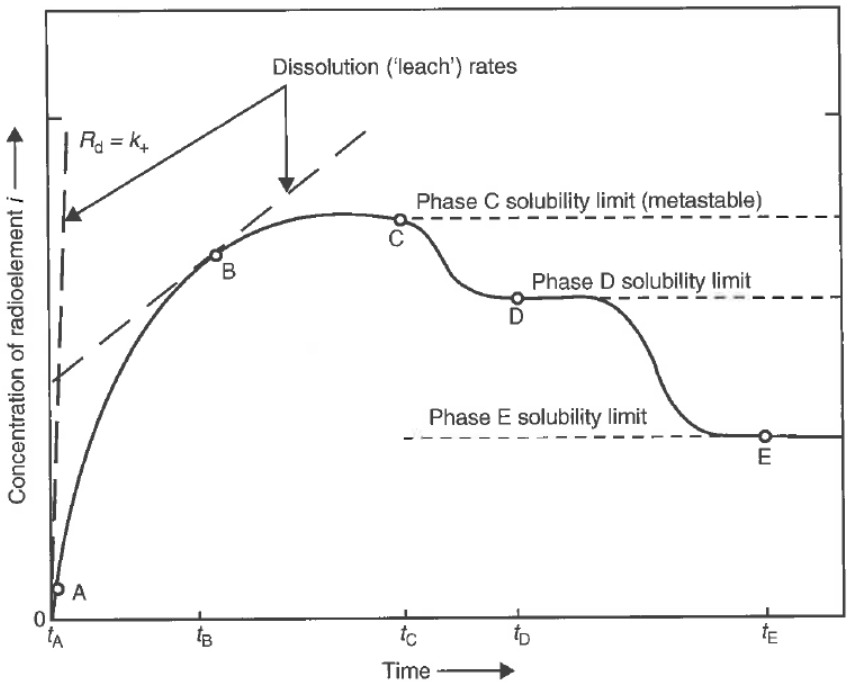

Figure 1.6: Schematic diagram of the evolution of concentration of a representative radionuclide i at the surface of a dissolving nuclear waste glass under expected repository conditions (Apted and Ahn, 2010).

were reached between the contacting groundwater and the waste glass (i.e. point C in Figure 1.6). Therefore, a good understanding of waste glass behaviour in the near field is important when making a safety case for a geological repository.

1.7 The UK HLW Geological Disposal Concept

The UK repository concept for the disposal of HLW is based on the kärnbränslesäkerhet-3 (KBS-3) concept developed by Svensk Kärnbränslehantering AB (SKB) for spent fuel in Sweden (Nirex, 2005a). The KBS-3 repository concept is based on encapsulating spent fuel in copper canisters with a cast iron insert, as shown in Figure 1.7 (SKB, 2000). The geological disposal concept optioneering work undertaken to date in the UK has assumed that the disposal of HLW and spent fuel will be based on the use of a single disposal concept, which is consistent with the development of disposal concepts in other national programmes: for example, the national geological disposal programmes in Belgium (Bel *et al.*, 2006; ONDRAF/NIRAS, 2008), France (Andra, 2005) and Switzerland (Nagra, 2002).

In the UK, the near field of a geological repository would be constructed at a depth of between 200 and 1,000 m (NDA, 2010). At this stage in the geological disposal programme, three generic geological environments are under consideration, namely, lower-strength sedimentary rock (LSSR), higher-strength rock (HSR) and evaporite.

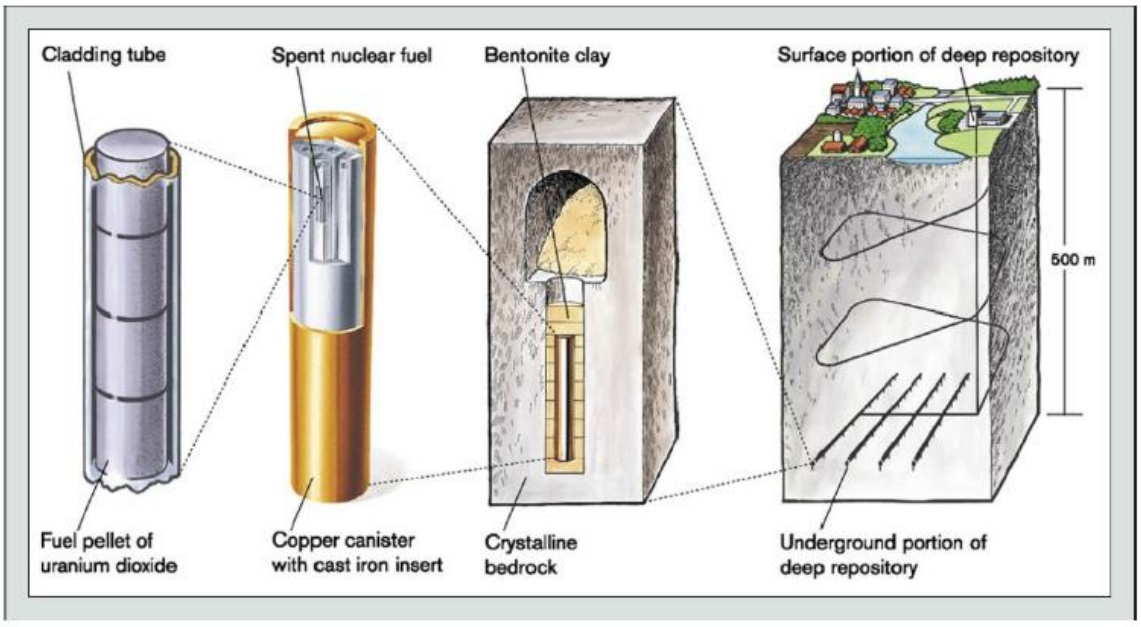

Figure 1.7: The KBS-3 concept for the disposal of spent nuclear fuel (SKB, 2004).

Although these rock types are present in the UK, no specific site for disposal has been selected. There is an ongoing national geological screening exercise, which is designed to provide information about potential geological suitability for the development of geological disposal facilities across the country (DECC, 2014).

Although the UK concept has its roots in the KBS-3 concept, the waste packaging options have been adapted in terms of length, diameter and specific design of cast iron insert, to allow variants to be used for the UK designs of spent fuel and vitrified HLW. The waste packaging option for HLW waste in the UK is such that liquid HLW is converted to a solid, more stable form by immobilising it in a borosilicate matrix (the process of vitrification) contained within sealed stainless steel containers known as WVP canisters (Figure 1.8) (Nirex, 2005a). The vitrified HLW package is designed to accommodate two standard WVP canisters, as illustrated in Figure 1.9. An outer copper (including a copper lid welded in place after waste loading) and an internal cast iron insert are being considered to provide additional long-term containment of the radioactivity, while also providing shielding to reduce external radiation levels. However, it is still a subject of debate whether copper should be included given the possibility of adverse effects on the steel canister after failure of the outer copper shell (NDA, 2014).

Figure 1.8: WVP canister for vitrified HLW in the UK (Nirex, 2005a,b).

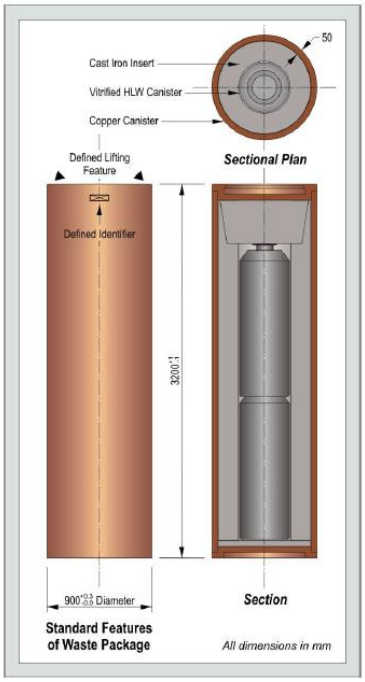

Figure 1.9: Standard features of vitrified HLW waste package in the UK (Nirex, 2005a,b).

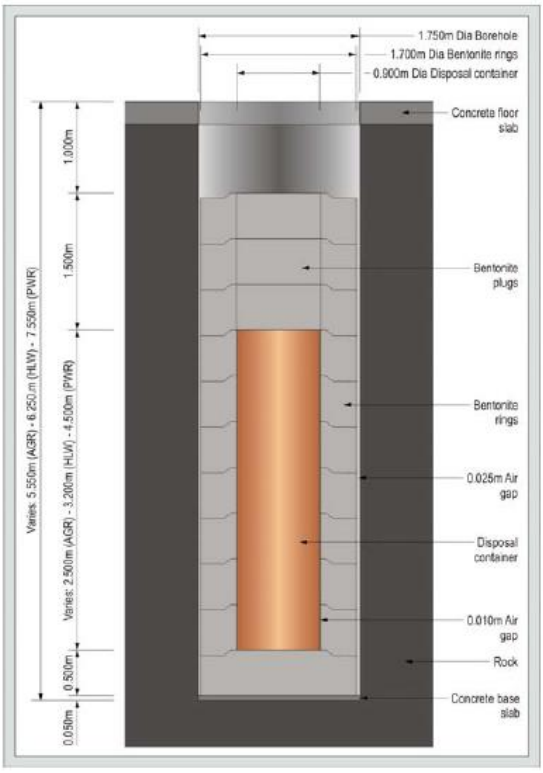

Figure 1.10: Schematic diagram showing the emplacement of the complete waste package in a depositional hole surrounded by an enveloping bentonite liner (Nirex, 2005a,b).

Following packaging, the complete waste packages would be transferred underground and emplaced in vertical deposition holes, surrounded by an enveloping bentonite liner, as shown in Figure 1.10 (Nirex, 2005a).

1.8 Performance Assessment of a Geological Repository

An assessment of the long-term performance of the geological repository is imperative in order to demonstrate its long-term safety. One major goal of performance assessment is to understand the relative contribution of repository components, particularly nuclear waste glass, to the overall safety of the disposal system. Nuclear waste glasses have been studied extensively using bench-scale experiments to understand their behaviour under repository conditions; however, as a result of the short duration of laboratory experiments, the best approach to conducting a performance assessment of a geological repository is by coupling experimental data with mathematical models (Ebert, 2015).

An important consideration in assessing the performance of the repository components is to address all the relevant migration pathways in the geological repository. However, it is noted that if the entire repository system were considered, the safety function of the waste glass would be masked by the efficiency of the host rock, as well as by the parameters controlling mass transfer in the far field (e.g. advection, diffusion, sorption). This implies that the study of near-field performance assessment is essential for demonstrating repository safety.

1.8.1 Modelling Radionuclide Transport in Geological Repository

As noted above, coupling transport and chemical reactions is necessary to understand how species are transported in a repository system. Reactive transport can be complex because it involves many species that need to be transported and reactions that modify the system. Models for the reactive transport of radionuclides in the repository vary greatly in scope and complexity, and have improved over the years. Today, there is considerably more emphasis on the use of physically based models to underpin the parameter values and modelling assumptions adopted in assessment-type models (Vikström and Gustafsson, 2006).

The main issue that arises in these models is the incorporation of uncertainty. Best-estimate point values were previously considered appropriate for model input parameters and to present the output of the model as best estimate results. However, there is increasing recognition that this can be misleading because it can give an

inappropriate indication of the degree of confidence in the results, since it is not associated with any measure of uncertainty (Thorne, 2012). It is now considered more appropriate to explore the range of results that can be obtained from models through the application of sensitivity and uncertainty analyses. Sensitivity analysis allows the values of the input parameters to be varied singly or in combination, and the resultant changes in the values of the output parameters are determined. In uncertainty analysis, the values of the input parameters are selected from their associated pdfs and the model is used to generate pdfs of the output parameters (SKB, 2006). The results from uncertainty analysis may be used to investigate the global sensitivity of the model to changes in one or more input parameters in the presence of uncertainties in others.

Because repository performance assessment models typically represent the redistribution of radionuclides in the environment with time, many of the equations used are ordinary differential equations. In physically based models, the advection–dispersion equation is used extensively, with water flow velocity obtained from the application of Darcy's Law in saturated material or a straightforward extension of it in unsaturated materials. However, the concept of compartmental modelling, in which the environment to be represented is partitioned into a finite number of compartments, is even more extensively used (Thorne, 2012).

1.8.2 GoldSim

A recent innovation in repository modelling is GoldSim. GoldSim is a dynamic, probabilistic simulation software developed by the GoldSim Technology Group (GTC). It is a general-purpose simulator written in C++ and is a hybrid of several simulation approaches, combining an extension of system dynamics with some aspects of discrete event simulation, and embedding the dynamic simulation engine within a Monte Carlo simulation framework (GTC, 2014). Although GoldSim can be used to solve a wide variety of complex problems, it is particularly well suited (and was originally developed) to supporting the evaluation of existing and proposed radioactive waste-management facilities. The contaminant transport features allow almost any kind of natural or man-made environmental system to be simulated. The GoldSim program has been used for numerous nuclear waste repository performance assessment studies: for example, the Yucca Mountain Project (Total Assessment System Performance; TSPA) (Bechtel SAIC, 2001) and the assessment of Granite Disposal of US High-Level Radioactive Waste (Mariner *et al.*, 2011).

As a compartmental-based model, GoldSim considers each compartment of the model to be well mixed. Therefore, if a quantity of a radionuclide enters a compartment it is instantaneously uniformly distributed throughout that compartment. Transfers between compartments or losses from the domain of the model are taken to be governed by first-order kinetics; that is, each rate of transfer is taken to be proportional to the quantity of radionuclide in the source compartment.

1.9 Open Scientific Questions

1. As discussed in Section 1.4, many aspects of nuclear waste dissolution in the presence of water have been understood and there is general agreement on the initial dissolution rate (especially with regard to experimental set-up); however, it remains unclear how interdiffusion and hydrolysis are coupled (Gin, 2014), as well as parameter dependence of dissolution rate. This highlights the need for a better understanding of the physical and chemical processes at a molecular level. In addition, there are significant uncertainties in the existing methods for estimating the evolving surface area of glass powder during reaction with solution (Fournier *et al.*, 2016). Therefore, designing a new surface area estimation method deserves serious consideration in order to reduce the uncertainties and increase the reliability of glass dissolution rates.
2. Although UK Magnox glass is a contemporary of French R7T7 glass (Harrison, 2014a), its dissolution behaviour has been studied less than R7T7-type glasses and is therefore less well understood. This indicates that there is a need for clarification on a number of important questions:
    a. What is the maximum dissolution rate of Magnox glass? Which are the rate-limiting mechanisms? Which are the most important parameters influencing the initial rate? What is the effect of flow rate on the dissolution rate? What is the role of H_4SiO_4? Does Mg have any role to play? How will the elemental components of the glass behave when the glass reacts with solutions at different temperatures?
    b. How will Magnox glass behave if it is dissolved in water with similar compositions to repository groundwater? What effects will the groundwater components have on the maximum rate? What implications would the interaction of the groundwater components with the glass have for the ability of the glass to retain radionuclides within its network bond?

3. For the reason that nuclear waste packaging options are still being examined in the UK and potential sites for construction of a geological repository are currently under screening, it is important to find answers to the following important questions:
    a. What is the role of waste glass in the retardation and release of radionuclides in the near field of a geological repository? How effective are other near-field components in isolating radionuclides?
    b. Which disposal concept in the UK would be optimal in effectively isolating radionuclides from the accessible environment for long periods of time? Would having an outer copper canister around the steel canister or a steel canister alone be advantageous in containing radionuclides, and to what degree?

1.10 Structure of the Thesis

This thesis is designed to answer all the questions highlighted in Section 1.9. The initial dissolution rates and dissolution behaviour of MW25 – a non-radioactive simulant of UK Magnox glass – were studied under different experimental conditions. The experimental method used to investigate the dissolution behaviour of MW25 in this study is the single-pass flow-through (SPFT) system. Chapter 2 provides detailed information regarding this experimental method and the procedures that were used in conducting the experiments; a new method for estimating the evolving surface area of powdered glass during reaction with solution is also presented in this chapter. Chapter 3 presents the results of experiments conducted at 40 and 90 ^{o}C and circum-neutral pH using deionised water. It should be noted that the initial rate of MW25 has never been studied at 90 ^{o}C using the SPFT. This is important because the majority of UK operational glass dissolution data held by Sellafield Ltd and the UK National Nuclear Laboratory relate to accelerated leaching experiments carried out at 90 ^{o}C; therefore, the understanding of this in the context of a ~40˚C repository has been identified as a research requirement for UK HLW glass disposal. Chapter 4 presents the results of experiments conducted at 40 ^{o}C and pH 7 using simulant groundwaters with similar compositions to those of the groundwaters of the two rock volumes, Callovo-Oxfordian clay and Borrowdale Volcanic Group rocks, that could potentially be suitable for the geological disposal of nuclear waste in the UK. Conducting experiments using deionised water and simulant groundwaters is useful and necessary in understanding the dissolution behaviour of MW25 in the presence and absence of solution compositions.

Detailed discussions of experimental results in Chapters 3 and 4 are presented in Chapter 5. This chapter also compares the dissolution rates and behaviour of MW25 under the different experimental conditions investigated. In Chapter 6 the experimental results in Chapter 4 (forward dissolution rates) are provided as source terms for reactive transport modelling using GoldSim. The main objective of this chapter is to understand the contribution of the nuclear waste glass to the release of radionuclides in a geological repository.

2 EXPERIMENTAL METHODS

2.1 Introduction

This chapter describes an experimental programme of work designed to measure the maximum dissolution rates of MW25, a non-radioactive simulant of UK Magnox glass. The experiments were divided into two parts. Experiments in part one were conducted with deionised water, whereas simulant groundwaters were selected as test solutions for part two of the experiments. The conditions of the experiments were intended to be representative of geological repository environments to which vitrified waste may be exposed after canister failure. The experimental programme consists of dependent tasks, which were carried out in sequence as illustrated in Figure 2.1.

Various experimental methods have been applied to modelling glass-dissolution behaviour, and both the experimental conditions and the parameters used are known to affect the response of the glass in the experiments. The objective of most experiments with waste glasses is to determine a parameter value for a mechanistic model to calculate long-term behaviour, where the release is controlled by diffusion, dissolution, or another process. Dynamic experiments, in which test solution flows through a bed of powdered material (or around a monolithic test specimen), simulate a geological repository environment more realistically than any other experimental methods (Ebert, 2010). Dynamic experimental methods are usually classified according to the apparatus used to control the flow rate and interaction with the test specimen; they include: single-pass flow-through (SPFT) reactor (McGrail *et al.,* 1997a), column reactor (White and Brantley, 2003), fluidised bed recirculating reactor (Chou and Wollast, 1984), pressurised unsaturated flow (PUF) reactor (McGrail *et al.,* 1997b), forced-through reactor (Butcher *et al.,* 1996), and Soxhlet reactor (Delage and Dussossoy, 1991). With

the exception of SPFT method, the reactors of all the dynamic experiments take the form of a column. The effect of several processes that occur simultaneously in the column, including solution flow, waste degradation, secondary phase formation and decrease of waste glass surface area, have been noted to complicate the interpretation of experimental results (Ebert, 2010).

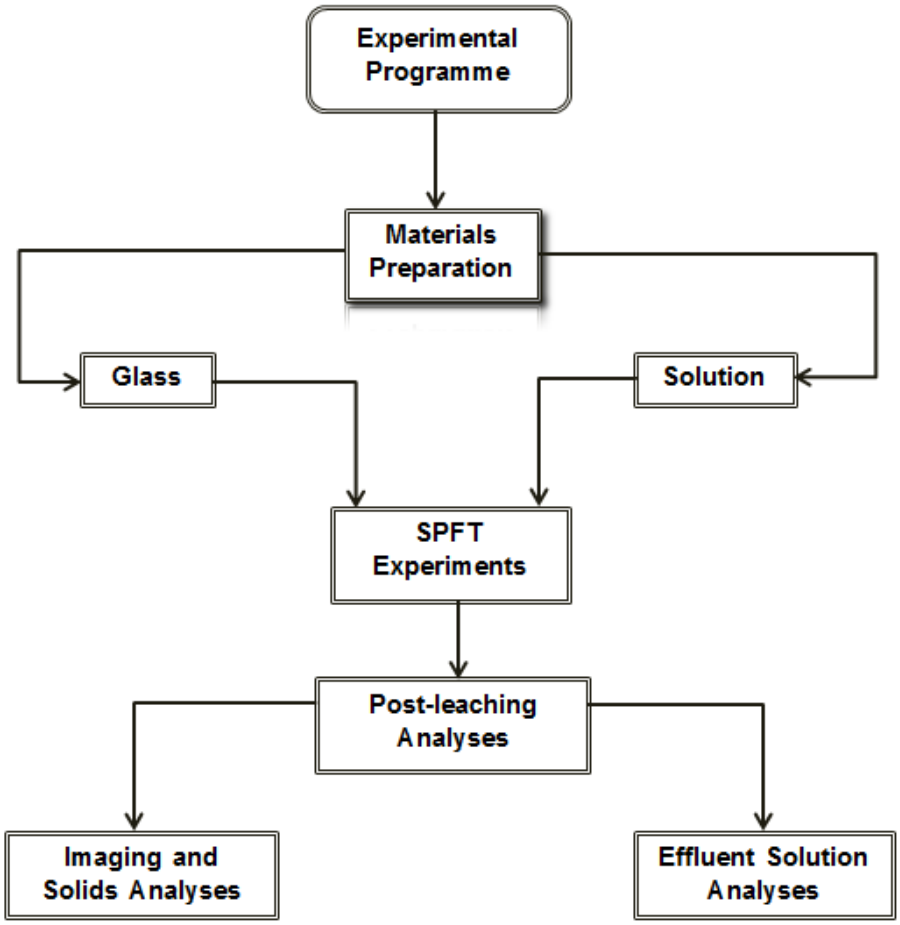

Figure 2.1: Flowchart showing the sequence of the main tasks of the experimental programme.

In the SPFT method, however, the dissolution of waste glass occurs by an affinity-controlled mechanism, wherein the dissolved components (e.g. silica) moderate the intrinsic dissolution rate of the glass, which is accomplished by continuously replacing the solution contacting the test specimen with fresh solution at constant flow rate (McGrail *et al.*, 1997a).

Post-leaching analyses, including inductively coupled plasma mass-spectrometry (ICP-MS) analysis, pH measurement, B.E.T. surface-area analysis, particle-size analysis, and

imaging and solids analyses, are used to investigate the dissolution behaviour of glass by examining both the solution and reacted glass specimen recovered from an experiment. The imaging and solids analyses are carried out using surface analytical techniques, including scanning electron microscopy (SEM), energy dispersive X-ray spectroscopy (EDX) and X-ray powder diffraction (XRD). These techniques are very useful in providing evidence regarding whether the glass is dissolving stoichiometrically, and whether particular leached layers and secondary phases were formed on the specimen surface. For the reason that the accumulation of leached layers and secondary phases on the glass surface is restricted through continuous solution renewal, surface precipitation is only expected at low thresholds of flow rate in the SPFT method.

All experiments and analyses in this study were carried out with strict adherence to the Control of Substances Hazard to Health (COSHH) guidelines, which cover all chemical handling and use in a workplace, as well as the local safety guidelines of the Department of Earth Sciences and Department of Materials Science and Mineralogy (University of Cambridge), where all experiments and analyses were conducted.

2.2 Material Preparation

2.2.1 Glass

The Magnox (MW25) glass used in this study, which was provided by the National Nuclear Laboratory (NNL) of the United Kingdom, is a simulant inactive HLW glass obtained from a container of simulated standard Magnox waste vitrified product with a 25 wt% waste loading manufactured on the vitrification test rig (VTR) at Sellafield. A picture of one of the pieces of the glass is shown in Figure 2.2. The chemical composition, as determined by analysis, is given in Table 2.1, on both a mole and weight per cent basis. The waste composition for this MW25 glass is based on a simplified inventory, with the radioactive elements replaced by their non-radioactive isotopes to maintain the chemistry and to come up with a non-radioactive simulant that is practical to use on a large scale and in large volumes. Samples from the pour of these demonstration products have been characterised in terms of their physical and chemical properties and were found to be homogeneous with about 1.3% uniformly distributed crystalline phases by volume, comprising ruthenium dioxide and a spinel phase (Scales, 2011). The density of the glass was measured independently by the Archimedes method, which gave a value of ~2.65 g/cm^3.

The powdered glass sample used in the dissolution experiments was prepared by crushing the glass sample in a mortar, and was then sieved to achieve a particle size of between 75 μm and 150 μm (i.e. -100 +200 mesh fraction). After crushing and sieving, the powdered sample was rinsed and cleaned ultrasonically in deionised water for 15 min and then rinsed in absolute ethanol to remove adhering particles that were outside the desired size range. This step was repeated several times until the decanted ethanol was clear. The glass powder was later dried for 12 h in an oven, which was set to 50 ^{o}C, and was subsequently stored at room temperature (~25 ^{o}C) in a sealed container containing silica gel desiccant.

Figure 2.2: A piece of the MW25 weighing approximately 300 g. The scale on the ruler on the lower edge of the photograph is in cm (by courtesy of NNL, UK).

2.2.2 Test Solution

For the reason that the site, design and local geology of a geological repository is, hitherto, unspecified in the UK, a range of test solutions representative of those that could be present in the final disposal environment were considered to investigate the chemical durability of MW25 in this study.

As mentioned previously the experimental programme was conducted in two parts, based on test solutions. The choice of deionised water in part one was motivated by two reasons:

Table 2.1: Analysed chemical composition, in weight and mole %, of MW25 glass.

Components	Oxide Wt.%	Element Mol%
Al_2O_3	4.30	3.97
B_2O_3	16.70	22.60
BaO	0.52	0.16
CeO_2	1.10	0.40
Cr_2O_3	0.64	0.40
Cs_2O	1.00	0.33
Fe_2O_3	3.00	1.77
Gd_2O_3	0.10	0.03
La_2O_3	0.56	0.16
Li_2O	4.00	12.61
MgO	4.50	5.26
MoO_3	1.40	0.46
Na_2O	8.50	12.92
Nd_2O_3	1.60	0.45
NiO	0.48	0.30
PO_4^{2}-	0.16	0.08
Pr_2O_3	0.52	0.15
RuO_2	0.49	0.17
SO_4^{2-}	0.10	0.05
SiO_2	47.10	36.93
Sm_2O_3	0.36	0.10
SrO	0.29	0.13
TeO_2	0.17	0.05
Y_2O_3	0.17	0.07
ZrO_2	1.40	0.54

- the leaching behaviour of glass in this solution can provide insights into the dissolution of the glass without the need to consider initial solution composition; and
- the pH range of deionised water is circum-neutral (pH 6.5–7.5), which is the natural pH range of most groundwater (Nelson, 2002).

For part two of the experiments, the test solutions used in the dissolution experiments are described as follows:

I. a simulant groundwater representative of lower strength sedimentary rock (LSSR) groundwater, based on Callovo-Oxfordian argillite groundwater composition from Bure in France (Gaucher *et al.*, 2006); and
II. a simulant groundwater representative of higher strength rock (HSR) groundwater, based on a groundwater composition RCF3 DET5 from Borrowdale Volcanic Group rocks near Sellafield in the UK (Bond and Tweed, 1995).

The target compositions of the two simulant groundwaters are presented in Table 2.2. The recipes used in the dissolution experiments were prepared to meet these target compositions. The test solutions were prepared by dissolving the required masses of component salts in deionised water. The deionised water was used within 5 min of being collected, eliminating the need for de-aeration prior to use. Because of its low concentration in the groundwaters, silicon was added as standard solution (1000 μg L^{-1}) in 2% sodium hydroxide solution. For the same reason, aluminium was added in HSR only as standard solution (50 μg L^{-1}) in 2% HCl solution. Approximately 60 g L^{-1} of saturated calcium hydroxide solution [$Ca(OH)_2$] was added in the LSSR solution as a result of the relative insolubility of calcium sulphate ($CaSO_4$). The pH of the resultant simulant groundwaters was maintained at ~7 by the addition of 1% HNO_3 solution.

2.3 Single-pass Flow-through (SPFT) Method

A recent innovation in simulating repository environment at bench-scale is the single-pass flow-through (SPFT) experimental method. The SPFT is a dynamic experiment, in which solution flows at a constant rate and constant temperature through reaction vessels containing test samples of nuclear waste glasses (or waste itself) (McGrail, *et al*. 1997a; Ebert, 2005). It is analogous to a column experiment, but no recirculation of solution occurs in the SPFT method (Neeway *et al.*, 2012). The SPFT method is the most appropriate for determining the reaction kinetics of glass dissolution (McGrail and

Peeler, 1995; McGrail *et al.*, 1997a; Abraitis, 2000a; Pierce *et al.*, 2008a). Experiments are conducted to attain steady-state conditions, as determined by the test solution composition, flow rate and the glass dissolution rate. Experiments can be conducted to maintain particular solution conditions to measure the effects of specific variables on the dissolution rate of the specimen.

Table 2.2: Compositions of the two simulant groundwaters selected for use in this study.

Component	LSSR (g L^{-1})	HSR (g L^{-1})
NaCl	-	2.00×10^{1}
Na_2SO_4	1.91×10^{0}	1.65×10^{0}
$NaHSO_4$	4.89×10^{-1}	-
$NaHCO_3$	-	8.60×10^{-2}
NaOH	2.74×10^{-4}	-
NaBr	-	3.24×10^{-2}
NaF	-	5.04×10^{-3}
KCl	-	3.32×10^{-1}
K_2SO_4	3.65×10^{-1}	-
$KHCO_3$	2.98×10^{-1}	-
$MgCl_2.6H_2O$	-	1.16×10^{0}
$MgSO_4.7H_2O$	3.48×10^{-0}	-
$CaCl_{2.2}H_2O$	2.82×10^{0}	4.22×10^{0}
$SrCl_2.6H_2O$	2.96×10^{-1}	5.52×10^{0}
pH	7	7

The SPFT experiment was originally designed to measure durability, matrix dissolution and dissolution kinetics of minerals (Knauss and Wolery, 1986; Dove and Crerar, 1990; Wellman *et al.*, 2006), nuclear waste glasses (Coles, 1981; Bates *et al.*, 1992; McGrail and Peeler, 1995; Abraitis *et al.*, 2000a,b,c; McGrail *et al.*, 2000; Pierce *et al.*, 2008a,b; Neeway *et al.*, 2012) and ceramic waste forms (McGrail *et al.*, 1999; Icenhower *et al.*, 2006). Recently, however, its application has been extended to other areas, such as characterisation of fluidised bed steam reformed (FBSR) mineral waste forms (Jantzen *et al.*, 2007; Neeway *et al.*, 2012).

Configurations of apparatus in most SPFT experiments are based on setups developed at the Lawrence Livermore National Laboratory (LLNL) (Bates *et al.*, 1992) and Pacific Northwest National Laboratory (PNNL) (McGrail and Peeler, 1995). These setups are modified forms of the configuration described in Knauss and Wolery (1986), which was also modified from Weed and Jackson (1979). In both setups, test solution is pumped through a reaction vessel and the effluent is collected in a vial for analysis. The primary difference in the apparatus is the design of the reaction vessel; the test sample is held within a column between two filters in the LLNL design, while in the PNNL design the sample rests in the bottom of the vessel (Figure 2.3). It is noted that the PNNL reaction vessel design is more common among investigators; for example: McGrail *et al.* (2000); Icenhower *et al.* (2006); Icenhower *et al.* (2008); Wellman *et al.* (2006); Pierce *et al.* (2008a,b); Neeway *et al.* (2012); Cantrell *et al.* (2013). The advantage of the PNNL reaction vessel design is provided by Icenhower *et al.* (2006), showing that, with samples at the bottom of the reaction vessel, fluid is prevented from being pumped directly in the sample. Therefore, bubbles formed during the fluid transfer do not become entrained in the sample, which could alter the exposed surface area, as may be the case for fluid flowing directly through a powdered specimen.

The reactor is often made of perfluoroalkoxy (PFA) or polytetrafluoroethylene (PTFE) Teflon vessels (Savillex). The volume of the reaction vessels used in various SPFT experiments usually falls between 20 and 80 mL. The flow rate of test solution normally varies from 2 to 300 mL/d based on data from various studies. Infusion or computer controlled syringe pumps are used to control the flow rate. The duration of the SPFT experiment is based on the solution concentration achieving steady state, which is largely dependent on flow rate (Ebert, 2005; Pierce *et al.*, 2008a). Lower flow rates are run for longer period, whereas higher flow rates enhance the achievement of steady state more rapidly. High flow rate, however, elevates the risk of the test yielding concentrations of elements in the effluent that are near or below the detection threshold.

A range of temperatures between 20 and 90 ^{o}C have been used in previous studies because this range is considered to be the most probable temperature range of the near field in a potential geological repository, with temperature gradient and heat from radioactive waste decay having been taken into account. Different solution pHs have been used by various investigators; however, the solution pH is almost always within the range of 7 to 12, which is consistent with the neutral to alkaline pH expected in a geological repository.

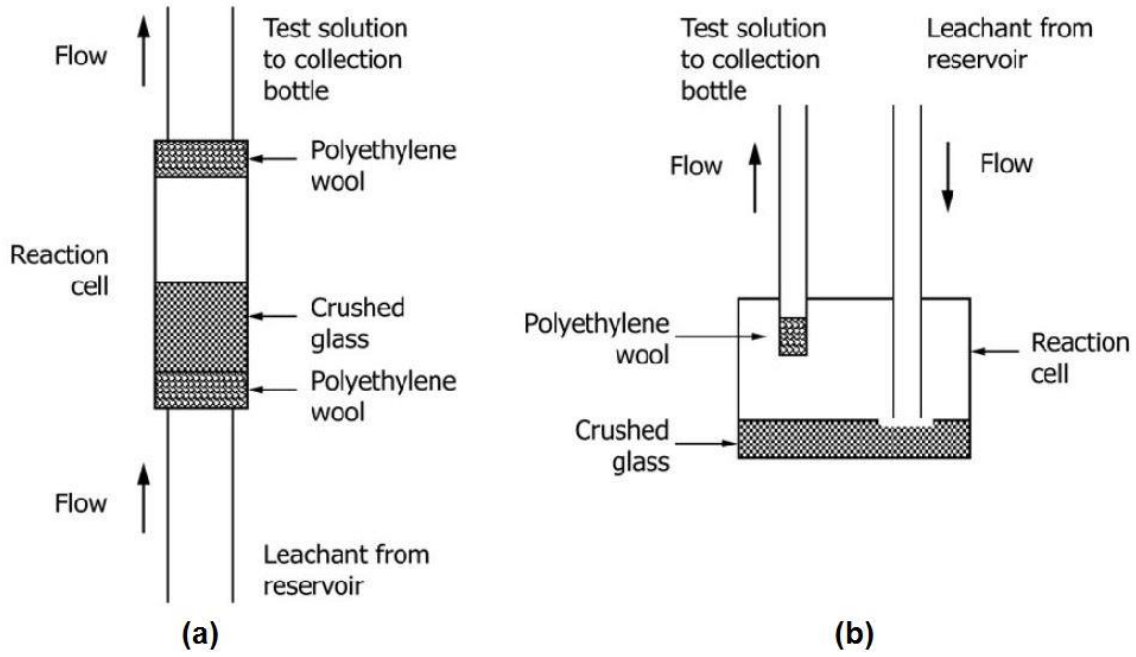

Figure 2.3: Reactor designs in SPFT method: (a) LLNL reactor design; (b) PNNL reactor design (adapted from Ebert [2005]).

2.3.1 SPFT Method and Affinity-controlled Dissolution

The effect of the affinity term, which is also known as the common ion effect, is often generically referred to as a solution feedback effect because it is the action of dissolved glass components promoting the reverse reaction that inhibits the net dissolution rate (McGrail *et al.*, 1997a; Abraitis, 2000a,b; Ebert, 2005). The SPFT experimental method has been designed to measure dissolution rate under conditions in which solution feedback effects are held constant by continuously replacing the solution in contact with the glass specimen with fresh solution (McGrail *et al.*, 1997a).

The rate law commonly used to model the kinetics of glass dissolution is consistent with the transition state theory (TST) (Åagaard and Helgeson, 1982), which, for the purpose of borosilicate glass dissolution modelling, has been simplified by Grambow (1985):

$$r = \vec{k}_0 v_i e^{-E_a/RT} a_{H^+}^{\eta} \left[1 - \left(\frac{Q}{K_g}\right)^{\sigma}\right] \prod_j a_j^{\eta_i}, \qquad i = 1, 2, \ldots, N \tag{2.1}$$

where r is the dissolution rate (g m^{-2} d^{-1}), k_0 is the intrinsic rate constant (g m^{-2} d^{-1}), v_i is the mass fraction of element *i*, E_a is the activation energy (kJ mol^{-1}), R is the gas constant (kJ mol^{-1} K^{-1}), *T* is the temperature (K), a_{H^+} is the hydrogen ion activity, η is the pH power law coefficient, Q is the activity product (unitless), K_g is the pseudo-equilibrium constant (unitless) and σ is the Temkin coefficient (reaction order).

Thermodynamic reaction affinity is represented by the term in squared brackets, where $\boldsymbol{Q}/K_g$ gives the ratio of the solution concentration to that of an apparent saturated solution. The term $\boldsymbol{\Pi}_j a_j^{ni}$ represents additional terms that may be needed to model some materials to take into account other chemical effects, such as solutes that catalyse (or inhibit) the reaction.

The rate law in Eq. (2.1) indicates that reactions governing dissolution are microscopically reversible, as implied by the presence of an affinity term (Lasaga, 1981). Glass is thermodynamically unstable; therefore, the solution can never become saturated and a true equilibrium between the glass phase and the solution cannot exist (McGrail *et al.*, 1997a). The application of Eq. (2.1) for modelling glass dissolution in a geological repository system requires the determination of k_0, E_a and η under experimental conditions, where the value of $\boldsymbol{Q}$ is maintained near zero, so that the affinity term remains near unity. The dissolution rate under these conditions is referred to as the forward dissolution rate, which is the highest dissolution rate that can occur at a particular pH and temperature. The value of the parameter K_g is determined from experiments in which the value of $\boldsymbol{Q}$ approaches the value of K_g, resulting in a decrease in the affinity term and dissolution rate. The mass fraction, v_i, is determined by glass composition, while σ is often assigned as 1, as suggested by Lasaga (1995) for dissolution of minerals.

2.3.2 Measurement of Forward Dissolution Rate in the SPFT Method

For a reaction that is at equilibrium, the chemical affinity, as well as the net reaction rate, is zero. The affinity term provides the link between the kinetics of a system in disequilibrium and the thermodynamics of that disequilibrium. For a system that is not at equilibrium, the forward rate will be modulated by a term having a value between zero and unity that represents the degree of disequilibrium (Ebert, 2010). This implies that the forward rate is moderated by the affinity term. The forward rate describes the kinetics of the reaction that leads to the dissolution of the glass; that is, the rate-limiting step in the reaction mechanism. The forward rate includes all the terms that precede the affinity term in Eq. (2.1) and depends on glass composition, temperature and pH, and may also depend on other solute concentrations (McGrail *et al.*, 1997a; Ebert, 2005).

SPFT experiments are conducted under several experimental conditions to yield a range of quantifiable solution concentrations. Dissolution rates are measured from the steady-state concentrations and the mass fraction of the component that is being used to track

the extent of dissolution, along with the solution flow rate and glass surface area. To estimate the forward rate, ASTM C1662 (ASTM, 2010) recommends extrapolation of the plot of the measured dissolution rates and steady-state concentrations to zero (i.e. an infinitely dilute solution). However, because the dissolution rate is sensitive to the ratio of the solution flow rate to glass surface area (q/S), the preferred approach among researchers in determining the forward rate is to plot the measured dissolution rates as a function of q/S.

The dependence of the forward rate on experimental conditions, including temperature and pH, can be modelled based on mechanistic or empirical insights (McGrail *et al.*, 1997a; Abraitis *et al.*, 2000a; Pierce *et al.*, 2008a). Temperature and pH dependence of dissolution rates of glasses are commonly modelled as:

$$r_i = \vec{k}_0 . 10^{\eta pH} . e^{\frac{-E_a}{RT}} \quad \textbf{(2.2)}$$

where r_i is the dissolution rate of glass component *i* (g m^{-2} d^{-1}), k_0 is the intrinsic rate constant (g m^{-2} d^{-1}), η is the pH dependence, E_a is the activation energy kJ mol^{-1}, R is the gas constant (kJ mol^{-1} K^{-1}), and T is the temperature (K). The effects of pH and temperature on the net-dissolution rate expressed as η and E_a can be determined by conducting a separate series of experiments with the same glass at constant pH or constant temperature (McGrail *et al.*, 1997a). For example, in the present study, the pH of the test solutions was maintained at a constant value to enable the determination of the dependence of rate of dissolution of MW25 on temperature.

2.3.3 Preference of SPFT Method over Batch Experimental Method

The benefit of employing the SPFT method to simulate a geological repository environment is clear, although it is batch experiments that are the most extensively used. The periodic manual replenishment of solution in batch experiments imposes severe complications on the interpretation of the experimental results (McGrail *et al.*, 1997a). Abraitis *et al.* (2000a) posit that the excellent fit obtained by matching a multiple barrier model to batch experimental data does not necessarily indicate that the model is correct, since model parameters are often obtained from the same experiments to which the model is applied (Bourcier, 1994). They argue that maintaining solute concentrations below levels likely to result in secondary product, and maintaining far-from-saturation conditions, are experimentally difficult given the typical rate of glass dissolution. In addition, distinguishing between inhibitory effects and potential

contributions to affinity term for glass-derived species in batch experiments is problematic (McGrail *et al.,* 1997a; Abraitis *et al.,* 2000a). Recently, Cassingham *et al.* (2015) alluded to solution feedback effects, which are intrinsically associated with batch experiments, as the cause of inconsistencies in the forward rate of UK Magnox glass measured in previous studies (Utton *et al.,* 2012; Corkhill *et al.,* 2013).

The preference for the SPFT method in this study stems from the fact that it is the most appropriate for maintaining far-from-saturation conditions that can be used to determine the reaction kinetics of glass dissolution (McGrail *et al.,* 1997a). In the SPFT method, solution replenishment is automatic and continuous. The design of SPFT experiments enables fixed solution chemistry to be maintained by balancing the flow rate with the glass dissolution rate, which is indicated by species participating in the balanced reaction attaining steady-state concentrations (McGrail *et al.,* 1997a; Ebert, 2005). These features of SPFT are imperative in minimising the uncertainty associated with rate-constant determination, and because the solution always remains dilute this method allows key rate-influencing factors to be systematically isolated and makes possible the parameterisation of the general rate law expression (McGrail *et al.,* 1997a). Studies by Pierce *et al.* (2008b) on aluminoborosilicate waste glass have indicated that flow rate has a significant influence on the release behaviour of glass components. This underlines the importance of running tests at several flow rates, which is only achievable using the SPFT method.

2.3.4 Powdered and Monolithic Glass Specimens in SPFT Experiments

Most SPFT experiments have been conducted with powdered glass specimen, although quantifying the available surface area is more straightforward in experiments conducted with monolith samples with measurable dimensions. Icenhower and Steefel (2015) conducted SPFT experiments using both powders and monoliths of glass and reported that rates determined from the two specimens agreed within experimental uncertainty. The preference in this study was powdered glass because of the relatively high specific surface area (i.e. surface area per unit mass) and greater homogeneity expected for small particles. The proportionately higher specific surface area of small particles at laboratory-scale is easy to scale and enables reliable characterisation of the surface properties of the very large volumes of material that are of interest to field analyses (Ebert, 2010). A spherical particle with diameter d and density ρ has a surface area-to-volume ratio of 6/d and a specific surface area of 6/(dxρ). Assuming that a powdered

glass specimen has a nominal density of 3 g cm^{-3}, the specific surface area will scale as 2/d. This implies that the specific surface area decreases rapidly with particle diameter, such that a particle that is 20 mm in diameter has a specific surface area that is 10% that of a 2-mm diameter particle. Therefore, particles that are 2 mm and smaller provide the maximum surface area (and representation of the mineralogy) with the minimum volume in laboratory experiments, such as SPFT.

The surface area of a reacted powdered glass can be estimated based on the geometric method (McGrail *et al.,* 1997a) or measured by B.E.T. analysis (Brunauer *et al.,* 1938). Given that the irregular shapes and surface roughness of glass particles create difficulties in the measurement of the surface area of glass powder, dissolution rates measured using both surface area estimation methods have often yielded different values. Although neither method provides an accurate estimate of the surface area of powdered glass, for the reasons outlined in previous studies (McGrail *et al.* 2000; Wolff-Boenisch *et al.*, 2004; Icenhower and Steefel, 2013), the geometric estimate is a more appropriate appraisal. Recently, Fournier *et al.* (2016) found that initial rates measured using the geometric estimate were closer to initial rates measured using the monolith sample than those measured using the BET method. Based on these findings, they concluded that the geometric estimate provides a better estimate of the surface area of glass powder than the BET method; however, an important caveat placed on this conclusion is that the initial rates measured using both surface area estimates can be up to 25% uncertain. McGrail *et al.* (1997a) have postulated that the geometric estimate should be within the error margin of the actual surface area. Because of the large uncertainties in surface area, the need for more work has been emphasised in order to reduce the uncertainties and increase the reliability of glass dissolution rates (Ebert, 2005; Neeway *et al.*, 2012).

2.4 Design of the SPFT Experiment

All dissolution experiments in this study were conducted with the single-pass flow-through (SPFT) system. The design of the SPFT system is shown schematically in Figure 2.4. Two automated programmable syringe pumps (Kloehn; V6 55 Series multi-channel model) operate in an asynchronous manner, such that as one pump is dispensing, the other pump is refilling, thereby continuously transferring solution from the input reservoir to the reactor. The transfer of the solution to and from the reactor was accommodated by 1/8 inch (outer diameter; OD) perfluoroalkoxy (PFA) pipes. The

output ports of both pumps were connected together with a T-connection to sum the two outputs into a single delivery line, facilitating a continuous fluid flow. The continuous flow of solution in SPFT experiments moderates the accumulation of reaction products in the reactor, which is essential in:

- minimising the build-up of reaction products;
- maintaining the bulk solution composition throughout the duration of reaction; and
- quantifying the dissolution rate directly.

The polytetrafluoroethylene (PTFE) reactor vessels (Savillex) consisted of lids and jars that combined together to form a total inner volume of 60 mL. The ingress and egress of solutions through each reactor was accommodated by two 1/8 inch (OD) ports in the lid. Each reactor was emplaced inside an aluminium block and both were housed within an oven (SciQuip; model 30S), which served as the heat source. The final 60 cm of the inlet pipe was placed inside the oven in order to maintain the temperature of the influent solution within 1 ^{o}C of the temperature inside the oven (i.e. test temperature). To eliminate the formation of bubbles in the pipes, the solution reservoir was placed inside a heating block (Grant; model QBH2), which was set to the test temperature, so that outgassing occurred within the reservoir and gases were not pumped through the system. Aliquots of effluent solution were delivered into tared effluent collection vessels placed outside the oven. The collection vessels were washed sequentially with 1% nitric acid solution and deionised water, and were left to dry prior to use. The pH of the solutions was maintained by purging an N_2 gas stream into the headspace between the solution in the reservoir and the lid of its container to prevent the uptake of CO_2.

Two blank solutions were drawn prior to placing the glass sample in the reactor as control tests. The background concentration was set to the value of the machine detection limit for an element in the case that the element was not detected. In addition to the control tests, the system was flushed between each test with three reactor volumes of 1% nitric acid solution, and subsequently with four reactor volumes of deionised water prior to conducting each test, to ensure that contamination from the previous test was at the bare minimum.

2.4.1 Test Temperatures

Temperature is an important parameter for the release rate because the forward dissolution rate of waste glass has been found to increase exponentially with increasing temperature (Pierce *et al.,* 2008a). Previous studies on the dissolution of UK Magnox glass were conducted using a wide range of temperatures; for example: 40 ^{o}C (Abraitis *et al.* 2000a); 90 ^{o}C (Curti *et al.,* 2006); 30, 50, 70 and 90 ^{o}C (Utton *et al.,* 2012); 50 ^{o}C (Utton *et al.,* 2013); and 23, 40 and 70 ^{o}C (Cassingham *et al.,* 2015).

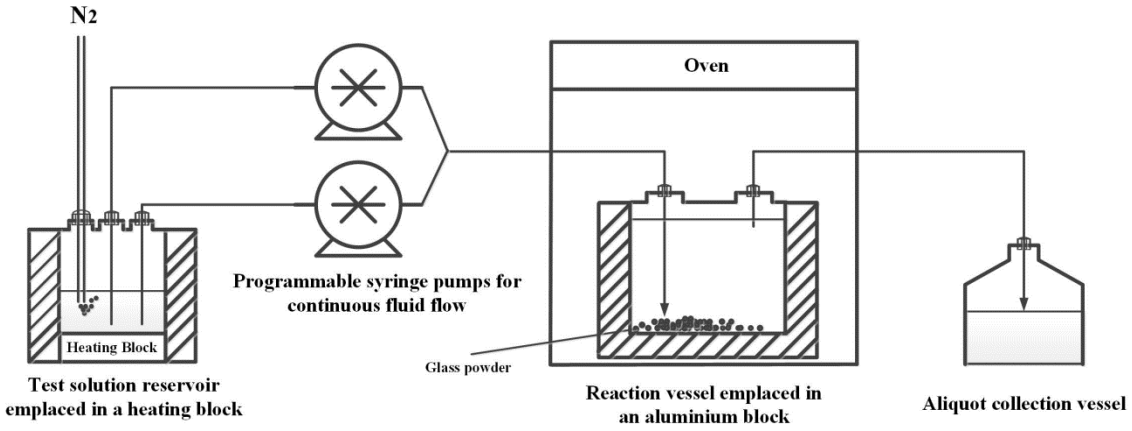

Figure 2.4: Schematic of the single-pass flow-through system. The PNNL reactor design was used. The illustration only shows a single reactor vessel; the apparatus used has a capacity of eight separate reactor vessels that can be run simultaneously at the same temperature and flow rate.

In this study, test temperatures of 40 and 90 ^{o}C were chosen for the experiments that were conducted with deionised water, whereas only 40 ^{o}C was selected for the experiments that were conducted with simulant groundwaters. The test temperatures were continuously monitored during the experiments using a digital thermocouple that was fixed to the oven.

The scientific rationales behind the choice of these test temperatures are listed below:

- 40 ^{o}C lies within 30 and 50 ^{o}C, which is the expected temperature range at the time of canister failure when the glass may be exposed to solution (Bond and Tweed, 1995);
- the choice of 90 ^{o}C enables a comparison of this study with the available dissolution data, as large numbers of experiments have been conducted at this temperature for many nuclear waste glasses; and

- ease of conducting experiments at 40 and 90 ^{o}C, considering solution analysis detection limits and measurement of solution concentrations of leached glass components.

2.4.2 Solution Flow Rates

The design of the SPFT system permits independent control over flow rates and all experiments were conducted at flow rates ranging from ~10 mL d^{-1} to 250 mL d^{-1} (~0.2 to 4.2 reactor volumes per d). Specifically, 6 different flow rates were used in both experimental parts, which are: 10, 25, 50, 75, 125 and 250 mL d^{-1}. Computer programs were used in setting the speed of the pumps, which were converted to the target flow rates used in running the experiments (see Appendix 1 for details of the programming of the pumps and conversion from pumps' speeds to the target flow rates).

The wide range in flow rates, together with adjustments to the sample surface area, which was achieved by varying the mass of glass powder between ~0.1 g and 0.5 g, were used to produce a range of ratios of flow rate to surface area (q/S) values for the experiments conducted with deionised water. However, experiments with simulant groundwaters were conducted with ~0.5 g glass powder, so that ratios of flow rate to surface area (q/S) values were obtained by varying only the flow rates. Although flow rate was programmed before the start of the experiments, the flow rate used in the computation of dissolution rate was determined gravimetrically. That is, the mass of the solution collected at each sampling was divided by the duration of the experiment and the density of the solution to obtain the volumetric flow rate. Variations in flow rates with each aliquot taken during an experiment were typically less than 2%.

2.4.3 Determination of Surface Area of Glass Powder

2.4.3.1 Initial Surface Area Determination

The pre-leaching surface area was calculated by multiplying the sample mass of glass powder by the specific surface area. The specific surface area of the glass powder was estimated using the geometric formula:

$$\boldsymbol{SSA_{geo} = \frac{6}{\rho d}} \qquad \textbf{(2.3)}$$

Where SSA_{geo} is the specific surface area (m^2 g^{-1}), ρ is the glass density (g m^{-3}) and d is the average diameter (m). The geometric formula assumes that the glass particles are

uniformly spherical with no porosity, and the estimated specific surface area is 0.0201 $m^2\ g^{-1}$.

The specific surface area of the unleached glass powder was also estimated using B.E.T. method, with N_2 as the adsorbing gas. The B.E.T. analysis was carried out in the Department of Materials Science and Metallurgy at the University of Cambridge, UK. Results of triplicate analyses yielded a mean specific surface area of 0.192 m^2/g, which is approximately ten times larger than the corresponding geometric estimate. The ratio of B.E.T. with geometric surface area is commonly referred to as the surface roughness (SR) factor. The SR factor of ~10 obtained in the present study is consistent with that from a study conducted with MW25 glass (Schofield *et al.*, 2016); however, an SR factor that ranges from 3 to 7 is typically reported for other nuclear waste glasses.

2.4.3.2 Post-leaching Surface Area Determination

Estimation of the surface area of powdered glass during glass dissolution experiments, such as SPFT experiments, is complicated by the changes that each sample undergoes over the duration of the experiment. To consider this effect, McGrail *et al.* (1997a) used a geometric calculation to estimate the surface area of reacted glass powder, which is given as follows:

$$\boldsymbol{s_i = \frac{6}{\rho d_o} m_o^{1/3}\, m_i^{2/3}} \qquad \textbf{(2.4)}$$

where s_i is the surface area of the glass sample at time interval i (m^2), ρ is the density (g m^{-3}), d_o and m_o are the diameter (m) and mass (g) of the powder sample, respectively, before leaching. The parameter m_i represents the mass of sample remaining at time interval i and is computed from the following expression:

$$\boldsymbol{m_i = m_o - \frac{1}{f_k}\left[\sum_{j=1}^{i-1} q_j\, C_{j,k} \Delta t_j + q_i C_{i,k} \frac{\Delta t_i}{2}\right], \quad i \geq 1} \qquad \textbf{(2.5)}$$

where f_k and C_k are the mass fraction (unitless) and concentration (g/L), respectively, of the most representative element of the true amount of glass dissolved, q is the flow rate, the accumulated mass loss up to time step $i - 1$ is represented by the summation term, and the second term in the brackets represents half of the total mass loss from time $i - 1$ to i.

The geometric method presented in Eq. (2.4) assumes that the powdered glass is adequately represented by spherically shaped particles. McGrail *et al.* (1997a), and

others (Icenhower and Steefel, 2013), have shown that the geometric method provides a better estimate of the surface area than the B.E.T. method; indeed, this method has been applied to estimate the post-leaching surface area in several studies (e.g. Abraitis *et al.*, 2000a; Ebert, 2005; Pierce *et al.*, 2008a,b). However, the diameter (d_o) in Eq. (2.4), which is assumed to be constant over the duration of the experiment, represents a flaw in the geometric method, even though d_o is normally taken to be the mean diameter of the unreacted glass particles. This is because the diameter of each glass particle does not remain constant but changes in the course of the reaction. In addition, finer-grained particles present higher specific surface area to the test solution; therefore, they dissolve more rapidly than coarser-grained particles. Eventually, this results in a skewed distribution of the glass particles, which cannot be appropriately represented by the mean value of the diameters of the unreacted particles.

2.4.3.3 A New Method to Estimate the Post-leaching Surface Area

In order to resolve the inadequacy of the geometric method, an effort has been made in this study to develop a new method, which uses a numerical approach to estimate the surface area of reacted glass powder. Grain size analysis was conducted on unreacted glass powder as the starting point. The grain size analysis was carried out in the Department of Materials Science and Metallurgy at the University of Cambridge, UK. The instrument used was MasterSizer 3000 (Malvern Instruments, UK), which uses a laser diffraction technique to measure the size of the particles. This instrument has the capability to measure particle sizes in the distribution between 0.01 and 3500 μm with 0.6% accuracy, according to the manufacturer's manual. The results of triplicate grain size analyses show that the size distribution of the particles falls roughly within the 75–150 μm size range (Figure 2.5).

Assuming that each glass particle is spherical in shape and there is an absence of surface roughness, such as cracks and pits, the size of each particle can be considered as the diameter (*d*). Moreover, assuming that the grain size distribution is a plot of percentage (*f*) of the number of particles, and if the total number of glass particles in the distribution is N, the number of particles (N_d) with a given diameter will be:

$$\boldsymbol{N_d = \frac{fN}{100}}$$

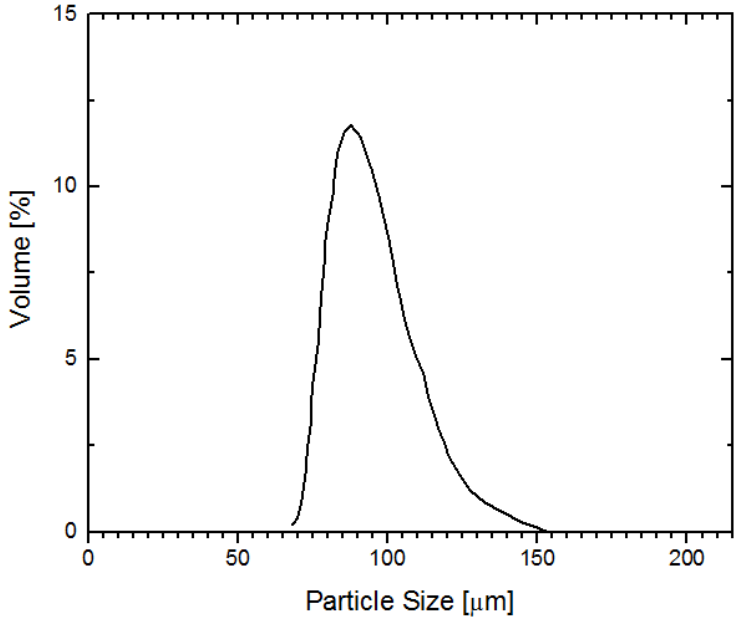

Figure 2.5: Size distribution of the particles in the unleached powdered glass.

If we define,

$$\boldsymbol{F = \frac{f}{100}}, \qquad \boldsymbol{\sigma = d^2}, \qquad \boldsymbol{\tau = d^3}$$

the volume (V_p) of a glass particle will be:

$$\boldsymbol{V_p = \frac{\pi\tau}{6}} \tag{2.6}$$

Hence, the mass (m_p) of a glass particle will be:

$$\boldsymbol{(m_p) = \frac{\rho\pi\tau}{6}} \tag{2.7}$$

where ρ is the glass density.

Therefore, the mass (m) of the powder sample can be derived:

$$\boldsymbol{m = \int_0^\infty \frac{fN}{100} d\left(\frac{\rho\pi\tau}{6}\right)}$$

$$\boldsymbol{m = \left(\frac{\rho\pi N}{6}\right) \int_0^\infty F d\tau} \tag{2.8}$$

By rearranging Eq. (2.8), the number of glass particles in the powder sample is obtained, as shown in Eq. (2.9):

$$\boldsymbol{N = \frac{6m}{\rho\pi \int_0^\infty F d\tau}} \tag{2.9}$$

Surface area (S_p) of a glass particle is:

$$(\boldsymbol{S_p}) = \boldsymbol{\pi\sigma} \tag{2.10}$$

Therefore, the surface area (S) of the powdered glass sample can be derived:

$$\boldsymbol{S} = \int_0^\infty \frac{\boldsymbol{fN}}{\mathbf{100}} \boldsymbol{d(\pi\sigma)}$$

$$\boldsymbol{S} = \boldsymbol{\pi N} \int_0^\infty \boldsymbol{F d\sigma} \tag{2.11}$$

Since the rate of reaction is proportional to the surface area, and surface area is proportional to the square of the diameter, change in mass ($\boldsymbol{\Delta}$m) can be expressed as:

$$\boldsymbol{\Delta m} = \boldsymbol{K_t S} \tag{2.12}$$

where K_t is a constant of proportionality, which contains the kinetics of the reaction.

Therefore,

$$\boldsymbol{K_t} = \frac{\boldsymbol{\Delta m}}{\boldsymbol{S}} \tag{2.13}$$

For each glass particle, therefore:

$$\boldsymbol{\Delta m} = \boldsymbol{\pi K_t \sigma} \tag{2.14}$$

Similarly, the change in volume ($\boldsymbol{\Delta}$V) of each glass particle can be expressed as:

$$\boldsymbol{\Delta V} = \frac{\boldsymbol{\pi K_t \sigma}}{\boldsymbol{\rho}} \tag{2.15}$$

Hence, volume (V_i) at time interval *i* can be calculated as shown in Eq. (2.16):

$$\boldsymbol{V_i} = \frac{\boldsymbol{\pi\tau}}{\mathbf{6}} - \frac{\boldsymbol{\pi K_t \sigma}}{\boldsymbol{\rho}} \tag{2.16}$$

Equating Eq. (2.16) with the volume estimated when the diameter of the glass particle has changed gives:

$$\frac{\boldsymbol{\pi d_i^3}}{\mathbf{6}} = \frac{\boldsymbol{\pi\tau}}{\mathbf{6}} - \frac{\boldsymbol{\pi K_t \sigma}}{\boldsymbol{\rho}} \tag{2.17}$$

where d_i is the diameter at time interval i .

Therefore,

$$\boldsymbol{d_i} = \left(\boldsymbol{\tau} - \frac{\mathbf{6}\boldsymbol{K_t \sigma}}{\boldsymbol{\rho}}\right)^{\mathbf{1/3}} \tag{2.18}$$

This new method can be used to estimate the post-leaching surface area of powdered glass by solving Eqs. (2.9), (2.11) and (2.18) numerically using computational software, such as MATLAB or OCTAVE. The computer codes that were used to estimate the post-leaching surface area in the present study are presented in Appendix 2.

Importantly, the mass lost after leaching is required in order to use this new method, and this can be obtained from Eq. (2.5) by subtracting mass after a particular time interval from the mass of the glass specimen before leaching.

2.4.4 Pre- and Post-leaching Solution Analyses

2.4.4.1 Measurement of pH

Test solutions and aliquots of effluent solutions were routinely monitored for pH. The pH probe (Mettler Toledo) was calibrated with the National Institute of Standards and Technology Traceable Reference Material (NTRM^{TM}) buffer (pH 7.00 and pH 4.01). The pH of the deionised water ranged from 6.91$\pm$0.02 to 7.26$\pm$0.02 and that of both simulant groundwaters was 7.00$\pm$0.02. The pH of a portion of the aliquot was measured within 30 min after each experiment had been completed. The remainder of the effluent solution was acidified to ~1% HNO_3 and kept at room temperature for analysis of the glass components using ICP-MS.

2.4.4.2 Inductively Coupled Plasma Mass Spectrometry (ICP-MS) Analysis

All samples were analysed on a Perkin Elmer Nexion 350D ICP-MS (Inductively Coupled Plasma - Mass Spectrometer) in the Department of Earth Sciences at the University of Cambridge, UK. The calibration standards were prepared as an external calibration using serial dilutions of standards (blank, 1, 5, 10, 100, 200 ppb) prepared from single-element high-purity standards (CPI, California, USA) in high-purity 1% HNO_3 (quartz distilled in-house). The ICP-MS internal standards were 10 ppb Rh, In and Re, and each sample was prepared in 1% HNO_3, added online with a t-piece and mixing tube prior to the nebuliser. An independently prepared quality control standard (SPS-SW2, LGC Standards, UK) was repeatedly analysed throughout the run to check for calibration accuracy (~5%) with similar precision. Instrumental drift was less than 10% measured for the raw intensity of the internal standards during the entire analytical run (50 or more solutions per batch). Solutions were analysed using a Micromist FM05 microconcentric nebuliser using a pumped flow rate of 80 ul/min (Glass Expansion, Australia) and a quartz cyclonic baffled spray chamber with nickel sampler and

skimmer cones. ICP-MS sensitivity in this configuration was 1.5×10^5 cps/ppb In with CeO/Ce ratios = 2%. Concentration results were calculated using the Syngistix 1.1 software with a simple linear calibration line and intercept set to zero. The raw intensities were blank subtracted and internal-standard normalised before calibration calculations were performed. All results (unknowns and standards) were accurately corrected for dilutions by mass.

2.4.5 Rate Determination and Error Calculation

Normalised dissolution rates were calculated based on steady-state concentrations of the elements in the effluent using the following formula (McGrail *et al.*, 1997a):

$$\boldsymbol{r_i = \frac{(C_i - \overline{C}_{i,b})q}{f_i S}} \qquad \textbf{(2.19)}$$

where r_i is the normalised dissolution rate (NR_i) for element *i* (g m^{-2} d^{-1}), C_i is the concentration of the element *i* in the effluent (g L^{-1}), $C_{i,b}$ is the average background concentration of the element of interest (g L^{-1}), q is the volumetric flow rate (mL d^{-1}), f_i is the mass fraction of element *i* in the original glass (unitless) and S is the surface area of the glass sample (m^2). Details of the computation of mass fraction together with mole per cent of each element based on the compositions of the glass are presented in Appendix 3.

The rate in Eq. (2.19) is based on the release of element and normalised to the surface area of the glass used in the test, and is therefore referred to as the normalised dissolution rate (NR_i) (Ebert, 2005). The geometric method (Eq. [2.4]) is commonly used to take the change in surface area during the test into consideration; however, based on the foregoing argument, the geometric method is not entirely adequate for this purpose. Therefore, the new method (numerical approach) discussed in Subsection 2.4.3.3, which considers the change in diameter of the glass sample as the reaction proceeds, was used to estimate the surface area of the reacted glass sample in this study.

The propagation-of-error method was employed to estimate uncertainties in the rates calculated for individual tests within each set of experiments, taking into account the uncertainties of each parameter in Eq. (2.19) (Ebert, 2005). The probable error ($\boldsymbol{Q}$) associated with a property *P* that is a function of measured values x_1, x_2, x_3,…, x_N can be expressed in terms of the probable error in the means of the measured values as:

$$\boldsymbol{Q_P}^2 = \left(\frac{\boldsymbol{\delta P}}{\boldsymbol{\delta x_1}}\right)^2 . \boldsymbol{Q_1}^2 + \left(\frac{\boldsymbol{\delta P}}{\boldsymbol{\delta x_2}}\right)^2 . \boldsymbol{Q_2}^2 + \left(\frac{\boldsymbol{\delta P}}{\boldsymbol{\delta x_3}}\right)^2 . \boldsymbol{Q_3}^2 + \ldots \quad \textbf{(2.20)}$$

Therefore, the probable error in the normalised rate (NR_i) calculated in Eq. (2.19) is:

$$\boldsymbol{Q_{NR_i}}^2 = \left(\frac{\boldsymbol{\delta NR_i}}{\boldsymbol{\delta C_i}}\right)^2 . \boldsymbol{Q_{C_i}}^2 + \left(\frac{\boldsymbol{\delta NR_i}}{\boldsymbol{\delta q}}\right)^2 . \boldsymbol{Q_q}^2 + \left(\frac{\boldsymbol{\delta NR_i}}{\boldsymbol{\delta S}}\right)^2 . \boldsymbol{Q_S}^2 + \left(\frac{\boldsymbol{\delta NR_i}}{\boldsymbol{\delta f}}\right)^2 . \boldsymbol{Q_{f_i}}^2 \quad \textbf{(2.21)}$$

where $\boldsymbol{Q}_{\mathrm{NRi}}$, $\boldsymbol{Q}_{\mathrm{Ci}}$, $\boldsymbol{Q}_{\mathrm{q}}$, $\boldsymbol{Q}_{\mathrm{S}}$, and $\boldsymbol{Q}_{\mathrm{fi}}$ are the uncertainties in normalised rate, steady-state concentration, flow rate, surface area and elemental mass fraction, respectively.

The partial differential terms in Eq. (2.21) are given in Eqs. (2.22) to (2.25):

$$\left(\frac{\boldsymbol{\delta NR_i}}{\boldsymbol{\delta C_i}}\right) = \frac{\boldsymbol{q}}{\boldsymbol{S \times f_i}} \quad \textbf{(2.22)}$$

$$\left(\frac{\boldsymbol{\delta NR_i}}{\boldsymbol{\delta q}}\right) = \frac{\boldsymbol{C_i}}{\boldsymbol{S \times f_i}} \quad \textbf{(2.23)}$$

$$\left(\frac{\boldsymbol{\delta NR_i}}{\boldsymbol{\delta S}}\right) = \frac{-\left(\boldsymbol{C_i} - \boldsymbol{\overline{C}_{i,b}}\right) \times \boldsymbol{q}}{\boldsymbol{S^2 \times f_i}} \quad \textbf{(2.24)}$$

$$\left(\frac{\boldsymbol{\delta NR_i}}{\boldsymbol{\delta f}}\right) = \frac{-\left(\boldsymbol{C_i} - \boldsymbol{\overline{C}_{i,b}}\right) \times \boldsymbol{q}}{\boldsymbol{S \times f_i}} \quad \textbf{(2.25)}$$

The uncertainty in elemental mass fraction $\boldsymbol{Q}_{\mathrm{fi}}$ was estimated by determining the reproducibility standard deviation of the mass fraction (σ_f) between the analysed chemical composition of MW25 in Scales (2011) and the MW25 used in the present study, as both were taken from the same batch (Appendix 4). Because $\boldsymbol{Q}_{\mathrm{Ci}}$ and $\boldsymbol{Q}_{\mathrm{q}}$ are, respectively, best captured by variations in steady-state concentration of an element and flow rate between individual sampling in a test, $\boldsymbol{Q}_{\mathrm{Ci}}$ and $\boldsymbol{Q}_{\mathrm{q}}$ were, respectively, taken to be the standard deviation of steady-state concentrations (σ_{Ci}) and flow rates (σ_{q}) of the series of samplings. Estimation of σ_{S} requires considerations of uncertainties in the initial surface area and the surface area as the glass dissolves. The uncertainty in the specific surface area dominates the uncertainty in the initial surface area, and it was therefore considered to be two times the calculated surface area based on the inference given in Ebert (2005); likewise, uncertainties in the change in surface area as glass dissolves were correlated with uncertainties in steady-state concentration (σ_{Ci}). For approximately 92% of the measured dissolution rates, the 2σ uncertainties were less than 30%, which falls within the typical range for uncertainties for SPFT dissolution rates. Very few (~3%) of the measured rates had 2σ uncertainties above 40%.

2.5 Imaging and Solids Analyses

Surface analytical techniques are complementary tools to waste-form dissolution experiments, as they provide additional information regarding the dissolution behaviour of glass after reaction with solution. In this section the basic principles of these techniques are briefly introduced. A more in-depth discussion of the specific methods, such as the results of the analyses of the unreacted and reacted glass specimens, is given in subsequent chapters as necessary.

2.5.1 Scanning Electron Microscopy (SEM)

SEM is designed primarily for producing images of three-dimensional objects. It uses a focused-beam of secondary electrons to generate various signals at the surface of the glass specimen (Figure 2.6). The electron-sample interactions signals reveal information about the glass sample including morphology, crystalline structure and orientation of particles that make up the glass sample. Typically, data is collected from selected areas of the surface of the sample, and a two-dimensional image displaying spatial variations in these properties is generated. Areas ranging from approximately 1 cm to 5 μm in width can be imaged in a scanning mode (Reimer, 1998; Goldstein *et al.,* 2003).

Ideally, the detector is positioned adjacent to the top of the scanned raster, giving a top-lighting effect. As the angle between beam and specimen surface decreases, the secondary electron yield increases, making the topographic information in images easy to understand. Typical minimum magnification with a scanned area of 1 cm^2 is ~10. Images can be magnified by reducing the amplitude of the scanning beam. Secondary-electron emission is not composition-dependent, meaning that it is often necessary to complement SEM with other techniques such as EDX and XRD for compositional analysis (Reed, 2005).

SEM is a very effective tool for studying the morphology of glass particles on a microscale; however, it has a few limitations. When a high accelerating voltage is used more secondary electrons can escape from the sample at an edge, causing it to appear bright (edge effect), which can lead to difficulty in interpreting the data. Additionally, the SEM has a low depth of focus because the energy of secondary electrons is insufficient to travel distances of greater than 10 nm in solid materials (Reimer, 1998; Reed, 2005). Apart from these inherent limitations, other ways in which SEM images may also be degraded include specimen charging and astigmatism.

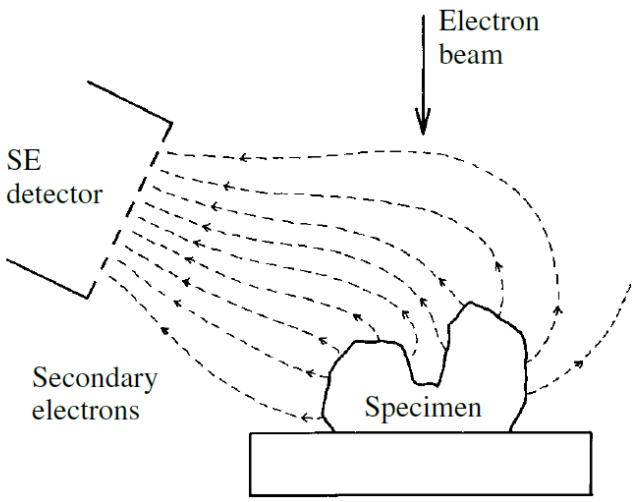

Figure 2.6: Collection of electrons from a three-dimensional specimen by a detector (adapted from Reed [2005]).

Any charge present on the surface of the specimen can cause secondary electrons to be deflected to the effect that the image appears blurred. Specimen charging can be prevented by coating the sample with a conducting material. Another way that charging can be avoided is by selecting low accelerating voltage or by using a low vacuum. The number of secondary electrons can be increased by tilting the specimen, which can also reduce charging. Astigmatism – an aberration caused by small lens imperfection or contamination on an aperture – can be cured by means of a stigmator, which consists of coils that create astigmatism that neutralises that which is already present (Reed, 2005). The stigmator can be adjusted while observing a scanning image and varying the stigmator control.

Most specimens often require some preliminary treatment before mounting for examination in the SEM. These processes, as well as the procedures for mounting, are discussed in the following subsections. These discussions only cover specimen preparations that are relevant to this study. For further information on these and other aspects of specimen preparation, see Humphries (1992).

2.5.1.1 Sample Cleaning and Drying

Cleaning is usually required for pre-leached glass powder in order to remove unwanted components, such as adhering fines that are outside the desired size range. The sample is subsequently dried. The procedures in cleaning and drying the samples used in this study are presented in Section 2.2.1.

2.5.1.2 Mounting

Specimens for SEM examination are commonly mounted on a stub consisting of a metal disc, usually made of aluminium, with a projecting peg for attachment to the stage mechanism (Figure 2.7). There are different methods used to attach specimens to the stub; the use of double-sided sticky tape is the quickest method. In this study, specimens were glued to the stub by means of sticking carbon stabs.

2.5.1.3 Coating

Glass samples, being non-conductors of electricity, require a conductive coating to prevent charging as the samples are bombarded by electrons. It should be noted that coatings are not totally free of structure and can cause artefacts in high-magnification images, so that a suitable choice of coating material is necessary. Although carbon coating is most prevalent among researchers, it is not ideal for SEM imaging as a result of its low secondary electron yield (Purvis, 1991). For this purpose, gold coating is preferable. It is on this basis that samples used in the experiments that were conducted with deionised water were gold coated. Alternatively, the necessity for coating can be precluded if low accelerating voltage is selected or a low vacuum is used, as in part two of the experiments, which were conducted with simulant groundwaters.

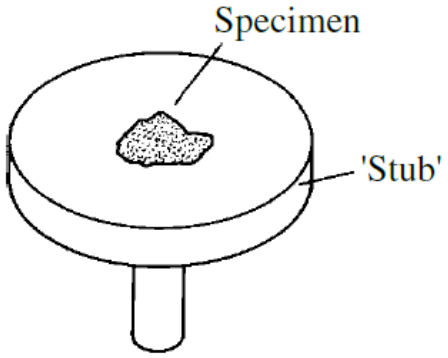

Figure 2.7: Stub used for mounting specimens in SEM imaging.

2.5.1.4 Specimen Labelling, Handling and Storage

Specimens are normally labelled for identification purposes. One way of labelling a specimen is to write on aluminium stubs with a marker. Specimens are kept in a dust-free environment, such as a desiccator (Section 2.2.1). SEM stubs are kept in plastic boxes. Handling the specimen requires the wearing of gloves to prevent contamination

that may arise from touching the specimen with bare hands. Any dust on the stub can be removed with a compressed air-jet.

2.5.2 Energy dispersive X-ray Spectroscopy (EDX)

EDX is usually integrated with SEM for microanalysis of powdered glass and the ED detector is usually attached to the SEM. To characterise the elemental compositions of the analysed volume, the ED detector records X-rays emitted from the sample during bombardment by an electron beam. EDX has the capability to analyse surface features or phases as small as 1 μm or less. However, high beam current required by ED spectrometers means that the depth of penetration can be as high as 10 μm.

2.5.2.1 ED Detector

X-rays reach the detector through a window, which has the capability to withstand atmospheric pressure. This allows the vacuum chamber of the SEM to which the detector is attached to be vented to air safety. The detector is usually a lithium-drifted silicon or Si(Li). A typical detector consists of a 3-mm-thick silicon slice, with an area of 10 mm^2 or larger. A thin layer of gold covers the front surface, which serves as a contact for the bias voltage. The preamplifier – field-effect transistor (FET) – is connected to the rear. The other end of the copper rod, on which the detector and FET are mounted, is immersed in liquid nitrogen. The whole assembly is sealed inside an evacuate housing, or cryostat (Figure 2.8) (Reed, 2005).

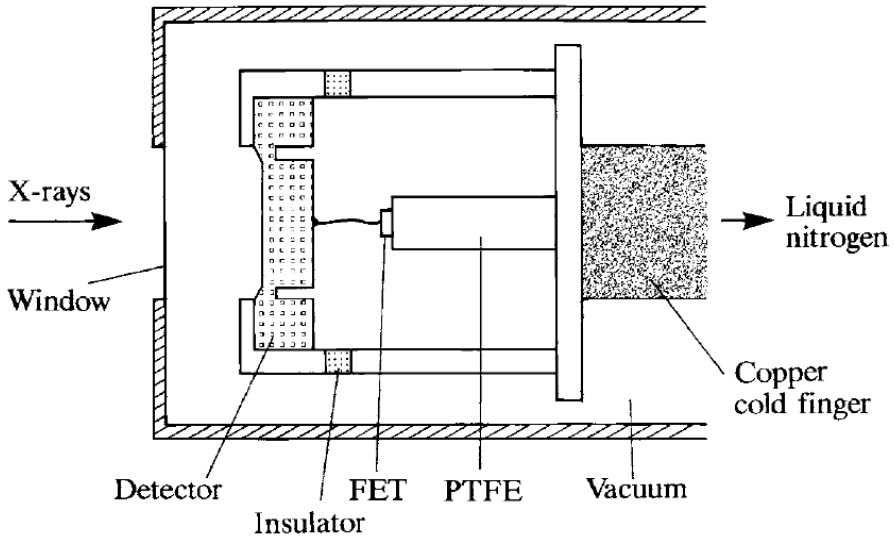

Figure 2.8: Mounting arrangements for detector used for EDX.

Spectrum produced from EDX may contain an unwanted contribution from other regions of the specimen, such as the specimen holder. This is caused as a result of a wide angle of acceptance by ED detectors, as well as non-discrimination between the X-ray produced at the point of impact of the beam and those generated by stray electrons. Although it is impossible to achieve perfect discrimination, a collimator can be fitted in front of the detector to restrict the range of angle that can be accepted (Figure 2.9). In addition, most ED detectors cannot detect the lightest elements (Severin, 2004).

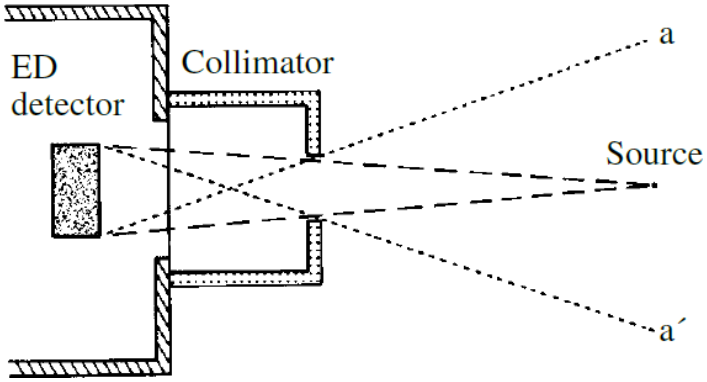

Figure 2.9: The acceptance of X-rays originating between a and a' are restricted by collimator attached to the front of ED detector.

2.5.2.2 Efficiency, Pulse Processing and Dead-Time

The efficiency of X-rays reaching the detector – determined primarily by the solid angle subtended by the detector – is close to 100% over a wide energy range. The solid angle is given by the area of the detector divided by the square of its distance from the source.

A size suitable for pulse-height analysis is amplified from preamplifier to yield output pulses. The signal is averaged over a time interval (typically a few tens of microseconds) defined by a parameter known as process time, which minimises the effect of noise. While each pulse is being processed, the system is 'dead'; this means that no further pulses will be responded to by the system. System dead-time, which is related to the process time, is the time frame between the arrival of a pulse and the moment when the system is live again (Severin, 2004; Reed, 2005).

2.5.2.3 Spectrum Display

Signals from the detector are sent to a multichannel pulse-height analyser, which sorts pulses by voltage and assigns each pulse to a channel. The energy that is determined from the voltage measurements for each channel is sent to a computer, where it is

displayed as a histogram. X-ray lines of interest typically fall within the range of 0–10 keV. Labelling the elemental peaks can assist identification.

2.5.3 X-ray Diffraction (XRD)

XRD is used in waste-form dissolution studies for the identification of crystalline phases. In particular, it is very useful in detecting whether additional crystalline phases such as secondary layers have formed on the glass surface after the reaction of the glass specimen with solution. XRD is wavelength-dispersive and is distinguished from EDX by the fact that it makes use of Bragg reflection by a crystal to disperse X-rays according to their wavelengths. It operates in series, such that the spectrometer can be tuned to only one wavelength at a time. The spectral resolution in XRD is better than for EDX, although EDX is more convenient to use and faster.

2.5.3.1 Basic Principles of Diffraction

As illustrated in Figure 2.10, the intensity of waves is enhanced when waves are scattered from successful layers of atoms. The difference in path length between X-rays diffracting off two adjacent planes, represented by ABC and A'B'C', is an integral multiple of wavelength, λ. This results in the reflection of X-rays of a given wavelength by atomic layers with spacing, d, at an angle of incidence and reflection known as the Bragg angle, θ. These variables are related by Bragg's law:

$$n\lambda = 2d \sin\theta \qquad (2.26)$$

where n is the order of reflection. The first order (n = 1) are the most intense reflections normally used in XRD analysis.

2.5.3.2 Powder X-ray Diffraction

The surface of the crystal in XRD analysis should ideally lie on the Rowland circle – an imaginary circle on which crystal, source, spectrometer and detector are located (Figure 2.11) (Reed, 2005). This requires the glass sample to be ground in order to achieve a radius, r, known as Johansson geometry. The powdered sample allows a larger reflecting area to be obtained and the atomic planes are curved to twice the radius of the Rowland circle, resulting in the Bragg angle being the same at all points.

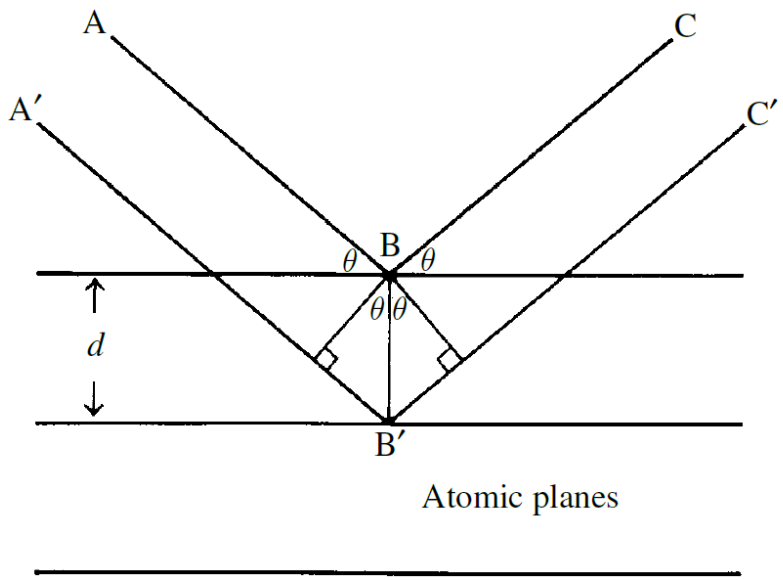

Figure 2.10: Bragg reflection: two X-rays (ABC and A'B'C') diffracted off atoms in different lattice planes.

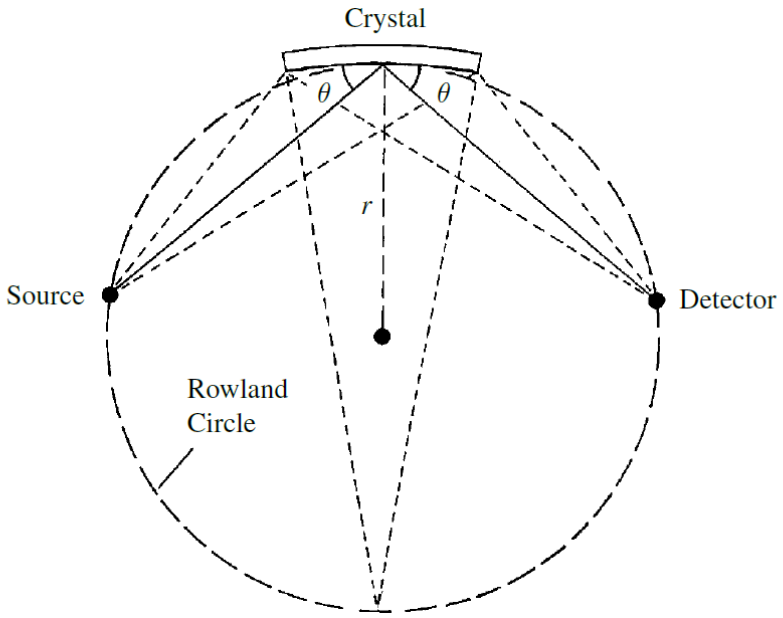

Figure 2.11: Alignment of source, crystal and detector on the circumference of a circle gives a constant Bragg angle.

3 RESULTS OF EXPERIMENTS CONDUCTED WITH DEIONISED WATER

3.1 Introduction

The results of part one of the experiments, which were conducted with deionised water, are presented in this chapter. The experimental parameters used in this part are listed in Table 3.1. The raw data, including mass of tared collection bottle, mass of collection bottle with effluent solution, initial powder mass, measured flow rate, pH of solution before and after reaction with the glass, solution concentrations of the elements and concentrations of the elements in the control tests, are listed in Appendices 5 to 16. The experiments were divided into two sets based on temperature. A test temperature of 40 ^{o}C was selected for the first set of experiments (MW-T_1 – MW-T_12). The second set of experiments (MW-T_13 – MW-T_24) was conducted at 90 ^{o}C. A total of 288 experiments were carried out; experiments were conducted in triplicate, resulting in 36 independent tests in each set of experiments, and 4 samples were collected during each test. The results of the triplicate experiments were averaged to obtain 12 test results in each set of experiments, which were used to compute the rate. Both sets of experiments were conducted at flow rates ranging from ~10 mL d^{-1} to 250 mL d^{-1} (~0.2 to 4.2 reactor volumes per day). The duration of each test varied between 16 h and 18 days, depending on flow rate. The wide range in flow rates, together with adjustments to the sample surface area, which was achieved by varying the mass of glass powder between ~0.1 g and 0.5 g, were used to produce a range of ratios of flow rate to surface area (q/S) values.

Table 3.1: Experimental parameters, including the glass powder mass, solution pH, initial surface area, and the ratio of flow rate to surface area, at the start of the experiments. Experimental ID of 40 ^{o}C experiments range from MW-T_1 to MW-T_12, and those of 90 ^{o}C experiments range from MW-T_13 to MW-T_24. All values are an average of triplicate experiments. Uncertainties are in parentheses. Note that experiments with the same pH value were run simultaneously.

Experiment ID	Powder Mass (g)	Solution pH	Time (hr)	Flow Rate (q) (mL/d)	Surface area (S) (m^2)	q/S Ratio (m/s)
MW-T_1	0.105 (0.009)	7.08	16	247.53 (2.04)	0.0021 (0.000052)	1.36×10^{-6}
MW-T_2	0.503 (0.016)	7.08	16	247.57 (2.87)	0.0101 (0.000790)	2.84×10^{-7}
MW-T_3	0.107 (0.010)	7.13	32	123.82 (1.97)	0.0022 (0.000137)	6.65×10^{-7}
MW-T_4	0.505 (0.010)	7.13	32	123.34 (1.87)	0.0102 (0.001721)	1.41×10^{-7}
MW-T_5	0.102 (0.003)	7.24	51	73.21 (1.62)	0.0021 (0.000033)	4.13×10^{-7}
MW-T_6	0.508 (0.004)	7.24	51	73.24 (1.58)	0.0102 (0.000252)	8.30×10^{-8}
MW-T_7	0.107 (0.010)	7.22	125	48.97 (1.13)	0.0022 (0.000130)	2.64×10^{-7}
MW-T_8	0.504 (0.008)	7.22	125	48.92 (1.43)	0.0101 (0.000614)	5.60×10^{-8}
MW-T_9	0.109 0.008)	6.91	250	24.33 (1.09)	0.0022 (0.000085)	1.29×10^{-7}
MW-T_10	0.508 (0.010)	6.91	250	24.43 (1.21)	0.0102 (0.000076)	2.76×10^{-8}
MW-T_11	0.107 (0.006)	7.1	432	9.91 (0.15)	0.0022 (0.000049)	5.34×10^{-8}
MW-T_12	0.501 (0.006)	7.1	432	9.95 (0.14)	0.0101 (0.000270)	1.14×10^{-8}
Experiment ID						
MW-T_13	0.112 (0.047)	7.12	16	246.75 (4.38)	0.0021 (0.000181)	1.34×10^{-6}
MW-T_14	0.506 (0.058)	7.12	16	245.37 (5.92)	0.0102 (0.000314)	2.81×10^{-7}
MW-T_15	0.109 (0.020)	7.04	32	122.69 (2.97)	0.0022 (0.000093)	6.48×10^{-7}
MW-T_16	0.509 (0.019)	7.04	32	123.27 (2.02)	0.0102 (0.000663)	1.38×10^{-7}
MW-T_17	0.116 (0.031)	7.26	51	74.16 (1.72)	0.0023 (0.000571)	3.68×10^{-7}
MW-T_18	0.517 (0.012)	7.26	51	74.12 (2.21)	0.0104 (0.001702)	8.26×10^{-7}
MW-T_19	0.121 (0.013)	7.06	125	49.28 (0.84)	0.0024 (0.000288)	2.34×10^{-7}
MW-T_20	0.513 (0.019)	7.06	125	49.28 (1.03)	0.0103 (0.000460)	5.53×10^{-8}
MW-T_21	0.107 (0.007)	7.18	250	24.15 (0.95)	0.0022 (0.000631)	1.30×10^{-7}
MW-T_22	0.508 (0.013)	7.18	250	24.42 (0.98)	0.0102 (0.000355)	2.74×10^{-8}
MW-T_23	0.105 (0.010)	7.11	432	9.55 (0.47)	0.0021 (0.000163)	5.26×10^{-8}
MW-T_24	0.504 (0.010)	7.11	432	9.63 (0.44)	0.0101 (0.000092)	1.10×10^{-8}

3.2 Attainment of Steady State

A major goal of the SPFT method is to maintain a constant concentration of dissolved glass components by the opposing effect of fixed solution flow rate, which is important in achieving a valid steady-state dissolution rate. For all the experiments, the concentrations of the elements became invariant with respect to time within four effluent samplings. As mentioned previously, experimental temperatures were fixed at 40 and 90 ^{o}C, but it is also vital to ensure that there is no significant variation in the pH of the effluent solutions between individual sampling in an experiment.

The time evolution of the effluent pH is given in Figure 3.1. The average pH of the effluent solution changed over the duration of the experiments, with all the measured pH levels falling within 2.0 pH unit from the nominal pH value. Most importantly, pH remained essentially constant with respect to time for experiments conducted at the same temperature and flow rate. The effluent pH ranged from 8.29 to 8.77 for 40 ^{o}C experiments, and from 8.23 to 8.57 for 90 ^{o}C experiments at various q/S, meaning that the pH was approximately 0.05 pH unit lower at 90 ^{o}C than at 40 ^{o}C.

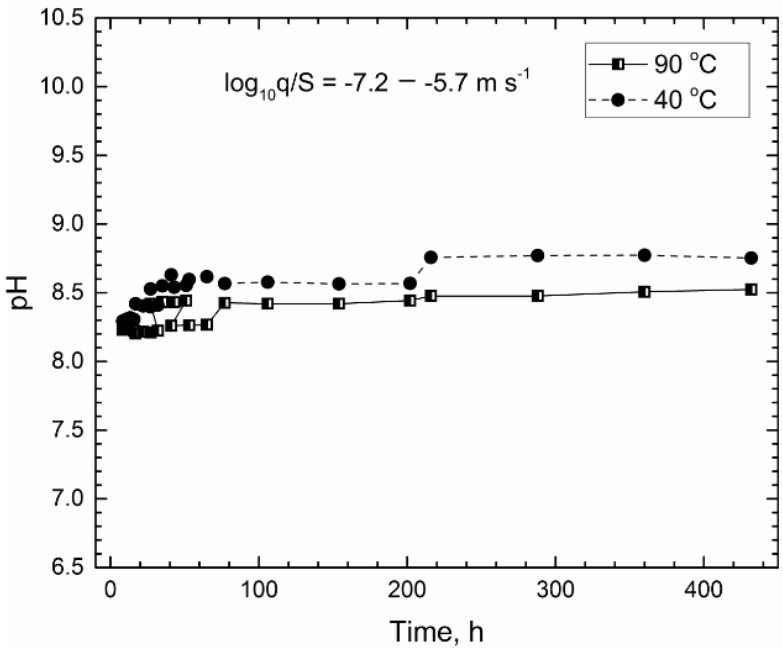

Figure 3.1: Time evolution of solution pH at 40 and 90 ^{o}C. The time evolution is the cumulative test duration. Experiment that was run at the fastest flow rate (250 mL/d) is to the left of the plot (0 h) and experiment that was run at the slowest flow rate (10 mL/d) is to the right (400 h).

Utton *et al.* (2013) measured pH at ambient temperature and ascribed this pH trend to an increase in the dissociation of water with temperature; however, temperature would

only affect the pH measured during the reaction but not the pH measured at ambient temperature. Therefore, the pH trend is most probably a result of different solution concentrations measured at both temperatures.

Tables 3.2 and 3.3 list the average steady-state concentrations of the elements in the effluent solution at 40 and 90 ^{o}C, respectively. The evidence for steady-state conditions for both the 40 and 90 ^{o}C experiments is illustrated by the measured concentrations for Al, B, Li, Mg, Na and Si being constant within analytical uncertainty with respect to time, as shown in Figures 3.2 and 3.3 for the experiments conducted at lowest and highest values of parameter q/S, respectively. The plots for experiments conducted at other q/S values are depicted in Appendix 17.

At the lowest flow rate ($q \approx 10$ mL d^{-1}) the concentrations of the elements in the effluent solutions were invariant after approximately 280 h at 40 ^{o}C, whereas the concentrations of the elements were only just invariant, by this criterion, at 90^{o}C. Steady state was achieved rapidly within 16 h for all the elements at the highest flow rate ($q \approx 250$ mL d^{-1}) at both temperatures. Higher elemental concentrations were observed for high-temperature experiments (90 ^{o}C) than low-temperature ones (40 ^{o}C) in tests at similar flow rates. A similar trend was observed for the variation of elemental concentration with flow rate, which suggests that temperature and flow rate have a prominent influence on the solution concentration. The dependence of the dissolution rate of this glass on flow rate and temperature is examined more closely in Chapter 5.

3.3 Determination of Forward Rates of Dissolution

Normalised average dissolution rates, based on the steady-state release of elements to solution, are listed – along with their associated 2-σ uncertainties, as well as their respective $\log_{10}$ of the q/S ratio, which ranged between -7.8 and -5.7 m s^{-1} – in Tables 3.4 and 3.5 for experiments at 40 and 90 ^{o}C, respectively. Normalised dissolution rates of elements measured at 40 and 90 ^{o}C for each test are listed in Appendices 18 and 19, respectively. The computations of the uncertainties in the release of the elements are presented in Appendix 20.

The data in Tables 3.4 and 3.5 indicates that there is an inverse correlation between the dissolution rates and steady-state concentrations of elements in the effluent solution shown in Tables 3.2 and 3.3, respectively. Dissolution rates were maximal at the higher values of $\log_{10}$q/S and minimal at the lower values of $\log_{10}$q/S. However, dissolution

Table 3.2: Steady-state concentrations of elements (in μg/L) in the effluent solution at 40 °C. All values are an average of triplicate measurements. Uncertainties are in parentheses.

Experiment ID	Al	B	Cs	Li
MW-T_1	2.5 (0.2)	149.0 (13.6)	19.9 (0.9)	37.9 (3.0)
MW-T_2	25.2 (2.1)	468.0 (44.5)	45.1 (2.7)	124.0 (17.6)
MW-T_3	15.0 (1.3)	185.0 (16.0)	25.2 (0.9)	45.0 (2.8)
MW-T_4	33.4 (6.2)	699.0 (42.7)	76.3 (3.3)	178.0 (14.8)
MW-T_5	17.9 (1.0)	277.0 (11.1)	37.5 (3.2)	69.5 (2.7)
MW-T_6	62.0 (2.5)	1030.0 (67.8)	112.3 (3.0)	255.0 (21.0)
MW-T_7	22.9 (1.9)	153.0 (19.4)	30.9 (1.0)	48.1 (3.9)
MW-T_8	80.9 (7.9)	833.0 (82.1)	136.1 (2.5)	243.0 (23.3)
MW-T_9	39.3 (2.4)	213.0 (13.0)	44.9 (3.6)	65.2 (4.3)
MW-T_10	128.9 (10.9)	1280.0 (87.1)	212.4 (20.0)	374.0 (31.6)
MW-T_11	40.1 (3.9)	349.0 (31.3)	77.3 (60.2)	111.0 (10.8)
MW-T_12	123.8 (12.3)	3260.0 (68.9)	476.6 (36.3)	949.0 (68.1)
Experiment ID	**Mg**	**Mo**	**Na**	**Si**
MW-T_1	39.0 (3.0)	16.7 (0.8)	162.0 (13.2)	408.2 (27.3)
MW-T_2	70.9 (1.5)	54.5 (4.9)	488.0 (41.3)	1082.1 (93.2)
MW-T_3	57.6 (6.5)	21.7 (1.5)	202.0 (14.6)	608.6 (46.7)
MW-T_4	130.2 (10.6)	88.4 (82.5)	746.0 (67.7)	1913.5 (126.2)
MW-T_5	90.1 (4.7)	34.3 (3.3)	295.0 (10.6)	862.8 (62.6)
MW-T_6	202.1 (7.0)	135.4 (18.7)	1050.0 (79.6)	2625.4 (223.0)
MW-T_7	78.2 (6.7)	26.7 (1.8)	195.0 (8.7)	546.3 (27.2)
MW-T_8	257.0 (18.1)	139.8 (20.0)	973.0 (21.3)	1672.1 (134.0)
MW-T_9	106.0 (8.5)	34.9 (3.2)	257.0 (12.6)	619.3 (17.2)
MW-T_10	398.5 (10.1)	215.0 (21.3)	1450.0 (138.0)	2501.5 (99.6)
MW-T_11	190.4 (15.4)	64.0 (4.2)	400.3 (32.7)	1265.7 (123.8)
MW-T_12	783.0 (48.7)	591.1 (35.6)	3520.0 (137.5)	4912.9 (437.6)

Table 3.3: Steady-state concentrations of elements (in µg/L) in the effluent solution at 90 °C. All values are an average of triplicate measurements. Uncertainties are in parentheses.

Experiment ID	Al	B	Cs	Li
MW-T_13	135.7 (5.1)	425.1 (16.8)	119.6 (10.4)	158.2 (12.5)
MW-T_14	285.3 (7.1)	2496.7 (162.0)	543.6 (25.2)	870.4 (84.8)
MW-T_15	154.3 (6.6)	514.4 (45.8)	200.0 (14.2)	217.2 (18.6)
MW-T_16	333.1 (19.6)	3578.5 (204.2)	872.2 (8.0)	1252.0 (73.4)
MW-T_17	296.1 (28.8)	809.9 (65.1)	405.8 (25.4)	348.5 (30.8)
MW-T_18	356.3 (24.1)	5678.3 (244.9)	1519.0 (8.0)	1959.6 (93.2)
MW-T_19	567.0 (49.1)	3562.7 (288.6)	612.4 (44.7)	1022.5 (87.4)
MW-T_20	627.4 (38.8)	28038.9 (2397.8)	1410.0 (14.1)	7823.7 (473.8)
MW-T_21	959.0 (73.6)	5909.8 (74.8)	1033.0 (37.4)	2240.4 (171.0)
MW-T_22	230.0 (14.3)	57838.0 (4974.9)	1689.0 (49.1)	20589.9 (2010.1)
MW-T_23	593.1 (42.5)	25031.0 (1679.8)	1594.0 (77.0)	11128.1 (739.0)
MW-T_24	832.8 (5.4)	136089.3 (8608.5)	1901.0 (74.2)	45468.0 (1909.2)
Experiment ID	**Mg**	**Mo**	**Na**	**Si**
MW-T_13	257.3 (11.6)	104.4 (9.6)	687.0 (23.5)	2965.4 (218.8)
MW-T_14	285.0 (28.0)	716.2 (24.0)	3292.2 (286.8)	11183.7 (896.1)
MW-T_15	267.5 (22.2)	170.8 (11.7)	941.6 (82.9)	4185.1 (331.3)
MW-T_16	169.0 (14.9)	1300.0 (8.2)	5198.2 (440.8)	17149.1 (56.6)
MW-T_17	421.9 (35.9)	343.8 (22.8)	1482.1 (113.3)	7486.2 (642.2)
MW-T_18	137.1 (13.2)	2697.0 (6.5)	8352.0 (576.7)	27580.3 (2378.3)
MW-T_19	509.0 (45.1)	614.5 (42.2)	4594.8 (384.1)	11136.1 (1105.8)
MW-T_20	291.5 (18.8)	4736.0 (13.7)	25435.7 (1984.0)	41321.9 (3653.4)
MW-T_21	481.4 (44.9)	1043.0 (19.9)	8382.7 (477.7)	20166.6 (993.8)
MW-T_22	757.2 (54.1)	8666.7 (46.6)	71582.6 (6764.3)	82964.5 (5955.0)
MW-T_23	1574.2 (132.0)	4511.0 (69.5)	38952.2 (1041.1)	59644.7 (6453.0)
MW-T_24	2964.5 (130.6)	17090.0 (54.2)	139505.6 (7481.7)	108030.2 (4343.9)

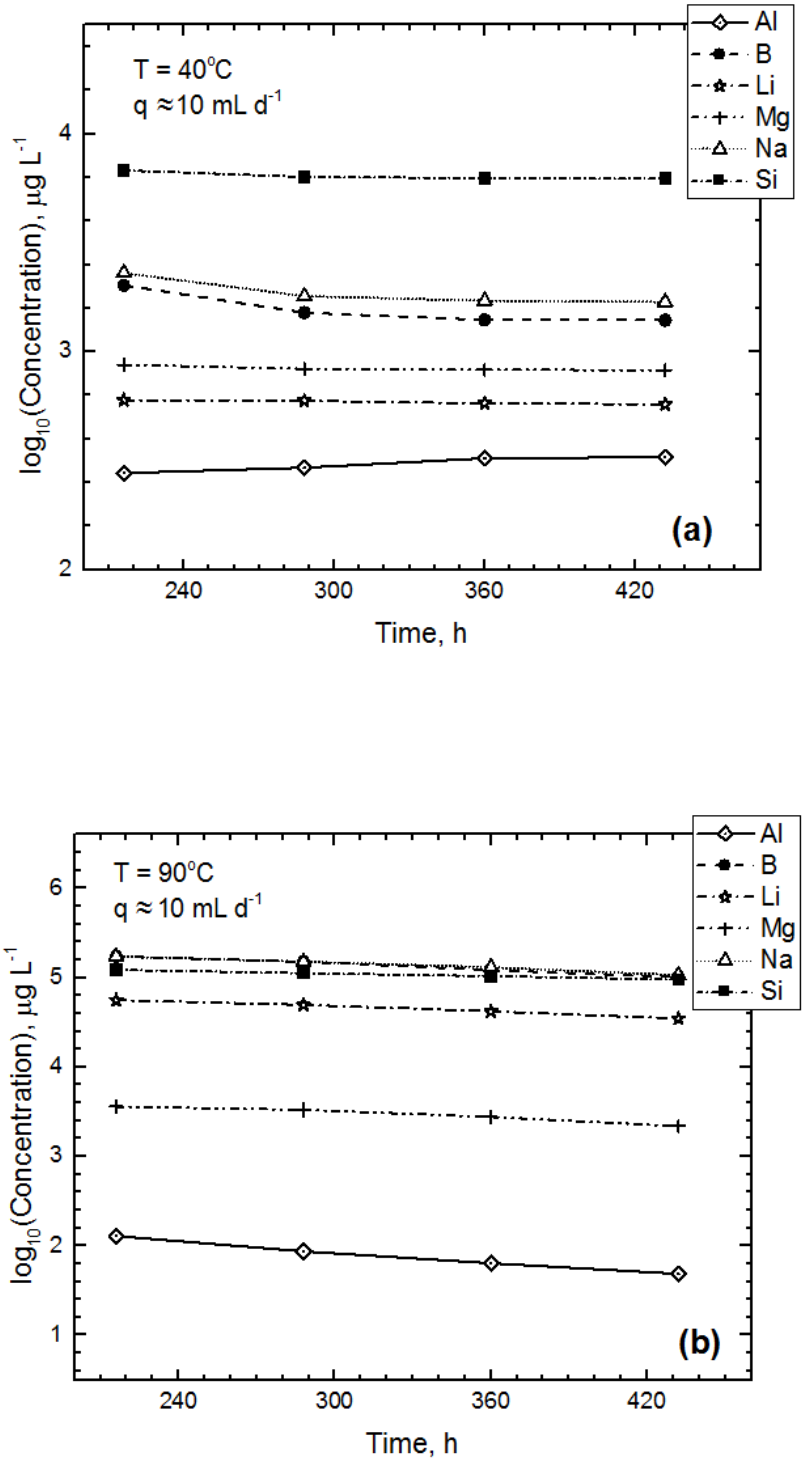

Figure 3.2: Plots of the log of background-corrected concentration (in µg/L) for Al, B, Li, Mg, Na and Si at 40 and 90 °C as a function of time (in hour) at the lowest value of q/S, plot (a) $\log_{10}$q/S = -7.17 m/s; (b) $\log_{10}$q/S = -7.78 m/s.

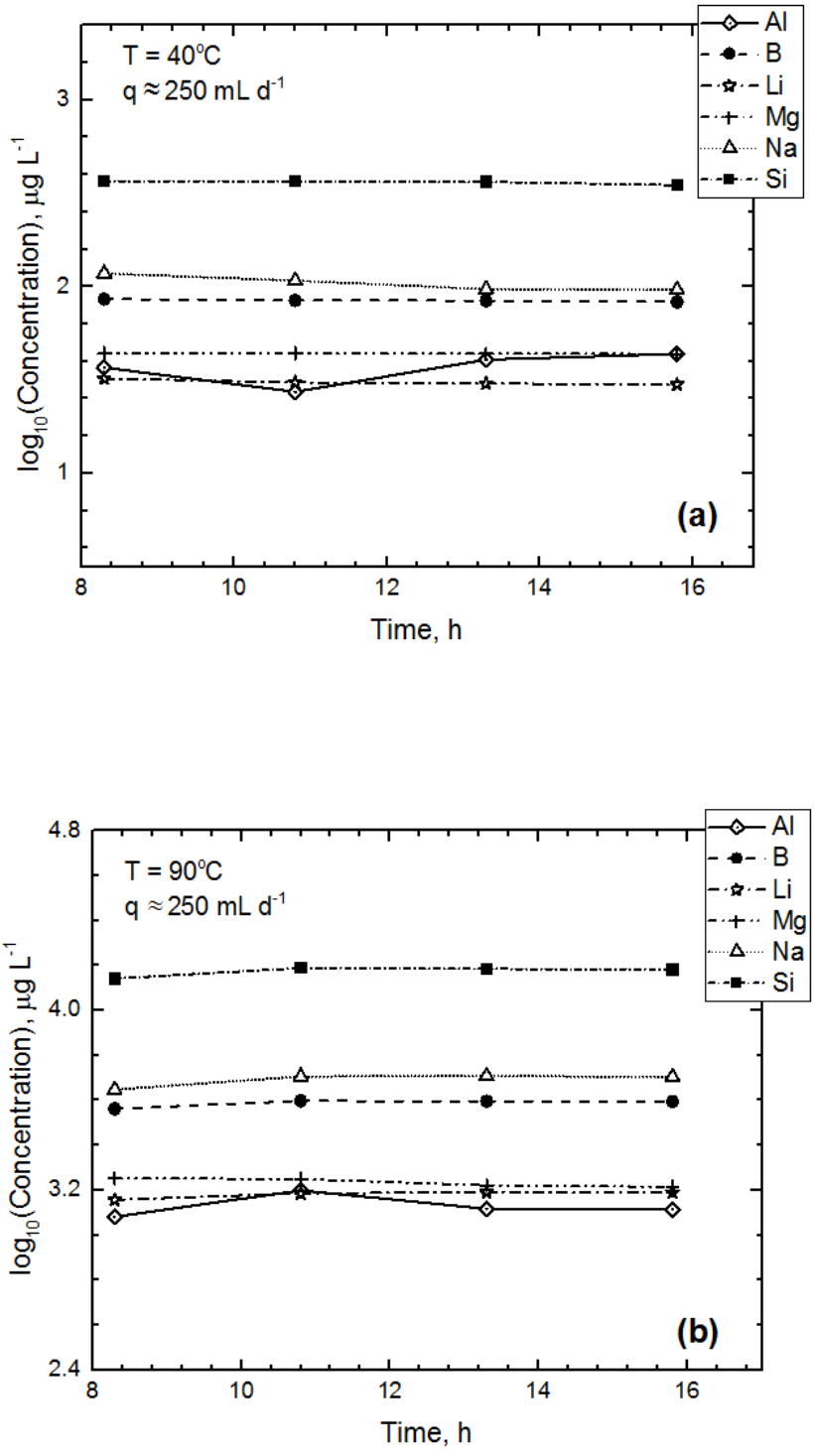

Figure 3.3: Plots of the log of background-corrected concentration (in µg/L) for Al, B, Li, Mg, Na and Si at 40 and 90 °C as a function of time (in hour) at the highest value of q/S, plot (a) $\log_{10}$q/S = -5.70 m/s; (b) $\log_{10}$q/S = -5.72 m/s.

rates were generally consistent over the range of q/S investigated; for example, experiments at 40 ^{o}C yielded dissolution rates based on B concentrations of between 0.100±0.015 g m^{-2} d^{-1} and 0.191±0.053 g m^{-2} d^{-1}. The mean rate of boron dissolution from all measurements at this temperature was 0.155±0.025 g m^{-2} d^{-1}, which indicates that nearly all the computed rates are within 0.08 g m^{-2} d^{-1} of one another. The data revealed that normalised elemental release was much slower at 40 ^{o}C than at 90 ^{o}C. In particular, normalised rates based on the most soluble glass components, including B, Cs, Na, Li and Mo, were more than an order of magnitude higher at 90 ^{o}C than at 40 ^{o}C, whereas only a small increase in the normalised rate values were recorded for Si, Mg, and Al, with an increase in temperature from 40 to 90 ^{o}C.

The normalised rates were plotted against the steady-state Si concentrations in Figure 3.4, as recommended in ASTM C1662 (ASTM, 2010). The ASTM C1662 approach relates intrinsic dissolution rate to variables of steady-state Si concentration, pH and temperature that are controlled during the experiments. The q/S ratios are used to minimise the Si concentration, which dominates the value of $\boldsymbol{Q}$ in Eq. (2.1). Minimising the experimental response provides the minimum rate that can be measured, which is necessarily slower than the forward rate and only provides a lower limit for the forward rate. It is important to note that dissolution rate cannot be measured in the total absence of feedback effects, for the reason that a minimum concentration is required for the analytical measurements used to determine the dissolution rate. The extrapolation to zero ($C_{Si} = 0$) is used to determine the theoretical forward rate required to use Eq. (2.1) to calculate rates under various levels of solution feedback to zero concentration. It is therefore clear that the objective of the ASTM C1622 approach is to show how SPFT results are mechanistically related to glass dissolution to support model calculations. The forward rates calculated using the q/S values are at $C_{Si} > 0$, albeit only very slightly. This will affect the calculated rates very slightly, but this effect can be eliminated by following the ASTM C1662 method.

Boron is usually assumed to be released completely into solution, with none retained in the surface alteration layer (Scheetz *et al.*, 1985), so that the boron release rate best represents the extent of glass dissolution and is commonly used as an index for matrix dissolution. However, the steady-state Si concentration is used in Figure 3.4 because glass dissolution rate is essentially a function of Si concentration, although others (Abraitis *et al.*, 2000 a,b; Oelkers and Gislason, 2001) have argued for some dependence on Al. SPFT experiments are being run to parameterise glass dissolution

kinetics; the Grambow model (Eq. [2.1]) (Grambow, 1985) identifies the hydrolysis of glass – $OSi(OH)_3$ bond as rate-limiting, and it is the kinetics of that reaction that SPFT experiments are used to measure. The steady-state Si concentration sets the glass dissolution rate as rate = $k_0(1 - [Si]/K_g)$, where K_g is the Si-saturation concentration. Boron (and the alkali metals) is released by other reactions (e.g. hydrolysis, ion exchange reactions) that occur simultaneously (and more rapidly), but is (modelled to be) constrained by the Si-hydrolysis reaction. Therefore, steady-state B concentration is not important to the glass dissolution mechanism or kinetics. In addition, the consideration of non-sequestration of B in the surface layer as a justification for using B as an index for matrix dissolution is not relevant in SPFT experiments, for obvious reasons: SPFT method is designed for modelling glass dissolution under conditions that are far from saturation (i.e. no surface layers and no accumulation of dissolved material in solution).

The y-intercepts of the regression lines in Figure 3.7 give forward rates of 0.19±0.02 g m^{-2} d^{-1} for experiments at 40 ^oC, and 1.84±0.35 g m^{-2} d^{-1} for 90 ^oC experiments. Uncertainties are the standard deviations in the regressed rate values obtained using a least-squares linear regression model. It appears that C_{Si} > 12 mg L^{-1} are attenuating the rate; however, extrapolated rate using only C_{Si} < 12 mg L^{-1} (indicated by a dashed line) is only slightly lower. Importantly, the forward rate measured at 90 ^oC for this glass is ~6 times higher than the forward rate (0.30 g m^{-2} d^{-1}) calculated from SPFT for SON68 glass at the same temperature (Icenhower and Steefel, 2015), which is consistent with the difference between MW25 and SON68 obtained by Curti *et al.* (2006) from batch dissolution experiments.

Note that high Si concentrations (C_{Si} > 25 mg L^{-1}) were excluded from the forward rate measured at 90 ^oC to ensure far-from-saturation conditions. The solubility of glass (thermodynamically undefined) is often approximated by that of cristobalite or amorphous silica and is usually near log K_g = -3 mol L^{-1}, with K_g as $[H_4SiO_4]$ (Figure 3.5) (Pederson *et al.*, 1983; Grambow, 1987).

Table 3.4: Normalised average dissolution rates based on release of Al, B, Cs, Li, Mg, Mo, Na and Si at 40 °C in g/(m^{2}d). 2-σ uncertainties are in parentheses.

Experiment ID	log_{10}(q/S)	Al	B	Cs	Li
MW-T_1	-5.7	0.190 (0.004)	0.191 (0.053)	0.189 (0.022)	0.191 (0.074)
MW-T_2	-6.4	0.083 (0.009)	0.153 (0.033)	0.163 (0.012)	0.155 (0.058)
MW-T_3	-6.0	0.174 (0.012)	0.182 (0.030)	0.176 (0.013)	0.180 (0.040)
MW-T_4	-6.7	0.051 (0.007)	0.140 (0.016)	0.144 (0.090)	0.146 (0.037)
MW-T_5	-6.2	0.097 (0.009)	0.151 (0.014)	0.160 (0.011)	0.149 (0.036)
MW-T_6	-6.9	0.029 (0.006)	0.100 (0.015)	0.125 (0.077)	0.120 (0.030)
MW-T_7	-5.8	0.187 (0.010)	0.188 (0.026)	0.183 (0.018)	0.185 (0.022)
MW-T_8	-6.5	0.072 (0.010)	0.150 (0.033)	0.153 (0.017)	0.149 (0.036)
MW-T_9	-6.1	0.148 (0.025)	0.174 (0.019)	0.167 (0.012)	0.172 (0.045)
MW-T_10	-6.8	0.040 (0.017)	0.129 (0.028)	0.125 (0.014)	0.128 (0.058)
MW-T_11	-6.5	0.060 (0.011)	0.137 (0.018)	0.143 (0.075)	0.139 (0.034)
MW-T_12	-7.2	0.124 (0.007)	0.160 (0.010)	0.122 (0.014)	0.158 (0.061)
Experiment ID	**log_{10}(q/S)**	**Mg**	**Mo**	**Na**	**Si**
MW-T_1	-5.7	0.191 (0.043)	0.188 (0.007)	0.193 (0.042)	0.192 (0.026)
MW-T_2	-6.4	0.143 (0.014)	0.164 (0.043)	0.159 (0.026)	0.142 (0.016)
MW-T_3	-6.0	0.183 (0.034)	0.179 (0.041)	0.184 (0.024)	0.180 (0.023)
MW-T_4	-6.7	0.117 (0.015)	0.152 (0.032)	0.136 (0.020)	0.118 (0.011)
MW-T_5	-6.2	0.145 (0.027)	0.166 (0.037)	0.156 (0.011)	0.143 (0.016)
MW-T_6	-6.9	0.079 (0.012)	0.153 (0.027)	0.120 (0.014)	0.082 (0.011)
MW-T_7	-5.8	0.192 (0.029)	0.184 (0.024)	0.192 (0.031)	0.190 (0.024)
MW-T_8	-6.5	0.136 (0.014)	0.159 (0.031)	0.147 (0.043)	0.138 (0.019)
MW-T_9	-6.1	0.170 (0.045)	0.173 (0.036)	0.177 (0.025)	0.168 (0.009)
MW-T_10	-6.8	0.098 (0.032)	0.133 (0.047)	0.130 (0.030)	0.100 (0.008)
MW-T_11	-6.5	0.140 (0.033)	0.156 (0.025)	0.132 (0.016)	0.130 (0.002)
MW-T_12	-7.2	0.150 (0.027)	0.169 (0.049)	0.165 (0.015)	0.149 (0.012)

Table 3.5: Normalised average dissolution rates based on release of Al, B, Cs, Li, Mg, Mo, Na and Si at 90 ^{o}C in g/(m^{2}d). 2-σ uncertainties are in parentheses.

Experiment ID	log_{10}(q/S) (m/s)	Al	B	Cs	Li
MW-T_13	-5.7	1.790 (0.300)	1.800 (0.283)	1.890 (1.01)	1.830 (0.419)
MW-T_14	-6.4	1.410 (0.091)	1.790 (0.174)	1.560 (0.844)	1.920 (0.361)
MW-T_15	-6.0	1.750 (0.120)	1.820 (0.107)	1.770 (0.524)	1.850 (0.220)
MW-T_16	-6.7	0.960 (0.053)	2.100 (0.078)	0.746 (0.471)	1.890 (0.228)
MW-T_17	-6.3	1.690 (0.154)	1.730 (0.119)	1.590 (0.606)	1.620 (0.216)
MW-T_18	-6.9	0.660 (0.033)	2.430 (0.054)	0.961 (0.413)	2.760 (0.276)
MW-T_19	-6.5	1.320 (0.164)	2.080 (0.230)	1.470 (0.992)	1.740 (0.355)
MW-T_20	-7.0	0.430 (0.041)	3.900 (0.358)	0.838 (0.152)	3.880 (0.602)
MW-T_21	-6.7	0.890 (0.154)	1.970 (0.081)	1.100 (0.824)	1.920 (0.424)
MW-T_22	-7.4	0.040 (0.008)	4.470 (0.431)	2.492 (0.182)	4.450 (0.951)
MW-T_23	-7.1	0.450 (0.040)	3.790 (0.365)	2.733 (0.174)	3.860 (0.966)
MW-T_24	-7.8	0.030 (0.010)	4.510 (0.315)	2.162 (0.177)	4.230 (0.785)
Experiment ID	**log_{10}(q/S)**	**Mg**	**Mo**	**Na**	**Si**
MW-T_13	-5.7	1.840 (0.384)	1.840 (0.225)	1.810 (0.374)	1.820 (0.484)
MW-T_14	-6.4	1.530 (0.075)	1.360 (0.234)	1.850 (0.220)	1.620 (0.181)
MW-T_15	-6.0	1.790 (0.160)	1.510 (0.116)	1.830 (0.172)	1.820 (0.193)
MW-T_16	-6.7	0.832 (0.019)	2.490 (0.164)	2.220 (0.130)	1.560 (0.032)
MW-T_17	-6.3	1.720 (0.154)	1.730 (0.110)	1.700 (0.170)	1.770 (0.256)
MW-T_18	-6.9	0.434 (0.009)	2.890 (0.146)	2.520 (0.097)	1.490 (0.110)
MW-T_19	-6.5	1.260 (0.104)	2.000 (0.284)	2.200 (0.233)	1.580 (0.172)
MW-T_20	-7.0	0.390 (0.013)	3.660 (0.523)	3.500 (0.245)	1.430 (0.122)
MW-T_21	-6.7	0.751 (0.055)	1.930 (0.268)	2.300 (0.173)	1.530 (0.108)
MW-T_22	-7.4	0.113 (0.019)	3.680 (0.602)	4.550 (0.473)	1.370 (0.243)
MW-T_23	-7.1	0.460 (0.082)	3.790 (0.515)	3.860 (0.302)	1.450 (0.252)
MW-T_24	-7.8	0.188 (0.029)	3.130 (0.606)	4.230 (0.239)	0.940 (0.034)

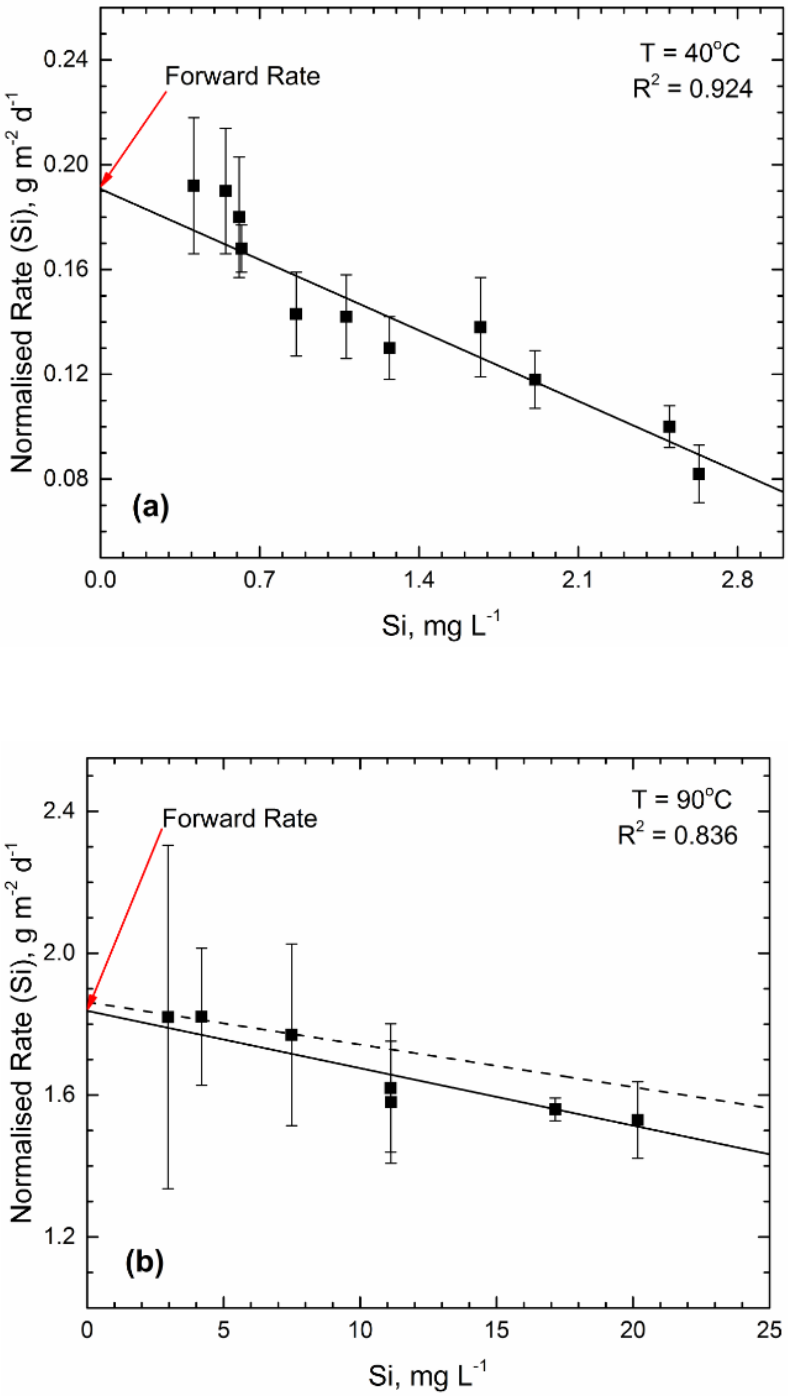

Figure 3.4: Plot of normalised rate [in g/(m^{2}d)] versus steady-state Si concentration (in mg/L) at: (a) 40 ^{o}C; (b) 90 ^{o}C. The forward dissolution rate (maximum rate), indicated by an arrow, is equal to the value at the y-intercept. Note that total Si concentration was used instead of H_4SiO_4 (or $SiO_2.2H_2O$) for convenience; there is often a factor of 28/96 difference. 2-σ uncertainties in the measured rates are indicated by error bars.

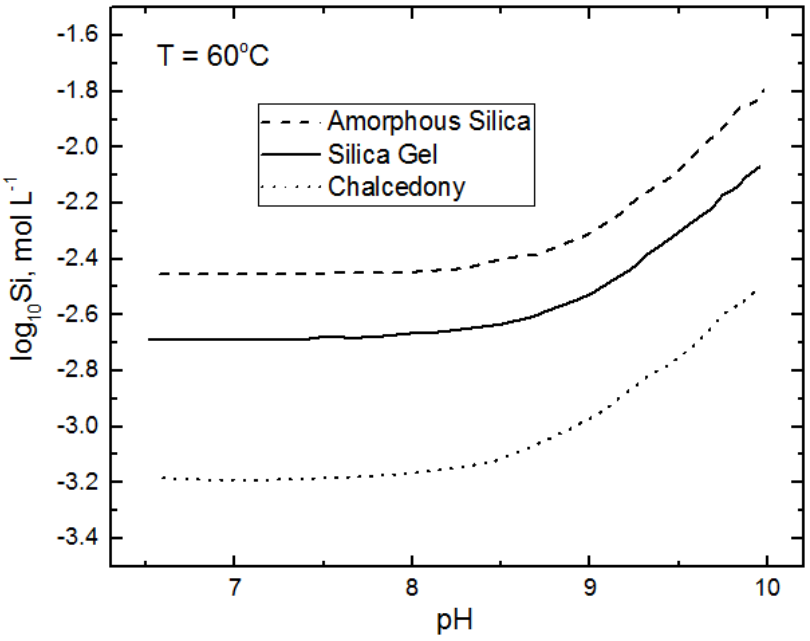

Figure 3.5: Plot of predicted Si concentrations at saturation with amorphous silica, silica gel and chalcedony. This estimation is usually derived from results of batch experiments (adapted from Abraitis *et al.*, 2000c).

3.3.1 Estimation of the Activation Energy of the Reaction

The effect of temperature on the glass dissolution rate can be seen in Figure 3.4, which indicates approximately one order of magnitude increase in the forward rate, with an increase in temperature from 40 to 90 ^{o}C. The observed temperature dependence of the forward rate is consistent with the Arrhenius-type behaviour, and can be described as follows:

$$\boldsymbol{r = Ae^{\frac{-E_a}{RT}}} \qquad \textbf{(3.1)}$$

where r is the dissolution rate (g m^{-2} d^{-1}), A is the Arrhenius parameter (g m^{-2} d^{-1}) , E_a is the activation energy (kJ mol^{-1}) , R is the ideal gas constant (8.314 J mol^{-1} K^{-1}) and T is the temperature (K).

The constant dissolution rates of B, Na and Si in the experiments conducted at both 40 and 90 ^{o}C were substituted into the integrated form of Eq. (3.1). Using the two temperatures, the apparent E_a associated with B, Na and Si release were estimated algebraically, which are 59.6 kJ mol^{-1} for B, 61.1 kJ mol^{-1} for Na and 55.4 kJ mol^{-1} for Si. These E_a values are comparable with the values reported in previous studies:

between 56 and 64 kJ mol^{-1} for Magnox glass (Abraitis *et al.,* 2000c); between 41 and 56 kJ mol^{-1} or basaltic glasses (Wolff-Boenisch *et al.,* 2004); and between 52 and 56 kJ mol^{-1} for immobilised low-activity waste (ILAW) glasses (Pierce *et al.,* 2008a).

3.4 Results of Imaging and Surface Analyses

Imaging and surface analyses, including SEM/EDX and XRD, were undertaken to investigate whether there were precipitation of secondary phases on the reacted glass samples. In the SPFT method, this is only expected at the low threshold of q/S; therefore, only the samples from experiments at the lowest q/S value were investigated. The analyses were carried out in the Department of Earth Sciences at the University of Cambridge, UK.

At the end of each test, the solution that was left in the reactor was carefully decanted and the reacted sample was air-dried at 50 ^{o}C and later collected and stored over silica gel at room temperature. Samples were classified based on temperatures and flow rates used in the tests and labelled accordingly. For the image analysis, specimens were prepared by sparingly sprinkling the glass samples with a spatula onto carbon adhesive discs mounted on aluminium stubs. The specimens were subsequently gold-coated to prevent charging under electron bombardment. Secondary electron images (SEI) were collected on a FEI Quanta650F SEM platform at 15.00 kV and high vacuum. Energy dispersive X-ray spectroscopy (EDX) data was analysed using the Bruker Esprit V 1.9 software programme. X-ray powder diffractograms in the 2θ range 10–60^{o} were collected in the open air in Bragg-Brentano geometry on a Bruker D5000 diffractometer equipped with sample spinner, Cu radiation and scintillation point detector. Data-collection conditions were: step size 0.05^{o}, divergence slit 0.06 mm, detector slit 0.02 mm, 30 x 20 kV x mA, 30 seconds/step. Powder samples were uncoated and were ground using an agate pestle and a mortar to ensure that large numbers of crystallites were available to the X-ray beam in every possible orientation. The samples were mounted on plastic holders and held in place using acetone.

The XRD spectra of the unleached glass specimen and glass specimens that reacted with solution at 40 and 90 ^{o}C are displayed together in Figure 3.6, so that similarities and differences can be studied simultaneously. The crystalline phases that were detected by XRD were the same as those typically found in UK Magnox glass, which include ruthenium dioxide (RuO_2) and a spinel phase [$(Fe,Mg)(Cr,Fe)_2O_4$] (Scales, 2011). The SEM/EDX result of the unleached specimen is shown in Figure 3.7, while those of the

specimens that were collected after dissolution at 40 and 90 ^{o}C are shown in Figures 3.8 and 3.9, respectively. Although SEM data collected at 90 ^{o}C was affected by edge effect (see Section 2.5.1), this did not impede the interpretation of the data. The images show that the quantity and size of leached products deposited on the surface of the reacted particles, as well as surface cracking and pitting, increase as temperature increases. Precipitates formed at both temperatures are morphologically distinguishable, with those formed at 40 ^{o}C demonstrating an acicular appearance, while those formed at 90 ^{o}C are globular. EDX of these features is displayed alongside the SEM data.

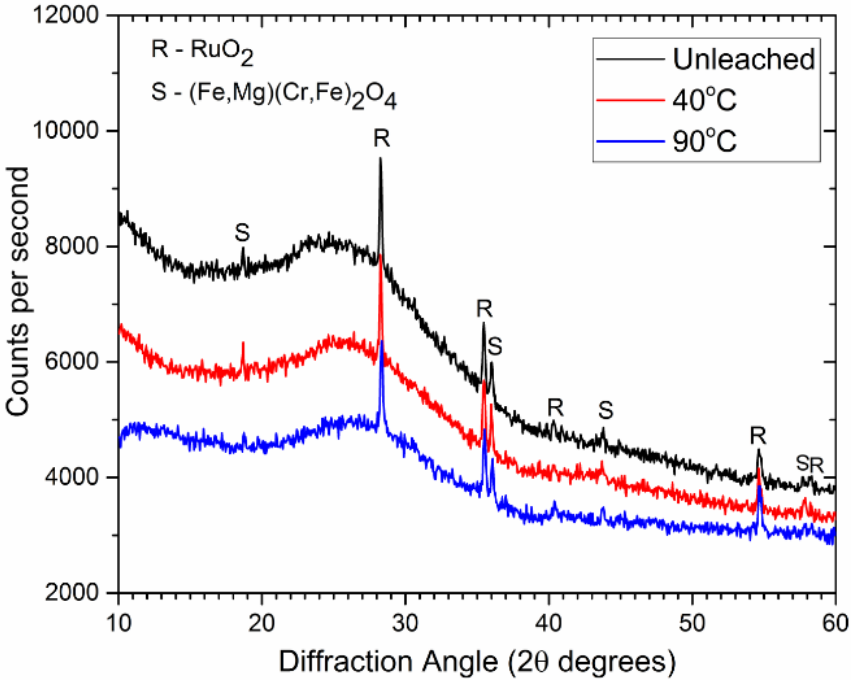

Figure 3.6: XRD patterns of MW25 before and after leaching in deionised water. The glass reacted with deionised water for 432 h. Experimental conditions are: (a) 40 ^{o}C and $\log_{10}$q/S = -7.17 m/s; and (b) 90 ^{o}C and $\log_{10}$q/S = -7.78 m/s.

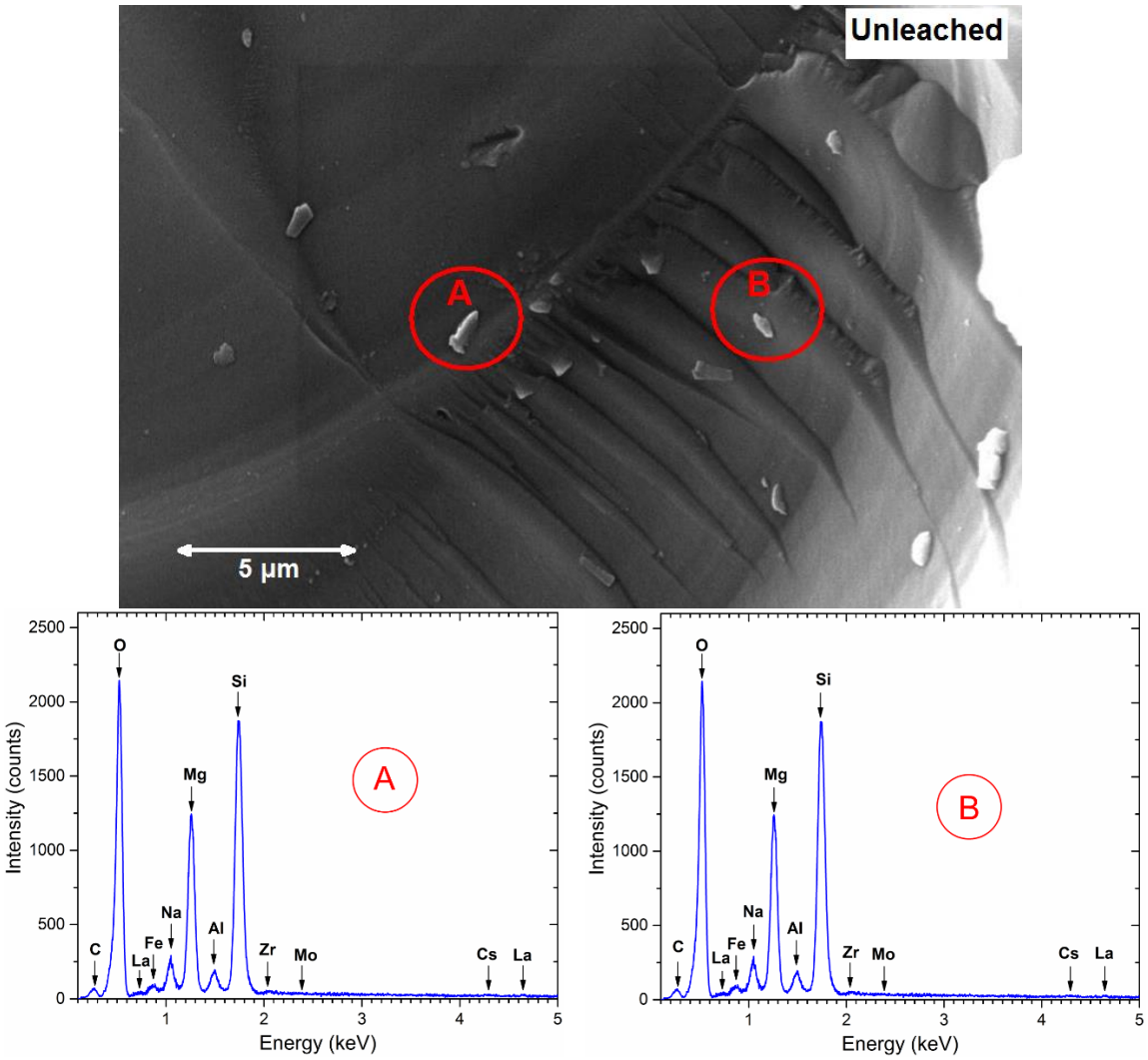

Figure 3.7: SEM data of MW25 and corresponding EDX spectra before reaction with solution.

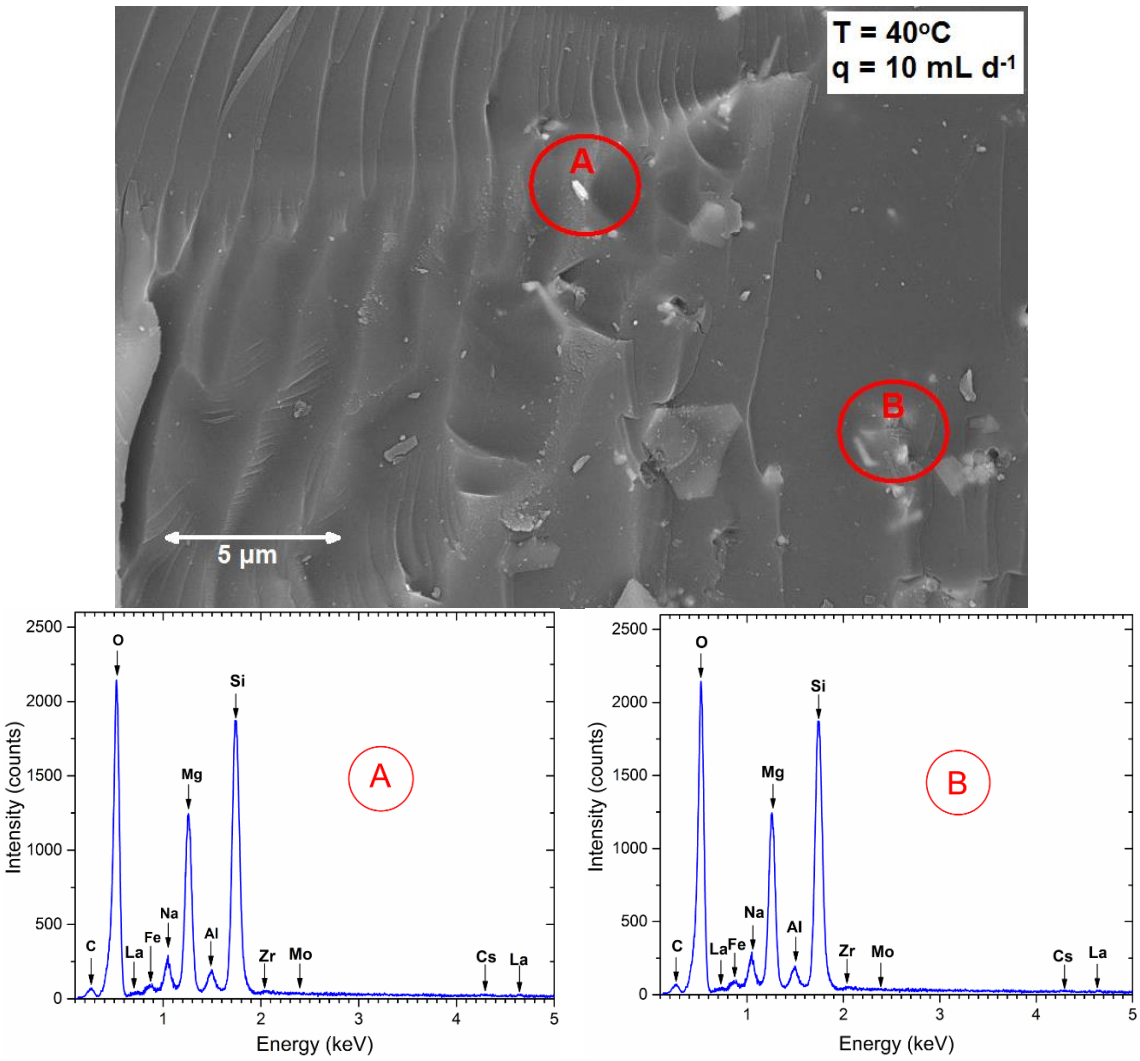

Figure 3.8: SEM data of MW25 and corresponding EDX spectra after reaction with deionised water. Experimental conditions are 40 °C and $\log_{10}q/S$ = -7.17 m/s.

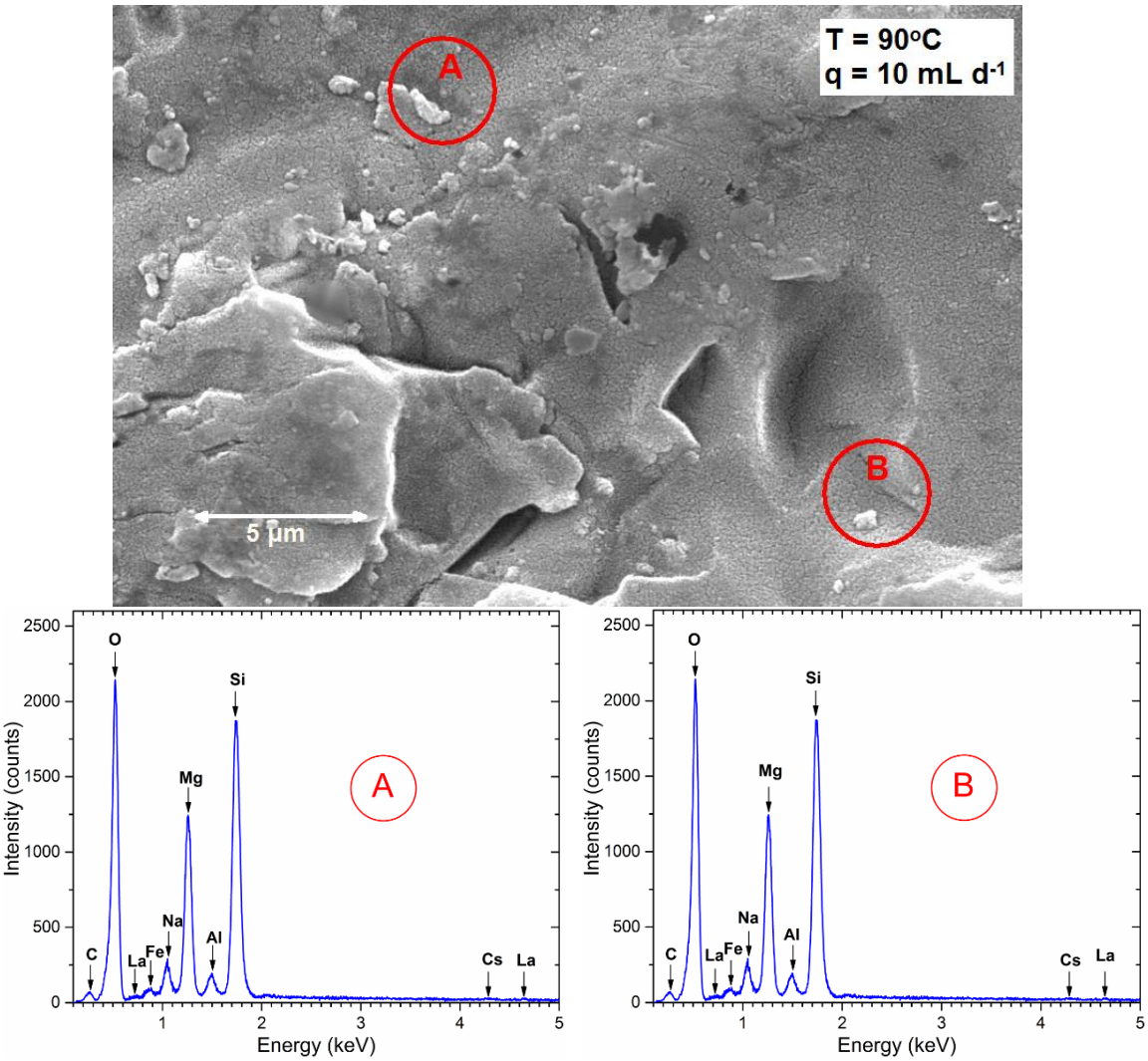

Figure 3.9: SEM data of MW25 and corresponding EDX spectra after reaction with deionised water. Experimental conditions are 90 °C and $\log_{10}q/S$ = -7.78 m/s.

4 RESULTS OF EXPERIMENTS CONDUCTED WITH SIMULANT GROUNDWATERS

4.1 Introduction

This chapter presents the results of part two of the experiments, which were conducted with simulant groundwaters. As discussed in Section 2.2.2, two generic groundwater compositions were chosen for their comprehensiveness, as follows: (1) based on Callovo-Oxfordian argillite groundwater composition from Bure in France, which is representative of lower-strength sedimentary rock (LSSR) groundwater; and (2) based on a groundwater composition RCF3 DET5 from Borrowdale Volcanic Group rocks near Sellafield in the UK, which is representative of higher-strength rock (HSR) groundwater. Table 4.1 lists the experimental parameters used in this part. The raw data, including mass of tared collection bottle, mass of collection bottle with effluent solution, initial powder mass, measured flow rate, pH of solution before and after reaction with the glass, solution concentrations of the elements and concentrations of the elements in the control tests, are listed in Appendices 21 to 26. A total of 144 experiments were carried out; experiments were conducted in triplicate, resulting in 18 independent tests in each set of experiments, and 4 samples were collected during each test. The experiments were divided into two sets based on solution compositions. The first set of experiments (GW_1 – GW_6) was conducted with solution based on LSSR groundwater compositions. The second set of experiments (GW_7 – GW_12) was conducted with solution based on HSR groundwater compositions. A test temperature of 40 ^{o}C was selected for both sets of experiments and the pH of both simulant groundwaters was set to 7. As in part one of the experiments, both sets of experiments were conducted at flow rates ranging from ~10 mL d^{-1} to 250 mL d^{-1} (~0.2 to 4.2 reactor

volumes per day) and the duration of each test varied between 16 h and 18 d, depending on flow rate. In this part, however, all the experiments were carried out with ~0.5 g of glass powder, so that a range of ratios of flow rate to surface area (q/S) values were produced by varying only the flow rates.

Table 4.1: Experimental parameters, including the mass of glass powder, initial surface area, and the ratio of flow rate to surface area, at the start of the experiments. Experimental ID of experiments conducted with LSSR groundwater range from GW_1 to GW_6, and those conducted with HSR groundwater range from GW_7 to GW_12. All values are an average of triplicate experiments. Uncertainties are in parentheses.

Experiment ID	Powder mass (g)	Reaction time (t)	Flow rate (q) (mL/d)	Surface area (S) (m^2)	q/S (m/s)
GW_1	0.511 (0.008)	16	247.77 (0.88)	0.0103 (0.000031)	2.02×10^{-6}
GW_2	0.506 (0.005)	32	124.10 (0.75)	0.0102 (0.000019)	4.17×10^{-7}
GW_3	0.506 (0.006)	51	73.78 (1.24)	0.0102 (0.000023)	9.86×10^{-7}
GW_4	0.501 (0.001)	125	48.48 (0.92)	0.0101 (0.000051)	2.08×10^{-7}
GW_5	0.502 (0.005)	250	24.48 (0.79)	0.0101 (0.000019)	6.09×10^{-7}
GW_6	0.506 (0.001)	432	9.77 (0.25)	0.0102 (0.000005)	1.23×10^{-7}
Experiment ID					
GW_7	0.509 (0.005)	16	247.68 (0.45)	0.0102 (0.000022)	1.56×10^{-6}
GW_8	0.506 (0.005)	32	123.93 (0.54)	0.0102 (0.000019)	3.30×10^{-7}
GW_9	0.507 (0.001)	51	73.88 (0.99)	0.0102 (0.000034)	7.60×10^{-7}
GW_10	0.508 (0.002)	125	48.98 (0.14)	0.0102 (0.000071)	1.63×10^{-7}
GW_11	0.501 (0.003)	250	24.33 (0.61)	0.0101 (0.000010)	3.16×10^{-7}
GW_12	0.504 (0.001)	432	9.80 (0.06)	0.0101 (0.000004)	6.76×10^{-8}

4.2 Interactions of Solution Components with Glass

There was a significant presence of calcium, magnesium and sodium in the compositions of both LSSR and HSR groundwaters. The concentrations of these elements were examined for evidence of their interaction with the glass by comparing their concentrations in the control tests – tests conducted without the glass specimen in the reactor – with their concentrations in the tests with the glass specimen in the reactor (i.e. leachate concentration). A better understanding of the test results is gained by plotting the solution concentrations at every sampling over flow rate.

The variations in Ca during the experiments is illustrated in Figure 4.1, which shows plots of concentrations of Ca in the leachate and the control test as a function of

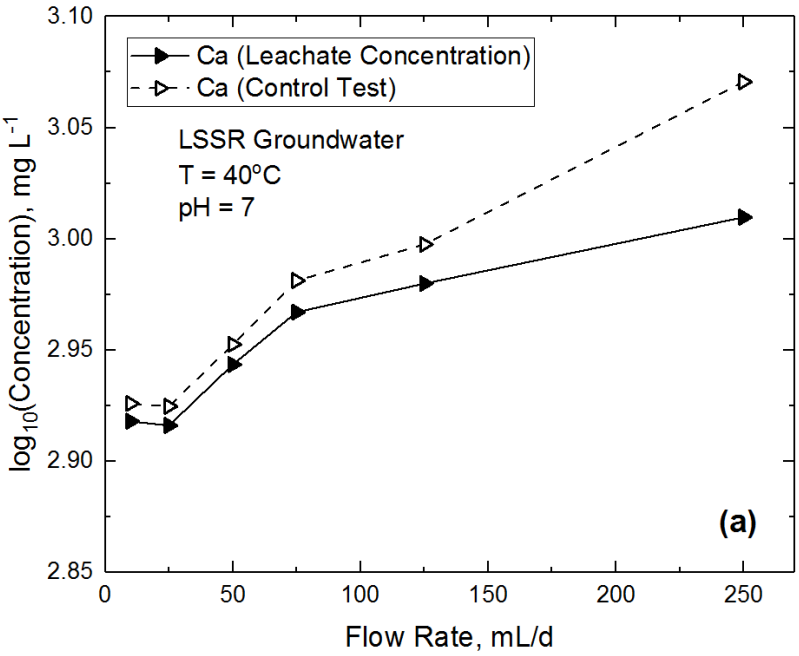

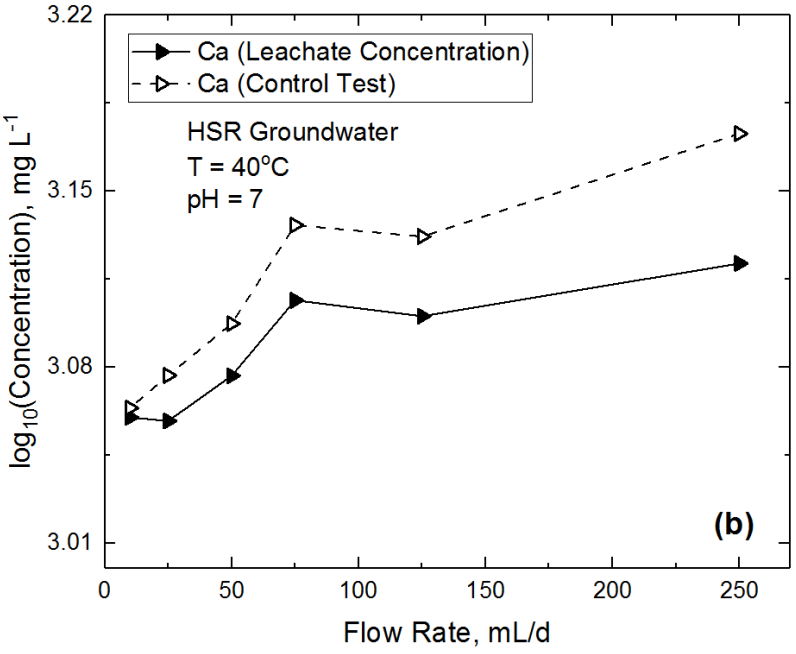

Figure 4.1: Variations in the concentrations of Ca (in mg/L) with flow rate in the experiments conducted with: (a) LSSR simulant groundwater; (b) HSR simulant groundwater.

flow rate for experiments conducted with LSSR groundwater (Figure 4.1a), as well as for experiments conducted with HSR groundwater (Figure 4.1b). The figures illustrate a general increase in Ca concentration as the flow rates were increased. The concentrations of Ca in the leachates of both groundwaters were only slightly higher than the concentrations of Ca in the control tests. The Ca concentration in the LSSR groundwater was found to be ~20% higher at the highest flow rate (250 mL/d) than at the lowest flow rate (10 mL/d), suggesting interaction with the glass surface; conversely, the Ca concentration was moderately higher at the highest flow rate than at the lowest flow rate in HSR groundwater. In the case of HSR groundwater, the interaction of the solution with the glass resulted in a ~13% increase in Ca concentration as the flow rate was increased from 10 mL/d to 250 mL/d. Ca concentrations in the leachates were lower than the Ca concentration in the control tests by an average of ~4.5% for experiments conducted with LSSR groundwater and ~6% for experiments conducted with HSR groundwater. Because Ca was not present in the composition of the glass, the slightly higher Ca concentrations in the control tests than in the leachates therefore suggest that Ca was removed from both groundwaters and was probably retained on the surface of the glass during the course of leaching due to interaction with the glass. For both groundwaters, it appears that the rate of Ca removal increases as the flow rates were increased.

Figure 4.2 shows the plots of concentrations of Mg in the leachates and the control tests versus flow rate for experiments conducted with both groundwaters. There was a ~2.5% and ~3.2% difference in the concentration of Mg in the experiments conducted with LSSR and HSR groundwaters, respectively, between the experiments conducted at the lowest flow rate (10 mL/d) and the experiments conducted at the highest flow rate (250 mL/d). The concentration of Mg in the leachates changed little in comparison with the Mg concentration in the control tests in both groundwaters. The average concentration of Mg in the leachates was higher than the average Mg concentration in the control tests in the experiments conducted with both groundwaters at a similar magnitude: 1.48% for LSSR and 1.46% for HSR. The higher Mg concentration in the leachates than in the control test indicates that Mg in both groundwaters was removed during leaching. The removal of magnesium was greater in the LSSR groundwater, which has a higher initial magnesium content than the HSR groundwater.

The plots of concentrations of Na in the leachates and the control tests, as a function of flow rate for experiments conducted with both LSSR and HSR groundwaters, are shown

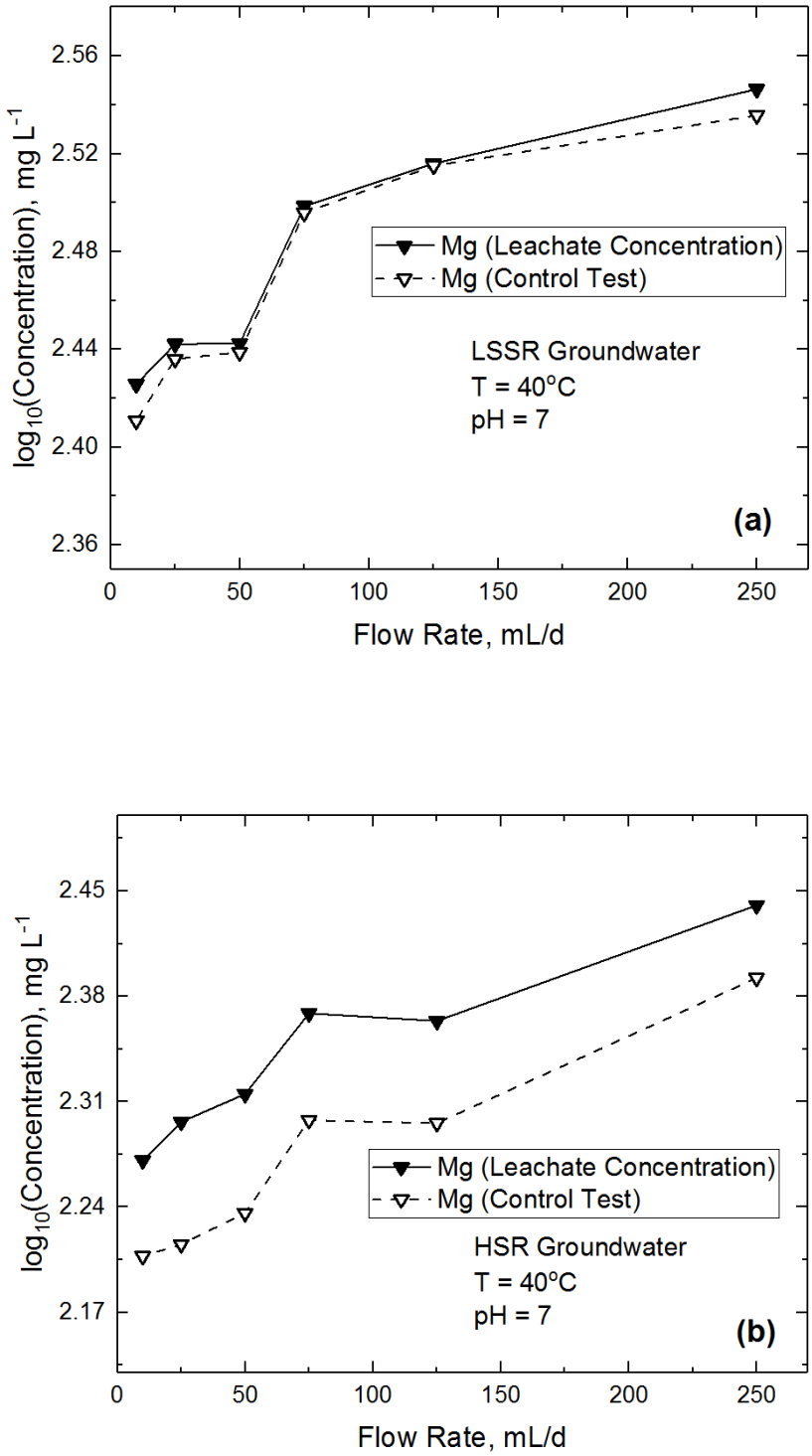

Figure 4.2: Variations in the concentrations of Mg (in mg/L) with flow rate in the experiments conducted with: (a) LSSR simulant groundwater; (b) HSR simulant groundwater.

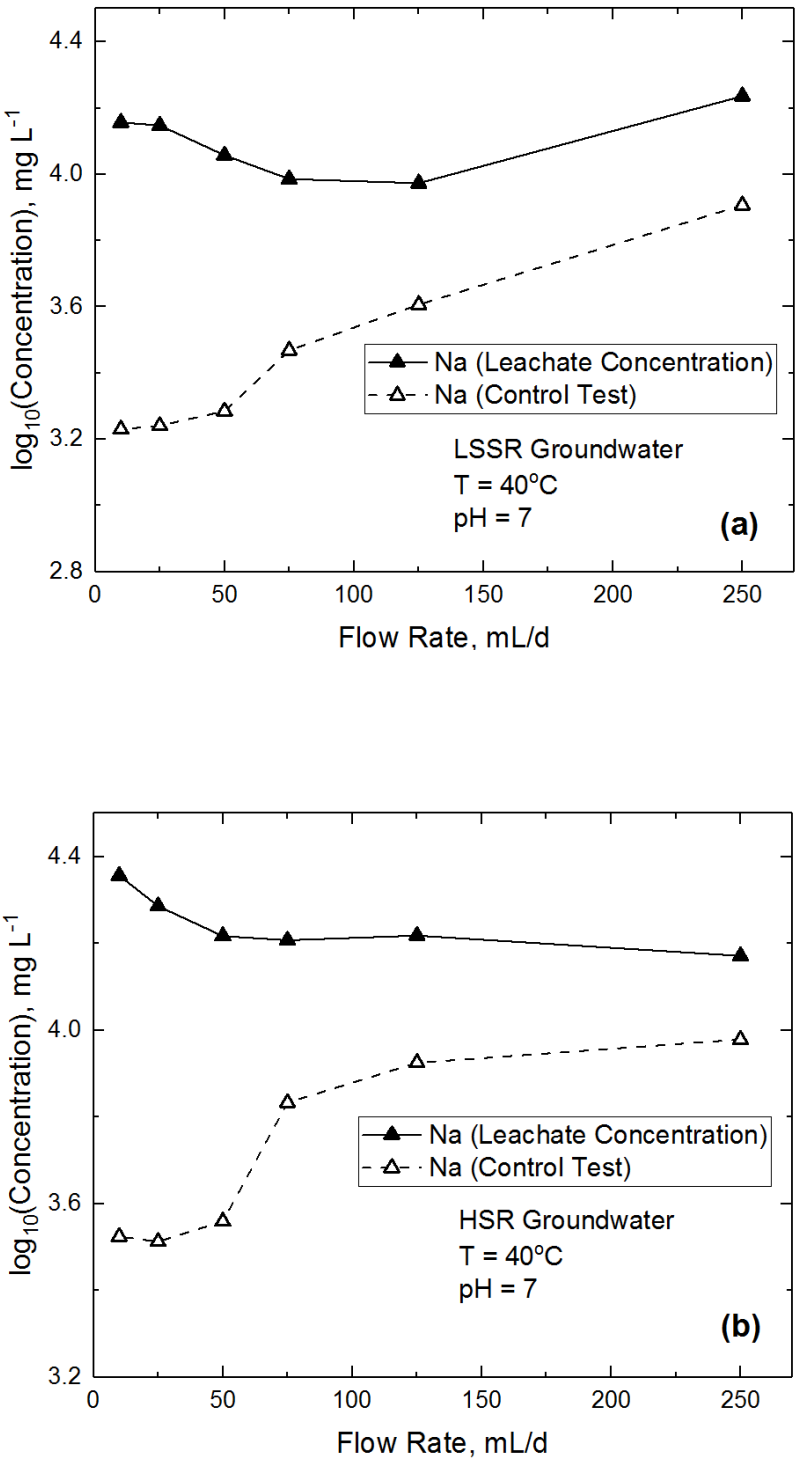

Figure 4.3: Variations in the concentrations of Na (in mg/L) with flow rate in the experiments conducted with: (a) LSSR simulant groundwater; (b) HSR simulant groundwater.

in Figure 4.3. The concentration of Na in the experiments with both groundwaters decreased by ~5% in the leachate and increased by approximately the same magnitude in the control test as the flow rate was increased from 10 mL/d to 75 mL/d. There was a ~10% increase in Na concentration in LSSR groundwater with an increase in flow rate from 75 mL/d to 250 mL/d, whereas the Na concentration remained essentially constant in HSR at these flow rates. The concentrations of Na in the leachate of both groundwaters were slightly higher than the concentrations of Na in the control tests. The average concentrations of Na in the leachate in the experiments conducted with LLSR and HSR groundwaters, respectively, were 7.3% and 6.5% higher than the average concentration of Na in the control tests. These results suggest that Na in the groundwaters was removed and sequestered on the surface of the glass during leaching.

4.3 Achievement of Steady State

As mentioned previously, the pH of both LSSR and HSR simulant groundwaters was set to 7 and this pH was maintained within the solution reservoir by purging an N_2 gas stream into the solution reservoir during the experiments (see Section 2.4). However, the average pH of the leachate changed little over the duration of the experiments, with all the measured pH levels falling within 0.5 pH unit from the nominal pH value for the experiments conducted with both simulant groundwaters, as shown in Figure 4.4. Most importantly, pH remained essentially constant with respect to time for the experiments conducted with the same groundwater. The pH of the leachates ranged from 6.73 to 6.82 for experiments conducted with LSSR simulant groundwater, and from 6.54 to 6.60 for experiments with HSR simulant groundwater, meaning that the pH was approximately 0.25 pH of a unit lower in the experiments with HSR groundwater than in the experiments with LSSR groundwater. Because experiments with both groundwaters were conducted at the same temperature (i.e. 40 ^{o}C), the pH trend is most probably therefore a result of the different elemental compositions of both groundwaters.

The average steady-state concentrations of the elements in the leachate for the experiments conducted with LLSR and HSR groundwaters are listed – along with their associated 2-σ uncertainties – in Tables 4.2 and 4.3, respectively. Figures 4.5 and 4.6 illustrate the achievement of steady-state conditions in the experiments conducted with LSSR and HSR groundwaters, respectively. The figures show that measured concentrations for Al, B, Li and Si were constant within analytical uncertainty with respect to time. Importantly, steady state was not achieved with the measured

concentrations of Mg and Na, which is attributable to the marked interactions of both Mg and Na with the glass during leaching, as discussed in Section 4.2. Note that Figures 4.5 and 4.6 only show plots for the experiments conducted at the lowest and highest

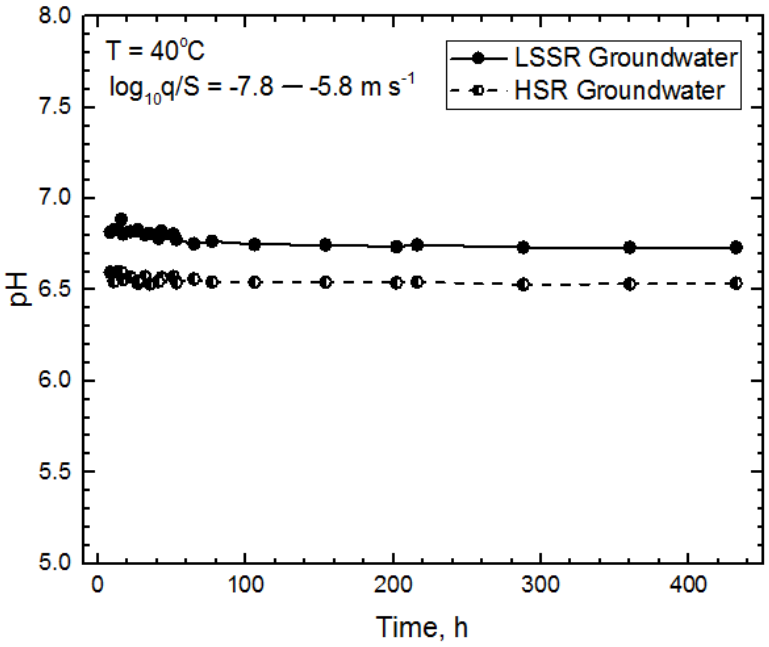

Figure 4.4: Time evolution of pH of LLSR and HSR groundwaters at 40 °C. The time evolution is the cumulative test duration. Experiment that was run at the fastest flow rate (250 mL/d) is to the left of the plot (0 h) and experiment that was run at the slowest flow rate (10 mL/d) is to the right (400 h).

values of parameter q/S, respectively. The plots for experiments conducted at other q/S values are shown in Appendix 27.

For experiments conducted with LSSR simulant groundwater, the concentrations of the elements in the leachates were invariant after approximately 216 h at the lowest flow rate ($q \approx 10$ mL d^{-1}), whereas steady state was achieved after 360 h for experiments conducted with HSR groundwater at the same flow rate. Steady state was achieved rapidly within 16 h for all the elements at the highest flow rate ($q \approx 250$ mL d^{-1}) for both groundwaters. Slightly higher concentrations of Al, B and Li were measured at the highest flow rate in the experiments conducted with LSSR groundwater than in the experiments with HSR groundwater; this phenomenon was reversed at the lowest flow rate. In the case of Si, the measured concentrations in the experiments with HSR groundwater were slightly higher than those measured in the experiments with LSSR groundwater at both the highest and lowest flow rates.

Table 4.2: Steady-state concentrations of elements (in µg/L) in the effluent solution at 40 °C in the experiments conducted with LSSR simulant groundwater. All values are an average of triplicate measurements. Uncertainties are in parentheses.

Experiment ID	Al	B	Cs	Li
GW_1	153.4 (0.15)	333.7 (0.10)	115.6 (0.02)	116.7 (0.02)
GW_2	188.3 (0.22)	492 (0.07)	107.8 (0.03)	185.9 (0.06)
GW_3	20.6 (0.10)	576.1 (0.07)	98.3 (0.01)	238.1 (0.02)
GW_4	119.0 (0.07)	806.2 (0.24)	188.9 (0.07)	292.9 (0.08)
GW_5	7.8 (0.03)	938.3 (0.08)	219.4 (0.05)	331.1 (0.04)
GW_6	6.6 (0.03)	1407.0 (0.39)	364.1 (0.18)	493.5 (0.13)
Experiment ID	**Mg**	**Mo**	**Na**	**Si**
GW_1	852.2 (1.08)	91.9 (0.01)	9144000 (30963.65)	1118.0 (0.67)
GW_2	695.2 (1.44)	100.7 (0.03)	5360000 (10788.16)	1507.0 (1.71)
GW_3	1988.0 (0.62)	93.0 (0.01)	6733000 (10895.55)	2412.0 (4.41)
GW_4	2290.0 (1.33)	164.9 (0.06)	9484000 (16526.52)	2716.0 (0.57)
GW_5	3862.0 (0.60)	196.6 (0.04)	12300000 (19049.08)	3168.0 (1.34)
GW_6	8970.0 (14.52)	336.6 (0.16)	12640000 (14495.51)	3939.0 (1.22)

Table 4.3: Steady-state concentrations of elements (in µg/L) in the effluent solution at 40 °C in the experiments conducted with HSR simulant groundwater. All values are an average of triplicate measurements. Uncertainties are in parentheses.

Experiment ID	Al	B	Cs	Li
GW_7	118.9 (0.07)	300 (0.17)	93.0 (0.03)	105.3 (0.11)
GW_8	137.7 (0.18)	414.8 (0.23)	125.4 (0.04)	149.0 (0.07)
GW_9	53.9 (0.04)	574.8 (0.09)	104.5 (0.01)	238.5 (0.03)
GW_10	25.4 (0.07)	921.0 (0.56)	231.8 (0.14)	383.3 (0.17)
GW_11	17.1 (0.04)	975.6 (0.16)	250.4 (0.06)	370.3 (0.06)
GW_12	8.6 (0.01)	1761.0 (0.44)	452.4 (0.15)	597.0 (0.14)
Experiment ID	**Mg**	**Mo**	**Na**	**Si**
GW_7	970.1 (99.27)	86.1 (0.03)	8496000 (17282.26)	1175.0 (0.66))
GW_8	275.6 (2.23)	113.3 (0.04)	9551000 (16780.21)	1405.0 (0.47)
GW_9	2114 (0.47)	95.6 (0.01)	10510000 (22515.47)	2181.0 (0.69)
GW_10	3133.0 (11.43)	211.4 (0.12)	13300000 (23472.40)	2311.0 (0.43)
GW_11	3863.0 (1.58)	231.2 (0.06)	16500000 (28362.65)	2766.0 (1.30)
GW_12	9850.0 (15.09)	424.9 (0.14)	19850000 (30381.80)	4101.0 (0.97)

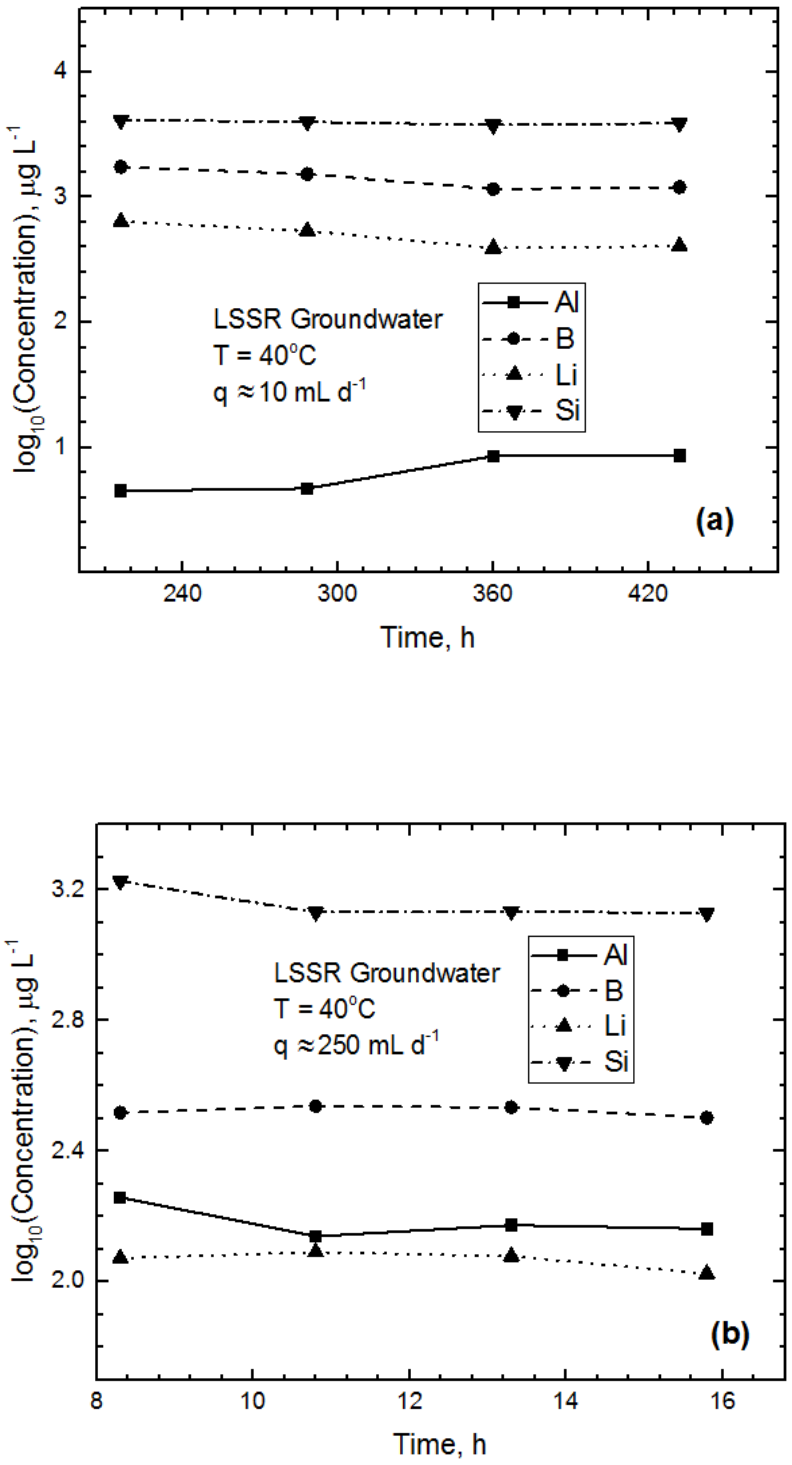

Figure 4.5: Plots of the log of background-corrected concentration (in µg/L) for Al, B, Li and Si at 40 °C as a function of time (in hour) at the lowest and highest values of q/S for experiments conducted with LSSR simulant groundwater, plot (a) $\log_{10}$q/S = -5.8 m/s; (b) $\log_{10}$q/S = -7.8 m/s.

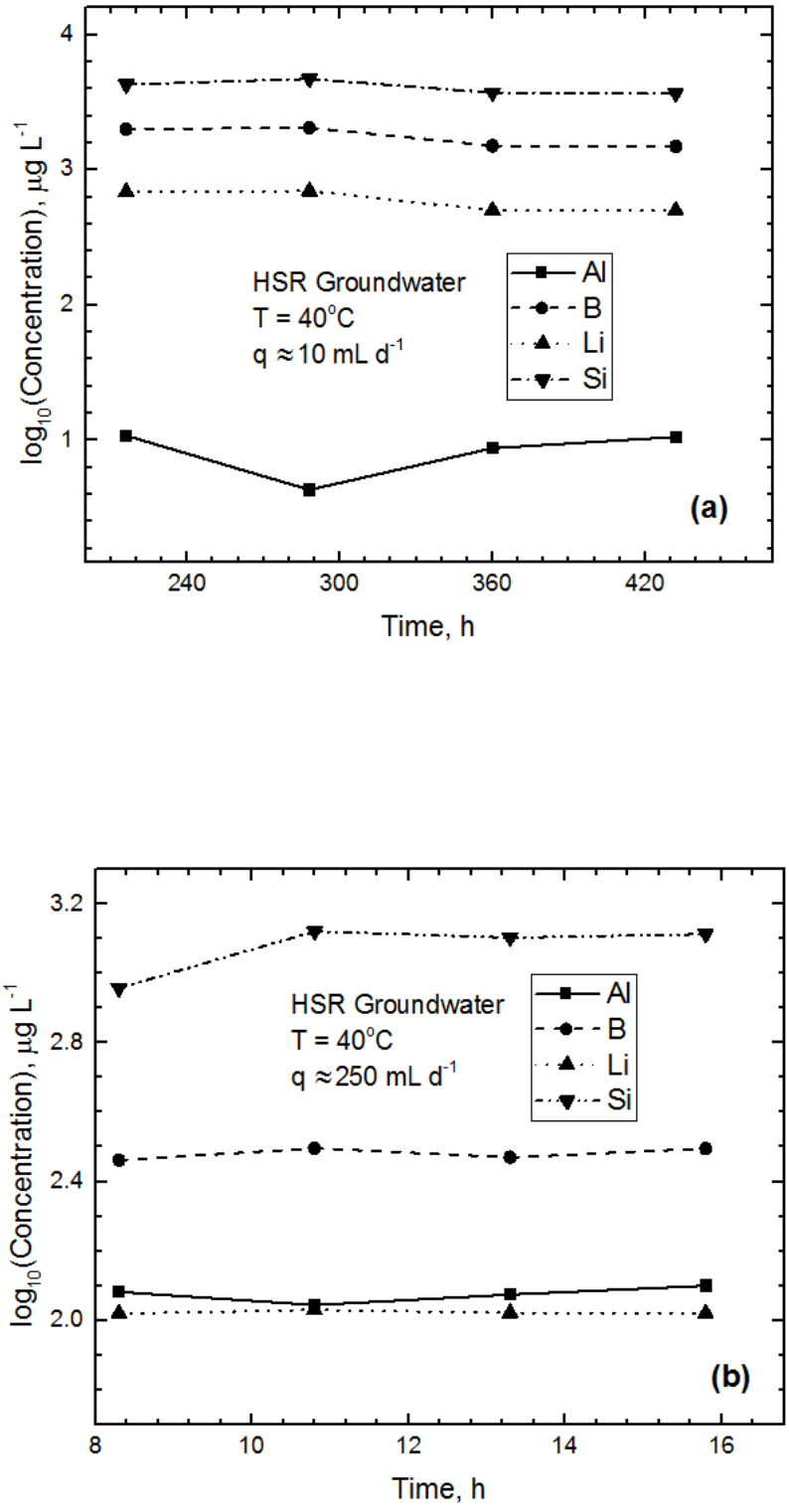

Figure 4.6: Plots of the log of background-corrected concentration (in µg/L) for Al, B, Li and Si at 40 °C as a function of time (in hour) at the lowest and highest values of q/S for experiments conducted with HSR simulant groundwater, plot (a) $\log_{10}$q/S = -7.8 m/s; (b) $\log_{10}$q/S = -5.8 m/s.

4.4 Normalised Dissolution Rates of Elements

Tables 4.4 and 4.5 list the normalised average dissolution rates, based on the steady-state release of elements to solution – along with their associated 2-σ uncertainties, as well as their respective $\log_{10}$ of the q/S ratio, which ranged between -7.8 and -5.8 m s^{-1} – for experiments conducted with LSSR and HSR groundwaters, respectively. Normalised dissolution rates of elements measured for LSSR and HSR groundwaters for each test are listed in Appendices 28. The computations of the uncertainties in the release of the elements are presented in Appendix 29.

The normalised dissolution rates of elements are plotted against the cumulative test duration for experiments conducted with both groundwaters, as shown in Figure 4.7. The figures illustrate similar dissolution rates of elements in both groundwaters; the release rates of elements in the LLSR groundwater ranged between 0.0 and 3.7 g m^{-2} d^{-2} (Figure 4.7a), whereas the release rates of elements in HSR groundwater ranged between 0.0 and 3.0 g m^{-2} d^{-2} (Figure 4.7b). Normalised rates based on the most soluble glass components, including B, Cs, Li and Mo, were slightly higher than the normalised rates of low-solubility elements (Si and Al) in both groundwaters. The normalised release of elements in both groundwaters was slightly faster in the initial stage (i.e. at higher flow rates) than at the later stage (i.e. at lower flow rates). This trend in dissolution rates indicates that the rates at the later stage (i.e. lowest flow rate) were approaching the border of rate drop regime.

Table 4.4: Normalised average dissolution rates based on release of Al, B, Cs, Li, Mo and Si at 40 ^{o}C in g/(m^2d) in the experiments conducted with LSSR simulant groundwater. 2-σ uncertainties are in parentheses.

Experiment ID	$\log_{10}$(q/S)	Al	B	Cs
GW_1	-5.8	0.1642 (0.0951)	0.1815 (0.028)	0.3669 (0.027)
GW_2	-6.1	0.1192 (0.0691)	0.1352 (0.009)	0.1727 (0.021)
GW_3	-6.3	0.007051 (0.0037)	0.09421 (0.006)	0.09388 (0.004)
GW_4	-6.5	0.02957 (0.0089)	0.08756 (0.013)	0.1197 (0.020)
GW_5	-6.8	0.000952 (0.0004)	0.05143 (0.003)	0.07013 (0.007)
GW_6	-7.8	0.0003096 (0.0001)	0.03053 (0.004)	0.04611 (0.02)
Experiment ID	**$\log_{10}$(q/S)**	**Li**	**Mo**	**Si**
GW_1	-5.8	0.1756 (0.015)	0.2913 (0.05)	0.1778 (0.043)
GW_2	-6.1	0.1411 (0.023)	0.1613 (0.03)	0.121 (0.055)
GW_3	-6.3	0.1077 (0.006)	0.08881 (0.01)	0.09656 (0.043)
GW_4	-6.5	0.08789 (0.012)	0.1045 (0.02)	0.07057 (0.007)
GW_5	-6.8	0.05014 (0.003)	0.06285 (0.01)	0.04132 (0.009)
GW_6	-7.8	0.02959 (0.004)	0.04263 (0.01)	0.02033 (0.003)

Table 4.5: Normalised average dissolution rates based on release of Al, B, Cs, Li, Mo and Si at 40 ^{o}C in g/(m^{2}d) in the experiments conducted with HSR simulant groundwater. 2-σ uncertainties are in parentheses.

Experiment ID	log_{10}(q/S)	Al	B	Cs
GW_7	-5.8	0.1489 (0.0418)	0.1644 (0.048)	0.2964 (0.037)
GW_8	-6.1	0.08584 (0.0566)	0.1143 (0.032)	0.2012 (0.029)
GW_9	-6.3	0.02027 (0.0071)	0.09399 (0.008)	0.09961 (0.005)
GW_10	-6.5	0.00624 (0.0040)	0.09983 (0.031)	0.1466 (0.039)
GW_11	-6.8	0.002148 (0.0006)	0.05338 (0.005)	0.08002 (0.009)
GW_12	-7.8	0.0004281 (0.0001)	0.03846 (0.005)	0.05766 (0.009)
Experiment ID	**log_{10}(q/S)**	**Li**	**Mo**	**Si**
GW_7	-5.8	0.1583 (0.081)	0.2745 (0.06)	0.1525 (0.042)
GW_8	-6.1	0.1134 (0.026)	0.1819 (0.04)	0.09253 (0.015)
GW_9	-6.3	0.1077 (0.006)	0.0911 (0.01)	0.08559 (0.013)
GW_10	-6.5	0.1013 (0.026)	0.1337 (0.04)	0.05971 (0.006)
GW_11	-6.8	0.05598 (0.005)	0.07388 (0.01)	0.03624 (0.008)
GW_12	-7.8	0.03603 (0.004)	0.05416 (0.01)	0.02137 (0.003)

4.5 Measurement of Forward Dissolution Rates in LSSR and HSR Simulant Groundwaters

As recommended in ASTM CI662 (see Section 3.4 for a discussion of this), the forward dissolution rates of MW25 in both LSSR and HSR groundwaters were determined from the plot of the normalised rate against steady-state Si concentration, as shown in Figure 4.8. In order to consider the concentration of Si initially present in both groundwaters (see Section 2.2.2), the rates were extrapolated to C_{Si} = 1 mg/L.

The forward rates are given by the y-intercepts of the regression lines in Figure 4.8, which indicates forward rates of 0.14±0.02 g m^{-2} d^{-1} and 0.09±0.03 g m^{-2} d^{-1} for experiments with LSSR and HSR groundwaters, respectively. Uncertainties are the standard deviations in the regressed rate values obtained using a least-squares linear regression model. The relationship between the rates and the steady-state Si concentrations is explained by the regression equations, such that R^2=0.941 and R^2=0.849 for experiments conducted with LSSR and HSR groundwaters, respectively, indicate that 94% and 85% of the variations in the database is explained by the regression equations. The higher forward rate measured in LSSR groundwater correlates to the higher alkalinity of the leachates collected in the experiments with LSSR groundwater illustrated in Figure 4.4, which shows that the pH of leachates in experiments with LSSR groundwater is approximately 0.25 pH unit higher than the pH

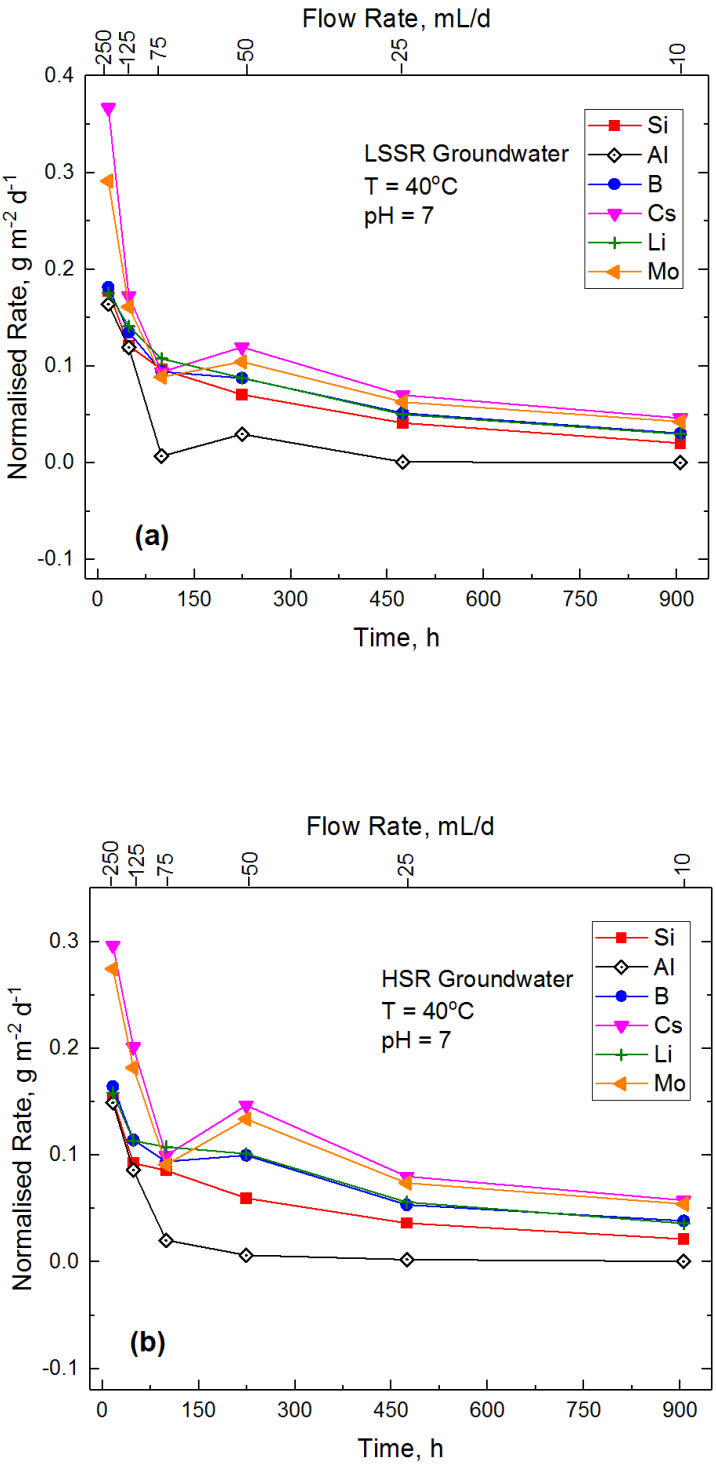

Figure 4.7: Release of Al, B, Cs, Li, Mo and Si [in g/(m^{2}d)] as a function of test duration and flow rate in the experiments conducted with: (a) LSSR simulant groundwater; (b) HSR simulant groundwater.

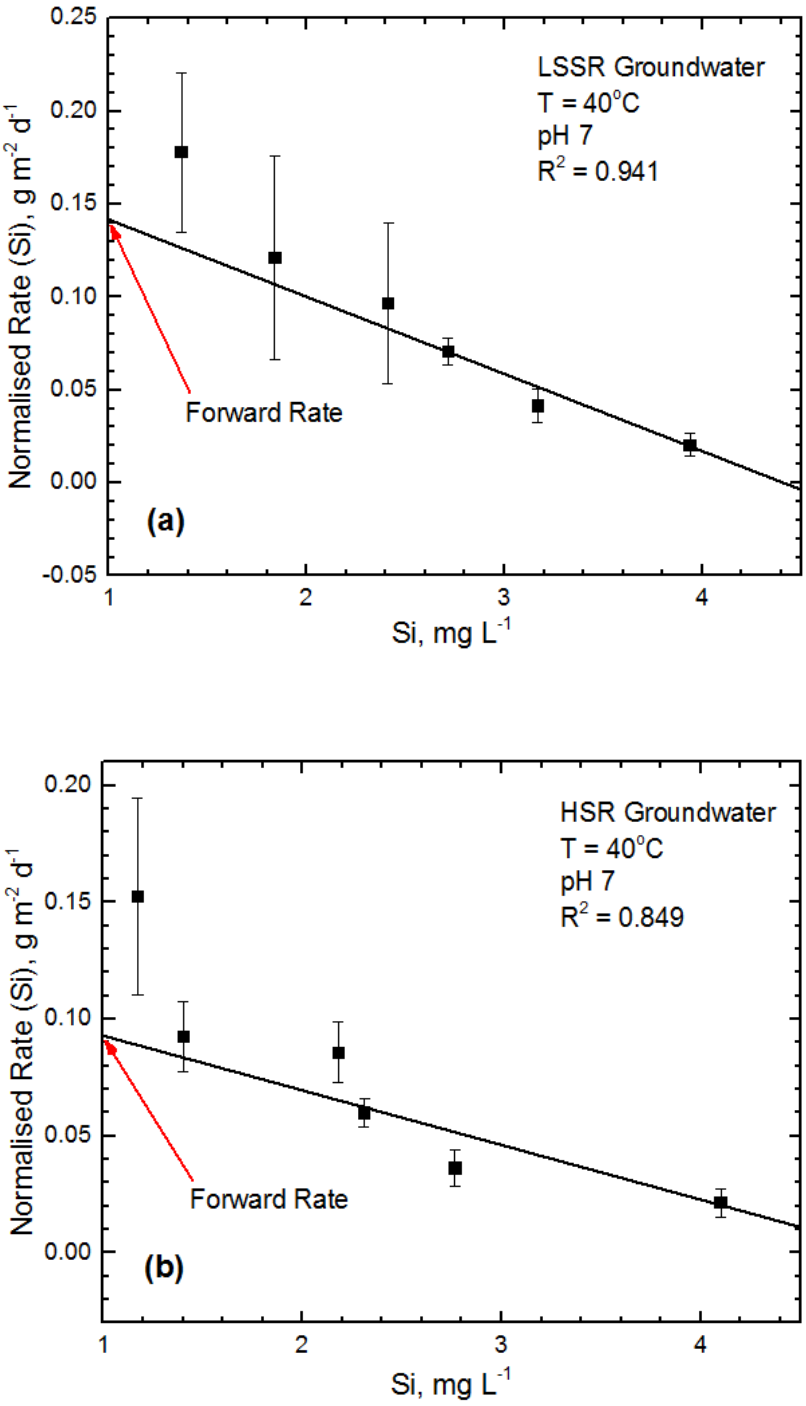

Figure 4.8: Plot of normalised rate [in g/(m^2d)] versus steady-state Si concentration (in mg/L) at 40 ^{o}C, plot (a) LSSR groundwater; (b) HSR groundwater. The forward dissolution rate (maximum rate), indicated by an arrow, is equal to the value at the y-intercept. Note that total Si concentration was used instead of [H_4SiO_4](or $SiO_2.2H_2O$) for convenience; there is often a factor of 28/96 difference. 2-σ uncertainties in the measured rates are indicated by error bars.

of leachates in experiments with HSR groundwater. This finding is consistent with the batch dissolution studies on MW25 using the same groundwaters (Corkhill *et al.,* 2013; Schofield *et al.,* 2016).

4.6 Results of Post-leaching Solids Analysis

Examinations using SEM/EDX and XRD analyses were undertaken to investigate whether there was precipitation of secondary phases on the reacted glass samples. Only the samples from experiments at the lowest q/S value were investigated because the accumulation of leached layers and secondary phases on the glass surface is restricted through continuous solution renewal in the SPFT method, so that the precipitation of secondary phases on the reacted glass samples is only possible at low flow rates. The analyses were carried out in the Department of Earth Sciences at the University of Cambridge, UK.

The procedure used in preparing the glass specimens was similar to the one described in Section 3.4; thus, the reacted sample was air-dried at 50 ^{o}C and later collected and stored over silica gel at room temperature. Samples were classified based on simulant groundwater type and flow rates used in the tests, and labelled accordingly. For SEM/EDX analysis, specimens were prepared by sparingly sprinkling the glass samples with a spatula onto carbon adhesive discs mounted on aluminium stubs. Secondary electron images (SEI) were collected on an FEI Quanta650F SEM platform at 15.00 kV and low vacuum. Note that the use of low vacuum in this case obviated the necessity to coat the samples because positively ionised gas atoms neutralise specimen charging when the machine is set to a low vacuum, so that secondary electrons leaving the specimen balance those arriving in the beam (Danilatos, 1994). For XRD analysis, powder samples were ground using a pestle and a mortar to ensure that large numbers of crystallites were available to the X-ray beam in every possible orientation. The samples were mounted on plastic holders and held in place using acetone. X-ray powder diffractograms in the 2θ range 10–60^{o} were collected in the open air in Bragg-Brentano geometry on a Bruker D5000 diffractometer equipped with sample spinner, Cu radiation and scintillation point detector. Data-collection conditions were: step size 0.05^{o}, divergence slit 0.06 mm, detector slit 0.02 mm, 30 x 20 kV x mA and 30 seconds/step.

The SEM/EDX images of the specimens collected after leaching in LSSR and HSR simulant groundwaters are shown in Figures 4.9 and 4.10, respectively. Globular and

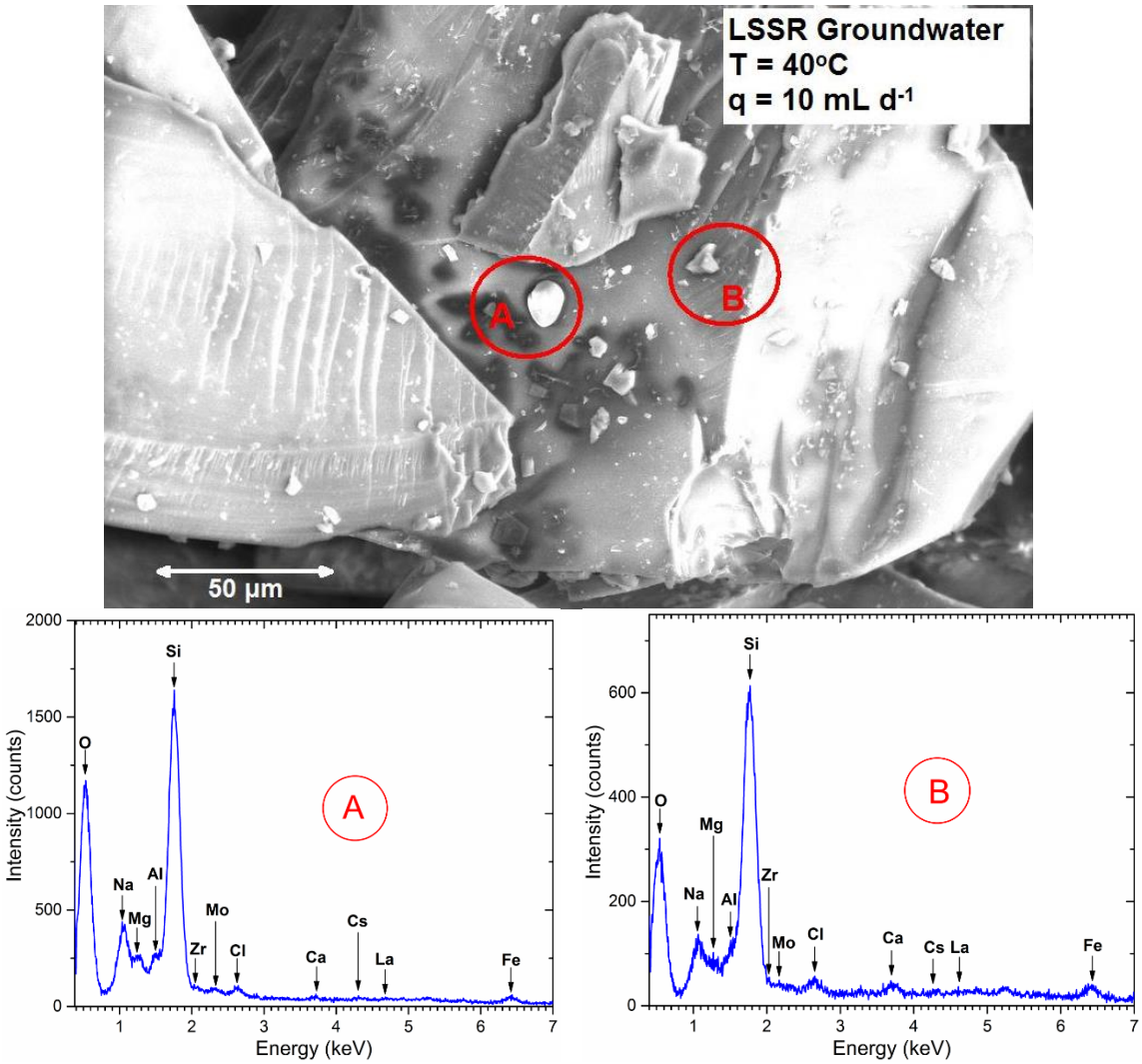

Figure 4.9: SEM data of MW25 and corresponding EDX spectra after reaction with LSSR simulant groundwater. Experimental conditions are 40 °C and $\log_{10}q/S$ = -7.8 m/s.

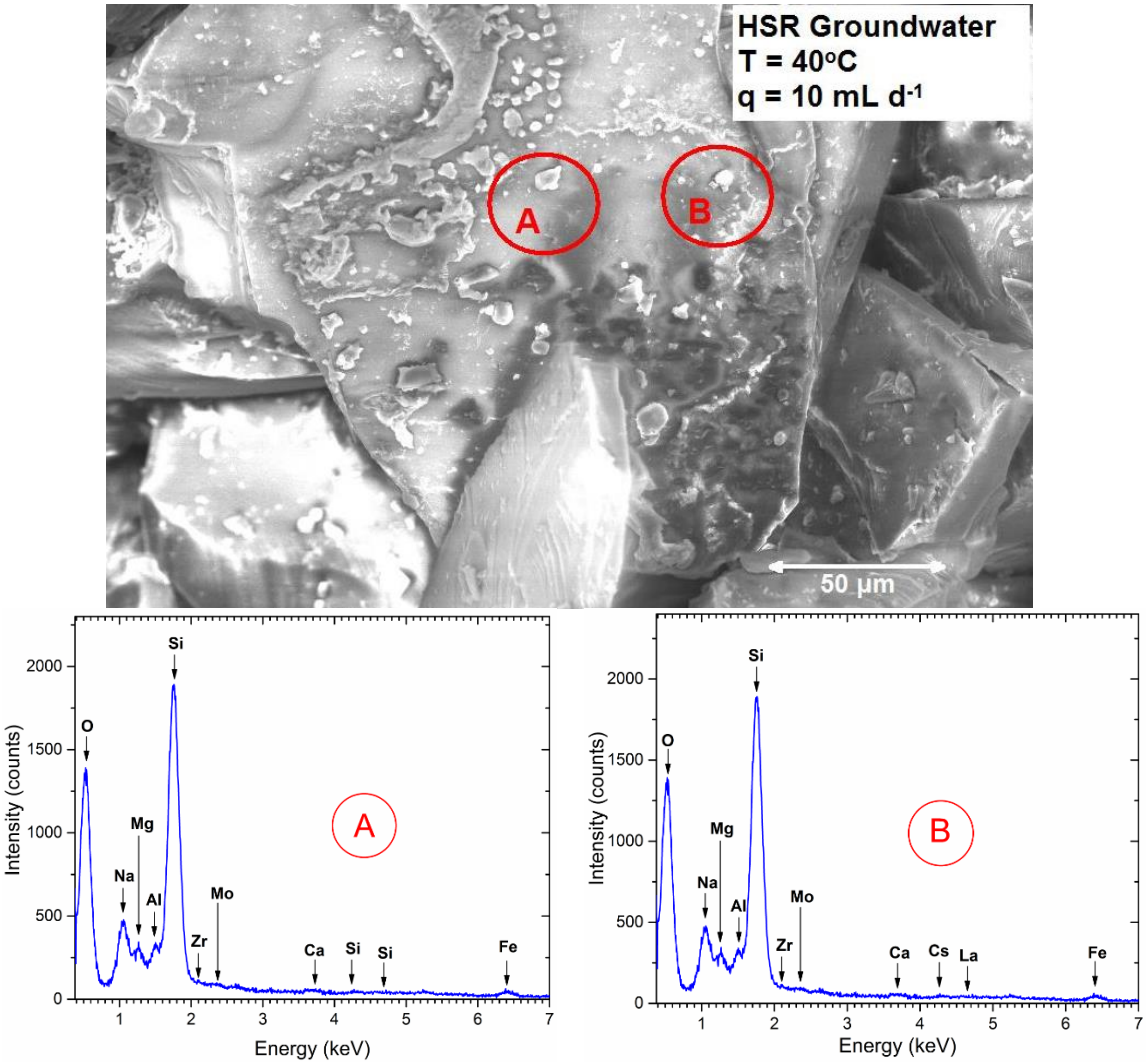

Figure 4.10: SEM data of MW25 and corresponding EDX spectra after reaction with HSR simulant groundwater. Experimental conditions are 40 °C and $\log_{10}q/S$ = -7.8 m/s.

acicular precipitates were formed on the surface of the specimen leached in LSSR groundwater, whereas only acicular particles appear on the specimen leached in HSR groundwater; the precipitates are ~5 μm in size. Analysis of the specimens by powder XRD revealed the presence of ruthenium dioxide (RuO_2) and a spinel phase [$(Fe,Mg)(Cr,Fe)_2O_4$] on the glass surface, which is the same as the phases present in the unleached glass specimen (Figure 4.11).

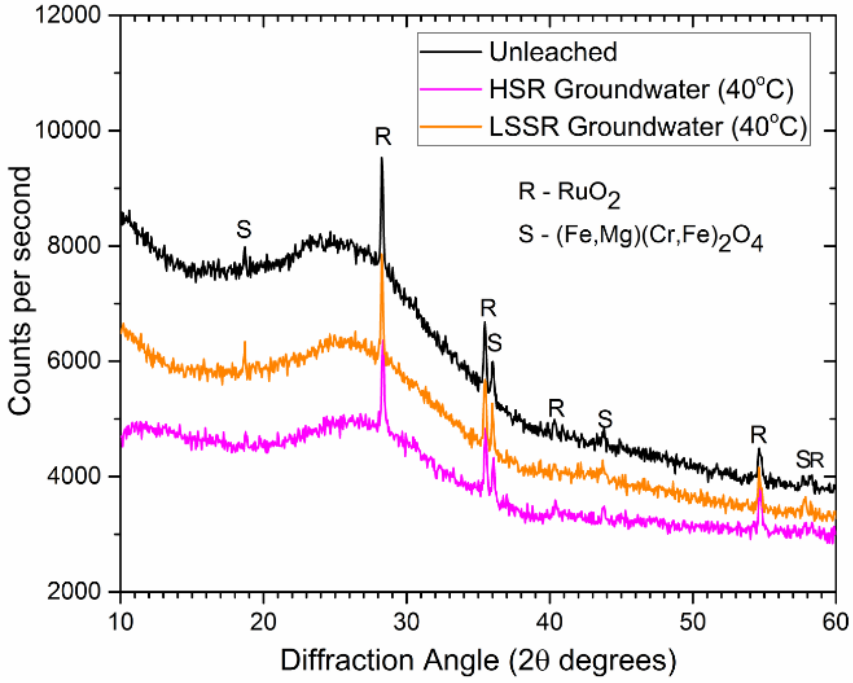

Figure 4.11: XRD patterns of MW25 before and after leaching in LSSR and HSR groundwaters at 40 °C.

5 DISCUSSION OF EXPERIMENTAL RESULTS

5.1 Introduction

The aim of this chapter is to integrate key experimental results from the previous chapters in order to enhance the scientific understanding of dissolution kinetics of MW25 glass under the different experimental conditions used in this study. To achieve this, some of the important results that were discussed in the experimental chapters (Chapters 3 and 4) are revisited and some of the pre-existing research cited in those chapters is recapped with a view to blending the new results in the present study with the existing literature. Importantly, the discussion of the experimental results is focused principally on the release of elemental components of MW25 glass, which forms part of the overarching goals of this study. Ancillary results, such as the effect of silica on release rates and dependence of rates on temperature, are also discussed.

5.2 Comparison of the Surface Area Estimation Methods

In order to avoid misinterpretation, a physically plausible verification of the numerical method was carried out by analysing the sizes of the particles in the reacted powder sample in the MW-T_22 experiment using MasterSizer 3000. The resulting particle size distribution curve was superimposed on the size distribution curve obtained using the numerical method as shown in Figure 5.1, which indicates a good match between the analysed and calculated particle distributions. This suggests that the numerical estimate is reproducible and provides an excellent estimate of the evolving surface area of the reacted glass sample.

The normalised dissolution rate of Si in experiment MW-T_22 was used to compare the new surface area estimation method (numerical estimate) with geometric and BET

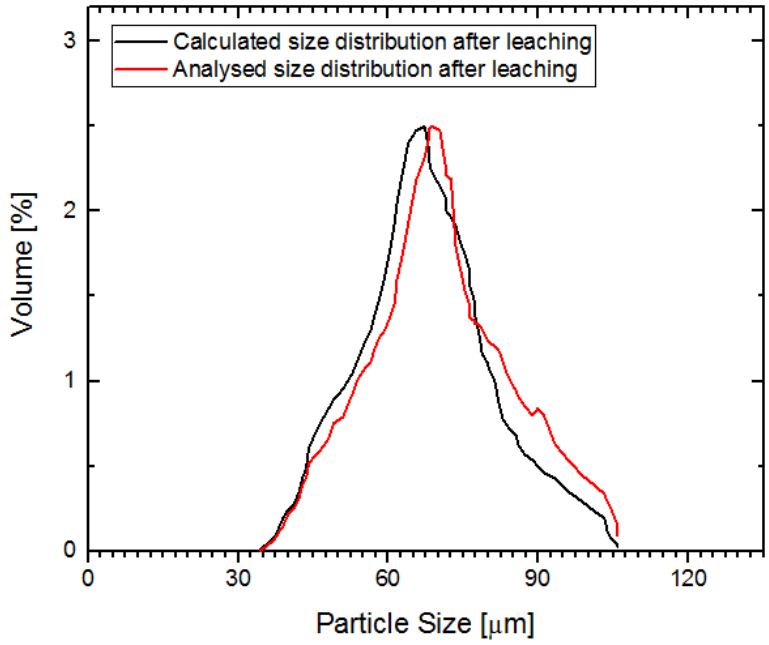

Figure 5.1: Comparison of the analysed and calculated particle size distributions after leaching in experiment MW-T_22. The analysed distribution was obtained from particle-size analysis using MasterSizer 3000 and the calculated distribution was obtained using the numerical method of surface area estimation.

methods. The dissolution rate of this experiment is 1.37±0.234 g m^{-2} d^{-1} using the numerical method. If the geometric method had been used to estimate the surface area in the same experiment, it would have yielded a dissolution rate of 1.13 g m^{-2} d^{-1}. The resulting dissolution rate would be 0.219 g m^{-2} d^{-1} if the BET method were used, which is markedly different from the results obtained using numerical and geometric methods.

It is noted that the dissolution rates measured using the geometric estimate are within the experimental uncertainty of the dissolution rates measured using the numerical estimate, as shown in Figure 5.2, which illustrates rates measured at each sampling in experiment MW-T_22 using the three surface area methods. Therefore, although the numerical estimate provides a more accurate appraisal of the surface area of reacted glass powder, the geometric estimate is also suitable. It seems that the use of change in mass (Eq. [2.5]) (see Section 2.4.3) to scale the mass lost relative to the initial surface area calculated with the initial diameter in the geometric method is effective.

Recently, Fournier *et al.* (2016) compared the initial rates measured using the geometric and BET surface area estimation methods with the initial rates measured using a monolith glass sample. The use of particle size distribution for the numerical estimation

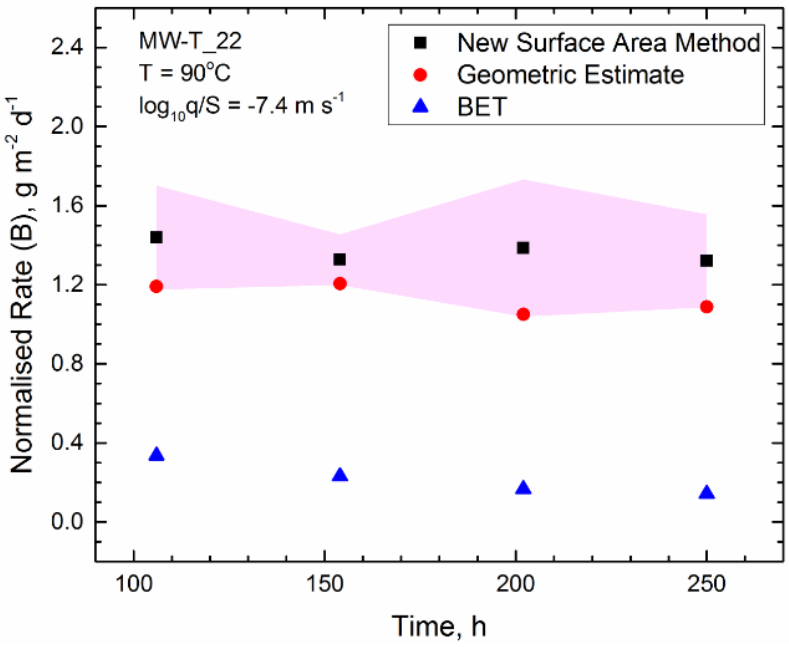

Figure 5.2: Comparison between dissolution rates measured using the new surface area method (numerical estimate), the geometric estimate and the BET method. The shaded region represents uncertainties in the rates measured using the numerical estimate.

of the surface area of powdered glass particles in the present study is similar to the approach used by Fournier *et al.* (2016). However, in this study the distribution of the glass particles was assumed to be continuous, whereas Fournier *et al.* (2016) used statistical summation to recalculate the geometric surface area of glass particles. The approach of numerical integration and assumption of a continuous distribution used in the present study represents an advancement over the statistical approach used by Fournier *et al.* (2016) because it reduces the computation needed to evaluate the surface area. Importantly, although the shape of glass particles was assumed to be spherical, the new surface area estimation method in the present study can be applied to any collection of similar shapes, as volume can easily be linked to the cube of any dimension, and also for the fact that surface area is directly proportional to the square of the same dimension.

5.3 Comparison of the Forward Rates Measured in Deionised Water at 40 and 90 ^{o}C

The forward rates of 0.19±0.02 g m^{-2} d^{-1} and 1.84±0.35 g m^{-2} d^{-1} (see Figure 3.4 in Section 3.3) measured at 40 and 90 ^{o}C, respectively, imply that the maximum rate of dissolution of MW25 in circum-neutral media is approximately one order of magnitude

higher at 90 ^{o}C than at 40 ^{o}C. These forward rates are comparable with ~0.23 g m^{-2} d^{-1} and ~1.50 g m^{-2} d^{-1} measured for a similar Magnox glass at 40 ^{o}C by Abraitis *et al.* (2000a) in moderately alkaline solution, and at 90 ^{o}C by Werme *et al.* (1990) in neutral solution, respectively. Abraitis *et al.* (2000a) identified weak Si-dependence of dissolution rate of a MW25-type glass, which necessitated the investigation of the dependence of rate of dissolution of the glass on Al species in Abraitis *et al.* (2000b). The similarity of forward rates measured in these studies reflects weak Si-dependence, which could be a characteristic of the UK Magnox glass, as suggested by Abraitis *et al.* (2000b). It should be beneficial, therefore, to understand how the release of elements in this glass is constrained by silica, which is the dominant aqueous species released from the glass.

5.3.1 Effect of Silica Saturation on Dissolution Rates

Dissolution rates with respect to the major glass components (Al, B, Li, Mg and Na) are plotted in Figure 5.3 against the activity of the major silica species in solution (silicic acid; $H_4SiO_4^o$) at 40 and 90 ^{o}C. The data indicates that the release of Al decreased rapidly with increasing activity of silicic acid at both temperatures, with Mg exhibiting similar release behaviour as Al at 90 ^{o}C. However, there was a relatively moderate decrease in the release of Mg at 40 ^{o}C. Similarly, at 40 ^{o}C the release of B, Li and Na were constrained as more silicic acid was released into solution (Figure 5.3a). This trend was reversed at 90 ^{o}C, as B, Li and Na were increasingly released despite the increasing activity of silicic acid (Figure 5.3b). This seems to contradict the Grambow model, in which the activity of silica is assumed to control the dissolution rate of borosilicate glass; however, interestingly a recent study carried out on international reference glass (ISG) at pH 7 and 90 ^{o}C also found that the release of mobile elements, including B and Na, is not dependent on silica activity (Gin *et al.*, 2015). The differing chemical compositions of ISG and MW25 may lead one to conclude that the independent behaviour of B (and the alkali metals) relative to Si is absolute. However, given the similarity in experimental conditions, particularly the concordant temperature, it would appear that the preferential release of B, Li and Na is temperature-dependent. It seems that the main cause of the independent behaviour of the mobile elements relative to Si is that the experiments conducted at 90 ^{o}C and lower q/S values were barely at steady state. This hypothesis is reinforced by the fact that Gin *et al.* (2015) conducted their experiments using the batch method, which is not designed to establish a steady state. In addition, because this behaviour was not exhibited by the mobile elements at 40 ^{o}C,

their independent release relative to Si release cannot be generalised. Importantly, the plots in Figure 5.3 clarify that releases are only congruent under test conditions where Si concentration remains low – when glass dissolves at very near forward rate; otherwise, B and the alkali metals are released preferentially. This finding is consistent with the observations of Pierce *et al.* (2008b) and highlights the importance of using Si to evaluate the forward rate. An additional discussion of the temperature dependence of the dissolution rate of this glass is provided in the following section.

5.3.2 Remarks on Temperature Dependence of Dissolution Rates

The magnitude of the activation energy (E_a) provides important insights into the mechanisms involved in composite reaction processes, such that reactions are classified into transport control, surface control and mixed control (Lasaga, 1995). The range of E_a values associated with B, Na and Si-release rates in the case of MW25 in the present study (see Section 3.3.1) is consistent with a surface-controlled reaction mechanism that has an E_a in the range 41 and 84 kJ mol^{-1} (Lasaga, 1981). The temperature and silicic acid dependence of the dissolution rate can be understood better by considering the higher E_a values associated with B and Na release (relative to Si release).

At the molecular scale, silicate glass and mineral dissolution are governed by surface complexation reactions (Brady and House, 1996). The higher E_a values of B and Na are due to the number of metal sites that the cation creates on the glass surface, and point to proton-promoted hydrolysis of B – O bonds and ion exchange of bond-modifying alkali metals (Na and Li) at non-Si sites as the predominant reaction processes, such that the selective release of B and Na leads to an increase in the concentration of silicic acid. There is general acknowledgement that alkali metals [M] interact with Si sites (Dugger *et al.*, 1964); thus, the resultant SiO–M surface sites weaken the SiO bond, making it more susceptible to hydrolysis (Strandh *et al.*, 1997). The equations describing the hydrolysis of siloxane bonds, such as those in the MW25 glass network, may be written as:

$$< Si - O - Si < + H_2O = 2(Si - OH) \quad \textbf{(5.1)}$$

$$> Si - O - Si(OH)_3 + H_2O = > SiOH + H_4SiO_4 \quad \textbf{(5.2)}$$

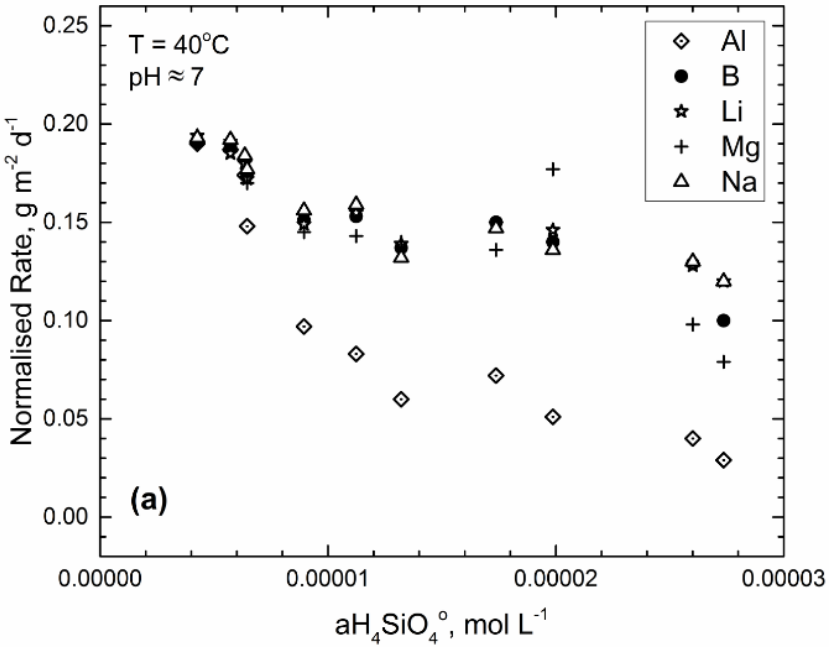

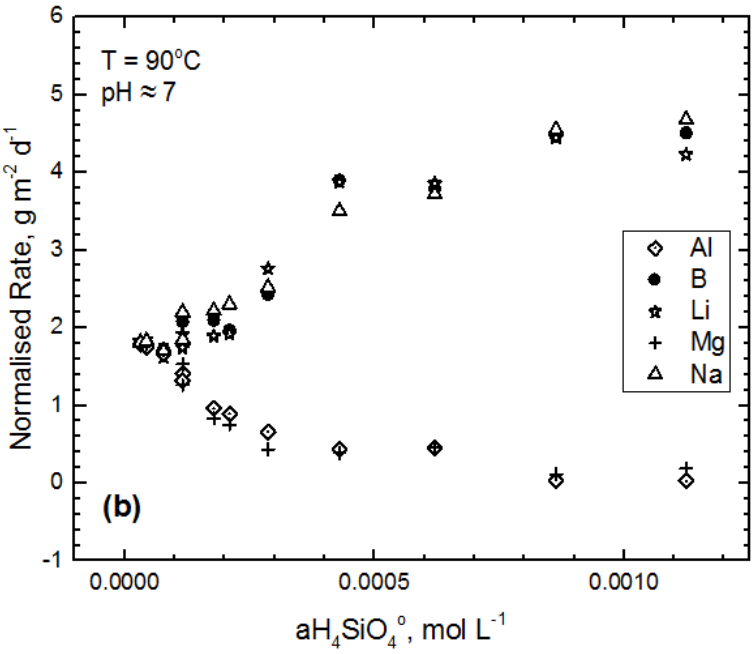

Figure 5.3: Effect of solution activity of silicic acid (in mol/L) on the release of Al, B, Li, Mg, and Na (in g/[m^{2}d]) at: (a) 40 ^{o}C; (b) 90 ^{o}C.

Siloxane bonds (Si – O – Si) at the Si site are continuously hydrolysed, resulting in the development and hydrolysis of silanol groups (>Si – OH) and ultimately the detachment of Si. The increase in concentration of silicic acid acts as an inhibitor for the rate of Si detachment and ultimately the glass dissolution rate. This would explain the equivalent dissolution rates achieved at the higher temperature. At 90 ^{o}C, the dissolution rate of silicic acid increases and eventually reaches a similar magnitude to the release rates of B and alkali metals, resulting in congruent dissolution. It seems clear that the surface-controlled hydrolysis of siloxane bonds is dominated by the hydrolysis of B – O bonds and ion exchange of the alkali metals at 90 ^{o}C, making it appear that the release of B, Li and Na are independent on the solution activity of silicic acid. As can be deduced from the foregoing, there is Si-dependence, albeit weak.

5.3.3 Effect of Ratio of Flow Rate to Surface Area (q/S) on Dissolution Rates for the Experiments with Deionised Water

The plots of normalised dissolution rates of the major glass components (Al, B, Li, Mg, Na and Si) as a function of the $\log_{10}$ of parameter q/S are shown in Figures 5.4 and 5.5 for experiments at 40 and 90 ^{o}C, respectively. The figures illustrate an initial transient release behaviour such that, as the q/S is increased (i.e. with increasing flow rate), the dissolution rates increase, with the exception of Figure 5.5b, in which the dissolution rates of B and alkali metals (Li and Na) decrease with increasing q/S. Normalised release rates of B, Li and Na are significantly higher than the rate of release of Si, Al and Mg at the lower values of $\log_{10}$q/S for experiments at 90 ^{o}C. A similar trend was shown by the 40 ^{o}C experiments, although at a lesser extent than observed at 90 ^{o}C.

Following the transient dissolution stage, the dissolution rates reach a constant (equivalent) value at 40 ^{o}C in the experiments conducted with $\log_{10}$q/S > -6.0 m s^{-1}, and at 90 ^{o}C in the experiments with $\log_{10}$q/S > -6.4 m s^{-1}. These equivalent rates provide evidence of congruent dissolution of this glass and are comparable with the results of a previous study (Abraitis *et al.,* 2000a), in which constant rates were attained for MW25 in a moderately alkaline media at 40 ^{o}C in experiments conducted with $\log_{10}$q/S > -6.5 m s^{-1}. However, in a recent study on Magnox-ThORP-blend glasses (Cassingham *et al.,* 2015), constant dissolution rates were achieved at $\log_{10}$q/S > -7.5 m s^{-1}, which is a slight deviation from the $\log_{10}$q/S reported by Abraitis *et al.* (2000a) and in the present study.

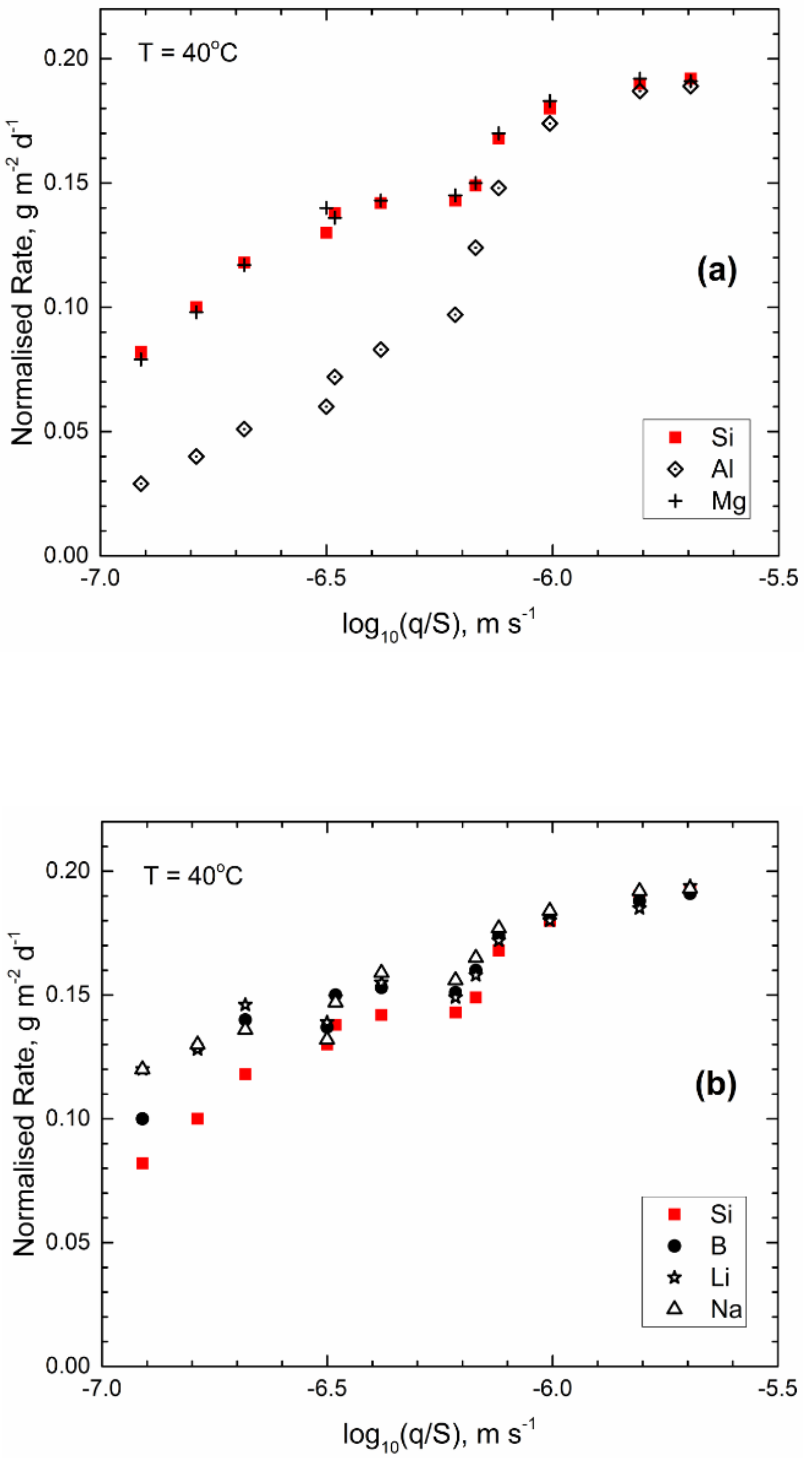

Figure 5.4: Steady-state dissolution rate [in g/(m^{2}d)] based on Al, B, Li, Mg, Na and Si at 40 ^{o}C as a function of log$_{10}$q/S (in m/s).

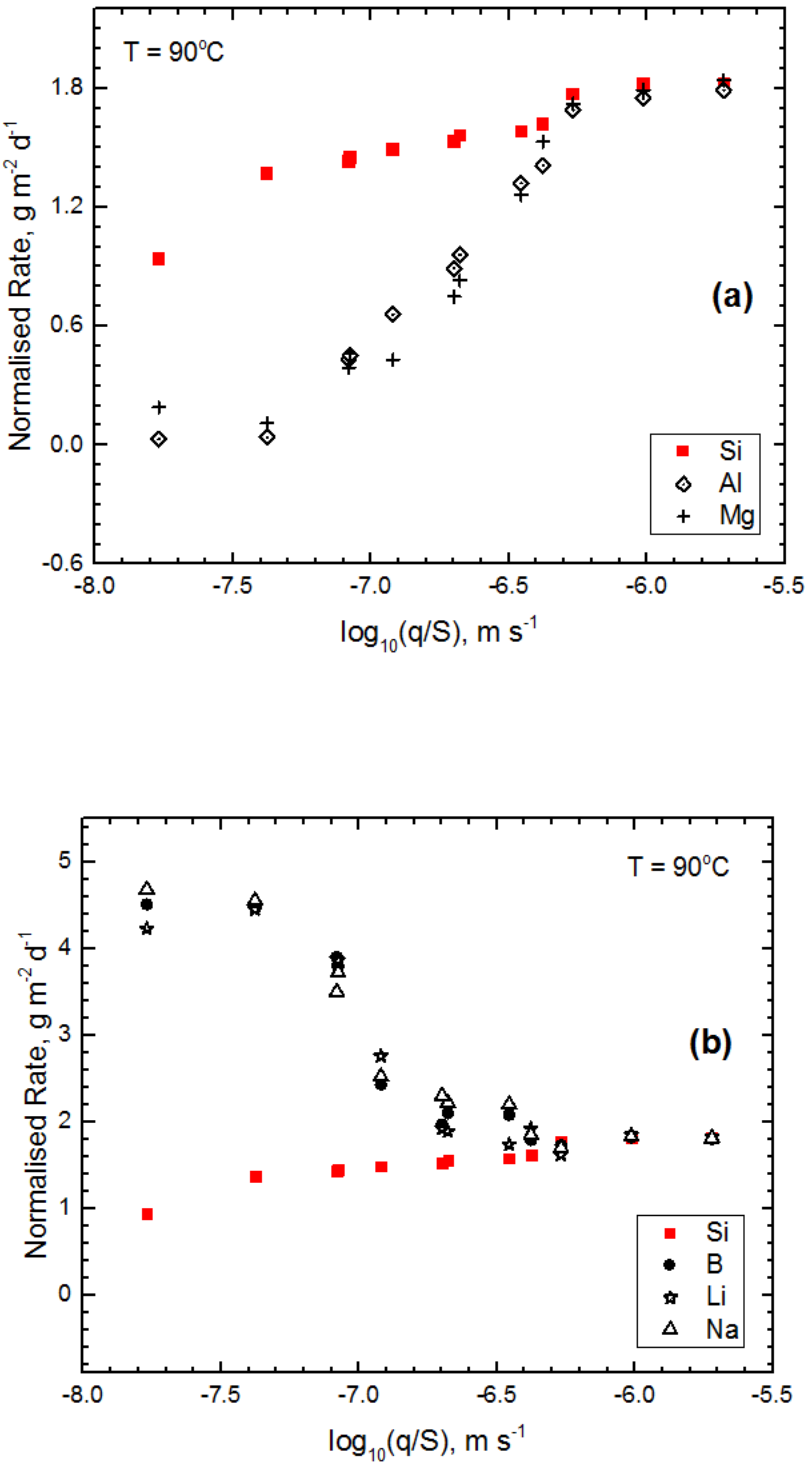

Figure 5.5: Steady-state dissolution rate [in g/(m^{2}d)] based on Al, B, Li, Mg, Na and Si at 90 ^{o}C as a function of log$_{10}$q/S (in m/s).

It should be noted that the compositions of Magnox-ThORP-blend glasses are different to the MW25 compositions; in particular, the Al and Mg contents are significantly lower (~1/3) in the Magnox-ThORP-blend glasses (Harrison, 2014b). Therefore, the slight deviation in the $\log_{10}$q/S in which constant rates were achieved in the study by Cassingham *et al.* (2015) can be attributed to these compositional variations.

On the basis of the combined data, it seems that the dissolution process is dominated by the hydrolysis of B and ion exchange of the alkali metals (Li and Na) at non-Si sites. This suggests that the reaction of this glass with solution is governed by independent mechanistic processes, including ion exchange and matrix dissolution. The roles of hydrolysis and ion exchange, respectively, in the releases of boron (Scholze *et al.*, 1982) and alkali metals (McGrail *et al.*, 2001) are well established.

5.4 Comparison of Dissolution Rates of Elements in Deionised Water at 40 and 90 ^{o}C

Figures 5.6 and 5.7 show the plots of normalised rates of the high-solubility cations (i.e. B, Cs, Li, Mo and Na) and low-solubility cations (i.e. Al, Mg and Si), respectively, in deionised water at 40 and 90 ^{o}C against the cumulative test duration. The dissolution rates of all the elements are higher at 90 ^{o}C than at 40 ^{o}C, which indicates that the release of the elements is sensitive to temperature. Moreover, there is a noticeable difference in the release behaviour of elements at both temperatures. At 40 ^{o}C the normalised dissolution rates of the elements are essentially constant over the test duration. The sensitivity of the dissolution rates of the mobile elements, including B, Cs, Li, Mo and Na, to q/S values is negligible at this temperature, whereas the release rates of the network formers, including Al, Mg and Si, are slightly higher in the experiments conducted at higher q/S values than at lower q/S values. At 90 ^{o}C there is an opposing trend in the normalised rates of the elements, such that the release rates of Al, Mg and Si decrease from 0 h (high q/S value) to 906 h (low q/S), whereas the release rates of B, Cs, Li, Mo and Na increase from 0 h (high q/S value) to 906 h (low q/S value). This release behaviour suggests weak dependence of the release of the mobile elements relative to the release of the network formers at 90 ^{o}C and low values of parameter q/S. This finding is consistent with the results of a previous study on international simple glass (ISG) (Gin *et al.*, 2015), which was conducted at the same temperature. Generally, the normalised rates of the high-solubility cations (B, Cs, Li, Mo and Na) are higher at both 40 and 90 ^{o}C than the normalised rates of the low-solubility cations (Al, Mg and Si).

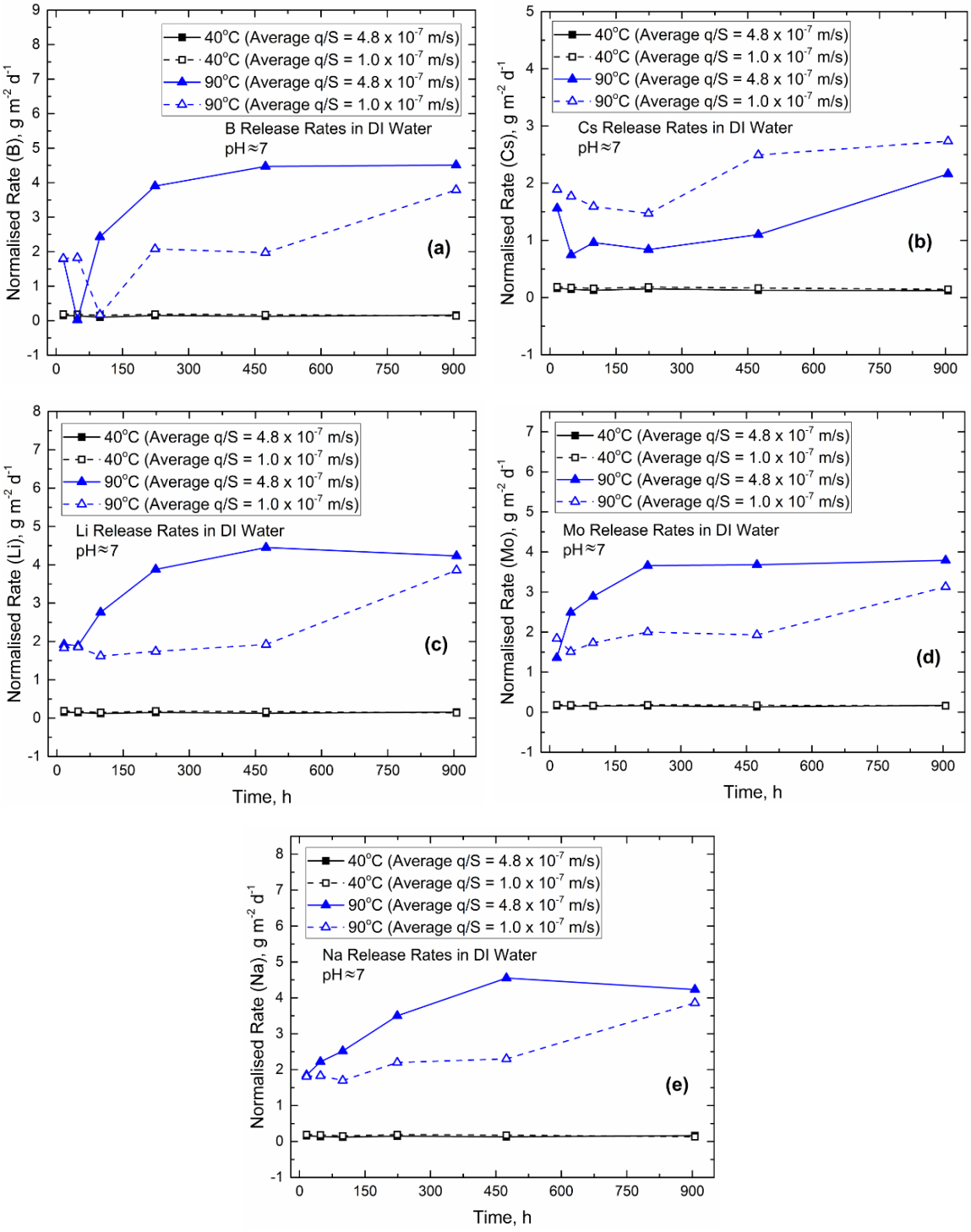

Figure 5.6: Average release of high-solubility cations (B, Cs, Li, Mo and Na) from glass in deionised water at 40 and 90 ^{o}C with respect to time. The two flow rates at each temperature correspond to separate samples with initial mass of 0.1 g (q/S = 4.8x10^{-7} m/s) and 0.5 g (q/S = 1.0x10^{-7} m/s).

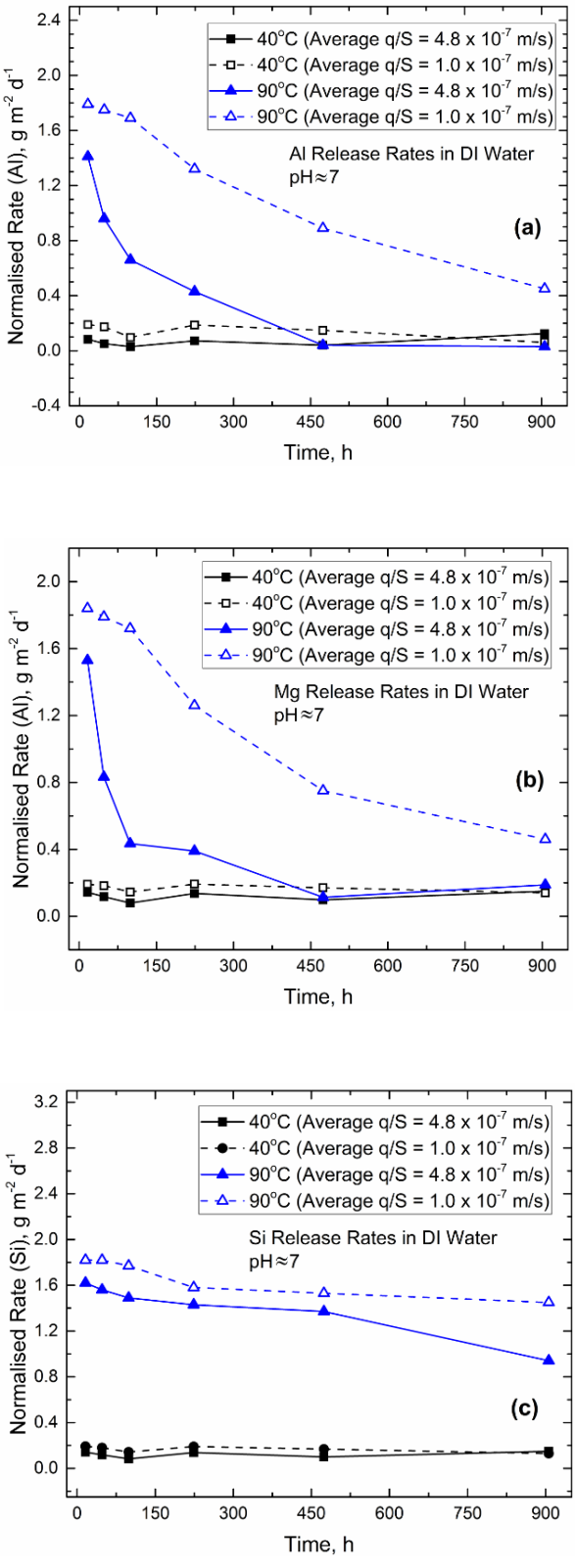

Figure 5.7: Average release of low-solubility cations (Al, Mg and Si) from glass in deionised water at 40 and 90 °C with respect to time. The two flow rates at each temperature correspond to separate samples with initial mass of 0.1 g (q/S = 4.8x10^{-7} m/s) and 0.5 g (q/S = 1.0x10^{-7} m/s).

5.5 Remarks on Solids and Imaging Analysis Results for the Experiments with Deionised Water

The detection of the same crystalline phases as those typically found in UK Magnox glass by XRD, including ruthenium dioxide (RuO_2) and a spinel phase [$(Fe,Mg)(Cr,Fe)_2O_4$], demonstrates that no new crystalline phases were formed as a result of the reaction of the glass with solution under the experimental conditions investigated. However, the preferential release of boron and the alkali metals relative to Si release at 90 ^oC, and the low q/S values shown in Figure 5.5b raises an important question regarding whether or not the release behaviour exhibited by boron and the alkali metals under these experimental conditions is an indication of phase separation of the glass.

Although SEM data shows a more extensive formation of surface precipitates on the reacted glass sample at 90 ^oC than at 40 ^oC, EDX of these features, illustrated as spectra A and B, formed at both temperatures revealed that the precipitates contain similar elements, including Al, Cs, Fe, La, Mg, Mo, Na, Si and Zr. Each element has a similar weight per cent to that in the unreacted Magnox glass (Table 5.1). However, it should be noted that the depth of penetration of the EDX instrument used in this study is between 3 and 5 μm, which implies that X-rays from the underlying glass constitute the data obtained. Therefore, the EDX spectra were collected for qualitative purpose only.

Note that the C (i.e. carbon) that is displayed in all the EDX spectra, which is also listed in Table 5.1, is most likely an artefact from the carbon adhesive discs used to keep the specimens on the aluminium stub, as ED detectors have a wide angle of acceptance (see Section 2.5.2.1). These similarities between the spectra collected at 40 and 90 ^oC to that of the unreacted glass indicate that the glass was not phase separated, and also provide evidence of the stoichiometry of the dissolution process, as well as compositional homogeneity of MW25. The absence of Mo and the depletion of Na in the spectra collected at 90 ^oC explain why Mo and Na result in much higher concentrations at this temperature than at 40 ^oC. Mo and Na are one of the elements that make up the crystalline alkali molybdate phase, which is a characteristic property of MW25; its absence in the 90 ^oC spectra suggests that part of the molybdate in the glass had exsolved.

Table 5.1: MW25 sample EDX (spectrum A) corresponding to SEM micrographs in Figures 3.7, 3.8 and 3.9. The C is probably from the carbon adhesive discs used to keep the specimens on the aluminium stub.

Element	Wt% (Unleached)	Wt% (40 °C)	Wt% (90 °C)
O	39.8	43.9	41.7
Si	24.9	24.4	25.2
Na	5.4	5.6	2.9
Fe	2.6	5.1	0.2
Mg	2.4	2.7	13.5
Al	2.3	2.3	0.7
C	1.7	3.0	1.9
Cs	1.1	1.3	0.6
La	1.0	1.7	0.1
Mo	0.8	0.8	0.0
Zr	1.1	1.0	0.0
Total	83.1	91.8	86.8

5.6 Comparison of Forward Dissolution Rates Measured in LSSR and HSR Simulant Groundwaters with Forward Rate in Deionised Water

The forward rates measured in deionised water and the two simulant groundwaters (LSSR and HSR) under the same experimental conditions (i.e. same temperature) were combined, as shown in Figure 5.8. According to the ASTM C1162 (ASTM, 2010) recommendation, the forward rates were determined on the basis of steady-state Si concentrations (C_{Si}), and the rates obtained at each C_{Si} were extrapolated to C_{Si} = 0 mg L^{-1} in the experiments conducted with deionised water. In the case of the simulant groundwaters, however, the rates were extrapolated to C_{Si} = 1 mg L^{-1} to account for 1000 μg L^{-1} of Si that constitutes the compositions of both groundwaters (see Section 2.2.2). As mentioned previously, the rationale behind the extrapolation was to ensure that forward rate is determined under infinitesimally dilute conditions.

As illustrated in Figure 5.8, the forward rate measured in deionised water (i.e. 0.19±0.02 g m^{-2} d^{-1}) was higher than those measured in LSSR and HSR groundwaters, which were 0.14±0.02 g m^{-2} d^{-1} and 0.09±0.03 g m^{-2} d^{-1}, respectively. The highest forward rate measured in deionised water is due to its lower ionic strength than LSSR and HSR simulant groundwaters. In addition, as shown in Figure 5.9, deionised water has no pH-buffering potential, so that the elements leaching from the glass dominate its pH. This explains why the pH of deionised water after reaction with glass is more alkaline than

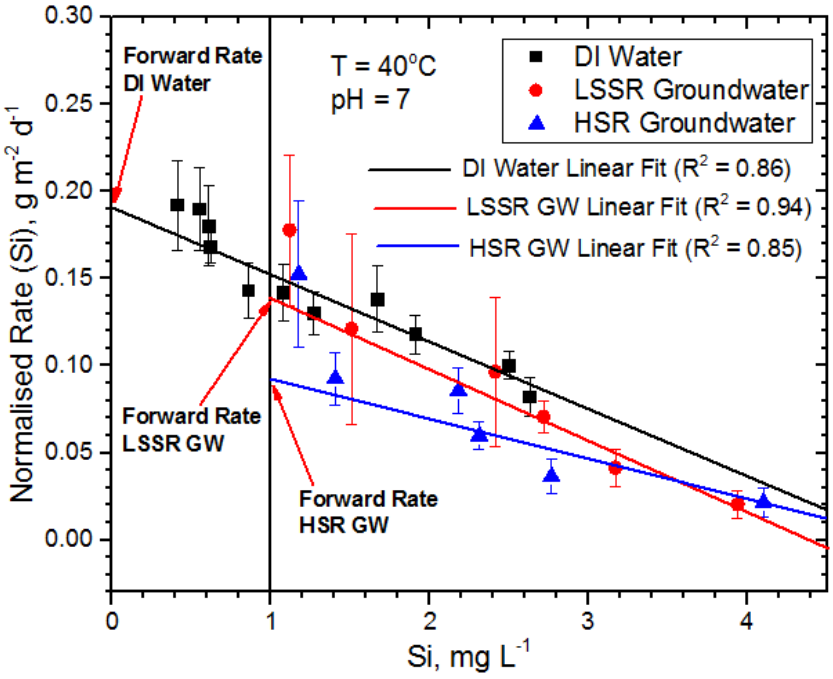

Figure 5.8: Comparison of forward dissolution rates in the experiments conducted with LSSR and HSR simulant groundwaters and deionised water. The conditions of the experiments were the same.

the pH of both LSSR and HSR groundwaters. Moreover, the higher forward rate measured in LSSR groundwater than in HSR groundwater correlates with higher alkalinity of the leachates collected in the experiments with LSSR groundwater. This finding is consistent with the observations in previous batch dissolution studies on MW25 using similar groundwater compositions (Corkhill *et al.*, 2013; Schofield *et al.*, 2016).

The forward rates of 0.14±0.02 g m^{-2} d^{-1} and 0.09±0.03 g m^{-2} d^{-1} measured for MW25 in LSSR and HSR groundwaters, respectively, in the present study are significantly higher than the initial dissolution rates reported in previous studies on MW25: 0.026±0.003 g m^{-2} d^{-1} in LSSR solution and 0.030±0.004 g m^{-2} d^{-1} in HSR solution based on boron release (Utton *et al.*, 2012); (3.32.18±0.3) x 10^{-7} g m^{-2} d^{-1} in LLSR solution based on Si release (Corkhill *et al.*, 2013); 0.035±0.005 g m^{-2} d^{-1} in LSSR solution, and 0.016±0.003

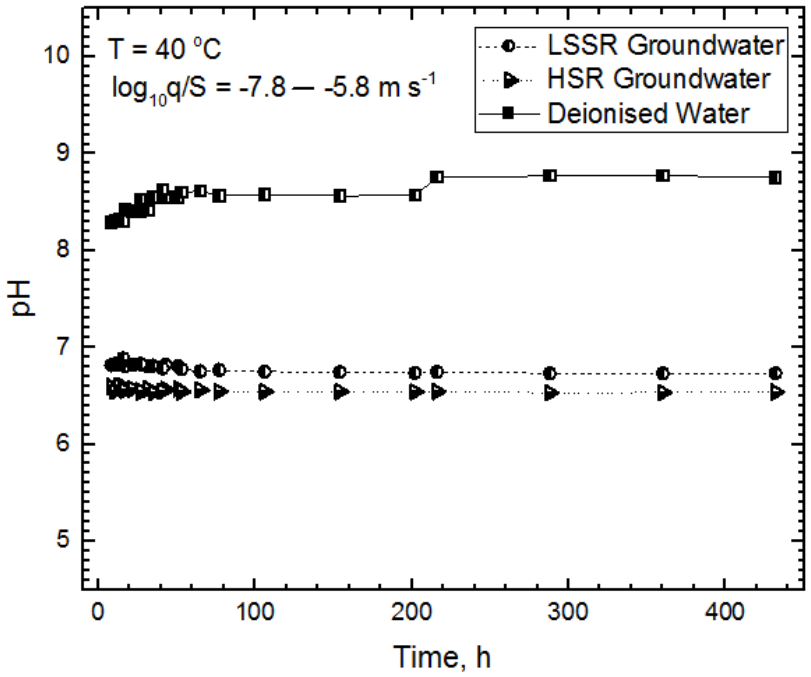

Figure 5.9: Plot of pH versus time in the experiments conducted with LSSR and HSR simulant groundwaters and deionised water. The conditions of the experiments were the same. Note that the time evolution is the cumulative test duration. Experiment that was run at the fastest flow rate (250 mL/d) is to the left of the plot (0 h) and experiment that was run at the slowest flow rate (10 mL/d) is to the right (400 h).

g m^{-2} d^{-1} in HSR solution based on boron release (Schofield *et al.*, 2016). It is noted, however, that studies by Utton *et al.* (2012), Corkhill *et al.* (2013) and Schofield *et al.* (2016) were conducted using the batch experimental method. As discussed previously (see Section 2.3.3), batch experiments are subject to solution feedback effects, which influence the dissolution rate. Therefore, the low initial rates measured in the previous studies can be attributed to the methodology employed, which highlights the importance of using the SPFT method to determine the forward dissolution rates of nuclear waste glasses both accurately and reproducibly.

5.6.1 Effect of Ratio of Flow Rate to Surface Area (q/S) on Dissolution Rates for the Experiments with Simulant Groundwaters

With the exception of Al, the data in Tables 4.4 and 4.5 (see Section 4.4) indicates an inverse correlation between the dissolution rates and steady-state concentrations of elements in the leachates shown in Tables 4.2 and 4.3 (see Section 4.3), respectively. Higher dissolution rates were measured at the higher $\log_{10}$q/S values and lower rates were measured at the lower values of $\log_{10}$q/S.

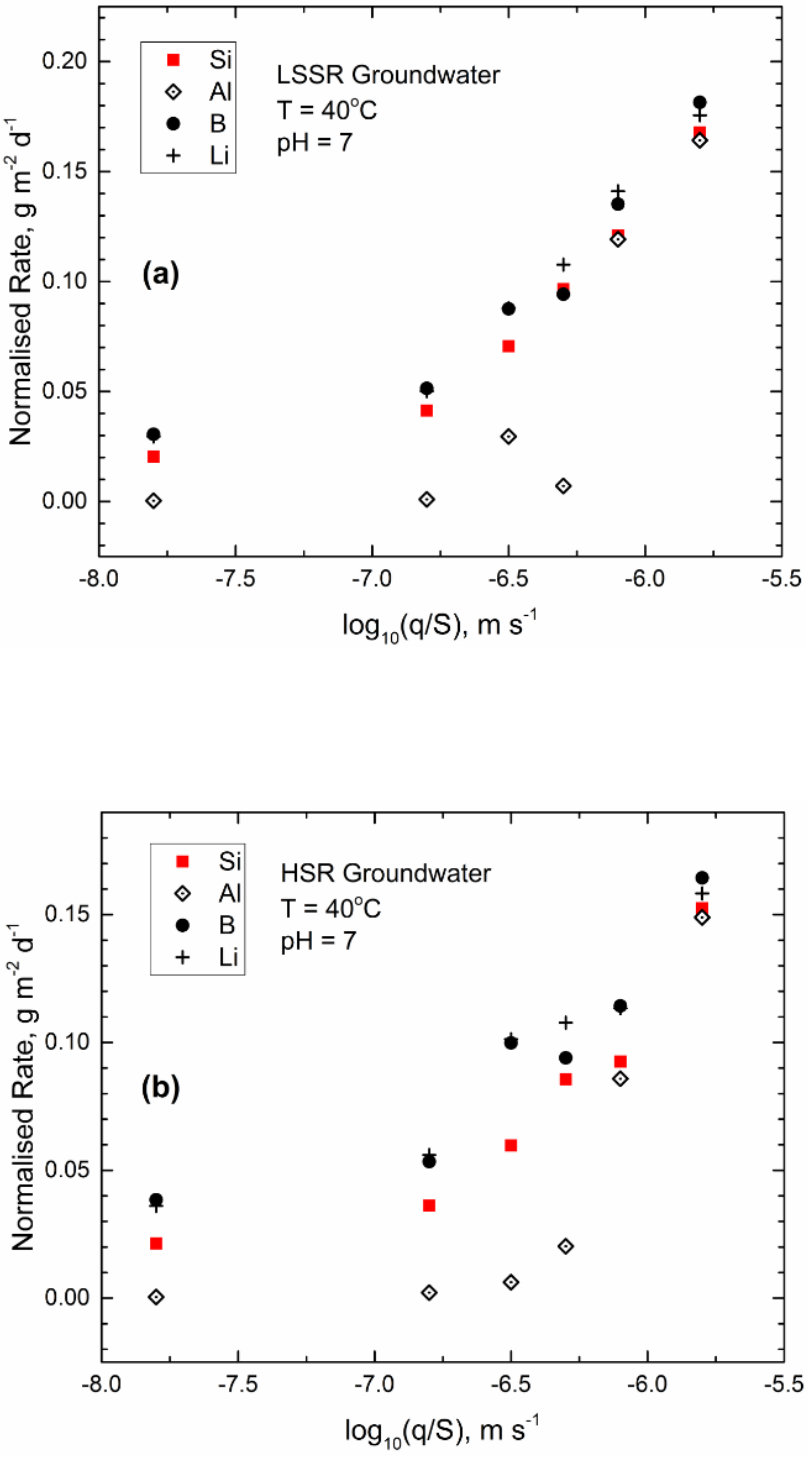

Figure 5.10: Steady-state dissolution rate [in g/(m^{2}d)] based on Al, B, Li and Si at 40 ^{o}C as a function of log$_{10}$q/S (in m/s), plot: (a) LSSR simulant groundwater; (b) HSR simulant groundwater.

Figure 5.10 shows the plots of normalised dissolution rates of the major glass components (Al, B, Li and Si) as a function of the $\log_{10}$ of parameter q/S in the experiments conducted with both groundwaters. The figures illustrate an initial transient release behaviour such that, as the q/S is increased (i.e. with increasing flow rate), the dissolution rates increase. The release behaviour of the elements in both groundwaters is similar to that observed in deionised water at 40 ^{o}C (see Section 5.3.3), which indicates slightly higher release rates for B and Li than the rate of release of Si and Al over the range of q/S investigated.

Following the transient dissolution stage, the dissolution rates reach a constant (equivalent) value in the experiments conducted with both groundwaters at $\log_{10}$q/S > -6.0 m s^{-1}. This value of the $\log_{10}$ of parameter q/S, in which a constant rate was achieved in the experiments with both groundwaters, is the same as that in the experiments with deionised water at 40 ^{o}C. The constant rates provide evidence of congruent dissolution of MW25 glass.

5.7 Comparison of Dissolution Rates of Elements in LSSR and HSR Simulant Groundwaters with Rates in Deionised Water

The plots of the dissolution rates in the experiments conducted at the same temperature (40 ^{o}C) and the same q/S values (average q/S = 4.8 x 10^{-7} m s^{-1}) in LSSR and HSR groundwaters, as well as in deionised water, were combined, as shown in Figure 5.11. As discussed previously (see Section 4.2), the interactions of Na and Mg present in the simulant groundwaters made it extremely difficult to measure the rates of dissolution of both elements; therefore, these elements have been excluded from the current discussion.

The plots in Figure 5.11 show that the dissolution rates of all the considered elements, including Al, B, Cs, Li, Mo and Si, were generally highest in deionised water over the duration of the experiments. The normalised rates of the most soluble elements, including B, Cs, Li and Mo, were, for the most part, higher in HSR groundwater than in LSSR groundwater; this phenomenon was reversed in the case of the low-solubility cations, including Al and Si. In the first hours of dissolution (i.e. at the highest flow rates), the normalised rates of all the elements were highest in LSSR groundwater, followed by HSR groundwater and then deionised water. Initially (i.e. between 0 and 48 h), the rates of dissolution of the elements diminished steeply by ~60% in both LSSR and HSR groundwaters and by ~25% in deionised water. Thereafter, the normalised

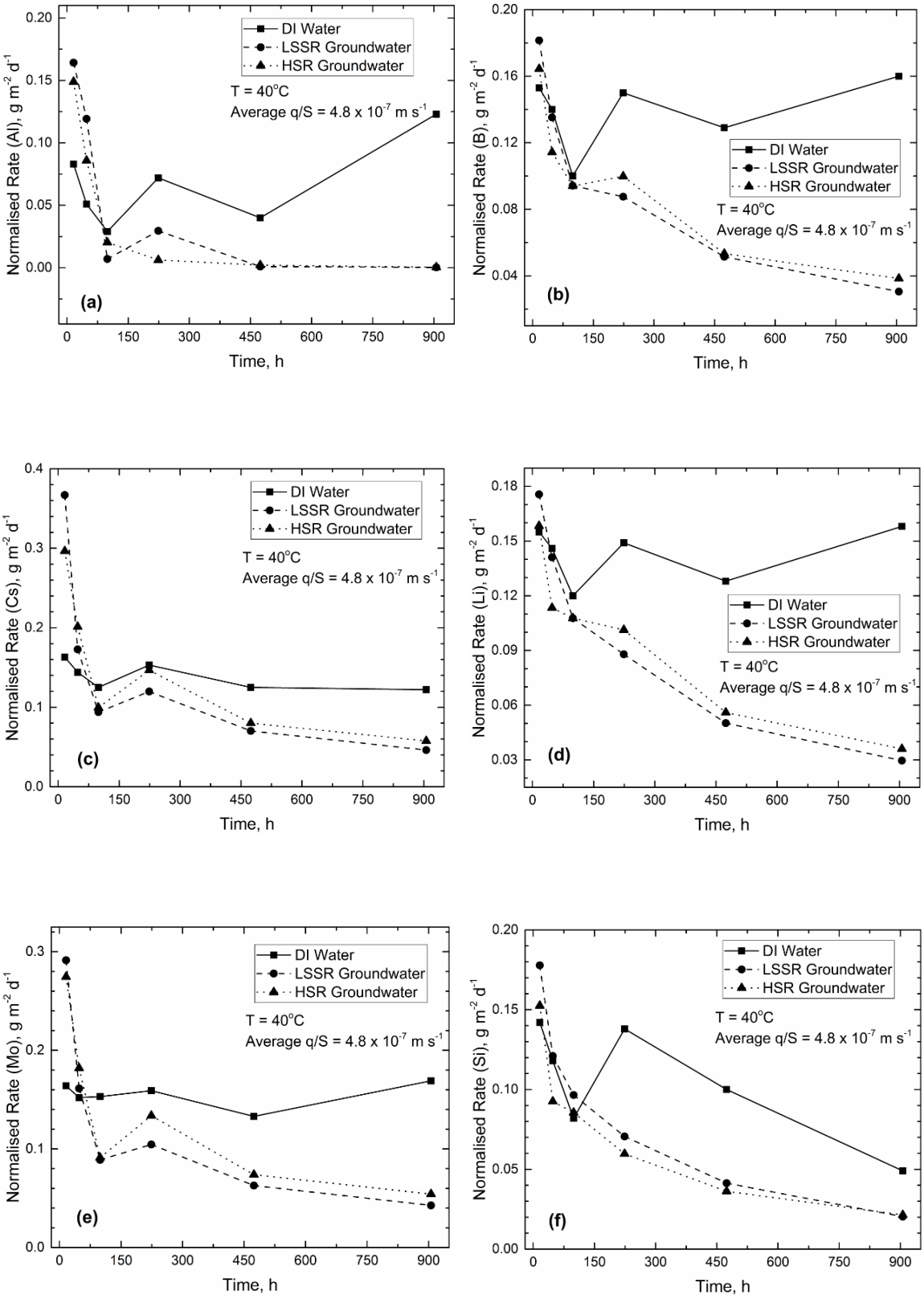

Figure 5.11: Comparison of rates in LSSR and HSR groundwaters with rates in deionised water measured under the same experimental conditions, plot: (a) Al; (b) B; (c) Cs; (d) Li; (e) Mo; (f) Si.

rates of the most soluble elements remained essentially constant in deionised water, whereas the rates decreased gradually in both LSSR and HSR groundwaters. The inverse of these phenomena is exhibited by the low-solubility elements, especially Si, which showed a continual decrease in rates in all the solutions from the first hour to 906 h. In the case of LSSR and HSR simulant groundwaters, more Si was measured over the duration of the experiments as a result of silicate being added in the solutions.

5.7.1 Effect of Solution Compositions on Dissolution Rates

It is noted that the glass dissolution rates in all the solutions, whether deionised water or groundwater, under the experimental conditions investigated fell between 0.01 and 0.2 g m^{-2} d^{-1} within experimental uncertainties, which indicates the internal consistency of the SPFT method. This implies that the variability of the dissolution rates in the solutions can only be attributed to the interactions of the groundwater solution compositions with the glass; thus, the highest normalised releases exhibited by all the elements in deionised water are the result of lower ionic strength of deionised water compared to LSSR and HSR groundwaters. Similarly, lower dissolution rates of the mobile elements in LSSR groundwater than in HSR groundwater are explained by the higher concentration of Ca in LLSR groundwater and thus higher ionic strength than HSR groundwater. Generally, the normalised rates of the elements in LSSR are similar to those in the HSR simulant groundwaters. The release rates of the elements in both groundwaters appeared to be faster initially which was in the range of maximum rate measured far from equilibrium (see Section 4.4), but appeared to be decreasing towards the residual rate at 906 h. This indicates that the interactions of the solution components with the glass (see Section 4.2), especially Ca and Na, inhibited the release of the elements and may have led to the rates of the elements reaching residual rate expeditiously if the experiments had proceeded further. Similar findings were observed by Utton *et al.* (2012), in which solution components of both LSSR and HSR groundwaters were found to constrain the release of elements from MW25 glass at longer times. They also reported the removal of Ca and Na that are present in the simulant groundwaters in the course of reaction with the glass.

A comparison of the interactions of Ca and Na in simulant groundwaters with MW25 glass as a function of time in Utton *et al.* (2012) and the present study is given in Figure 5.12. Although the concentrations of Ca and Na in both the leachate and control tests in

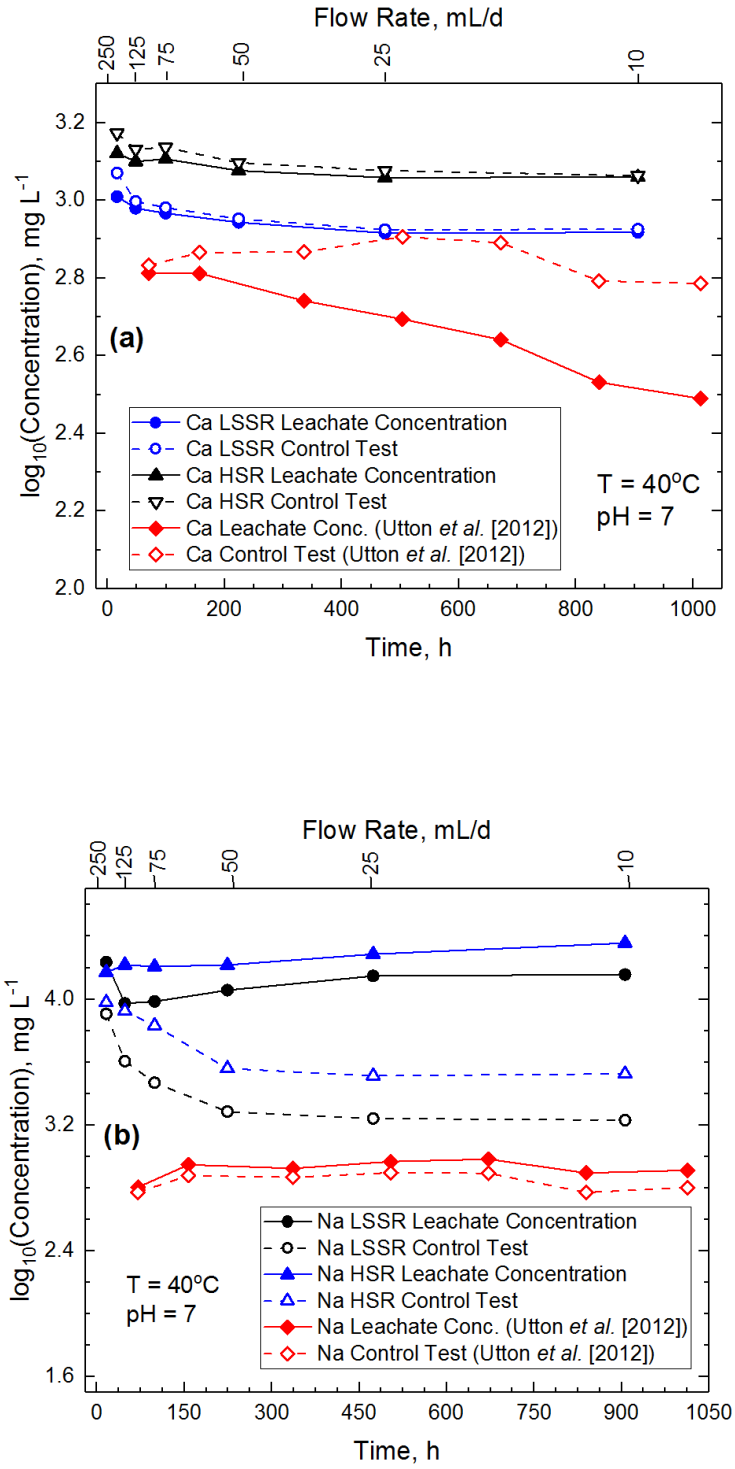

Figure 5.12: Comparison of concentrations of elemental components in LSSR and HSR simulant groundwaters at 40 °C in the present study and Utton *et al.* (2012), plot: (a) Ca concentrations; (b) Na concentrations.

the present study are higher than those reported in Utton *et al.* (2012), the removal of both elements from the solutions follows the same trend. That is, in both studies the removal of Ca from solution decreased gradually with respect to time, whereas Na was removed from solution at a relatively constant rate. Note that Utton *et al.* (2012) used the batch method in their investigation as opposed to the SPFT method used in the present study. Therefore, considering the experimental uncertainties and different methodologies used in both studies, the higher concentration of Ca and Na by approximately one order of magnitude in the present study than in Utton *et al.* (2012) represents the difference between the SPFT and batch dissolution experiments. The most important factor, which deserves serious consideration, is whether the interactions of the solution components cause rate increase or decrease, which has been shown in the previous section. Another important consideration is whether the reactions of the solution components with glass result in the formation of secondary phases and whether the new phases lead to attenuation or an increase in rate. However, an investigation of the formation of secondary phases on the glass surface fell outside the scope of this study.

5.8 Discussion of Post-leaching Solids Analysis Results for the Experiments with Simulant Groundwaters

A comparison of the XRD spectra of the reacted glass specimens in the experiments conducted in LSSR and HSR simulant groundwaters with the XRD spectrum of the unleached glass specimen revealed no new crystalline phases (see Figure 4.11 in Section 4.6), with the exception of the ruthenium oxide and spinel phases, which are the same crystalline phases typically found in unleached UK Magnox glass (Scales, 2011). These results indicate that no secondary crystalline phases were formed as a result of the reaction of the glass with the solutions.

In comparison to the samples leached in deionised water, leaching in LSSR and HSR simulant groundwaters resulted in a glossy appearance of the glass particles, with the extensive formation of surface precipitates (see Figures 4.9 and 4.10 in Section 4.6). Globular and acicular precipitates were formed on the surface of the specimen leached in LSSR groundwater, whereas only acicular particles appeared on the specimen leached in HSR groundwater; the precipitates were ~5 μm in size – approximately 20 times the size of the precipitates found on the glass samples that reacted with deionised water at 90 ^{o}C. The appearance of the precipitates is similar to those observed in previous studies (Utton *et al.,* 2012; Corkhill *et al.*, 2013; Schofield *et al.*, 2016). The

EDX of these precipitates revealed the presence of Ca in the specimens leached in both groundwaters, which was not present in the spectra of the unleached glass sample (see Figure 3.7 in Section 3.4). This suggests that the glossy appearance of the secondary electron images of the specimens was a result of precipitated Ca.

A comparison of the results of the EDX of the specimens leached in both LSSR and HSR groundwaters with that of the unleached glass sample (Table 5.2) revealed the enrichment of Ca, Mg and Na on the surface of the glass samples leached in both groundwaters, which seems to corroborate the results of the interactions of the components of the simulant groundwaters with the glass presented in Section 4.2. Similarly, the surface of the specimens leached in both groundwaters contains precipitates slightly rich in Al and Mo. The surface of the specimen leached in LSSR groundwater was enriched in Cs, whereas there was depletion of Cs on the surface of the specimen leached in HSR groundwater.

Conclusively, the enrichment of the glass surface with the elemental components of LSSR and HSR simulant groundwaters, especially Ca, contributed significantly to lower forward rates measured in both groundwaters compared to that measured in deionised water under the same experimental conditions. Importantly, there was 0.8 wt% Mo in the precipitates of the unleached glass specimen, whereas Mo had slightly higher wt% in the precipitates of the specimens leached in both groundwaters. Interestingly, however, Mo was absent in the composition of the simulant groundwaters, but the groundwaters contained significant amounts of Ca. Therefore, the glossy appearance of the surface of the specimens leached in both groundwaters suggests the formation of powellite ($CaMoO_4$) on the glass surface. This could have an important implication on the ability of the glass to retain radionuclides within its bond over long periods of time, as little Mo is left for the fixation of radionuclides. The performance assessment of glass in a geological repository is examined in more detail in the next chapter.

Table 5.2: MW25 sample EDX (spectrum A) corresponding to SEM micrographs in Figures 3.7, 4.9 and 4.10.

Element	wt% (Unleached)	wt% (LSSR at 40°C)	wt% (HSR at 40°C)
O	39.8	41.5	43.1
Si	24.9	17.5	17.8
Na	5.4	7.2	6.6
Fe	2.6	2.3	1.6
Mg	2.4	3.7	3.2
Al	2.3	2.6	2.7
C	1.7	0.0	0.0
Cs	1.1	1.0	0.1
La	1.0	1.2	0.2
Mo	0.8	1.3	1.1
Zr	1.1	0.9	0.9
Ca	0.0	0.5	0.2
Total	83.1	79.7	77.5

6 COUPLING CHEMISTRY WITH TRANSPORT

6.1 Introduction

The aim of this chapter is to provide insights into the release of radionuclides over long periods of time based on the most recent information about the disposal options currently under consideration in the UK; and also to evaluate the long-term performance of MW25 waste glass relative to the performance of other near-field components. In Chapter 4, a waste form dissolution model was used to calculate the forward dissolution rates of MW25 waste glass in simulant groundwaters having compositions similar to the compositions of the groundwaters of the two rock volumes [Callovo-Oxfordian clay (LSSR) and Borrowdale Volcanic Group rocks (HSR)] that could potentially be suitable for the geological disposal of nuclear waste in the UK. In the current chapter, the measured dissolution rates are provided as source terms for GoldSim (a compartmental-based dynamic, probabilistic reactive transport model) to calculate the release of radionuclides and to track radionuclide migration through a hypothetical near field for a million years. GoldSim uses the waste form dissolution rates, along with canister failures, to calculate radionuclides that are available for transport in each simulation timestep upon contact of the waste package (canister and waste form) with water. The waste form dissolution rates are the only direct laboratory measurements used to parameterise the reactive transport model; other data, including canister degradation, buffer and host rock properties, as well as radionuclide properties, was derived from the literature.

6.2 Theory

A simplified conceptual model of the hypothetical near field under consideration is illustrated in Figure 6.1. Although the conceptual model is fictitious, the most relevant features that are envisaged as being in the near field of the UK high-level waste (HLW) disposal system are represented in their approximate dimensions. Two waste packages (waste form enclosed in canisters) are assumed to be emplaced in a disposal vault, which is surrounded by a bentonite buffer at the top and on both sides. The disposal vault is situated within a host rock, sectionalising the host rock into two parts (base and crown) of equal dimensions.

The model assumes that interstitial groundwater in the rock beneath the disposal vault (i.e. base of the host rock) flows upward into the disposal vault, which would lead to the corrosion of canisters and the production of corrosion products, which would modify the chemistry of the water filling the package (in-package solution (IPS)). Upon the breaching of the canisters, the groundwater would react with the waste glass, leading to dissolution of its constituents, which would further modify the chemistry of the IPS and generate waste glass dissolution products. The continued dissolution of the waste glass would lead to the release of radionuclides into the disposal vault. Free radionuclides would diffuse into the surrounding bentonite buffers and would be transported both diffusively and advectively through the buffers and eventually into the crown of the host rock.

In this model, waste glass dissolution rates, canister degradation, groundwater flow rates, radionuclide sorption on bentonite buffer and host rock, radioactive decay, radionuclide solubility limits and radionuclide diffusivity in groundwater facilitate or retard the transport of radionuclides from the near field to the far field; therefore, all these parameters were applied as inputs for the reactive transport model. There is a possibility of generation of colloids because dilute groundwater could potentially penetrate the repository. In this study, however, colloidal transport was removed from consideration because it has been established that the hydrated bentonite buffer will prevent colloid transport and the high ionic strength at near-field depth (between 200 m and 1,000 m below ground surface) will chemically limit colloid stability (Buck and Sanssani, 2007).

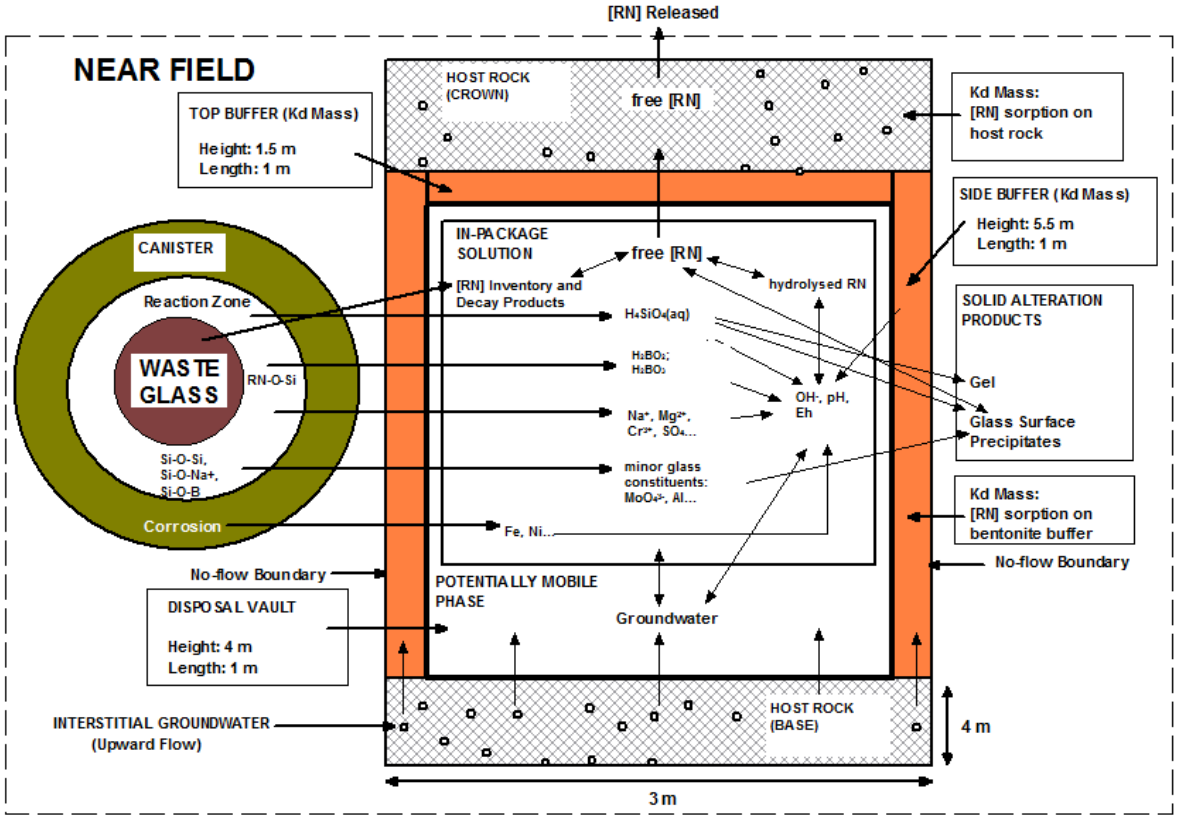

Figure 6.1: Conceptual model showing key processes and interactions in the near field. Note that the figure is not to scale; it is for illustrative purpose only.

6.3 Scenarios

For the purpose of investigating the sensitivity of near-field performance with respect to differences in disposal concepts, four different scenarios were considered in the present study, which are based on the multibarrier concepts under consideration for the disposal of high-level waste (HLW) in the UK. The scenarios are distinguished by both the waste packaging options and host rock types. They are:

Scenario 1: This assumes that the waste package comprises the waste glass enclosed in a steel canister (outer barrier) and the disposal vault is located within a lower strength sedimentary rock (LSSR).

Scenario 2: This assumes that the waste package comprises the waste glass enclosed in a steel canister (inner barrier), which is covered by a copper canister (outer barrier), and the disposal vault is located within a lower strength sedimentary rock (LSSR).

Scenario 3: This assumes that the waste package comprises waste glass enclosed in a steel canister (outer barrier) and the disposal vault is located within a higher-strength rock (HSR).

Scenario 4: This assumes that the waste package comprises the waste glass enclosed in a steel canister (inner barrier), which is covered by a copper canister (outer barrier), and the disposal vault is located within a higher-strength rock (HSR).

Importantly, all four scenarios assume that the radionuclides are encapsulated in waste glass, which is enclosed in canisters.

6.4 Reactive Transport Model

In order to simulate the transport of radionuclides numerically through the near field shown in Figure 6.1, the reactive transport model was sectionalised into six compartments, as shown in Figure 6.2, which include the base of the host rock (Base_HostRock), the buffer on the right and left sides of the disposal vault (Right_Buffer and Left_Buffer, respectively), the disposal vault containing the source (Canisters_Plus_WasteGlass), the buffer at the top of the disposal vault (Top_Buffer) and the crown of the host rock (Crown_HostRock). The immobile solid media (i.e. host rock and bentonite buffer) of the model, with the exception of Top_Buffer, were discretised into numerical elements, making the model a multi-rate-mass-transfer (MRMT) reactive transport system. However, to avoid overcrowding with elements, the numerical elements were put in containers, since doing this enhances the intelligibility of the model. It is important to note that the source element acts as a special container, which contains the disposal vault (i.e. the associated cell).

The numerical elements are represented using cell elements. The mathematics of the cell element is such that everything within it is instantaneously mixed, homogenised and partitioned between media. The radionuclide mass balance equation for cell i is as follows:

$$\boldsymbol{m'_{is} = -m_{is}\lambda_s + \sum_{p=1}^{NP_s} m_{ip}\lambda_p f_{ps} R_{sp}\left(\frac{A_s}{A_p}\right) + \sum_{c=1}^{NF_i} f_{cs} + S_s} \qquad \textbf{(6.1)}$$

where m'_{is} is the rate of increase of mass of radionuclide s in cell i [M]; m_{is} is the mass of radionuclide s in cell i [M]; λ_s is the decay rate for s [T^{-1}]; NP_s is the number of direct parents for s; f_{ps} is the fraction of parent p which decays into radionuclide s; R_{sp} is the stoichiometry ratio of moles of s produced per mole of p decayed; A_s and A_p are the molecular weight of s and parent p, respectively [M/mol]; NF_i is the number of mass flux links from/to cell i; f_{cs} is the influx rate of s into cell i through mass flux link c [M/T]; and S_s is the rate of direct input of s to cell i from external sources [M/T].

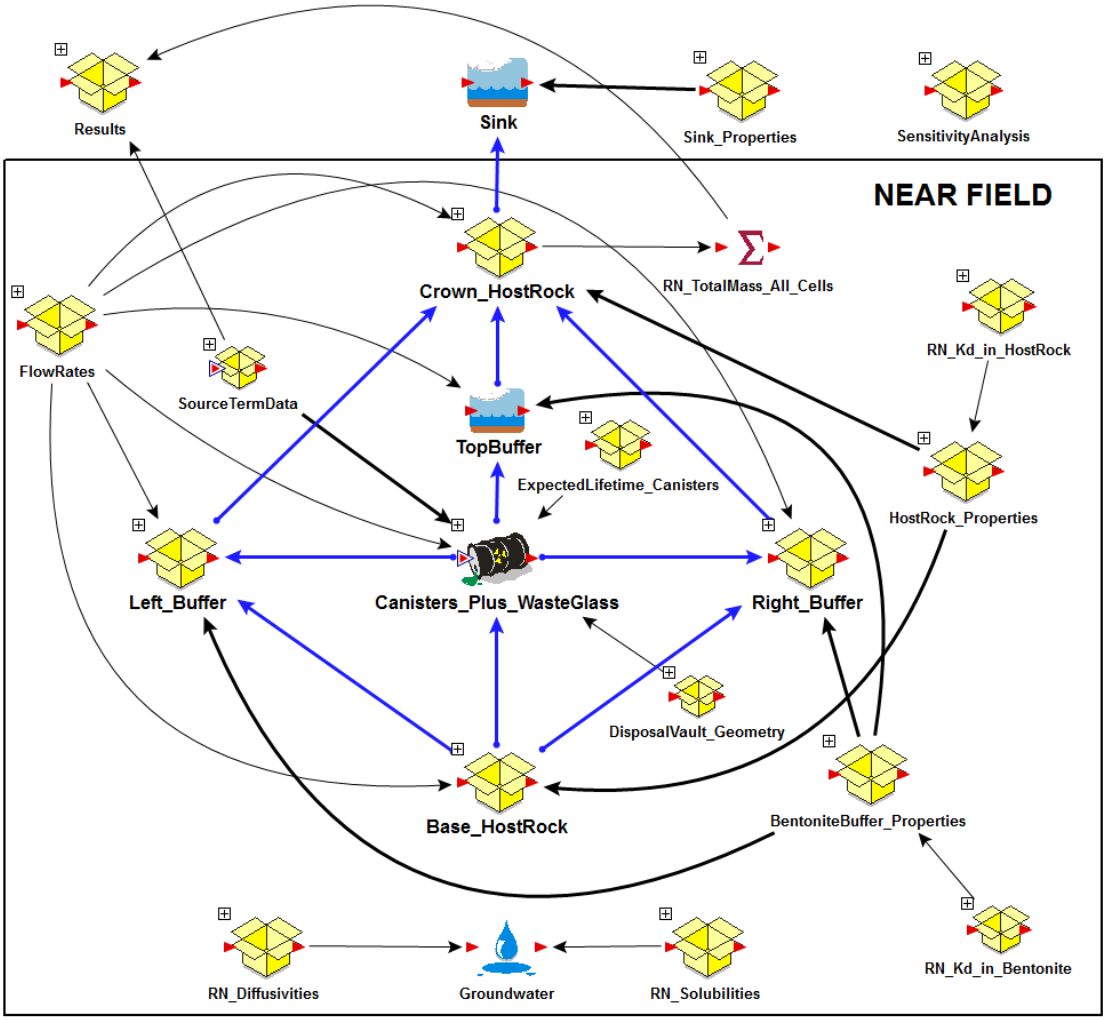

Figure 6.2. The setup of the model as presented on GoldSim graphic pane. The blue arrows indicate the coupling of the model compartments and the direction of radionuclide transport. The black arrows indicate assignment of parameters to the compartments of the model.

The cells within each compartment of the model, as well as adjacent compartments, in the direction of groundwater flow were coupled using an advective mass flux link, which computes the flux, f_a, of radionuclide s from cell i to cell j, as follows:

$$f_{a,i\to j} = c_{ims}q + \sum_{t=1}^{NPT_{im}} PF_t \cdot c_{its} \cdot vm_t \cdot cp_{imt}q_c \qquad (6.2)$$

where q is the rate of advection of groundwater for the mass flux link [L^3/T]; c_{ims} is the total dissolved, sorbed or precipitated concentrations of s in groundwater within cell i [M/L^3]; NPT_{im} and NPT_{jm} are the number of solid media suspended in groundwater within cell i and cell j, respectively; PF_t is a Boolean flag (0 or 1) which indicates whether advection of solid t suspended in groundwater is allowed for the mass flux link;

c_{its} is the sorbed concentration of s in solid medium t within cell i [M/M]; v_{mt} is the advective velocity multiplier for solid particle t; and cp_{imt} is the concentration of suspended solid particle t within groundwater in cell i [M/L^3].

The flow through the LSSR host rock (Scenarios 1 and 2) is through the internal porosity, whereas the flow through the HSR host rock (Scenarios 3 and 4) is through both the internal porosity and blocks of sparsely fractured granite. The flow through the fractured granite was represented as advective flow using cell elements.

A diffusive mass flux link was used to couple each cell to the adjoining cells in the model. Diffusive mass transport is proportional to a concentration difference, such that diffusive conductance is the constant of proportionality. The diffusive conductance, D, of groundwater (being the only fluid medium in the system) can be computed as follows:

$$\boldsymbol{D = adtrn/L} \qquad \textbf{(6.3)}$$

where A is the mean cross-sectional area of the connection (L^2); d is the diffusivity of the fluid [L^2/T]; n and t are the porosity and tortuosity of the medium, respectively; r is a reduction factor that varies with saturation (1 if fully saturated); and L is the diffusive length [L].

The diffusive flux, f_d, from cell i to cell j is computed as follows:

$$\boldsymbol{f_{d,i\rightarrow j} = D_s\left(c_{ims} - \frac{c_{jns}}{K_{nms}}\right) + \sum_{t=1}^{NPT_{im}} PF_t \cdot D_t\left(c_{its} \cdot cp_{imt} - c_{jts} \cdot cp_{jnt}\right)} \qquad \textbf{(6.4)}$$

where D_s is the diffusive conductance for radionuclide s in the mass flux link (L^3/T); c_{ims} and c_{jn} are the dissolve concentrations of s in groundwater within cell i and cell j, respectfully (M/L^3); K_{nms} is the partition coefficient between groundwater in cell j and cell i; NPT_{im} is the number of particulate solid media in groundwater within cell i; PF_t is a Boolean flag (0 or 1) which indicates whether diffusion of solid t suspended in groundwater is allowed for the mass flux link; D_t is the diffusive conductance for particulate t in the mass flux link [L^3/T]; c_{its} and c_{jts} are the sorbed concentration of s associated with solid t within cell i and cell j, respectively [M/M]; and cp_{imt} and cp_{jnt} are the concentrations of solid particle t within fluid m in cell i [M/L^3].

6.4.1 Computation of Radionuclide Exposure Rates

As the waste glass is assumed to be enclosed in canisters in all four scenarios under consideration, radionuclides can only be exposed when the canisters are breached and water is able to contact the waste glass. In this study, radionuclides were assumed to be exposed through fractional degradation of the waste glass (or solubility-controlled dissolution of the waste glass), so that exposure rate is a function of the mass of the radionuclide that is unprotected but still bound in the waste glass, and the dissolution rate of the waste glass is as follows:

$$\boldsymbol{e_{s,b}(n,t) = N \times M_s(t) \times k_s(t) \times I_s(n,t)} \quad \textbf{(6.5)}$$

where $e_{s,b}(n,t)$ is the exposure rate for radionuclide n bound in bound inventory s for the source at time t [M/T]; N is the number of bound inventories for the source; $k_s(t)$ is the fractional degradation rate of waste matrix for bound inventory s (1/T); $I_s(n,t)$ is the mass of radionuclide n per unfailed package in bound inventory s at time t [M]; and $M_s(t)$ is the fraction of unprotected but undegraded waste matrix, which can be determined from the following differential equation:

$$\boldsymbol{dM_s(t)/dt = h(t) - M_s(t) \times k_s(t)} \quad \textbf{(6.6)}$$

The product of $M_s(t)$ and $k_s(t)$ is the rate at which the unprotected waste glass is being degraded, and h(t) is the rate at which the waste glass is being unprotected, which depends on the packaging option.

If the waste glass is within only the steel canister (outer barrier), as in Scenario 1 and Scenario 3, h(t) is equal to c(t) (outer barrier failure rate at time t [1/T]). For Scenario 2 and Scenario 4, in which the waste glass is assumed to be within the steel canister (inner barrier) enclosed in the copper canister (outer barrier), h(t) is equal to g(t), which is a function of both the outer and inner barrier failure rates and is expressed as follows:

$$\boldsymbol{g(t) = \int_0^1 [c(t)\, w(\tau,t) + c(\tau)\, w(t,\tau)]\, d\tau} \quad \textbf{(6.7)}$$

where the first term $[c(t)w(\tau, t)]$ represents the contribution from outer barriers that are failing at time t whose inner barrier had previously failed; and the second term $[c(\tau)w(t,\tau)]$ is the contribution from outer barrier that had failed prior to time t whose inner barrier is failing at time t.

6.4.2 Simulation Time and Boundary Conditions

On the basis of the proposed framework for managing HLW in the UK (DECC, 2014), the simulation duration in the present study was set to a million years. The timestep for the first 10,000 years was assigned as 200 years, while the timesteps between 10,000 and 100,000, and between 100,000 and 1,000,000, were assigned as 500 and 1,000 years, respectively. The gradation of the timesteps is a result of the expected behaviour of the system, in that reaction and transport would be rapid at the start and would slow down with time.

The boundary condition assigned to the disposal vault (the associated cell) was the cumulative input of the mass of each radionuclide from the source (i.e. the waste package). For all the other cells, the boundary condition was assigned as input rate, which represents the rate at which the mass of each radionuclide is added to the cell over the next timestep.

6.4.3 The Coupling of the Waste Glass Dissolution Rates with the Reactive Transport Model

The forward (initial) dissolution rates measured using the SPFT experiments represent Stage 1 of the three reaction regimes of waste glass dissolution commonly observed in static and slow-flowing systems (see Section 1.4.2). The initial dissolution rates expressed in units $g/m^2/d$ were coupled with the reactive transport model by converting the initial rate to a first-order rate constant through multiplication by the specific surface area of the waste glass expressed in units m^2/g. The constant rate expressed in unit d^{-1} is the $k_s(t)$ (fractional degradation rate) of the waste glass and provides the source term for the radionuclide migration out of the breached waste package. The long-term dissolution of the waste glass is described as being in three dissolution stages: initial dissolution (Stage 1), residual dissolution (Stage 2) and rate resumption of alteration (Stage 3). Stage 2 and Stage 3 dissolutions were extrapolated from the initial rate. The residual rate was obtained by dividing the initial rate by 1,000, as suggested by Grambow (1992), while rate resumption was obtained by dividing the initial rate by 10. The coupling of the waste glass dissolution with the transport model is illustrated in Figure 6.3.

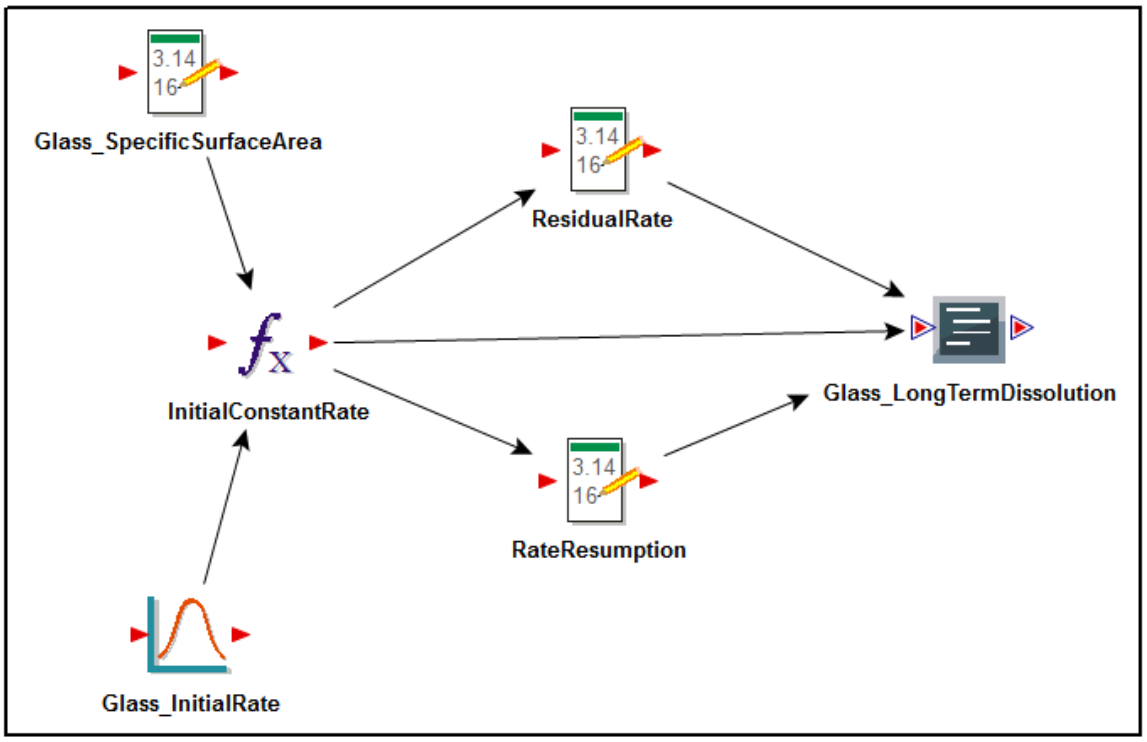

Figure 6.3: The coupling of waste glass dissolution data with GoldSim.

6.5 Input Parameters

6.5.1 System Data and Treatment of Uncertainties

Table 6.1 shows the system data used in the model. As previously stated, the model inputs were derived from the SPFT experiments and literature data, which were obtained from well-constrained experiments. In order to consider uncertainties in the input data, limits were explicitly derived for the parameters and these limits were implemented in the model as probability distributions. With the exception of groundwater flow rates, which were assigned to the model using log-normal distributions, the piecewise uniform distribution was used to assign all the other parameters to the model, as it is easier to describe mathematically; the centre piece should hold 50% of the area, while the other pieces should hold 25% each, such that the values are set symmetrically. Importantly, the expected lifetimes of both the copper and steel canisters were assigned to the model using exponential distribution.

6.5.2 System Radionuclide Inventory and Physicochemical Properties

The UK high-level waste (HLW) glass contains a wide range of radionuclides, which include fission products and actinides; however, in the present study the focus is on the

Table 6.1: System data used in the model.

Parameter	Value	Note
Bentonite density	Uniform distribution from 1160 - 2010 kg/m^3	Johannson and Nilson (2006), Ochs and Telerico (2004)
Bentonite porosity	Uniform distribution from 0.15 - 0.44	SKB (2006), Posiva (2010)
Bentonite tortuosity	Uniform distribution from 0.115 - 0.137	Approximated from (tortuosity)^-2 = [(porosity)^1/3]/10
Clay density	Uniform distribution from 1050 - 2150 kg/m^3	Johannson and Nilson (2006)
Clay porosity	Uniform distribution from 0.05 - 0.2	(Robinet *et al.,* 2015)
Clay tortuosity	Uniform distribution from 0.131 - 0.165	Approximated from (tortuosity)^-2 = [(porosity)^1/3]/10
Granite density	Uniform distribution from 2075 - 2650 kg/m^3	Lama and Vukuri (1978), Carmichael (1982)
Granite porosity	Uniform distribution from 0.003 - 0.01	Vilks *et al.* (2003), Selnert *et al.* (2008)
Granite tortuosity	Uniform distribution from 0.316 - 0.464	Approximated from (tortuosity)^-2 = [(porosity)^1/3]/10
Initial dissolution rate of the waste glass in clay (LSSR) groundwater	Uniform distribution from 0.12 and 0.16 g/m^2/d	From the experimental results in Chapter 4
Initial dissolution rate of the waste glass in granite (HSR) groundwater	Uniform distribution from 0.06 and 0.12 g/m^2/d	From the experimental results in Chapter 4
Residual dissolution rate of the waste glass	(Initial rate/1000) g/m^2/d	Extrapolated from the initial dissolution rate
Rate resumption of the waste glass	(Initial rate/10) g/m^2/d	Extrapolated from the initial dissolution rate
Copper expected lifetime	Uniform distribution from 300 - 50000 yr	Szakalos and Seetharaman (2012)
Steel expected lifetime	Uniform distribution from 1000 - 10000 yr	Marsh and Taylor (1988) JNC (2000), Johnson and King (2003)
Number of waste packages (waste glass encapsulated in canisters)	2	Nirex (2005a,b)
Groundwater flow rate in disposal vault	Log-normal distribution, mean: 0.059313 m^3/yr	
Groundwater flow rate in clay, bentonite and granite	Log-normal distribution, mean: 0.01095 m^3/yr	
Groundwater flow rate in internal fracture	Log-normal distribution, mean: 0.1095 m^3/yr	
Dimension of the disposal vault	height 4 m, length 1 m, width 1 m	
Dimension of left- and right-side buffers	height 5.5 m, length 1 m, width 1 m	
Dimension of top buffer	height 1.5 m, length 1 m, width 1 m	
Dimension of base and crown of the host rock	height 4 m, length 3 m, width 1 m	
Discretisation of cells in left- and right-side buffers	1 (column) x 3 (rows)	
Discretisation of cells in base and crown of the host rock	3 (column) x 3 (rows)	

radionuclides with high specific activity (^{90}Sr, ^{137}Cs, ^{241}Am), as well as those with long half-lives (^{79}Se, ^{99}Tc, ^{129}I, ^{237}Np, ^{238}U, ^{239}Pu).

The inventory and physicochemical properties of the radionuclides are listed in Tables 6.2 and 6.3, respectively. The same partition coefficient (K_d) value was assigned for clay and bentonite because the K_d values were obtained from montmorillonite, which is the main sorbing component in clay minerals. As a result of the uncertainties in the data, K_d were assigned to clay and bentonite using log-normal distributions, while K_d were assigned to granite using uniform distributions. The diffusivities of the radionuclides in groundwater, as well as solubility limits, were also assigned as input for the transport calculations with GoldSim using uniform distributions.

The solubility limits applied to ^{90}Sr, ^{79}Se, ^{99}Tc, ^{237}Np, ^{238}U, ^{239}Pu and ^{241}Am imply that every cell in the model will have a saturation capacity with respect to these radionuclides. The saturation capacity represents the maximum mass of the radionuclides that the cell can hold before the radionuclide starts to precipitate out of the solution.

Table 6.2: Radionuclide Inventory.

Radionuclides	Half-life (yr)	Specific Activity (Bq/g)	Initial Inventory per Disposal Package* (TBq)
Fission Products			
^{79}Se	2.95×10^{5}	5.68×10^{8}	1.47×10^{-1}
^{90}Sr	28.79	5.11×10^{12}	2.28×10^{3}
^{99}Tc	2.11×10^{5}	6.34×10^{8}	8.89×10^{-1}
^{129}I	1.57×10^{7}	6.54×10^{8}	1.78×10^{-5}
^{137}Cs	30.167	3.20×10^{12}	3.28×10^{3}
Actinides			
^{237}Np	2.14×10^{6}	2.60×10^{7}	1.07×10^{-3}
^{238}U	4.47×10^{9}	1.24×10^{4}	1.94×10^{-5}
^{239}Pu	2.41×10^{4}	2.30×10^{9}	2.08×10^{-2}
^{241}Am	432.2	1.27×10^{11}	4.28×10

*Nirex (2005b)

Table 6.3: Physicochemical properties of the radionuclides.

Radionuclides	K_d Clay/Bentonite* (L/kg)	K_d Granite** (m^3/kg)		Solubility*** (mol/L)		Diffusivity**** (m^2/s)	
Fission Products	**Geometric mean**	**Upper Limit**	**Lower Limit**	**Lower Limit**	**Upper Limit**	**Lower Limit**	**Upper Limit**
^{79}Se	740	0.0005	0.005	$2x10^{-11}$	$1x10^{-5}$	$3.0x10^{-12}$	$3.0x10^{-11}$
^{90}Sr	110	0.005	0.05	0	$1.9x10^{-5}$	$4.94x10^{-11}$	$1.91x10^{-10}$
^{99}Tc	1	0.3	3	$1x10^{-9}$	$1x10^{-8}$	$3.0x10^{-12}$	$3.0x10^{-11}$
^{129}I	1	0	0	Unlimited	Unlimited	$3.0x10^{-12}$	$3.0x10^{-11}$
^{137}Cs	1900	0.5	1.5	Unlimited	Unlimited	$4.94x10^{-11}$	$1.91x10^{-10}$
Actinides							
^{237}Np	55	1	10	$3x10^{-9}$	$1x10^{-8}$	$4.94x10^{-11}$	$1.91x10^{-10}$
^{238}U	1600	1	10	$3x10^{-10}$	$5x10^{-7}$	$4.94x10^{-11}$	$1.91x10^{-10}$
^{239}Pu	5100	1	10	$3x10^{-9}$	$1x10^{-6}$	$4.94x10^{-11}$	$1.91x10^{-10}$
^{241}Am	8400	1	10	$5x10^{-8}$	$3x10^{-5}$	$4.94x10^{-11}$	$1.91x10^{-10}$

*Thibault *et al.* (1990)

**SKB (1997)

***Berner (2002)

****Ochs and Telerico (2004)

6.5.3 Groundwater Flow Rates and Waste Glass Dissolution

The groundwater flow rates of the model varied between each compartment, ranging between 0.059313 m^3/yr and 0.1095 m^3/yr. These low flow rates were chosen given the very low hydraulic conductivity of the potential host rocks and the low hydraulic gradient expected at the repository depth (between 200 and 1,000 m below ground surface). The groundwater must contact the waste packages in the disposal vault in order for the radionuclides to be released, and this contact was assumed to occur after 10 years.

The fractional degradation rate of the waste glass was derived from the glass dissolution rate together with the specific surface area of the glass. The forward rates measured in LSSR and HSR groundwaters were assigned as input as the initial rates for LSSR and HSR host rocks, respectively. As mentioned previously, residual rate and rate resumption were extrapolated from the initial rate. The time it took for the waste glass to dissolve at each dissolution stage was computed from the total mass of glass per container, which is ~400 kg (see Section 1.3.4). The assumption in this study is that the waste glass takes the shape of the cylindrical container shown in Figure 1.10 (see

Section 1.7); therefore, it was assumed that the surface area of the waste glass is the same as the surface area of the cylinder. The initial height and initial diameter of the cylindrical container are 3.2 m and 0.9 m, respectively.

6.6 Results and Discussions

The time it took for the canisters to fail is illustrated in Figure 6.4. In Scenarios 1 and 3, in which waste glass is enclosed in the steel canister only, it took 40,000 years for all the canisters to completely fail, whereas in the cases in which waste glass is enclosed in both steel and copper canisters (Scenarios 2 and 4), it took 130,000 years for all the canisters to fail completely.

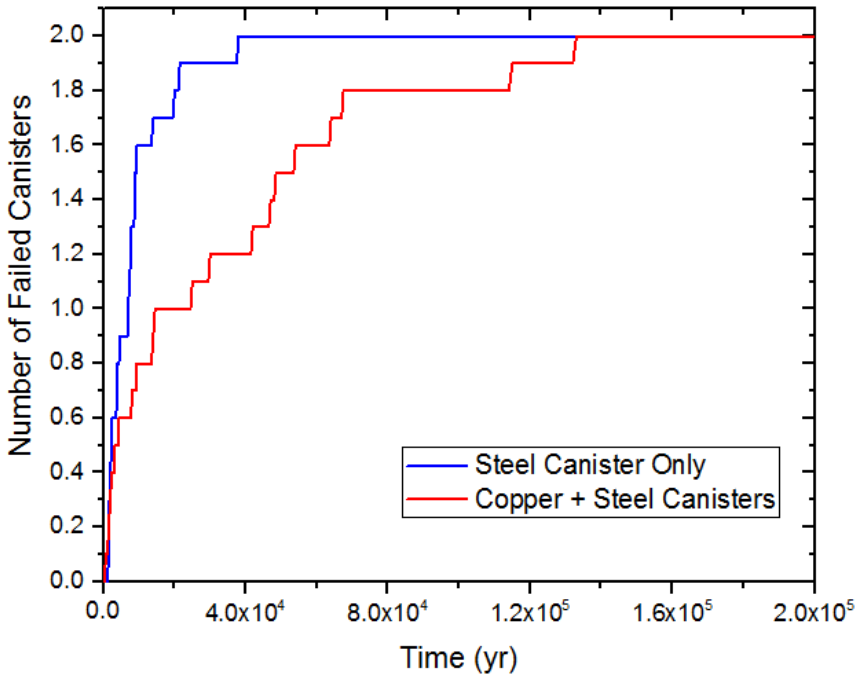

Figure 6.4: Failure of canisters in the near field with respect to time. Note that there are two waste packages in the disposal vault; therefore, point 2 on the vertical axis represents the failure of all the canisters in the waste package. The blue graph represents canister failure for Scenarios 1 and 3, while the red graph represents canister failure for Scenarios 2 and 4.

The long-term fractional degradation of the waste glass is shown in Figure 6.5. Given an initial dissolution rate of 0.14 g/m^2/d and the extrapolated values of the residual dissolution rate and final dissolution rate of 0.00014 and 0.014 g/m^2/d, respectively, the initial rate regime, residual regime and resumption of alteration regime were estimated to last for 500 years, 500000 years and 5000 years, respectively. The computer codes used in estimating the time taken for the waste glass to dissolve at each dissolution stage

are presented in Appendix 30. Importantly, the time estimation was computed such that the height and the diameter of the waste glass decrease proportionately as the glass dissolves.

As soon as the canisters fail in their containment safety functions, groundwater will contact the waste glass, which will lead to the dissolution of the waste glass and the concomitant release of radionuclides into the disposal vault compartment, where they will be transported through the bentonite buffers into the crown compartment. In order to cope with uncertainties in the model outputs, Monte Carlo simulation was set to 10 realisations, which were averaged to obtain the mean.

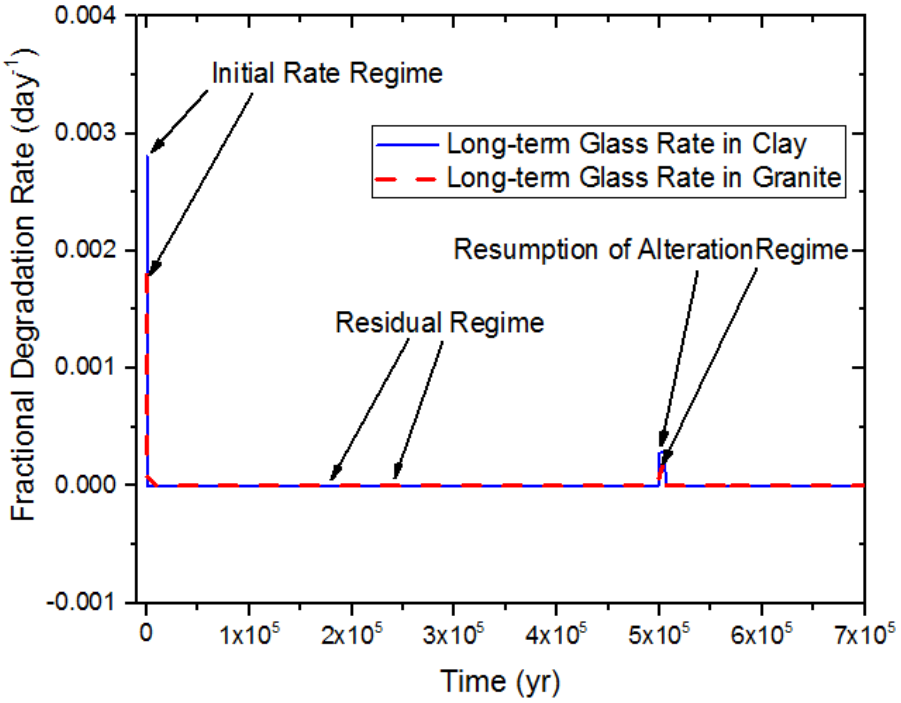

Figure 6.5: Long-term fractional degradation of the waste glass in the near field (in 1/day). The blue line represents the fractional degradation of the waste glass in LSSR (clay) groundwater, while the red dotted lines represent the fractional degradation of the waste glass in HSR (granite) groundwater.

6.6.1 The Release and Transport of the Radionuclides in the Near Field

The flux of the radionuclides in the disposal vault and crown compartments expressed in activity unit (Bq) is presented in Figure 6.6 and Figure 6.7, respectively. The release of the radionuclides from the waste packages started after 400 years. The activity of the radionuclides released into the disposal vault was significantly lower than in the initial

inventory, which points to the effectiveness of the containment and retardation safety functions of the canisters and the waste glass. The radionuclides exhibit different individual flux patterns; however, an identical flux pattern was exhibited by each radionuclide within the disposal vault compartment for all the scenarios, as well as within the crown compartment.

The contribution of the waste glass to the retardation and spread release of the radionuclides can be observed by comparing the radionuclide fluxes in the disposal vault compartment to those of the crown compartment. In the disposal vault compartment, the flux of most of the long-half-life radionuclides was highest at the beginning and decreased precipitously towards the end of the simulation; conversely, the flux of the long-half-life radionuclides was lowest at the beginning and increased

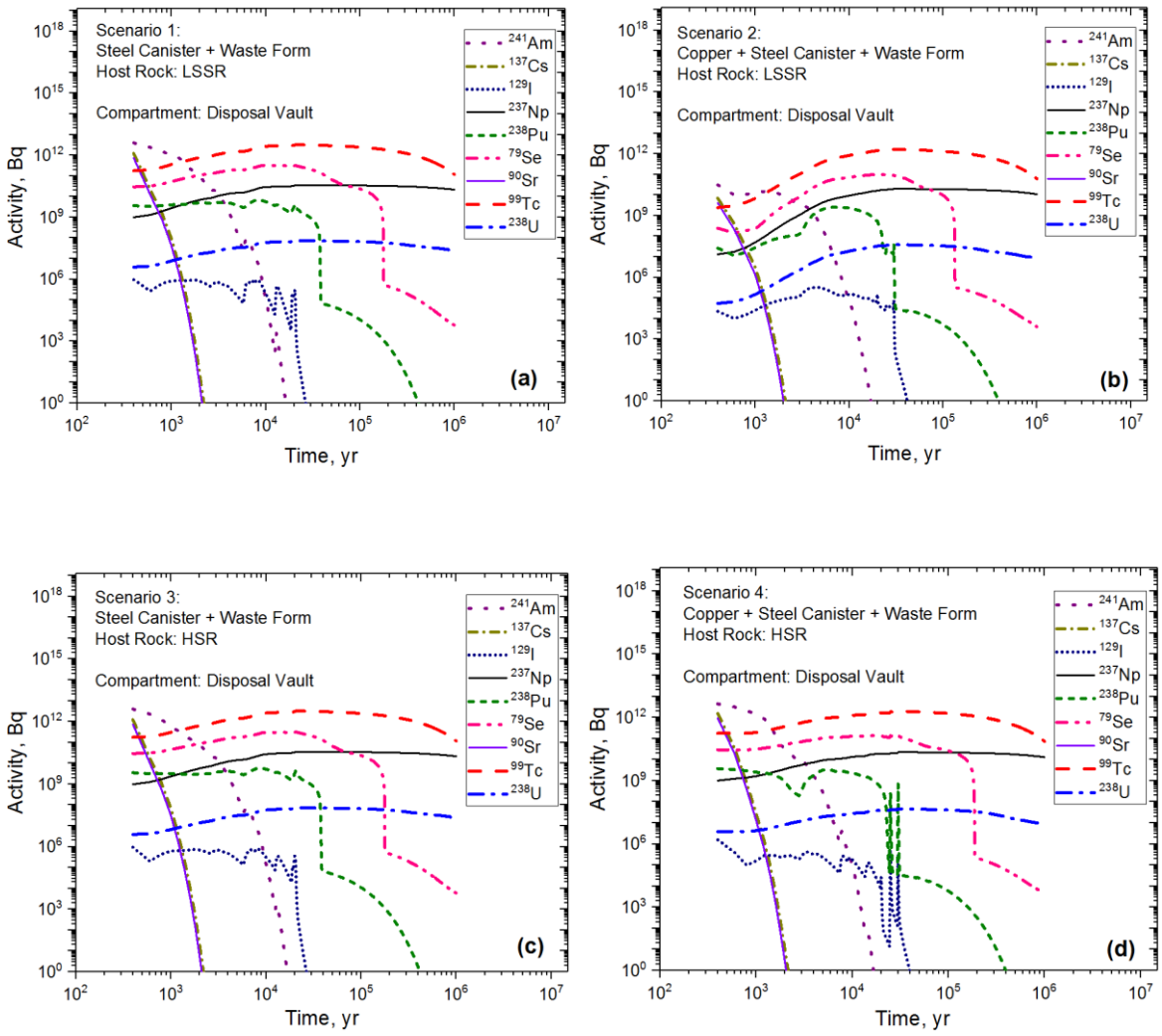

Figure 6.6: Simulated radionuclide release into the disposal vault considering four different scenarios.

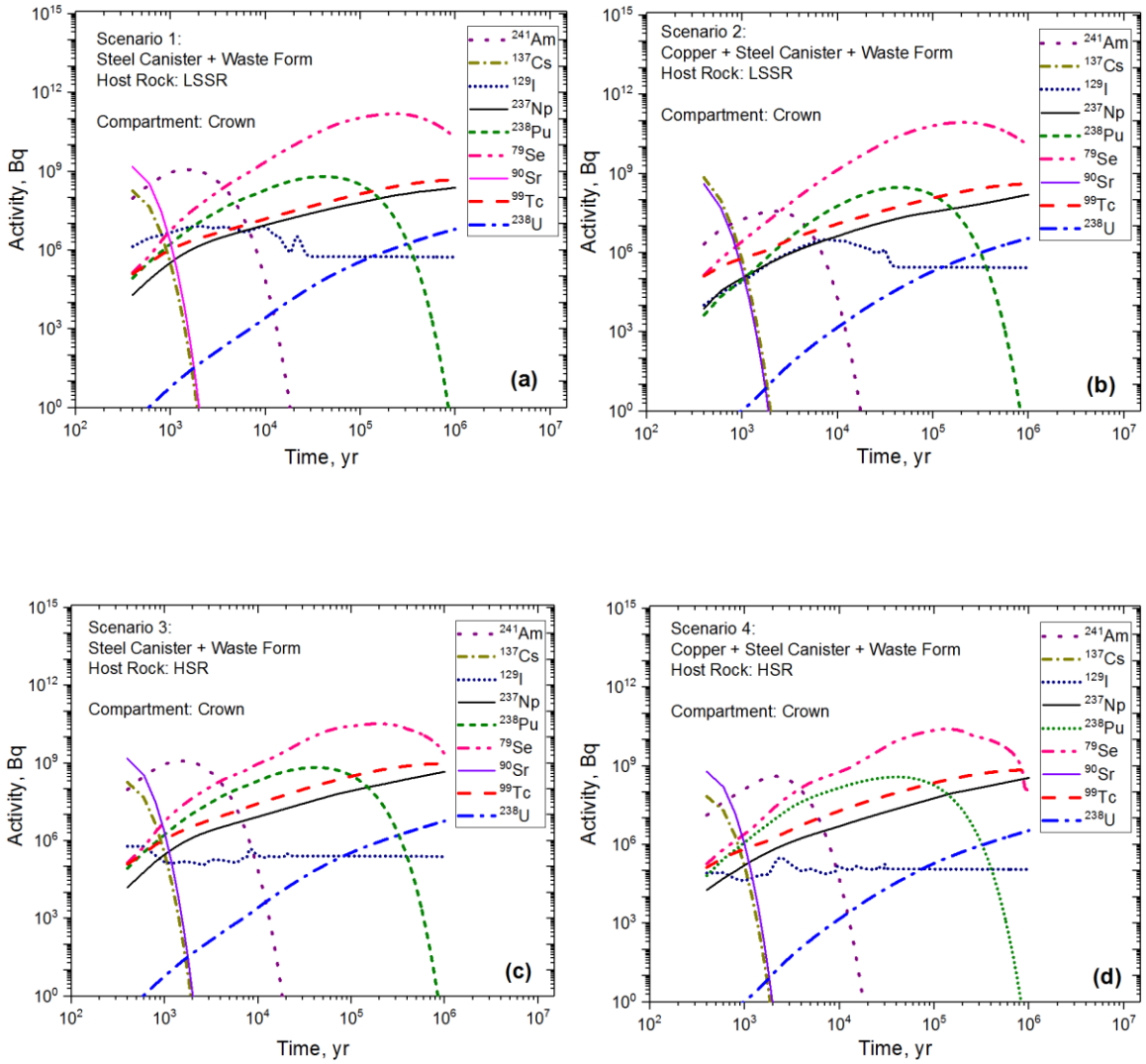

Figure 6.7: Simulated radionuclide flux in the crown of the host rock considering four different scenarios.

towards the end of the simulation time in the crown compartment. The exceptions were ^{99}Tc, ^{237}Np and ^{238}U, whose activity increased modestly between 400 and 1,000,000 years in the disposal vault compartment. ^{129}I exhibited a nearly uniform flux over the simulation time in the crown compartment, which is similar to the behaviour of ^{129}I observed in a study by Mallants *et al.* (2001). The sharp decrease of long-half-life radionuclides, including ^{79}Se, ^{129}I and ^{238}Pu, towards the end of their lifetimes in the disposal vault compartment is most likely because they reached their solubility limits. The short-half-life radionuclides, including ^{90}Sr, ^{137}Cs and ^{241}Am, were constrained by the waste package until they were completely removed by decay. The transport time of the radionuclides (400 years) is greater than 10 times the half-lives of ^{90}Sr, ^{137}Cs and

nearly the same as the half-life of ^{241}Am, reinforcing retardation and decay as the best explanation for their early removal from the near field. The increase in the flux of ^{237}Np with time in both compartments can be attributed to the decay of ^{241}Am, as well as its high mobility.

Importantly, the increase in the activity of ^{99}Tc, ^{237}Np and ^{238}U in the disposal vault compartment from the beginning to the end of the simulation indicates that waste glass dissolution rate had a relatively greater influence than diffusive transport away from the waste-glass surface with respect to the release of these radionuclides. In contrast, diffusive transport away from the waste-glass surface was relatively faster than waste glass dissolution rate in the case of ^{79}Se, ^{90}Sr, ^{129}I, ^{137}Cs, ^{238}Pu and ^{241}Am because of the decrease in their activity in the disposal vault compartment with time. This implies that dissolution rate of the waste glass may not be a long-term constraint to release and transport in the near field; in other words, solubility limit will play a significant role in the retardation and spread release of the radionuclides at long time.

The highest activity in the disposal vault compartment for all four scenarios was ~10^{12} Bq, and this was recorded by ^{99}Tc over the simulation time, whereas ^{79}Se recorded an activity of around ~10^{11} Bq for all the scenarios between 100,000 and 800,000 years, which is the highest in the crown compartment. Both ^{237}Np and ^{238}Pu recorded a maximum activity of ~10^{10} Bq and 10^{9} Bq in the disposal vault and crown compartments, respectively, while the activity of ^{129}I in the crown compartment was nearly uniform at ~10^{6} Bq over the simulation time. These results suggest that ^{79}Se, ^{99}Tc and ^{237}Np will most likely be the radionuclides having the greatest impact at long time. These results are consistent with the findings of previous similar studies (Mallants *et al.*, 2001; Mariner *et al.*, 2011). With the exception of non-sorbing ^{129}I, whose maximum activity increased from an average of ~10^{4} Bq in the disposal vault to an average of ~10^{6} Bq in the crown compartment, the activity of all the radionuclides decreased as they migrated from the disposal vault into the crown compartment. This phenomenon is more pronounced in the strongly sorbed radionuclides, including ^{90}Sr, ^{137}Cs, ^{238}U and ^{241}Am, whose maximum activity decreased by approximately two orders of magnitude as they migrated from the disposal vault compartment to the crown compartment. The lower activity of the radionuclides in the crown compartment than in the disposal vault compartment is probably a result of the retardation safety function of the bentonite buffer, which sorbs the radionuclides as they pass through it into the crown compartment.

These results indicate that the long-half-life radionuclides, especially ^{79}Se, ^{99}Tc, ^{129}I and ^{237}Np, will most likely survive any physical confinement and may reach the accessible environment at long times even though they are retarded by the bentonite buffer and host rock.

6.6.2 Comparison between the fluxes of radionuclides Based on the Scenarios

One of the objectives of this study is to compare the long-term flux of radionuclides based on the disposal options under consideration in the UK, which are classified into four different scenarios in the present study. However, as a result of the identical flux patterns exhibited by the radionuclides in the disposal vault and crown compartments for all the scenarios, it was difficult to obtain a reliable comparison of the scenarios from Figures 6.6 and 6.7. Therefore, the activity of all the radionuclides was summed up for each scenario in the disposal vault and in the crown compartments in order to obtain comparisons between the scenarios with some confidence.

The total flux of all the radionuclides in the disposal vault and crown compartments for the four scenarios were compared, as illustrated in Figure 6.8. For the reason of the barrier property of the intervening bentonite buffer, the total activity of the radionuclides for all the scenarios over the simulation time was higher in the disposal vault compartment than in the crown compartment by an average of two orders of magnitude. With the exception of Scenario 2, the maximum fluxes in the disposal vault compartment occurred between 400 and 1,000 years, whereas all the scenarios had maximum fluxes between 70,000 and 600,000 years in the crown compartment. The maximum fluxes recorded between 400 and 1,000 years in the disposal vault compartment reflect the influence of the waste glass in the spread release of the radionuclides. However, it seems that the combined containment property of copper and steel canisters in Scenario 2, in which total activity was approximately 3.8×10^{12} Bq lower than that of the other scenarios, was effective in preventing early contact of water with the waste glass, which would have resulted in a higher release of radionuclides in the first 1,000 years. The fluxes of the radionuclides in the disposal vault compartment between 10,000 and 1,000,000 years were the same for Scenarios 1 and 3, which show the highest fluxes in the compartment in the 990,000-year time span. The total flux of

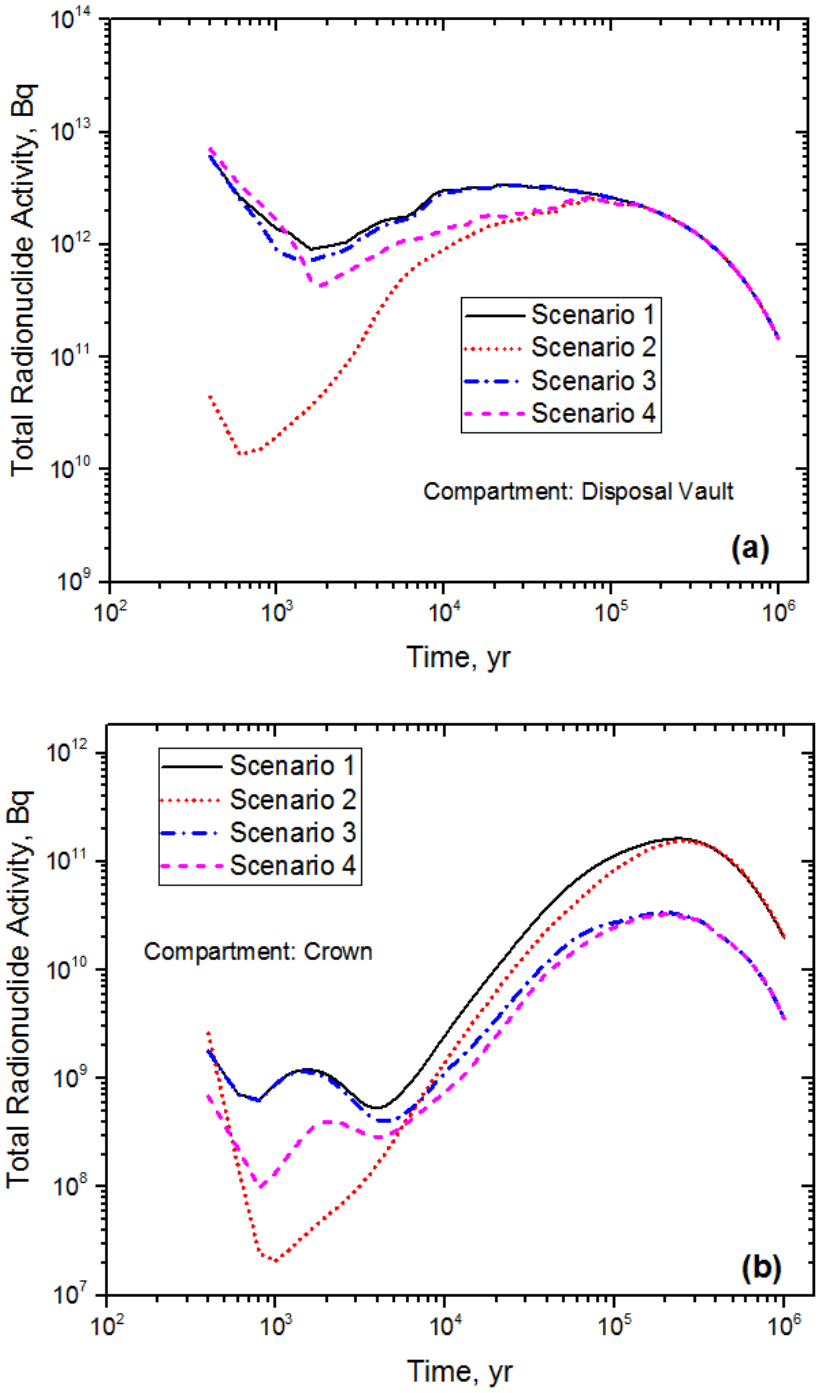

Figure 6.8: Comparison between the fluxes of radionuclides in the near field based on the four scenarios. Scenario 1: LSSR host rock + steel canister, Scenario 2: LSSR host rock + steel + copper canisters, Scenario 3: HSR host rock + steel canister, and Scenario 4: HSR host rock + steel + copper canisters.

Scenario 2 between 400 and 1,000 years was the lowest in the disposal vault compartment, being roughly 10^{10} Bq lower than the total flux of Scenario 4 within this time span.

Scenario 2 had the lowest total flux in the first 10,000 years in the crown compartment; however, henceforth the total flux of Scenario 4 was the lowest. As a result of the fact that the containment imperative of the waste package is less significant in the crown compartment than in the disposal vault compartment, the lowest total flux of Scenario 4 at long time can be attributed to the retardation property of the granite host rock. Indeed, the total flux of Scenario 3 between 10,000 and 1,000,000 years, which also has granite host rock, was lower than the total flux of Scenarios 1 and 2, in which the host rock is clay. Furthermore, the total flux of Scenario 2 was lower throughout the simulation time than the total flux of Scenario 1, excepting the 400,000-year life span at the end of the simulation; likewise, with the exception of between 200,000- and 1,000,000-year lifetime, Scenario 4 showed a slower release during the million-year lifetime of the repository than Scenario 3. Collectively, these results show that HSR host rock would be a more effective barrier at long time than LSSR host rock in restricting the transport of most of the radionuclides until their activity has become negligible. However, the effectiveness of having copper and steel canisters combined in the waste package would be negligible in confining the radionuclides compared to having only the steel canister in the waste package.

Based on these results, it is clear that all the near-field components, including waste glass, steel and copper canisters, bentonite buffer and host rock, play significant roles in the long-term retardation and release of the radionuclides. Importantly, it is noted that the average activity of the radionuclides in all the scenarios over the simulation time is roughly 10^{12} Bq (1 TBq). If this is compared to the total initial activity in the inventory, which is 4603.86 TBq, it means that most of the radionuclides do not leave the canisters and only about 0.8 to 1.2 % of the total activity in the initial inventory was released into the disposal vault after 400 years. This suggests that the containment safety function of the canisters was effective. However, it seems that the retardation properties of the host rock, and probably those of the bentonite buffer, are most important over the long term. The performance assessment of the near-field components is evaluated more closely in the next section.

6.6.3 Performance Assessment

The contribution of waste glass, in combination with other near-field components, to the overall performance of the near field was studied by investigating the effects of the near-field processes on the transport of ^{79}Se, ^{99}Tc, and ^{237}Np, which are the most important radionuclides at long times, in the crown compartment of the model. The performance assessment was conducted using regression analysis, which explains the effect of one predictor variable on the response variable, while other predictor variables in the model are held constant. In the present study the response variable is the mass of the radionuclide that is being transported, while the predictor variables are the near-field processes: waste glass dissolution rate, expected lifetime of copper and steel canisters, partition coefficients of the bentonite, clay and granite, groundwater flow rates through the buffer, host rock, fracture and disposal vault, and the solubility limits of the radionuclides.

The results of the regression analysis are presented in Table 6.4 for Scenarios 1 and 2, and Table 6.5 for Scenarios 3 and 4. In order to ease the interpretation of the results, the absolute values of the regression coefficients are given in the tables. The coefficient of determination (R^2) of each correlation varied between 81 and 100%. It is evident that there is high multicollinearity among the near-field processes (i.e. the predictor variables), as some of the coefficient values are above unity. This was expected considering the complexities of the near field and the interdependence of the near-field processes.

The regression coefficients represent the change in the mass of the radionuclide as a result of a unit change in the value of a near-field process, neglecting the effect of other near-field processes. For example, if Scenario 1 were used, a unit change in the waste glass dissolution rate would lead to a 1.177 g change in the mass of ^{79}Se in the crown compartment, and a unit change in the K_d of bentonite would lead to a 0.106 g change in the mass of ^{99}Tc. In addition, a unit change in the expected lifetime of the steel canister would lead to a 6.215 g change in the mass of ^{237}Np in the crown compartment if Scenario 3 were used, whereas if Scenario 4 were used, a unit change in the expected lifetime of the steel canister would lead to a 0.458 g change in the mass of ^{237}Np in the crown compartment.

From Tables 6.4 and 6.5, it is clear that all the near-field processes that are present in every scenario had an effect on the retardation and transport of the radionuclides at different proportions, and this effect varies among scenarios. As can be deduced from

Table 6.4: Sensitivity analysis results for Scenarios 1 and 2. The values are regression coefficients indicating change in mass of the radionuclides with a unit change in a near-field process. Largest value in this table equals the most sensitive parameter.

Near-field Processes	Scenario 1			Scenario 2		
	^{79}Se	^{99}Tc	^{237}Np	^{79}Se	^{99}Tc	^{237}Np
Waste glass dissolution rate	1.177	0.246	0.507	0.813	0.694	0.285
Copper expected Lifetime	-	-	-	0.819	0.431	0.013
Steel expected Lifetime	1.045	0.243	0.402	0.591	0.383	0.202
K_d in bentonite	0.348	0.106	0.372	1.608	0.045	0.058
K_d in LSSR	2.194	0.049	0.389	2.493	0.403	0.102
K_d in HSR	-	-	-	-	-	-
Advective transport through bentonite	1.462	0.716	0.380	1.597	0.939	0.478
Advective transport through LSSR	0.395	0.201	0.752	0.916	0.328	0.494
Advective transport through disposal vault	2.435	0.000	0.603	3.058	0.123	0.028
Advective transport through HSR	-	-	-	-	-	-
Advective transport through fracture	-	-	-	-	-	-
Diffusive transport	0.912	0.028	0.319	0.011	0.038	0.068
Solubility limit	0.875	0.224	0.468	0.026	0.144	0.349

Table 6.5: Sensitivity analysis results for Scenarios 3 and 4. The values are regression coefficients indicating change in mass of the radionuclides with a unit change in a near-field process. Largest value in this table equals the most sensitive parameter.

Near-field Processes	Scenario 3			Scenario 4		
	^{79}Se	^{99}Tc	^{237}Np	^{79}Se	^{99}Tc	^{237}Np
Waste glass dissolution rate	5.515	0.709	6.690	0.693	1.208	0.691
Copper expected Lifetime	-	-	-	0.935	0.859	0.009
Steel expected Lifetime	1.239	0.468	6.215	0.518	0.522	0.458
K_d in bentonite	0.671	0.320	0.438	0.521	0.409	0.126
K_d in LSSR	-	-	-	-	-	-
K_d in HSR	4.459	0.366	4.333	0.082	0.868	0.104
Advective transport through bentonite	4.176	0.231	6.531	1.029	0.311	0.207
Advective transport through LSSR	-	-	-	-	-	-
Advective transport through disposal vault	5.684	0.145	8.005	0.614	0.408	0.611
Advective transport through HSR	0.231	0.627	5.858	0.592	0.468	0.866
Advective transport through fracture	2.268	0.183	6.672	0.594	0.252	0.486
Diffusive transport	0.474	0.197	0.209	0.581	0.159	0.156
Solubility limit	0.358	0.110	0.349	0.680	0.303	0.701

the results, waste glass dissolution is one of the most important near-field processes, contributing significantly to the release of radionuclides in all the scenarios. This is especially true for ^{99}Tc, for which waste glass dissolution had the highest regression coefficients in Scenarios 3 and 4, and second highest in Scenarios 1 and 2. This implies that the contribution of waste glass is important to the overall performance of the disposal system.

This inference seems to be at odds with the findings of Mallants *et al.* (2001), who conclude that the contribution of waste glass to the overall performance of a geological repository is insignificant. However, it is noted that the study by Mallants *et al.* (2001) was based on the whole geological repository (i.e. both near field and far field), as opposed to only the near field being considered in the present study. In a model that considers transport in both near field and far field, the parameters controlling mass transfer in the far field (advection, diffusion, sorption, desorption) will obscure the contribution of waste glass, making it appear that the contribution of the waste glass is unimportant. As has been shown in the present study, the waste glass is important to the overall performance of the repository. Consequently, studies on waste glass performance assessment are essential for demonstrating repository safety.

The GoldSim model files for all the scenarios are supplied in the CD, which is attached to this thesis. Details about the contents of the CD, and how to access the contents, are provided in Appendix 31.

7 CONCLUSIONS

The overarching goal of this work was to understand the dissolution behaviour of MW25 nuclear waste glass under conditions that are representative of a geological repository and to investigate the contribution of the waste glass to the overall performance of the near field of a geological repository. This was achieved by conducting single-pass flow-through experiments (SPFT) in two parts and implementing the experimental results in a reactive transport model. The original contributions of this work to these questions are summarised in the concluding remarks below.

7.1 Main Findings

1. Experiments were performed on glass powder, and reacted surface area was estimated using a new approach – a numerical method. This method considers changes in the diameter of particles as the glass dissolves. The starting and ending surface areas were more accurately determined using the numerical method than using geometric surface area estimate, which is the preferred standard method among researchers. In the experiment conducted here, this did not impact the rate calculation, as the rates calculated using this new method and the geometric method were within the uncertainties of one another. However, it does provide a better description of the glass particle distribution before and after dissolution and results in a higher release rate that the geometric calculation.
2. The forward dissolution rate of MW25 is ~10 times faster at 90 ^{o}C than at 40 ^{o}C in the experiments conducted with deionised water. The forward rate measured

at 90 ^{o}C was found to be ~6 times higher than the forward rate measured for the French SON68 in a previous study under these laboratory test conditions.

3. A similar release was observed for Si, Mg and Al at 40 ^{o}C and 90 ^{o}C in the experiments conducted with deionised water, whereas the B, Cs, Na, Li and Mo showed an order of magnitude increase when the temperature was increased from 40 to 90 ^{o}C for low q/S values.
4. The range of E_a values associated with B, Na and Si release rates in the case of MW25 in the experiments conducted at 40 and 90 ^{o}C using deionised water is consistent with a surface-controlled reaction mechanism that has an E_a in the range of 41 and 84 kJ/mol.
5. At 90 ^{o}C, hydrolysis and ion-exchange reactions occurring at non-Si sites dominated the dissolution process in the transit stage, and silicic acid concentration was increased as boron and alkali metals (Li and Na) were preferentially released relative to Si. Congruent dissolution achieved at both 40 and 90 ^{o}C was controlled by the same mechanism – hydrolysis of siloxane bonds – at varying degrees, based on temperature, indicating a largely weak dependence of the initial glass dissolution rate on the solution activity of silicic acid.
6. The forward dissolution rate of MW25 glass measured at 40 ^{o}C in lower-strength sedimentary rock (LSSR) groundwater was slightly higher than that measured in higher-strength rock (HSR) groundwater. In addition, the forward dissolution rates measured in both simulant groundwaters were lower than the forward dissolution rate measured in deionised water at the same temperature. The higher forward rate measured in deionised water than in both groundwaters is attributable to the higher alkalinity of the leachate collected in the experiments with deionised water than in the simulant groundwaters. Similarly, the higher forward rate measured in LSSR groundwater than in HSR groundwater correlates to the higher alkalinity of the leachates collected in the experiments with LSSR groundwater.
7. The species Al, B, Li, Mg and Si exhibited similar release behaviour in simulant groundwaters and deionised water at 40 ^{o}C, such that higher dissolution rates were measured at the higher values of $\log_{10}$q/S and lower rates were measured at the lower values of $\log_{10}$q/S. Congruent dissolution was established at the same $\log_{10}$q/S value in the experiments with both groundwaters, as in the experiments with deionised water at 40 ^{o}C.

8. The detection of the same crystalline phases as those typically found in UK Magnox glass by XRD, including ruthenium dioxide (RuO_2) and a spinel phase [$(Fe,Mg)(Cr,Fe)_2O_4$], demonstrates that no new crystalline phases were formed as a result of the reaction of the glass with deionised water (at 40 and 90 ^oC) and simulant groundwaters (at 40 ^oC).
9. The SEM/EDX data of the reacted glass samples at 40 ^oC and 90 ^oC in deionised water revealed that the precipitates formed on the glass surface contain similar elements, including Al, Cs, Fe, La, Mg, Mo, Na, Si and Zr, which have a similar weight percentage to the unreacted Magnox glass. These similarities indicate that the glass was not phase separated, and provide evidence of the stoichiometry of the dissolution process, as well as the compositional homogeneity of MW25.
10. The SEM/EDX of the specimens leached in both LSSR and HSR simulant groundwaters revealed the enrichment of Ca, Mg and Na on the surface of the glass samples leached in both groundwaters. The enrichment of the glass surface with the elemental components of LSSR and HSR simulant groundwaters, especially Ca, contributed significantly to the lower forward rates measured in both groundwaters compared to that measured in deionised water under the same experimental conditions.
11. The glossy appearance of the surface of the specimens leached in both groundwaters suggests the formation of powellite ($CaMoO_4$) on the surface of the glass specimens, which suggests that little Mo may be left in the glass for the fixation of radionuclides. This implies that the presence of Ca in the repository groundwater may increase the mobility of the radionuclides.
12. The much lower activity of the radionuclides released into the disposal vault than their activity in the initial inventory points to the effectiveness of the containment and retardation safety functions of the waste package (canisters and the waste glass). Indeed, only about 0.8 to 1.2 % of the total activity in the initial inventory was released into the disposal vault. In particular, the waste package was effective in retarding the short-half-life radionuclides (^{90}Sr, ^{137}Cs and ^{247}Am) until their activity decays to insignificance. For long-half-life radionuclides (^{79}Se, ^{99}Tc, ^{237}Np, ^{238}U and ^{239}Pu), however, there is greater reliance on chemical retardation by sorption from the bentonite buffer and host rock at long times.

13. The long-half-life radionuclides, including ^{79}Se, ^{99}Tc, ^{237}Np, will most likely reach the far field before they become completely decayed; however, the bentonite buffer and the host rock will strongly limit the magnitude of their fluxes.
14. The results of performance assessment show that HSR host rock would be a more effective barrier at long time than LSSR host rock in restricting the transport of most of the radionuclides until their activity has become negligible. However, the composition of the copper and steel canisters in the waste package would only be slightly more effective in confining the radionuclides than having only the steel canister in the waste package. The effectiveness of the combination of the copper and steel canister in the waste package is stronger in the clay host rock than in the granite host rock.
15. The sensitivity analysis results revealed that the waste glass makes an important contribution to the overall performance of the near field. In particular, waste glass dissolution is more important than diffusive transport in the near field. The precise contribution of the waste glass, however, depends on a number of factors, including the disposal option considered and the radionuclide properties, especially the solubility limit. Efforts to improve glass durability are worthwhile in terms of repository performance.

7.2 Future Work

The following observations merit future attention:

1. Given that a Si- and Al-rich separate matrix makes up the bulk of the glass and is subject to solution feedback effects, the release of Si and Al to solution was relatively slow at low values of parameter q/S. As the flow rate increases, the solution was more dilute, allowing the Si- and Al-rich matrix to dissolve more quickly. Concentrations of B, Li and Na decrease as the flow rate increases because the release rate and the transport rate reach a pseudo-equilibrium point. This release behaviour of B and the alkali metals (Li and Na) was more pronounced at 90 ^{o}C than at 40 ^{o}C, raising important scientific questions. Is this behaviour characteristic of MW25? Or is it a result of phase separation of the glass in the course of reacting with solution at 90 ^{o}C? These questions require further exploration, which may involve geochemical modelling and/or advanced imaging.

2. At 40 ^{o}C Mg behaves in the same way as Si; however, at 90 ^{o}C the behaviour of Mg is similar to that of Al. These observations indicate that it would be beneficial to investigate the dependence of the dissolution rate of MW25 on Mg in combination with Al and Si for future work.
3. In the performance assessment, a number of issues can still be improved. Considerable uncertainty exists about the amount of elements present in the waste glass, in particular ^{129}I. In addition, there are uncertainties about the values of the Stage 2 (residual) and Stage 3 (resumption of alteration) dissolution rates of the waste glass. Therefore, the relative importance of waste glass in the overall performance of the near field requires further exploration. One possible scenario that can be explored is varying the lifetime of waste glass by considering different source term models.

8 REFERENCES

Åagaard, P. and Helgeson, H.C., (1982). Thermodynamic and Kinetic Constraints on Reaction Rates among Minerals and Aqueous Solutions. I. Theoretical Considerations. *Am. J. Sci.* **282**, 237–285.

Abraitis, P.K., McGrail, B.P., Trivedi, D.P., Livens, F.R. and Vaughan, D.J. (2000a). Single-pass flow-through experiments on a simulated glass in alkaline media at 40 ^{o}C. I. Experiments conducted at variable solution flow rate to glass surface area. *J. Nucl. Mater.* **280**, 196–205.

Abraitis, P.K., McGrail, B.P., Trivedi, D.P., Livens, F.R. and Vaughan, D.J. (2000b). Single-pass flow-through experiments on a simulated glass in alkaline media at 40 ℃. II. Experiments conducted with buffer solutions containing controlled quantities of Si and Al. *J. Nucl. Mater.* **280**, 206–215.

Abraitis, P.K., Livens, F.R., Monteith, J.E., Small, J.E., Trivedi, D.P., Vaughan, D.J. and Wogelius R.A. (2000c). The kinetics and mechanisms of simulated British Magnox waste glass dissolution as a function of pH, silicic acid activity and time in low-temperature aqueous systems. *Appl. Geochem.* **15**, 1399–1416.

Andra (2005). Dossier 2005 Argile. Architecture and management of a geological repository. Agence Nationale pour la Gestion des Déchets Radioactifs.

Apted, M. and Ahn J. (2010). Multibarrier geological repository design and operation strategies for safe disposal of radioactive elements. In: Ahn, J. and Apted, J. (Eds.), *Geological Repository Systems for Safe Disposal of Spent Nuclear Fuels and Radioactive Waste. Woodhead Publishing Series in Energy* **9**, 3–28.

ASTM (2010). *Standard Practice for Measurement of the Glass Dissolution Rate Using the Single-Pass Flow-Through Test Method*. ASTM C1662, American Society for Testing and Materials International, Philadelphia, PA.

Bates, J.K., Bradley, J.P., Teetsov, A., Bradley, C.R., Buchholtz ten Brink, M. (1992). Colloid formation during nuclear waste glass dissolution: Implications for nuclear waste disposal. *Science* **256**, 469 - 471.

Bechtel SAIC Company, LLC (2001). *Total system performance assessment: analyses for disposal of commercial and DOE waste inventories at Yucca Mountain – input to final environmental impact statement and site suitability evaluation*. Department of Energy, REV 40 ICN 02.

Bel, J.J.P., Wickham, S.M. and Gens, R.M.F. (2006). Development of the supercontainer design for deep geological disposal of high-level hear emitting radioactive waste in Belgium. *Mat. Res. Soc. Symp. Proc.* **932**, 23–32.

Berner, R. (1978). *Early diagenesis: a theoretical approach*. Princeton University Press, Princeton, NJ.

Berner, U. (2002). *Project opalinus clay: radionuclide concentration limits in the near field of a repository for spent fuel and vitrified high-level waste*. PSI Bericht 0 –26.

Bond, K.A. and Tweed, C.J. (1995). *Groundwater compositions for the Borrowdale Volcanic Group, boreholes 2, 4 and RCF3, Sellafield, evaluated using thermodynamic modelling.* Nirex, NSSlR397.

Bourcier, W.L. (1991). Overview of chemical modeling of nuclear waste glass dissolution. *Mater. Res. Soc. Symp. Proc.* **212**, 3–17.

Bourcier, W.L. (1994). Waste glass corrosion modeling: comparison with experimental results. *Mater. Res. Soc. Symp. Proc.* **333**, 69–81.

Brady, P.V. and House, W.A. (1996). Surface-controlled dissolution and growth of minerals. In: Brady, P.V. (Ed.), *Physics and Chemistry of Mineral Surfaces*. CRC Press, New York, pp. 249 - 256.

Brunauer S., Emmet, P.H. and Teller, E. (1938). Adsorption of gases in multimolecular layers. *J. Am. Chem. Soc.* **60**, 309-319.

Buck, E. and Sassani, D.C. (2007). *Waste Form and In-Drift Colloids-Associated Radionuclide Concentrations: Abstraction and Summary*. MDL-EBS-PA-000004 REV 03. Sandia National Laboratories, Albuquerque, New Mexico.

Bunker, B.C., Tallant, D.R., Headley, T.J., Turner, G.L. and Kirkpatrick, R.J. (1988). The structure of leached sodium borosilicate glass. *Phys. Chem. Glasses* **29**, 106–120.

Butcher, E.J., Cheesemen, C.R., Sollars, C.J., and Perry, R. (1996). Flow-through leach testing applied to stabilized/solidified wastes. In T.M. Gilliam and C.C. Wiles (Eds.), *Stabilization and Solidification of Hazardous, Radioactive, and Mixed Wastes:* 3rd Volume. ASTM STP 1240.

Cantrell, J.K., Carroll, K.C., Buck, E.C., Neiner, D., Geiszler, K.N. and Vaughan, D.J., (2013). Single-pass flow-through test elucidation of weathering behaviour and evaluation of contaminant release models for Hanford tank residual radioactive waste. *Appl. Geochem.* **28**, 119–127.

Carmichael, R.S. (1982). *Handbook of Physical Properties of Rocks, Volume II*. CRC Press, Boca Raton, Florida.

Cassingham, N., Corkhill, C.L., Backhouse, D.J., Hand, R.J., Ryan, J.V., Vienna, J.D. and Hyatt, N.C. (2015). The initial dissolution rates of simulated UK Magnox-ThORP blend nuclear waste glass as a function of pH, temperature and waste loading. *Mineral. Mag.* **79**, 1529-1542.

Chambre, P., Pigford, T.H., Fujita, A., Kanki, T., Kobayashi, A., Lung, H., Ting, D. Sato, Y. and Zavoshy, S.J. (1982). *Analytical performance models for geologic repositories.* LBL-14842, Lawrence Berkeley Laboratory, CA.

Chou, L. and Wollast, R. (1984). Study of the weathering of albite at room temperature and pressure with a fluidized bed reactor. *Geochimica et Cosmochimica Acta* **48**, 2205-2217.

Coles, D.G. (1981). A continuous-flow leach testing method for various nuclear waste forms. *Null. Chem. Waste Management* **2**, 245-252.

Corkhill, C.L., Cassingham, N.J., Heath, P.G. and Hyatt, N.C. (2013). Dissolution of UK high-level waste glass under simulated hyperalkaline conditions of a co-located geological disposal facility. *International Journal of Applied Glass Science* **4**, 341–356.

Curti, E., Crovisier, J.L., Morvan, G. and Karpoff, A.M. (2006). Long-term corrosion of two nuclear waste reference glasses (MW and SON68): A kinetic and mineral alteration study. *Applied Geochemistry* **21**, 1152–1168.

Danilatos, G.D. (1994). Environmental scanning electron microscopy and microanalysis. Mikrochim. Acta **114/5**, 14 –155.

DECC (2014). *Implementing Geological Disposal; A framework for the long-term management of higher activity radioactive waste.* URN 14D/235. Department of Energy & Climate Change, London.

Delage, F. and Dussossoy, J.L. (1991). R7T7 glass initial dissolution rate measurements using a high-temperature soxhlet devise. In: Scientific Basis for Nuclear Waste Management XIV: *Mater. Res. Soc. Symp. Proc.* **212**, 41-47.

Donald, I.W. (2010). *Waste immobilization in glass and ceramic based hosts*. Chippenham, UK.

Doresmus, R.H. (1975). Interdiffusion of hydrogen and alkali ions in a glass surface. *J. Non-Crystal. Solids* **19**, 137–144.

Dove, P.M. and Crerar, D.A. (1990). Kinetics of quartz dissolution in electrolyte solutions using a hydrothermal mixed flow reactor. *Geochim. Cosmochim. Acta* **54**, 955-969.

Dugger, D. L., Stanton, J. H., Irby, B. N., McConnell, B. L., Cummings, W. W., and Maatman, R. W. (1964). The exchange of twenty metal ions with the weakly acidic silanol groups of silica gel. *J. Phys. Chem.* **68**, 757-760.

Ebert, W.L. and Bates, J.K. (1991). The importance of secondary phases in glass corrosion. Scientific Bases for Nuclear Waste Management XIV. *MRS Proceedings* **212**, 89–97.

Ebert, W. L. and Mazer, J. J. (1993). Laboratory testing of waste glass aqueous corrosion; effects of experimental parameters. *MRS Proceedings* **333**. doi:10.1557/PROC-333-27.

Ebert, W.L. (2005). *Interlaboratory study of the reproducibility of the single-pass flow-through test method: measuring the dissolution rate of LRM glass at 70 ^{o}C And pH 10.* ANL-05/33, Argonne National Laboratory, Chicago, IL.

Ebert, W.L. (2010). *Radionuclide release from slag and concrete materials – Part 1: Conceptual model of leaching from complex materials and laboratory test methods*. NUREG/CR-7025, United States Nuclear Regulatory Commission.

Ebert, W.L. (2015). Glass degradation in performance assessment models. *MRS Proceedings* **1744**, 163–172.

Frugier, P., Chave, T., Gin, S. and Lartigue, J.E. (2008). Application of the GRAAL model to leaching experiments with SON68 nuclear glass in initially pure water. *J. Nucl. Mater.* **380**, 821.

Fournier, M., Ull, A., Nicoleau, E., Inagaki, Y., Odorico, M., Frugier, P. and Gin, S. (2016). Glass dissolution measurement and calculation revisited. *J. Nucl. Mater.* **476**, 140–154.

Gaucher, E.C., Blanc, P., Bardot, F., Braibant, G., Buschaert, S., Crouzet, C., Gautier, A., Girard, J., Jacquot, E., Lassin, A., Negrel, G., Tournassat, C., Vinsot, A and Altmann, S. (2006). Modelling the porewater chemistry of the Callovian – Oxfordian formation at a regional scale. *Comptes Rendus Geosciences* **338**, 917 – 930.

Gin, S., Jollivet, P., Mestre, J.P., Jullien, M. and Pozo, C. (2001). French SON 68 nuclear glass alteration mechanisms on contact with clay media. *Appl. Geochem.* **16**, 861–881.

Gin S., Abdelouas A., Criscenti L.J., Ebert W.L., Ferrand K., Geisler T., Harrison M.T., Inagaki Y., Mitsui S., Mueller K.T., Marra J.C., Pantano C.G., Pierce E.M., Ryan J.V., Schofield J.M., Steefel C.I and Vienna J.D. (2013). An international initiative on long-term behavior of high-level nuclear waste glass. *Mater. Today* **16**, 243–248.

Gin, S. (2014). Open scientific questions about nuclear glass corrosion. In: *2nd International Summer School on Nuclear Glass Wasteform: Structure, Properties and Long-Term Behavior, SumGLASS 2013, Procedia Materials Science* **7**, 163–171.

Gin, S., Jollivet, P., Fournier, M, Angeli, F, Frugier, P. and Charpentier, T. (2015). Origin and consequences of silicate glass passivation by surface layers. *Nature Communications* **6**, 6360.

Goldstein, J.I., Newbury, D.E., Joy, D.C., Lyman, C., Echlin, P., Lifshin, E., Sawyer, L. and Michael, J. (2003). *Scanning Electron Microscopy and X-Ray Microanalysis.* Kluwer Academic Publishers, New York.

Grambow, B. (1985). A general rate equation for nuclear waste glass corrosion. *Mater. Res. Soc. Symp. Proc.* **44**, 15–27.

Grambow, B. (1987). *Nuclear Waste Glass Dissolution: Mechanism, Model, and Application,* JSS Report, Number JSS-TR--87-02.

Grambow, B. (1992). Geochemical approach to glass dissolution. In: Clark D.E., Zoitos, B.K (Eds), *Corrosion of Glass, Ceramics and Ceramic Semiconductors*, Noyes Publications, Park Ridge, NJ.

Grambow, B. (2006). Nuclear waste glasses – how durable. *Elements* **2**, 357–364.

Grimes, R.W. and Nuttall, W.J. (2010). Generating the option of a two-stage nuclear renaissance. Science **329**, 799–803.

GTC (2014). *Radioactive and hazardous waste management applications using GoldSim*. GoldSim Technology Group LLC, White Paper.

Harrison, M.T. (2014a). Vitrification of high level waste in the UK. In: *2nd International Summer School on Nuclear Glass Wasteform: Structure, Properties and Long-Term Behavior, SumGLASS 2013, Procedia Materials Science* **7**, 10–15.

Harrison, M.T. (2014b). The effect of composition on short- and long-term durability of UK HLW glass. In: *2nd International Summer School on Nuclear Glass Wasteform: Structure, Properties and Long-Term Behavior, SumGLASS 2013, Procedia Materials Science* **7**, 186–192.

Humphries, D.W. (1992). *The Preparation of Thin Sections of Rocks, Minerals, and Ceramics.* Oxford University Press.

IAEA (International Atomic Energy Agency). (2004). *Developing multinational radioactive waste repositories: infrastructural framework and scenarios of cooperation.* IAEA TECDOC No. 1413, Vienna.

IAEA (International Atomic Energy Agency). (2011). *Geological disposal facilities for radioactive waste*. IAEA Safety Standards Series No. SSG-14, IAEA, Vienna.

Icenhower, J.P., Strachan, D.M., McGrail, B.P., Scheele, R.D., Rodriguez, E.A., Steele, J.L. and Legore, V.L. (2006). Dissolution kinetics of pyrochlore ceramics for the disposition of plutonium. *Am. Mineral.* **91**, 39–53.

Icenhower, J.P., McGrail, B.P., Shaw, W.J., Pierce, E.M., Nachimuthu, P., Shuh, D.K., Rodriguez, E.A. and Steele, J.L. (2008). Experimentally determined dissolution kinetics of Narich borosilicate glasses at far-from-equilibrium conditions: implications for transition state theory. Geochim. Cosmochim. Acta **72**, 2767–2788.

Icenhower, J.P. and Steefel, C.I. (2013). Experimentally determined dissolution kinetics of SON68 glass at 90 ^{o}C over a silica saturation interval: Evidence against a linear rate law. *J. Nucl. Mater.* **439**, 137–147.

Icenhower, J.P. and Steefel, C.I. (2015). Dissolution rate of borosilicate glass SON68: a method of quantification based upon interferometry and implications for experimentsl and natural weathering rate of glass. *Geochim. Cosmochim. Acta* **157**, 147-163.

Jantzen, C.M., Brown, K.G. and Picket, J.B. (2010). Durable glass for thousands of years. *Int. J. Appl. Glass Sci.* **1**, 38-62.

Jantzen, C.M., Lorier, T.H., Pareizs, J.M. and Marra, J.C. (2007). Fluidized bed steam reformed (FBSR) mineral waste forms:In: Characterisation and durability testing. Mater. Res. Soc. Symp. **985**, 421–428.

JNC (Japan Nuclear Commission). (2000). *H12 Project to establish the scientific and technical basis for HLW disposal in Japan, Japan Nuclear Cycle Development Institute*. Technical Report JNC/TN 1410.

Johannesson, L.E. and Nilsson, U. (2006). *Deep repository – Engineered barrier systems. Geotechnical properties of candidate backfill materials – Laboratory tests and calculations for determining performance.* SKB TR-06-73, Svensk Kärnbränslehantering AB, Sweden.

Johnson, L.H. and King, F. (2003). *Canister options for the disposal of spent fuel.* Nagra Technical Report 02-11. Nagra, Wettingen, Switzerland.

Jollivet, P., Gin, S. and Schumacher, S. (2012). Forward dissolution rate of silicate glasses of nuclear interest in clay-equilibrated groundwater. *Chemical Geology* **330–331**, 207–217.

Knauss, K. G. and Wolery, T.J. (1986). Dependence of albite dissolution on kinetics on pH and time at 25 ^{o}C and 70 ^{o}C. *Geochim. Cosmochim. Acta* **50**, 2481–2497.

Lama, R.D. and Vutukuri, V.S. (1978). *Handbook on Mechanical Properties of Rocks, Volume II Testing Techniques and Results*. Trans Tech Publications, Bay Village, Ohio.

Lasaga, A.C. (1981). Transition state theory. In: Lasaga, A.C., Kirkpatrick, R.J. (Eds), *Kinetics of Geochemical Processes*. Reviews in Mineralogy **8**, pp. 135–168.

Lasaga, A.C. (1995). Fundamental approaches in describing mineral dissolution and precipitation rates. In: White, A.F., Brantley, S.L. (Eds.), *Chemical Weathering Rates of Silicate Minerals*, vol. 31. Mineralogical Society of America, Washington, DC, pp. 3–86.

Mallants, D., Marivoet, J. and Sillen, X. (2001). Performance assessment of the disposal of vitrified high-level waste in a clay layer, J. Nucl. Mater. **298**, 125–135.

Marcfarlane, A.M. and Ewing, R.C. (2006). *Uncertainty underground: Yucca Mountain and the nation's high-level nuclear waste.* The MIT Press, Cambridge, MA.

Mariner, P.E., Lee, J.H., Hardin, E.L., Hansen, F.D., *et al.* (2011). *Granite disposal of US high-level radioactive waste.* SANDIA Report SAND2011-6203.

Marsh, G.P. and Taylor, K.J. (1988). An assessment of carbon steel canisters for radioactive waste disposal. Corrosion Science **28**, 289-320.

McGrail, B.P. and Peeler, D.K. (1995). *Evaluation of the single-pass flow-through test to support a low-activity waste specification*. PNL-10746, Pacific Northwest Laboratory, Richmond, Washington.

McGrail, B.P., Ebert, W.L., Bakel, A.J. and Peeler, D.K. (1997a). Measurement of kinetic rate law parameters on a Na-Ca-Al borosilicate glass for low activity waste. *J. Nucl. Mater.* **249**, 175–189.

McGrail, B.P., Martin, P.F. and Lindenmeier, C.W. (1997b). Accelerated testing of wasteforms using a novel pressurized unsaturated flow (PUF) method. *Mat. Res. Soc. Symp. Proc.* **465**, 253–260.

McGrail, B.P., Lindenmeier, C.W. and Martin, P.F. (1999). Characterization of pore structure and hydraulic property alteration in pressurized unsaturated flow tests. In: Wronkiewicz, D.J., Lee, J.H. (Eds.). Scientific Basis for Nuclear Waste Management, *Mater. Res. Soc. Symp. Proc.* **556**, 421–428.

McGrail, B.P., Icenhower, J.P., Martin, P.F., Rector, D.R., Schaef, H.T., Rodriguez, E.A. and Steele, J.L. (2000). *Low-Activity Waste Glass Studies: FY2000 Summary Report*, PNNL-13381, Pacific Northwest National Laboratory, Richland, WA.

McGrail, B.P., Icenhower, J.P., Shuh, D.K., Liu, P., Darab, J.G, Baer, D.R., Thevuthasen, S., Shutthanandan, V., Engelhard, M.H., Booth, C.H. and Nachimuthu, P. (2001). The structure of Na_2O-Al_2O_3-SiO_2 glass: impact on sodium ion exchange in H_20 and D_20. *J. Non-Cryst. Solids* **296**, 10-26.

Nagra (2002). *Project Opalinus Clay: Safety report. Demonstration of disposal feasibility for spent fuel, vitrified high-level waste and long-lived intermediate-level waste*. NAGRA NTB 02-05, Nagra, Wettingen, Switzerland.

NDA (Nuclear Decommissioning Authority). (2010). *Geological Disposal: Generic Post-closure Safety Assessment*. NDA Report no. NDA/RWMD/030.

NDA (National Decommissioning Authority). (2014). *Geological disposal: Feasibility studies exploring options for storage, transport and disposal of spent fuel from potential new nuclear power stations.* NDA Report no. NDA/RWMD/060/Rev1.

Neeway, J.J., Qafoku, N.P., Williams, B.D., Valenta, M.M., Cordova, E.A., Strandquist, S.C., Dage, D.C. & Brown, C.F. (2012). Single-pass flow-through test results of fluidized bed steam reforming (FBSR) waste forms used for LAW immobilization. In: *International Collaboration and Continuous Improvement 2*, Proceesings of the Annual Waste Management Symposium (WM2012), Paper #12252, February26 – March 1, 2012, Phoenix, AZ.

Nelson, D. (2002). Natural Variations in the Composition of Groundwater. *Groundwater Foundation Annual Meeting, Drinking Water Program*, Oregon Department of Human Services, Springfield, Oregon. November 2002.

Nirex (2005a). *Specification for waste packages containing vitrified high level waste and spent nuclear fuel.* Nirex Report no. N/124, United Kingdom Nirex Limited, UK.

Nirex (2005b). *Outline design for a reference repository concept for UK high level waste/spent Fuel*. Technical Note 502644, United Kingdom Nirex Limited, UK.

NRC (National Research Council). (1995). *Nuclear waste: technologies for separation and transmutation*. National Academy Press, Washington DC.

Ochs, M. and Talerico, C. (2004). *SR-Can. Data and uncertainty assessment. Migration parameters for the bentonite buffer in the KBS-3 concept*. SKB TR-04-18, Svensk Kärnbränslehantering AB, Sweden.

Oelkers, E.H. and Gislason, S.R. (2001). The mechanism, rates and consequences of basaltic glass dissolution: I. An experimental study of the dissolution rates of basaltic glass as a function of aqueous Al, Si and oxalic acid concentration at 25 °C and pH 3 and 11. *Geochimica et Cosmochimica Acta* **65**, 3671–3681.

Ojovan, M.I. and Lee, W.E. (2007). *New developments in glassy nuclear wasteforms*, Nova. Science Publishers, New York.

ONDRAF/NIRAS (2008). *Evolution of the near-field of the ONDRAF/NIRAS Repository concept for category C wastes*: First full draft report, ONDRAF/NIRAS report NIROND-TR 2007-07E.

Pederson, L. R., Buckwalter, C.Q., McVay, G.L. and Riddle, B.L. (1983). Glass surface area to solution volume ratio and its implications to accelerated leach testing. *Mat. Res. Soc. Symp. Proc.* **15**, 47-54.

Pierce, E.M., Rodriguez, E.A., Calligan, L.J., Shaw, W.J. and McGrail, B.P. (2008a). An experimental study of the dissolution rates of simulated aluminoborosilicate waste glasses as a function of pH and temperature under dilute conditions. *Appl. Geochem.* **223**, 2559–2573.

Pierce, E.M., Richards, E.L., Davis, A.M., Reed, L.R. and Rodriguez, E.A. (2008b). Aluminoborosilicate waste glass dissolution under alkaline conditions at 40 ℃: Implications for a chemical affinity-based rate equation. Environ. Chem. **5**, 73–85.

Poinssot, C., Fillet, C. Gras, J.M. (2010). Post-containment performance of geological repository systems: source-term release and radionuclide migration in the near- and far-field environments. In: Ahn, J. and Apted, J. (Eds.), *Geological Repository Systems for Safe Disposal of Spent Nuclear Fuels and Radioactive Waste*. *Woodhead Publishing Series in Energy* **9**, 429–493.

Poinssot, C. and Gin, S. (2012). Long-term Behavior Science: The cornerstone approach for reliably assessing the long-term performance of nuclear waste. *J Nucl Mater*. **420**, 182–192.

Posiva (2010). *Models and Data Report 2010*. POSIVA 2010-01. Posiva Oy, Olkiluoto, Finland.

Purvis, K. (1991). Fibrous clay mineral collapse produced by beam damage during scanning electron microscopy. Clay Mineral. **26**, 141–145.

Rebiscoul, D., Rieutord, F. Ne, F., Frugier, P., Cubbit, R. and Gin, S. (2007). Water penetration mechanisms in nuclear glasses by X-ray and neutron reflectometry. *J. Non-Crystal. Solids* **353**, 2221–2230.

Reed, S.J.B. (2005). *Electron Microprobe Analysis and Scanning Electron Microscopy in Geology, Second Edition*. Cambridge University Press.

Reimer, L. (1998). *Scanning Electron Microscopy: Physics of Image and Formation Microanalysis*. Springer Series in Optical Science, vol. 45.

Robinet, J.C., Sardini, P., Siitari-Kauppi, M., Prêt, D., Yven, B. (2015). Upscaling the porosity of the Callovo-Oxfordian Mudstone from the pore scale to the formation scale; insights from the 3H-PMMA autoradiography technique and SEM BSE Imaging. Sedimentary Geology, **321**, 1–10.

Scales, C.R. (2011). *Characterisation of Simulated Vitrified Magnox Product Manufactured on the VTR*. National Nuclear Laboratory Report NNL(10) 10929 Issue 6.

Scheetz, B.E., Freeborn, W.P., Smith, D.K., Anderson, C. and Zolensky, M. (1985). The role of boron in monitoring the leaching of borosilicate glass waste forms. In: *Mater. Res. Soc. Symp. Proc.* **44**, 129–134.

Schnatter, K.H., Doremus, R.H. and Lanford, W.A. (1988). Hydrogen analysis of soda-lime silicate glass. *J. Non-Crystal. Solids* **102**, 11–18.

Schofield, J.M., Swanton, S.W., Farahani, B., Myatt, B.J., Heath, T.G., Burrows, S.E., Holland, D., Moule, A., Bridgen, C.T. and Farnan, I. (2016). *Experimental studies of the chemical durability of UK HLW and ILW glasses*. Interim Progress Report, AMEC/103498/03 Issue 1.

Scholze, H., Conradt, R., Engelke, H. and Roggendorf, H. (1982). Determination of the corrosion mechanisms of high-level waste containing glass. In: Lutze, W. (Ed). Scientific Basis for Nuclear Waste Management V, *Mater. Res. Soc. Symp. Proc.* **11**, 173-180.

Selnert, E., Byegard, J. and Widestrand H. (2008). *Forsmark site investigation: Laboratory measurement within the site investigation programme for transport*

properties of the rock. SKB P-07-139. Swedish Nuclear Fuel and Waste Management Co., Stockholm, Sweden.

Severin, K.P. (2004). *Energy Dispersive Spectrometry of Common Rock Forming Minerals.* Kluwer Academic Publishers, New York.

SKB (Svensk Kärnbränslehantering AB). (1997). *Compilation of radionuclide sorption coefficients for performance assessment*. SKB TR-97-13. Swedish Nuclear Fuel and Waste Management Co., Stockholm, Sweden.

SKB (Svensk Kärnbränslehantering AB) (2000). *Integrated account of method, site selection and programme prior to the site investigation phase*. SKB TR-01-03. Swedish Nuclear Fuel and Waste Management Co., Stockholm, Sweden.

SKB (Svensk Kärnbränslehantering AB). (2004). *Integrated Near-field Evolution Model for a KBS-3 Repository*. SKB TR-04-36. Swedish Nuclear Fuel and Waste Management Co., Stockholm, Sweden.

SKB (Svensk Kärnbränslehantering AB). (2006). *Data report for the safety assessment SR-Can*. SKB TR-06-25. Swedish Nuclear Fuel and Waste Management Co., Stockholm, Sweden.

Smets, B.M.J. and Lommen, T.P.A. (1983). The role of molecular water in the leaching of glass. *Phys. Chem. Glasses* **24**, 35–36.

Strachan, D.M., Bourcier, W.L. and McGrail, B.P. (1993). Toward a consistent model for glass dissolution. *Radioactive Waste Management and Environmental Restoration* **000(2),** 1–17.

Strandh, H., Pettersson, L.G.M., Sjöberg, L. and Wahlgren, U. (1997). Quantum chemical studies of the effects on silicate mineral dissolution rates by adsorption of alkali metals. *Geochim. Cosmochim. Acta* **61**, 2577–2587.

Szakalos, P. and Seetharaman, S. (2012). *Corrosion of copper canister*. Swedish Radiation Safety Authority, SSM Technical Note 2012:17.

Thibault, D.H., Sheppard, M.I. and Smith, P.A. (1990). *A critical compilation and review of default soil solid/liquid partition coefficients, K_d, for use in environmental assessments.* Report No. AECL-10125. Whiteshell Nuclear Research Establishment, Atomic Energy of Canada Limited, Pinawa, Canada.

Thorn, M. (2012). Modelling radionuclide transport in the environment and calculating radiation doses. In: Poinssot C. and Geckeis, H. (Eds.), *Radionuclide behaviour in the natural environment: science, implications and lessons for the nuclear industry. Woodhead Publishing Series in Energy*, 517–569.

Utton, C.A., Swanton, S.W., Schofield, J., Hand, R.J., Clacher, A. and Hyatt, N.C. (2012). Chemical durability of vitrified wasteforms: effects of pH and solution composition. *Mineral. Mag.* **76**, 2919–2930.

Utton, C.A., Hand, R.J., Bingham, B.J., Hyatt, N.C., Swanton, S.W. and William, S.J. (2013). Dissolution of vitrified wastes in a high-pH calcium-rich solution. *J. Nucl. Mater.* **435**, 112-122.

Van Iseghem, P., Valcke, E., Gin, S., Deneele, D., Grambow, B., Strachan, D., McGrail, P. and Wicks, G. (2009). Glamor – or how we achieved a common understanding on the decrease of glass dissolution kinetics. Ceram. Trans. **207**, 115–126.

Vikström, M. and Gustafsson, L.G. (2006). *Modelling transport of water and solutes in future wetlands in Forsmark*. Report R-06-46, Swedish Nuclear Fuel and Waste Management Co.

Vilks, P., Cramer, J.J., Jensen, M., Miller, N.H., Miller, H.G. and Stanchell, F.W. (2003). In situ diffusion experiments in granite: phase I. Journal of Hydrology 61, 191–202.

Weed, H.C. and Jackson, D.D. (1979). *Design of a variable-flow-rate, single-pass leaching system*. UCRL-52785 Report, Lawrence Livermore Laboratory, Livermore, CA.

Wellman, D.M., Catalano, J.G., Icenhower, J.P. and Gamerdinger, A.P. (2005). Synthesis and characterization of sodium meta-autunite, Na[UO2PO4] 3H2O. *Radiochimica Acta* **93**, 393–399.

Werme, L., Bjorner, I.K., Bart, G., Zwicky, U., Grambow, B., Lutze, W., Ewing, R.C. and Magrabi, C. (1990). Chemical corrosion of highly radioactive borosilicate nuclear waste glass under simulated repository conditions. J. Mat. Res. **5**, 1130-1146.

White A.F. and Brantley, S.L. (2003). The effect of time on the weathering of silicate minerals: Why do weathering rates differ in the laboratory and field? *Chemical Geology* **202**, 479-506.

Wolff-Boenisch, D., Gislason, S.R., Oelkers, E.H. and Putnis, C. (2004). The dissolution rates of natural glasses as a function of their composition at pH 4 and 10.6, and temperatures from 25 to 74 C. *Geochim. Cosmochim. Acta* **68**, 4843–4858.

9 APPENDICES

APPENDIX 1 CONTINUOUS FLOW PROGRAMMING AND CONVERSION OF PUMPS' SPEED TO TARGET FLOW RATE

9.1 Flow Programming

KSerial – a command driven program operating at the command line pump – is used for communication between the pumps and the PC. KSerial commands follow QBASIC format and are saved as .bat files in the local disc of the PC. The commands are represented by special notations to form a command string. For example, Pump 1 can be instructed to undergo a full aspiration using the following commands:

K 1WR4

K 1A48000R

The first command initialises the pump, while the second command makes the pump to aspirate over a full stroke.

The following command sequence is used for the continuous flow:

Initialising Pump (Pump 1)

V2000	Set the dispense speed
h – n	Begin the handshake dispense immediately
:S	Label 'S'
O	Move the valve to the input port
V6000	Set the filling speed
A48000	Fill the syringe
I	Move the valve to the dispense port
V2000	Set the dispense speed
hn	Do a standard handshake
JS	Go to label 'S' for another cycle

Other Pump (Pump 2)

:S	Label 'S'
O	Move the valve to the input port
V6000	Set the filling speed

A48000 Fill the syringe

I Move the valve to the dispense port

hn Do a handshake dispense

JS Go to label ‘S’ for another cycle

The above command sequence is written in the KSerial in the form of command strings as below:

K 1V2000h-1:SOV6000A48000IV2000h1JSR

K 2:SO6000A48000IV2000h1JSR

Importantly, the aspiration speed is set at a higher value than the dispense speed so that there will be no break in the continuous flow.

Conversion of Pumps’ Speed to the Target Flow Rate

The following proportion is used to convert between speed in volume and speed in step per second (Hz):

$$\frac{volume\ per\ second}{speed\ in\ step\ per\ second} = \frac{volume\ per\ full\ stroke}{full\ stroke\ step}$$

Volume per full stroke and full stroke steps are the volume of the syringe and the pumps’ full stroke, respectively. Therefore,

$$\frac{volume\ per\ second}{speed\ in\ step\ per\ second} = \frac{50\ \mu L}{48000\ steps}$$

APPENDIX 2 CODES USED TO SOLVE EQS. (2.9), (2.11) AND (2.18)

```
function [S_init, V_init, N] = getnumber(f,d, mass, density)
m         = mass*1e-3;
rho       = density*1e3;
sigma     = d.^2;
tau       = d.^3;
F         = f/100;
sigma_int  = linspace(min(sigma),max(sigma),500);
tau_int    = linspace(min(tau),max(tau),500);
Fsig_int   = interp1(sigma,F,sigma_int);
Ftau_int   = interp1(tau,F,tau_int);
dsigma     = sigma_int(2) - sigma_int(1);
dtau       = tau_int(2) - tau_int(1);
Vold_N     = dtau/2*(Ftau_int(1) + Ftau_int(500) + 2*sum(Ftau_int(2:499)));
N          = 6*m/(rho*pi*Vold_N);
Aold_N     = dsigma/2*(Fsig_int(1) + Fsig_int(500) + 2*sum(Fsig_int(2:499)));
S_init     = N*pi*Aold_N/4;
V_init     = N*pi*Vold_N/6;
```

```
function [d_i, V_new, S_new] = newsize(f, d, N, Delta_m, rho)
global Sinit ff Nn delm Rho di
ff         = f;
di         = d;
Delta_m    = Delta_m*1e-3;
delm       = Delta_m;
rho        = rho*1e3;
Rho        = rho;
sigma      = d.^2;
F          = f/100;
sigma_dist  = linspace(min(sigma),max(sigma),500);
Fsig_dist   = interp1(sigma,F,sigma_dist);
Ainit_N    = trapz(sigma_dist, Fsig_dist)/4;
Sinit      = N*pi*Ainit_N;
Nn         = N;
d_i        = fsolve(@RES,d/10);
sigma_i    = d_i.^2;
tau_i      = d_i.^3;
F          = f/100;
sigma_idist = linspace(min(sigma_i),max(sigma_i),500);
tau_idist   = linspace(min(tau_i),max(tau_i),500);
Fsig_idist  = interp1(sigma_i,F,sigma_idist);
Ftau_idist  = interp1(tau_i,F,tau_idist);
Anew_N     = trapz(sigma_idist, Fsig_idist)/4;
Vnew_N     = trapz(tau_idist, Ftau_idist)/6;
```

```
S_new      = N*pi*Anew_N;
V_new      = N*pi*Vnew_N;
function res = RES(d)
global Sinit delm Rho di
tau        = di.^3;
sigma      = d.^2;
K          = delm/(Sinit);
Red        = 6*K*sigma/(pi*Rho);
Comb       = max(0,tau-Red);
d_i        = Comb.^(1/3);
res        = d - d_i;
```

```
%% Example on how to use the functions
% Get size distribution (a vector d containing their diameter and another
% vector f containing the percentage of abundance of the sizes in the
% powder.

% In this description, the vector of d and f already exist in data.txt file
data = load('Data2.txt');
d = data(:,1)*1e-6; % to convert from microns to metres
f = data(:,2);

% Get initial surface area, volume and particle number
[S_init, V_init, Num] = getnumber(f, d, init_m, 2.65);

% Compute the new size, volume and surface area
[d_i, V_new, S_new] = newsize(f, d, Num, deltaM, 2.65);

% Note: the calculated surface area is in squared metres, the volume in cubic
% volume and diameter in metres.
```

APPENDIX 3 COMPUTATIONS OF MOLE PERCENT AND MASS FRACTION OF THE ELEMENTS IN MW25.

Oxide	RAM (Element)	RMM Oxide	Oxide Wt.%	No Mole Oxide (per 100g)	Mol % Oxide	No Moles of element per 100g	Element Mol%	Element mass (g)	Element mass fraction
Al_2O_3	26.982	101.96	4.3	0.04	2.75	0.08	3.97	2.28	0.023
B_2O_3	10.81	69.62	16.7	0.24	15.65	0.48	22.6	5.19	0.0523
BaO	137.34	153.34	0.52	0	0.22	0	0.16	0.47	0.0047
CeO_2	140.12	172.12	1.1	0.01	0.42	0.01	0.4	0.9	0.009
Cr_2O_3	52	152	0.64	0	0.27	0.01	0.4	0.44	0.0044
Cs_2O	132.91	281.82	1	0	0.23	0.01	0.33	0.94	0.0095
Fe_2O_3	55.85	159.7	3	0.02	1.23	0.04	1.77	2.1	0.0212
Gd_2O_3	157.25	362.5	0.1	0	0.02	0	0.03	0.09	0.0009
La_2O_3	138.91	325.82	0.56	0	0.11	0	0.16	0.48	0.0048
Li_2O	6.94	29.88	4	0.13	8.73	0.27	12.61	1.86	0.0187
MgO	24.305	40.3	4.5	0.11	7.28	0.11	5.26	2.71	0.0274
MoO_3	95.94	143.94	1.4	0.01	0.63	0.01	0.46	0.93	0.0094
Na_2O	22.9898	61.98	8.5	0.14	8.95	0.27	12.92	6.31	0.0636
Nd_2O_3	144.24	336.48	1.6	0	0.31	0.01	0.45	1.37	0.0138
NiO	58.69	74.69	0.48	0.01	0.42	0.01	0.3	0.38	0.0038
PO_4^{2-}	30.9738	94.97	0.16	0	0.11	0	0.08	0.05	0.0005
Pr_2O_3	140.91	329.82	0.52	0	0.1	0	0.15	0.44	0.0045
RuO_2	101.07	133.07	0.49	0	0.24	0	0.17	0.37	0.0038
SO_4^{2-}	32.06	96.06	0.1	0	0.07	0	0.05	0.03	0.0003
SiO_2	28.086	60.08	47.1	0.78	51.14	0.78	36.93	22.02	0.222
Sm_2O_3	150.36	348.72	0.36	0	0.07	0	0.1	0.31	0.0031
SrO	87.92	103.92	0.29	0	0.18	0	0.13	0.25	0.0025
TeO_2	127.6	159.6	0.17	0	0.07	0	0.05	0.14	0.0014
Y_2O_3	88.91	225.82	0.17	0	0.05	0	0.07	0.13	0.0014
ZrO_2	91.224	123.22	1.40	0.01	0.74	0.01	0.54	1.04	0.0105
Total			99.16	1.53	100	2.12	100.1	51.21	0.5164

APPENDIX 4 COMPUTATIONS OF UNCERTAINTIES IN THE ANALYSED MASS FRACTION OF THE ELEMENTS IN MW25.

Composition	Mass Fraction (Current Study)	Mass Fraction (Scales [2011])	Mean	Uncertainty (σ)
Al_2O_3	0.0230	0.0227	0.0228	0.000154004
B_2O_3	0.0523	0.0518	0.0521	0.000350955
BaO	0.0047	0.0047	0.0047	3.15168E-05
CeO_2	0.0090	0.0089	0.0090	6.05984E-05
Cr_2O_3	0.0044	0.0044	0.0044	2.96328E-05
Cs_2O	0.0095	0.0094	0.0095	6.38281E-05
Fe_2O_3	0.0212	0.0210	0.0211	0.000141995
Gd_2O_3	0.0009	0.0000	0.0004	0.000618678
La_2O_3	0.0048	0.0048	0.0048	3.23126E-05
Li_2O	0.0187	0.0186	0.0187	0.000125741
MgO	0.0274	0.0271	0.0272	0.000183635
MoO_3	0.0094	0.0093	0.0094	6.31466E-05
Na_2O	0.0636	0.0630	0.0633	0.000426714
Nd_2O_3	0.0138	0.0137	0.0138	9.28271E-05
NiO	0.0038	0.0038	0.0038	2.55237E-05
PO_4^{2}-	0.0005	0.0000	0.0003	0.000372115
Pr_2O_3	0.0045	0.0044	0.0045	3.00675E-05
RuO_2	0.0038	0.0037	0.0037	2.51848E-05
SO_4^{2-}	0.0003	0.0000	0.0002	0.000238006
SiO_2	0.2220	0.2199	0.2210	0.001489864
Sm_2O_3	0.0031	0.0031	0.0031	2.10081E-05
SrO	0.0025	0.0025	0.0025	1.6603E-05
TeO_2	0.0014	0.0014	0.0014	9.19744E-06
Y_2O_3	0.0014	0.0013	0.0013	9.05873E-06
ZrO_2	0.0105	0.0104	0.0104	1.78452E-05

APPENDIX 5 RAW DATA OF EXPERIMENTS MW-T_1 AND MW-T_2. EXPERIMENTAL CONDITIONS ARE: Q = 250 ML/D, T = 40 ^{o}C). CONTROL-TEST DATA IS SHOWN IN THE LOWER TABLE.

Experiment ID	Mass of tared collection bottle (g)	Mass of collection bottle with solution (g)	Initial powder mass (g)	Measured flow rate (mL/d)	Initial pH	Final pH	Duration (hour)	Li (g/mL)	B (g/mL)	Na (g/mL)	Mg (g/mL)	Al (g/mL)	Si (g/mL)	Mo (g/mL)	Cs (g/mL)
MW-T_1-1A	24.214	49.93	0.106	246.912	7.08	8.25	2.50	3.243E-08	9.484E-08	1.151E-07	4.573E-08	3.784E-08	4.300E-07	1.555E-08	1.725E-08
MW-T_1-1B	24.256	50.12		248.277		8.27	5.00	3.140E-08	9.392E-08	1.183E-07	4.704E-08	3.761E-08	4.324E-07	1.550E-08	1.669E-08
MW-T_1-1C	24.118	50.02		248.643		8.26	7.50	3.175E-08	9.348E-08	1.110E-07	4.482E-08	3.725E-08	4.257E-07	1.576E-08	1.652E-08
MW-T_1-1D	24.153	49.82		246.408		8.26	10.00	3.100E-08	9.177E-08	1.124E-07	4.771E-08	3.646E-08	4.151E-07	1.585E-08	1.607E-08
MW-T_1-2A	24.166	50.07	0.099	248.714	7.08	8.28	2.50	3.245E-08	9.495E-08	1.131E-07	5.004E-08	3.868E-08	4.310E-07	1.517E-08	1.721E-08
MW-T_1-2B	24.219	49.87		246.202		8.27	5.00	3.201E-08	9.268E-08	1.165E-07	4.852E-08	3.761E-08	4.168E-07	1.563E-08	1.712E-08
MW-T_1-2C	24.204	49.87		246.396		8.28	7.50	3.118E-08	9.431E-08	1.120E-07	4.807E-08	3.735E-08	4.022E-07	1.529E-08	1.665E-08
MW-T_1-2D	24.152	49.95		247.638		8.26	10.00	3.076E-08	9.215E-08	1.133E-07	4.955E-08	3.639E-08	4.274E-07	1.541E-08	1.604E-08
MW-T_1-3A	24.226	50.01	0.107	247.519	7.08	8.27	2.50	3.196E-08	9.570E-08	1.179E-07	5.013E-08	3.889E-08	4.343E-07	1.399E-08	1.729E-08
MW-T_1-3B	24.223	49.96		247.099		8.26	5.00	3.173E-08	9.460E-08	1.154E-07	5.033E-08	3.868E-08	4.278E-07	1.140E-08	1.665E-08
MW-T_1-3C	24.251	50.22		249.326		8.25	7.50	3.092E-08	9.224E-08	1.146E-07	4.903E-08	3.817E-08	4.365E-07	1.552E-08	1.597E-08
MW-T_1-3D	24.207	49.96		247.205		8.27	10.00	3.079E-08	9.256E-08	1.207E-07	5.007E-08	3.787E-08	4.361E-07	1.527E-08	1.567E-08
MW-T_2-1A	24.116	50.09	0.499	249.331	7.08	8.29	2.50	1.221E-07	3.465E-07	4.390E-07	1.676E-07	8.108E-08	1.369E-06	6.134E-08	7.064E-08
MW-T_2-1B	24.243	50.15		248.712		8.32	5.00	1.213E-07	3.476E-07	4.342E-07	1.630E-07	7.899E-08	1.398E-06	6.092E-08	7.019E-08
MW-T_2-1C	24.228	50.22		249.504		8.30	7.50	1.212E-07	3.371E-07	4.248E-07	1.440E-07	8.037E-08	1.377E-06	6.149E-08	6.879E-08
MW-T_2-1D	24.167	50.09		248.902		8.29	10.00	1.151E-07	3.320E-07	4.207E-07	1.467E-07	7.387E-08	1.404E-06	6.149E-08	6.820E-08
MW-T_2-2A	24.231	49.83	0.503	245.785	7.08	8.31	2.50	1.258E-07	3.352E-07	4.234E-07	1.683E-07	8.144E-08	1.211E-06	6.204E-08	6.825E-08
MW-T_2-2B	24.182	49.76		245.512		8.29	5.00	1.223E-07	3.312E-07	4.119E-07	1.699E-07	8.079E-08	1.176E-06	6.184E-08	6.791E-08
MW-T_2-2C	24.191	50.03		248.097		8.33	7.50	1.221E-07	3.367E-07	4.219E-07	1.715E-07	7.946E-08	1.354E-06	6.194E-08	6.818E-08
MW-T_2-2D	24.184	49.90		246.917		8.31	10.00	1.215E-07	3.313E-07	4.167E-07	1.677E-07	7.944E-08	1.387E-06	5.828E-08	6.540E-08
MW-T_2-3A	24.225	49.97	0.514	247.114	7.08	8.28	2.50	1.243E-07	3.383E-07	4.317E-07	1.706E-07	7.943E-08	1.399E-06	6.136E-08	6.688E-08
MW-T_2-3B	24.182	49.90		246.905		8.31	5.00	1.213E-07	3.354E-07	4.346E-07	1.684E-07	7.715E-08	1.371E-06	6.123E-08	6.755E-08
MW-T_2-3C	24.268	49.86		245.728		8.32	7.50	1.202E-07	3.346E-07	4.314E-07	1.728E-07	7.340E-08	1.382E-06	6.100E-08	6.386E-08
MW-T_2-3D	24.253	50.12		248.312		8.32	10.00	1.170E-07	3.309E-07	4.314E-07	1.669E-07	7.306E-08	1.365E-06	6.068E-08	6.362E-08

ID	Li (g/mL)	B (g/mL)	Na (g/mL)	Mg (g/mL)	Al (g/mL)	Si (g/mL)	Mo (g/mL)	Cs (g/mL)
MW-T_1-1 (Average Blank)	7.94E-10	9.50E-09	8.60E-09	3.26E-09	1.58E-10	6.47E-08	8.17E-10	3.71E-10
MW-T_1-1 (Blank 1)	9.94E-10	1.20E-08	1.01E-08	4.72E-09	1.10E-10	6.47E-08	7.35E-10	5.62E-10
MW-T_1-1 (Blank 2)	5.94E-10	7.00E-09	7.05E-09	1.79E-09	2.06E-10	6.47E-08	8.99E-10	1.80E-10
MW-T_1-2 (Average Blank)	7.18E-10	9.50E-09	1.13E-08	6.16E-09	2.46E-10	6.47E-08	7.70E-10	6.13E-10
MW-T_1-2 (Blank 1)	9.81E-10	1.20E-08	1.32E-08	8.24E-09	2.86E-10	6.47E-08	7.86E-10	8.68E-10
MW-T_1-2 (Blank 2)	4.55E-10	7.00E-09	9.43E-09	4.07E-09	2.06E-10	6.47E-08	7.54E-10	3.57E-10
MW-T_1-3 (Average Blank)	7.87E-10	9.00E-09	1.12E-08	4.56E-09	1.56E-09	6.47E-08	4.53E-10	5.66E-10
MW-T_1-3 (Blank 1)	9.81E-10	1.10E-08	1.20E-08	6.41E-09	2.91E-09	6.47E-08	4.88E-10	6.58E-10
MW-T_1-3 (Blank 2)	5.93E-10	7.00E-09	1.04E-08	2.72E-09	2.06E-10	6.47E-08	4.17E-10	4.73E-10
MW-T_2-1 (Average Blank)	6.15E-10	1.10E-08	9.24E-09	4.96E-09	2.06E-10	6.47E-08	8.09E-10	1.43E-09
MW-T_2-1 (Blank 1)	7.59E-10	1.60E-08	8.23E-09	6.80E-09	2.06E-10	6.47E-08	7.84E-10	4.74E-10
MW-T_2-1 (Blank 2)	4.70E-10	6.00E-09	1.03E-08	3.11E-09	2.06E-10	6.47E-08	8.34E-10	2.38E-09
MW-T_2-2 (Average Blank)	1.36E-09	1.05E-08	1.19E-08	8.59E-09	2.06E-10	6.47E-08	1.35E-09	6.23E-10
MW-T_2-2 (Blank 1)	1.20E-09	1.00E-08	1.14E-08	1.04E-08	2.06E-10	6.47E-08	1.32E-09	7.29E-10
MW-T_2-2(Blank 2)	1.52E-09	1.10E-08	1.24E-08	6.73E-09	2.06E-10	6.47E-08	1.38E-09	5.17E-10
MW-T_2-3 (Average Blank)	1.02E-09	1.40E-08	1.37E-08	8.35E-09	5.61E-10	6.47E-08	6.33E-10	5.62E-10
MW-T_2-3(Blank 1)	1.26E-09	1.80E-08	1.37E-08	1.10E-08	9.16E-10	6.47E-08	4.96E-10	3.54E-10
MW-T_2-3 (Blank 2)	7.79E-10	1.00E-08	1.38E-08	5.67E-09	2.06E-10	6.47E-08	7.69E-10	7.69E-10

APPENDIX 6 RAW DATA OF EXPERIMENTS MW-T_3 AND MW-T_4. EXPERIMENTAL CONDITIONS ARE: Q = 125 mL/D, T = 40 °C. CONTROL-TEST DATA IS SHOWN IN THE LOWER TABLE.

Experiment ID	Mass of tared collection bottle (g)	Mass of collection bottle with solution (g)	Initial powder mass (g)	Measured flow rate (mL/d)	Initial pH	Final pH	Duration (hour)	Li (g/mL)	B (g/mL)	Na (g/mL)	Mg (g/mL)	Al (g/mL)	Si (g/mL)	Mo (g/mL)	Cs (g/mL)
MW-T_3-1A	24.174	49.74	0.112	122.698	7.13	8.37	5.00	6.074E-08	1.780E-07	2.125E-07	8.627E-08	7.161E-08	7.717E-07	2.915E-08	3.070E-08
MW-T_3-1B	24.179	50.06		124.211		8.39	10.00	5.894E-08	1.720E-07	2.145E-07	8.507E-08	7.151E-08	7.797E-07	2.895E-08	3.140E-08
MW-T_3-1C	24.305	50.24		124.485		8.37	15.00	6.094E-08	1.760E-07	2.115E-07	8.317E-08	7.121E-08	7.737E-07	2.915E-08	3.120E-08
MW-T_3-1D	24.323	50.22		124.325		8.40	20.00	6.144E-08	1.710E-07	2.095E-07	8.257E-08	7.081E-08	7.747E-07	2.865E-08	3.050E-08
MW-T_3-2A	24.129	49.92	0.103	123.775	7.13	8.36	5.00	6.187E-08	1.780E-07	2.129E-07	9.158E-08	7.171E-08	7.777E-07	2.917E-08	3.162E-08
MW-T_3-2B	24.237	50.20		124.636		8.37	10.00	6.177E-08	1.740E-07	2.139E-07	9.108E-08	7.151E-08	7.717E-07	2.877E-08	3.142E-08
MW-T_3-2C	24.212	49.94		123.514		8.39	15.00	6.147E-08	1.790E-07	2.149E-07	9.258E-08	7.121E-08	7.747E-07	2.907E-08	3.132E-08
MW-T_3-2D	24.207	50.19		124.732		8.37	20.00	6.067E-08	1.740E-07	2.129E-07	9.178E-08	7.111E-08	7.727E-07	2.857E-08	3.112E-08
MW-T_3-3A	24.134	49.40	0.105	121.284	7.13	8.40	5.00	6.396E-08	1.755E-07	2.209E-07	9.112E-08	7.151E-08	7.797E-07	3.030E-08	3.277E-08
MW-T_3-3B	24.232	50.18		124.539		8.36	10.00	6.386E-08	1.765E-07	2.249E-07	9.022E-08	7.121E-08	7.727E-07	3.010E-08	3.257E-08
MW-T_3-3C	24.219	49.99		123.724		8.38	15.00	6.406E-08	1.745E-07	2.189E-07	9.012E-08	7.121E-08	7.767E-07	2.990E-08	3.227E-08
MW-T_3-3D	24.276	50.09		123.931		8.36	20.00	6.276E-08	1.755E-07	2.199E-07	9.112E-08	7.121E-08	7.697E-07	2.970E-08	3.187E-08
MW-T_4-1A	24.152	49.87	0.503	123.442	7.13	8.39	5.00	2.302E-07	6.090E-07	7.350E-07	2.678E-07	9.911E-08	2.245E-06	1.063E-07	1.241E-07
MW-T_4-1B	24.203	50.21		124.819		8.42	10.00	2.362E-07	6.080E-07	7.310E-07	2.648E-07	1.012E-07	2.305E-06	1.113E-07	1.221E-07
MW-T_4-1C	24.286	50.16		124.188		8.41	15.00	2.332E-07	6.110E-07	7.360E-07	2.618E-07	1.012E-07	2.285E-06	1.123E-07	1.201E-07
MW-T_4-1D	24.279	50.13		124.104		8.41	20.00	2.342E-07	6.130E-07	7.130E-07	2.628E-07	9.751E-08	2.245E-06	1.083E-07	1.241E-07
MW-T_4-2A	24.117	49.48	0.511	121.727	7.13	8.43	5.00	2.388E-07	6.165E-07	7.198E-07	2.642E-07	9.791E-08	2.315E-06	1.185E-07	1.151E-07
MW-T_4-2B	24.264	50.08		123.913		8.41	10.00	2.398E-07	6.125E-07	7.148E-07	2.622E-07	1.012E-07	2.255E-06	1.155E-07	1.131E-07
MW-T_4-2C	24.163	49.82		123.143		8.39	15.00	2.338E-07	6.095E-07	7.148E-07	2.602E-07	9.921E-08	2.245E-06	1.185E-07	1.151E-07
MW-T_4-2D	24.154	49.95		123.826		8.40	20.00	2.408E-07	6.145E-07	7.168E-07	2.552E-07	9.921E-08	2.315E-06	1.155E-07	1.121E-07
MW-T_4-3A	24.189	49.59	0.502	121.903	7.13	8.44	5.00	2.265E-07	5.945E-07	7.300E-07	2.653E-07	9.221E-08	2.195E-06	1.193E-07	1.211E-07
MW-T_4-3B	24.231	49.98		123.587		8.38	10.00	2.225E-07	5.995E-07	7.200E-07	2.623E-07	9.121E-08	2.205E-06	1.123E-07	1.201E-07
MW-T_4-3C	24.100	49.69		122.829		8.39	15.00	2.125E-07	5.932E-07	7.150E-07	2.643E-07	9.221E-08	2.205E-06	1.093E-07	1.231E-07
MW-T_4-3D	24.267	49.81		122.615		8.42	20.00	2.105E-07	5.945E-07	7.300E-07	2.643E-07	9.431E-08	1.957E-06	1.133E-07	1.201E-07

ID	Li (g/mL)	B (g/mL)	Na (g/mL)	Mg (g/mL)	Al (g/mL)	Si (g/mL)	Mo (g/mL)	Cs (g/mL)
MW-T_3-1 (Average Blank)	3.37E-10	4.00E-09	1.48E-09	7.72E-10	2.06E-10	6.47E-08	2.54E-10	9.90E-11
MW-T_3-1 (Blank 1)	4.03E-10	5.00E-09	1.29E-09	1.04E-09	2.06E-10	6.47E-08	3.23E-10	1.27E-10
MW-T_3-1 (Blank 2)	2.71E-10	3.00E-09	1.67E-09	5.01E-10	2.06E-10	6.47E-08	1.85E-10	7.10E-11
MW-T_3-2 (Average Blank)	1.68E-10	5.00E-09	1.91E-09	1.28E-09	2.06E-10	6.47E-08	2.68E-10	1.18E-10
MW-T_3-2 (Blank 1)	2.49E-10	6.00E-09	2.18E-09	1.68E-09	2.06E-10	6.47E-08	3.55E-10	1.58E-10
MW-T_3-2 (Blank 2)	8.60E-11	4.00E-09	1.63E-09	8.82E-10	2.06E-10	6.47E-08	1.80E-10	7.70E-11
MW-T_3-3 (Average Blank)	2.76E-09	1.25E-08	1.59E-08	1.22E-09	2.06E-10	6.47E-08	1.50E-09	6.69E-10
MW-T_3-3 (Blank 1)	2.45E-10	5.00E-09	4.49E-09	1.26E-09	2.06E-10	6.47E-08	4.26E-10	1.44E-10
MW-T_3-3 (Blank 2)	5.27E-09	2.00E-08	2.74E-08	1.17E-09	2.06E-10	6.47E-08	2.57E-09	1.19E-09
MW-T_4-1 (Average Blank)	2.13E-10	4.00E-09	1.98E-09	1.77E-09	2.06E-10	6.47E-08	2.92E-10	1.32E-10
MW-T_4-1 (Blank 1)	3.03E-10	5.00E-09	2.67E-09	2.50E-09	2.06E-10	6.47E-08	3.00E-10	1.86E-10
MW-T_4-1 (Blank 2)	1.23E-10	3.00E-09	1.28E-09	1.05E-09	2.06E-10	6.47E-08	2.83E-10	7.70E-11
MW-T_4-2 (Average Blank)	8.06E-10	5.50E-09	4.84E-09	1.22E-09	2.06E-10	6.47E-08	4.72E-10	1.14E-10
MW-T_4-2 (Blank 1)	9.41E-10	7.00E-09	3.94E-09	1.55E-09	2.06E-10	6.47E-08	4.75E-10	1.10E-10
MW-T_4-2(Blank 2)	6.71E-10	4.00E-09	5.73E-09	8.93E-10	2.06E-10	6.47E-08	4.68E-10	1.18E-10
MW-T_4-3 (Average Blank)	5.14E-10	3.50E-09	2.97E-09	2.32E-09	2.06E-10	6.47E-08	3.13E-10	1.36E-10
MW-T_2-3(Blank 1)	2.71E-10	4.00E-09	1.86E-09	3.62E-09	2.06E-10	6.47E-08	2.62E-10	1.21E-10
MW-T_2-3 (Blank 2)	7.56E-10	3.00E-09	4.08E-09	1.02E-09	2.06E-10	6.47E-08	3.63E-10	1.51E-10

APPENDIX 7 RAW DATA OF EXPERIMENTS MW-T_5 AND MW-T_6. EXPERIMENTAL CONDITIONS ARE: Q = 75 mL/D, T = 40 °C. CONTROL-TEST DATA IS SHOWN IN THE LOWER TABLE.

Experiment ID	Mass of tared collection bottle (g)	Mass of collection bottle with solution (g)	Initial powder mass (g)	Measured flow rate (mL/d)	Initial pH	Final pH	Duration (hour)	Li (g/mL)	B (g/mL)	Na (g/mL)	Mg (g/mL)	Al (g/mL)	Si (g/mL)	Mo (g/mL)	Cs (g/mL)
MW-T_5-1A	24.261	48.54	0.101	72.842	7.24	8.49	8.00	8.416E-08	2.215E-07	3.085E-07	1.123E-07	6.375E-08	9.677E-07	4.162E-08	4.852E-08
MW-T_5-1B	24.196	48.41		72.634		8.51	16.00	8.356E-08	2.175E-07	3.055E-07	1.113E-07	6.415E-08	9.697E-07	4.212E-08	4.662E-08
MW-T_5-1C	24.202	48.45		72.738		8.49	24.00	8.346E-08	2.155E-07	2.975E-07	1.143E-07	6.495E-08	9.447E-07	4.122E-08	4.752E-08
MW-T_5-1D	24.235	48.62		73.154		8.50	32.00	8.386E-08	2.125E-07	3.075E-07	1.113E-07	6.325E-08	9.737E-07	4.142E-08	4.702E-08
MW-T_5-2A	24.098	48.82	0.104	74.157	7.24	8.51	8.00	8.048E-08	2.380E-07	3.045E-07	1.170E-07	6.376E-08	9.567E-07	4.463E-08	4.696E-08
MW-T_5-2B	24.117	48.84		74.163		8.48	16.00	8.208E-08	2.420E-07	3.055E-07	1.140E-07	6.366E-08	9.697E-07	4.453E-08	4.836E-08
MW-T_5-2C	24.097	48.81		74.142		8.50	24.00	8.138E-08	2.420E-07	3.005E-07	1.170E-07	6.346E-08	9.797E-07	4.473E-08	4.686E-08
MW-T_5-2D	24.182	48.84		73.986		8.49	32.00	8.208E-08	2.400E-07	2.995E-07	1.150E-07	6.336E-08	9.707E-07	4.373E-08	4.666E-08
MW-T_5-3A	24.142	48.09	0.102	71.855	7.24	8.50	8.00	8.105E-08	2.370E-07	2.748E-07	1.155E-07	6.594E-08	1.003E-06	4.327E-08	4.470E-08
MW-T_5-3B	24.226	48.36		72.413		8.53	16.00	8.115E-08	2.360E-07	2.778E-07	1.185E-07	6.534E-08	9.917E-07	4.347E-08	4.420E-08
MW-T_5-3C	24.180	48.36		72.551		8.52	24.00	7.935E-08	2.400E-07	2.798E-07	1.155E-07	6.614E-08	9.817E-07	4.417E-08	4.440E-08
MW-T_5-3D	24.295	48.90		73.821		8.52	32.00	8.145E-08	2.420E-07	2.548E-07	1.175E-07	6.774E-08	9.957E-07	4.347E-08	4.530E-08
MW-T_6-1A	24.218	48.22	0.507	71.996	7.24	8.54	8.00	3.092E-07	7.590E-07	1.104E-06	2.995E-07	9.137E-08	2.295E-06	2.011E-07	1.570E-07
MW-T_6-1B	24.221	48.35		72.381		8.51	16.00	3.222E-07	7.380E-07	1.094E-06	3.015E-07	9.137E-08	2.445E-06	1.971E-07	1.560E-07
MW-T_6-1C	24.187	48.32		72.405		8.55	24.00	3.272E-07	7.610E-07	1.094E-06	3.025E-07	9.147E-08	2.495E-06	1.951E-07	1.670E-07
MW-T_6-1D	24.166	48.68		73.552		8.54	32.00	3.322E-07	7.320E-07	1.114E-06	3.015E-07	9.177E-08	2.565E-06	2.011E-07	1.760E-07
MW-T_6-2A	24.255	48.56	0.510	72.903	7.24	8.53	8.00	3.142E-07	7.150E-07	1.105E-06	2.931E-07	9.749E-08	2.695E-06	1.892E-07	1.741E-07
MW-T_6-2B	24.212	48.88		74.005		8.56	16.00	3.172E-07	7.140E-07	1.115E-06	2.726E-07	9.599E-08	2.715E-06	1.687E-07	1.781E-07
MW-T_6-2C	24.262	48.92		73.971		8.53	24.00	3.072E-07	7.140E-07	1.085E-06	2.929E-07	9.429E-08	2.665E-06	1.852E-07	1.761E-07
MW-T_6-2D	24.077	48.39		72.936		8.55	32.00	3.222E-07	7.030E-07	1.095E-06	2.854E-07	9.539E-08	2.715E-06	1.862E-07	1.821E-07
MW-T_6-3A	24.101	48.80	0.507	74.092	7.24	8.51	8.00	3.183E-07	7.250E-07	9.945E-07	3.096E-07	9.795E-08	2.625E-06	1.943E-07	1.791E-07
MW-T_6-3B	24.239	48.92		74.041		8.58	16.00	3.093E-07	7.320E-07	9.915E-07	3.156E-07	9.495E-08	2.715E-06	1.933E-07	1.821E-07
MW-T_6-3C	24.177	48.38		72.596		8.54	24.00	3.193E-07	7.460E-07	1.003E-06	3.096E-07	9.565E-08	2.615E-06	1.943E-07	1.831E-07
MW-T_6-3D	24.207	48.89		74.062		8.57	32.00	3.143E-07	7.180E-07	1.094E-06	3.096E-07	9.865E-08	2.655E-06	2.003E-07	1.791E-07

ID	Li (g/mL)	B (g/mL)	Na (g/mL)	Mg (g/mL)	Al (g/mL)	Si (g/mL)	Mo (g/mL)	Cs (g/mL)
MW-T_5-1 (Average Blank)	1.56E-09	6.50E-09	8.53E-09	1.33E-09	5.53E-10	6.47E-08	2.19E-10	5.19E-10
MW-T_5-1 (Blank 1)	2.87E-09	8.00E-09	1.48E-08	2.19E-09	9.88E-10	6.47E-08	3.06E-10	9.89E-10
MW-T_5-1 (Blank 2)	2.56E-10	5.00E-09	2.31E-09	4.64E-10	1.17E-10	6.47E-08	1.31E-10	4.90E-11
MW-T_5-2 (Average Blank)	3.75E-10	7.00E-09	5.47E-09	3.03E-09	4.56E-10	6.47E-08	5.30E-10	4.64E-10
MW-T_5-2 (Blank 1)	4.22E-10	8.00E-09	4.82E-09	3.13E-09	8.78E-10	6.47E-08	2.40E-10	7.70E-10
MW-T_5-2 (Blank 2)	3.28E-10	6.00E-09	6.11E-09	2.94E-09	3.40E-11	6.47E-08	8.19E-10	1.57E-10
MW-T_5-3 (Average Blank)	4.53E-10	7.00E-09	5.75E-09	3.46E-09	8.41E-10	6.47E-08	2.72E-10	6.00E-10
MW-T_5-3 (Blank 1)	4.26E-10	8.00E-09	6.83E-09	2.26E-09	4.94E-10	6.47E-08	2.40E-10	3.72E-10
MW-T_5-3 (Blank 2)	4.80E-10	6.00E-09	4.68E-09	4.65E-09	1.19E-09	6.47E-08	3.03E-10	8.28E-10
MW-T_6-1 (Average Blank)	2.19E-10	6.00E-09	3.80E-09	1.47E-09	4.66E-10	6.47E-08	1.31E-10	4.65E-11
MW-T_6-1 (Blank 1)	3.01E-10	7.00E-09	5.44E-09	1.84E-09	8.40E-10	6.47E-08	1.31E-10	6.00E-11
MW-T_6-1 (Blank 2)	1.37E-10	5.00E-09	2.17E-09	1.11E-09	9.10E-11	6.47E-08	1.30E-10	3.30E-11
MW-T_6-2 (Average Blank)	1.94E-10	5.00E-09	4.93E-09	2.44E-09	6.89E-10	6.47E-08	2.56E-10	8.50E-11
MW-T_6-2 (Blank 1)	2.52E-10	6.00E-09	6.41E-09	4.12E-09	6.10E-10	6.47E-08	1.95E-10	1.08E-10
MW-T_6-2(Blank 2)	1.35E-10	4.00E-09	3.45E-09	7.54E-10	7.68E-10	6.47E-08	3.16E-10	6.20E-11
MW-T_6-3 (Average Blank)	3.06E-10	6.00E-09	4.35E-09	3.56E-09	4.25E-09	6.47E-08	2.95E-10	1.33E-10
MW-T_6-3(Blank 1)	3.57E-10	7.00E-09	4.12E-09	3.81E-09	8.26E-09	6.47E-08	1.94E-10	1.60E-10
MW-T_6-3 (Blank 2)	2.55E-10	5.00E-09	4.58E-09	3.30E-09	2.44E-10	6.47E-08	3.95E-10	1.05E-10

APPENDIX 8 RAW DATA OF EXPERIMENTS MW-T_7 AND MW-T_8. EXPERIMENTAL CONDITIONS ARE: Q = 50 mL/D, T = 40 °C. CONTROL-TEST DATA IS SHOWN IN THE LOWER TABLE.

Experiment ID	Mass of tared collection bottle (g)	Mass of collection bottle with solution (g)	Initial powder mass (g)	Measured flow rate (mL/d)	Initial pH	Final pH	Duration (hour)	Li (g/mL)	B (g/mL)	Na (g/mL)	Mg (g/mL)	Al (g/mL)	Si (g/mL)	Mo (g/mL)	Cs (g/mL)
MW-T_7-1A	24.141	73.01	0.112	48.873	7.22	8.51	24.00	1.699E-07	4.508E-07	5.818E-07	2.384E-07	1.939E-07	2.035E-06	7.195E-08	8.282E-08
MW-T_7-1B	24.284	73.52		49.235		8.54	48.00	1.634E-07	4.538E-07	5.858E-07	2.374E-07	2.019E-07	2.045E-06	7.305E-08	8.402E-08
MW-T_7-1C	24.126	73.15		49.019		8.54	72.00	1.624E-07	4.538E-07	5.578E-07	2.374E-07	1.959E-07	1.975E-06	7.045E-08	8.502E-08
MW-T_7-1D	24.130	74.04		49.911		8.56	96.00	1.644E-07	4.588E-07	5.728E-07	2.374E-07	1.959E-07	2.045E-06	7.325E-08	8.452E-08
MW-T_7-2A	24.175	74.07	0.102	49.892	7.22	8.52	24.00	1.482E-07	4.443E-07	5.792E-07	2.364E-07	1.919E-07	1.795E-06	7.803E-08	8.202E-08
MW-T_7-2B	24.254	72.71		48.451		8.51	48.00	1.462E-07	4.483E-07	5.802E-07	2.454E-07	1.654E-07	1.795E-06	7.813E-08	8.192E-08
MW-T_7-2C	24.252	72.06		47.805		8.48	72.00	1.452E-07	4.413E-07	5.782E-07	2.344E-07	1.994E-07	1.685E-06	7.493E-08	8.232E-08
MW-T_7-2D	24.200	73.17		48.968		8.51	96.00	1.522E-07	4.603E-07	5.792E-07	2.454E-07	2.004E-07	2.035E-06	7.523E-08	8.202E-08
MW-T_7-3A	24.221	73.21	0.106	48.992	7.22	8.56	24.00	1.643E-07	4.389E-07	5.234E-07	2.275E-07	2.012E-07	2.035E-06	7.556E-08	8.199E-08
MW-T_7-3B	24.193	72.99		48.795		8.53	48.00	1.593E-07	4.335E-07	5.094E-07	2.245E-07	1.982E-07	2.005E-06	7.396E-08	8.019E-08
MW-T_7-3C	24.163	72.93		48.763		8.56	72.00	1.633E-07	4.249E-07	5.194E-07	2.221E-07	2.022E-07	2.025E-06	7.506E-08	8.179E-08
MW-T_7-3D	24.159	73.05		48.890		8.53	96.00	1.633E-07	4.299E-07	5.114E-07	2.254E-07	1.942E-07	2.045E-06	7.656E-08	8.209E-08
MW-T_8-1A	24.187	73.73	0.503	49.541	7.22	8.59	24.00	5.507E-07	1.662E-06	1.854E-06	7.592E-07	3.452E-07	6.425E-06	2.963E-07	2.945E-07
MW-T_8-1B	24.286	74.07		49.788		8.61	48.00	5.517E-07	1.612E-06	1.844E-06	7.722E-07	3.462E-07	6.535E-06	3.023E-07	3.025E-07
MW-T_8-1C	24.191	74.10		49.912		8.57	72.00	5.597E-07	1.672E-06	1.834E-06	7.642E-07	3.532E-07	6.455E-06	2.983E-07	2.988E-07
MW-T_8-1D	24.199	73.92		49.725		8.61	96.00	5.507E-07	1.682E-06	1.814E-06	7.792E-07	3.562E-07	6.685E-06	3.103E-07	3.025E-07
MW-T_8-2A	24.248	73.25	0.501	49.003	7.22	8.62	24.00	6.011E-07	1.451E-06	2.044E-06	7.291E-07	3.562E-07	6.195E-06	3.022E-07	3.251E-07
MW-T_8-2B	24.207	73.10		48.892		8.61	48.00	6.061E-07	1.481E-06	1.964E-06	7.241E-07	3.492E-07	6.365E-06	3.102E-07	3.311E-07
MW-T_8-2C	24.139	72.48		48.341		8.58	72.00	5.881E-07	1.531E-06	2.034E-06	7.431E-07	3.442E-07	6.175E-06	3.062E-07	3.241E-07
MW-T_8-2D	24.171	73.40		49.226		8.63	96.00	5.911E-07	1.491E-06	2.004E-06	7.451E-07	3.432E-07	6.365E-06	3.042E-07	3.231E-07
MW-T_8-3A	24.266	72.26	0.509	47.997	7.22	8.60	24.00	6.083E-07	1.704E-06	1.952E-06	7.728E-07	3.343E-07	6.245E-06	2.805E-07	3.282E-07
MW-T_8-3B	24.177	72.18		48.003		8.67	48.00	5.893E-07	1.704E-06	1.972E-06	7.838E-07	3.263E-07	6.435E-06	2.795E-07	3.232E-07
MW-T_8-3C	24.238	72.46		48.217		8.64	72.00	6.103E-07	1.684E-06	2.002E-06	7.618E-07	3.233E-07	6.305E-06	2.845E-07	3.232E-07
MW-T_8-3D	24.121	72.53		48.413		8.61	96.00	6.113E-07	1.674E-06	2.022E-06	7.668E-07	3.283E-07	6.495E-06	2.745E-07	3.172E-07

ID	Li (g/mL)	B (g/mL)	Na (g/mL)	Mg (g/mL)	Al (g/mL)	Si (g/mL)	Mo (g/mL)	Cs (g/mL)
MW-T_7-1 (Average Blank)	1.43E-09	1.85E-09	5.77E-09	2.42E-09	8.67E-10	6.47E-08	3.51E-10	7.16E-10
MW-T_7-1 (Blank 1)	2.30E-09	2.84E-09	8.61E-09	3.01E-09	1.22E-09	6.47E-08	5.09E-10	1.15E-09
MW-T_7-1 (Blank 2)	5.66E-10	8.54E-10	2.94E-09	1.82E-09	5.15E-10	6.47E-08	1.92E-10	2.77E-10
MW-T_7-2 (Average Blank)	1.69E-10	2.31E-09	3.23E-09	1.39E-09	4.39E-09	6.47E-08	1.35E-10	1.18E-10
MW-T_7-2 (Blank 1)	1.30E-10	2.62E-09	2.98E-09	1.49E-10	1.17E-10	6.47E-08	1.77E-10	8.97E-11
MW-T_7-2 (Blank 2)	2.09E-10	2.01E-09	3.47E-09	2.64E-09	8.67E-09	6.47E-08	9.27E-11	1.47E-10
MW-T_7-3 (Average Blank)	3.15E-10	1.29E-08	4.36E-09	5.27E-10	2.32E-10	6.47E-08	3.55E-10	1.90E-10
MW-T_7-3 (Blank 1)	3.72E-10	2.28E-08	3.98E-09	1.93E-10	3.25E-10	6.47E-08	3.32E-10	2.17E-10
MW-T_7-3 (Blank 2)	2.58E-10	2.90E-09	4.75E-09	8.60E-10	1.39E-10	6.47E-08	3.79E-10	1.64E-10
MW-T_8-1 (Average Blank)	7.00E-10	1.96E-09	4.19E-09	1.65E-10	1.93E-10	6.47E-08	3.42E-10	4.54E-10
MW-T_8-1 (Blank 1)	2.77E-10	1.97E-09	3.54E-09	1.02E-10	1.00E-10	6.47E-08	2.71E-10	2.00E-10
MW-T_8-1 (Blank 2)	1.12E-09	1.94E-09	4.84E-09	2.27E-10	2.86E-10	6.47E-08	4.14E-10	7.08E-10
MW-T_8-2 (Average Blank)	1.28E-10	9.02E-10	4.26E-09	1.46E-10	1.85E-10	6.47E-08	1.85E-10	1.00E-10
MW-T_8-2 (Blank 1)	1.27E-10	1.37E-09	4.40E-09	1.48E-10	1.95E-10	6.47E-08	1.77E-10	9.86E-11
MW-T_8-2(Blank 2)	1.28E-10	4.30E-10	4.12E-09	1.44E-10	1.75E-10	6.47E-08	1.93E-10	1.02E-10
MW-T_8-3 (Average Blank)	3.02E-10	4.03E-09	1.83E-09	8.46E-10	2.54E-10	6.47E-08	5.14E-10	2.00E-10
MW-T_8-3(Blank 1)	3.34E-10	7.85E-09	2.22E-09	1.66E-09	1.68E-10	6.47E-08	7.87E-10	2.23E-10
MW-T_8-3 (Blank 2)	2.70E-10	1.99E-10	1.44E-09	2.68E-11	3.41E-10	6.47E-08	2.40E-10	1.77E-10

APPENDIX 9 RAW DATA OF EXPERIMENTS MW-T_9 AND MW-T_10. EXPERIMENTAL CONDITIONS ARE: Q = 25 mL/D, T = 40 °C. CONTROL-TEST DATA IS SHOWN IN THE LOWER TABLE.

Experiment ID	Mass of tared collection bottle (g)	Mass of collection bottle with solution (g)	Initial powder mass (g)	Measured flow rate (mL/d)	Initial pH	Final pH	Duration (hour)	Li (g/mL)	B (g/mL)	Na (g/mL)	Mg (g/mL)	Al (g/mL)	Si (g/mL)	Mo (g/mL)	Cs (g/mL)
MW-T_9-1A	24.132	74.12	0.107	24.992	6.91	8.53	48.00	3.102E-07	8.536E-07	1.021E-06	3.870E-07	2.972E-07	3.265E-06	1.431E-07	1.530E-07
MW-T_9-1B	24.247	74.22		24.985		8.53	96.00	2.972E-07	8.276E-07	1.041E-06	3.855E-07	2.942E-07	3.275E-06	1.461E-07	1.550E-07
MW-T_9-1C	24.148	73.75		24.801		8.55	144.00	3.072E-07	8.456E-07	1.061E-06	3.960E-07	2.942E-07	3.245E-06	1.451E-07	1.560E-07
MW-T_9-1D	24.200	73.95		24.873		8.53	192.00	3.042E-07	8.656E-07	1.031E-06	3.876E-07	3.002E-07	3.265E-06	1.421E-07	1.580E-07
MW-T_9-2A	24.228	71.42	0.108	23.598	6.91	8.56	48.00	2.794E-07	7.638E-07	9.916E-07	4.232E-07	3.101E-07	3.575E-06	1.462E-07	1.583E-07
MW-T_9-2B	24.214	72.97		24.379		8.52	96.00	2.734E-07	7.898E-07	9.826E-07	4.342E-07	3.151E-07	3.495E-06	1.412E-07	1.523E-07
MW-T_9-2C	24.248	71.81		23.783		8.55	144.00	2.804E-07	7.848E-07	9.846E-07	4.352E-07	3.081E-07	3.575E-06	1.422E-07	1.563E-07
MW-T_9-2D	24.151	71.88		23.865		8.51	192.00	2.874E-07	7.838E-07	9.935E-07	4.282E-07	3.111E-07	3.565E-06	1.412E-07	1.563E-07
MW-T_9-3A	24.165	71.40	0.112	23.619	6.91	8.51	48.00	3.031E-07	8.466E-07	1.071E-06	4.180E-07	3.151E-07	3.545E-06	1.371E-07	1.370E-07
MW-T_9-3B	24.088	72.58		24.244		8.54	96.00	3.071E-07	8.486E-07	1.061E-06	4.280E-07	3.211E-07	3.505E-06	1.371E-07	1.340E-07
MW-T_9-3C	24.157	73.77		24.805		8.53	144.00	3.001E-07	8.436E-07	1.031E-06	4.230E-07	3.101E-07	3.495E-06	1.321E-07	1.450E-07
MW-T_9-3D	24.158	72.15		23.995		8.53	192.00	2.991E-07	8.286E-07	1.041E-06	4.360E-07	3.191E-07	3.455E-06	1.381E-07	1.520E-07
MW-T_10-1A	24.262	73.87	0.507	24.805	6.91	8.56	48.00	1.010E-06	2.888E-06	3.501E-06	1.130E-06	3.641E-07	9.335E-06	4.881E-07	5.141E-07
MW-T_10-1B	24.112	74.10		24.996		8.59	96.00	1.030E-06	2.928E-06	3.541E-06	1.130E-06	3.691E-07	9.405E-06	4.841E-07	5.091E-07
MW-T_10-1C	24.159	74.16		24.998		8.57	144.00	1.000E-06	2.878E-06	3.591E-06	1.160E-06	3.651E-07	9.455E-06	4.821E-07	5.171E-07
MW-T_10-1D	24.089	73.99		24.952		8.57	192.00	1.010E-06	2.868E-06	3.541E-06	1.120E-06	3.701E-07	9.735E-06	4.801E-07	5.171E-07
MW-T_10-2A	24.263	71.97	0.513	23.852	6.91	8.55	48.00	9.893E-07	2.820E-06	3.362E-06	1.150E-06	3.941E-07	9.415E-06	5.121E-07	5.051E-07
MW-T_10-2B	24.274	74.03		24.877		8.59	96.00	9.963E-07	2.800E-06	3.292E-06	1.110E-06	4.001E-07	9.285E-06	5.171E-07	5.191E-07
MW-T_10-2C	24.188	71.56		23.685		8.57	144.00	9.933E-07	2.910E-06	3.252E-06	1.120E-06	3.861E-07	9.165E-06	5.221E-07	5.141E-07
MW-T_10-2D	24.122	71.93		23.904		8.58	192.00	9.923E-07	2.910E-06	3.342E-06	1.150E-06	3.971E-07	9.485E-06	5.011E-07	5.231E-07
MW-T_10-3A	24.226	71.48	0.503	23.627	6.91	8.61	48.00	1.030E-06	2.654E-06	3.512E-06	1.020E-06	3.952E-07	9.255E-06	5.001E-07	5.450E-07
MW-T_10-3B	24.114	71.52		23.705		8.54	96.00	1.030E-06	2.624E-06	3.622E-06	1.040E-06	3.882E-07	9.265E-06	5.031E-07	5.350E-07
MW-T_10-3C	24.226	74.03		24.902		8.56	144.00	1.060E-06	2.654E-06	3.602E-06	1.030E-06	3.962E-07	9.065E-06	5.061E-07	5.420E-07
MW-T_10-3D	24.137	73.89		24.877		8.58	192.00	1.040E-06	2.724E-06	3.552E-06	1.100E-06	3.852E-07	9.125E-06	5.011E-07	5.230E-07

ID	Li (g/mL)	B (g/mL)	Na (g/mL)	Mg (g/mL)	Al (g/mL)	Si (g/mL)	Mo (g/mL)	Cs (g/mL)
MW-T_9-1 (Average Blank)	1.93E-10	7.60E-09	1.45E-09	2.25E-11	1.62E-10	6.47E-08	1.00E-10	2.71E-11
MW-T_9-1 (Blank 1)	2.41E-10	7.60E-09	1.37E-09	4.49E-11	2.50E-10	6.47E-08	1.11E-10	3.24E-11
MW-T_9-1 (Blank 2)	1.45E-10	7.60E-09	1.53E-09	0.00E+00	7.44E-11	6.47E-08	9.00E-11	2.19E-11
MW-T_9-2 (Average Blank)	4.11E-10	8.32E-10	2.53E-09	1.91E-10	1.28E-10	6.47E-08	2.31E-10	2.59E-10
MW-T_9-2 (Blank 1)	5.40E-10	3.07E-10	1.97E-09	3.81E-10	2.25E-10	6.47E-08	3.66E-10	3.47E-10
MW-T_9-2 (Blank 2)	2.83E-10	1.36E-09	3.09E-09	0.00E+00	3.13E-11	6.47E-08	9.53E-11	1.71E-10
MW-T_9-3 (Average Blank)	7.75E-11	7.60E-09	1.21E-09	0.00E+00	1.05E-10	6.47E-08	1.21E-10	4.84E-11
MW-T_9-3 (Blank 1)	8.68E-11	7.60E-09	1.10E-09	0.00E+00	1.34E-10	6.47E-08	1.34E-10	5.08E-11
MW-T_9-3 (Blank 2)	6.82E-11	7.60E-09	1.31E-09	0.00E+00	7.72E-11	6.47E-08	1.07E-10	4.59E-11
MW-T_10-1 (Average Blank)	6.95E-11	7.60E-09	1.22E-09	2.09E-11	1.24E-10	6.47E-08	1.08E-10	5.27E-11
MW-T_10-1 (Blank 1)	8.34E-11	7.60E-09	1.09E-09	4.17E-11	1.31E-10	6.47E-08	1.21E-10	6.38E-11
MW-T_10-1 (Blank 2)	5.57E-11	7.60E-09	1.36E-09	0.00E+00	1.18E-10	6.47E-08	9.47E-11	4.17E-11
MW-T_10-2 (Average Blank)	1.60E-10	4.59E-10	1.92E-09	0.00E+00	7.02E-11	6.47E-08	1.08E-10	5.51E-11
MW-T_10-2 (Blank 1)	2.06E-10	4.93E-10	2.21E-09	0.00E+00	8.40E-11	6.47E-08	1.16E-10	5.08E-11
MW-T_10-2(Blank 2)	1.15E-10	4.25E-10	1.62E-09	0.00E+00	5.65E-11	6.47E-08	1.00E-10	5.94E-11
MW-T_10-3 (Average Blank)	8.03E-11	4.14E-09	2.00E-09	2.58E-10	2.34E-10	6.47E-08	1.13E-10	4.49E-11
MW-T_10-3(Blank 1)	1.11E-10	6.72E-10	2.01E-09	4.73E-10	3.13E-10	6.47E-08	1.48E-10	6.12E-11
MW-T_10-3 (Blank 2)	4.95E-11	7.60E-09	1.98E-09	4.27E-11	1.55E-10	6.47E-08	7.78E-11	2.85E-11

APPENDIX 10 RAW DATA OF EXPERIMENTS MW-T_11 AND MW-T_12. EXPERIMENTAL CONDITIONS ARE: Q = 10 mL/d, T = 40 ^{o}C. CONTROL-TEST DATA IS SHOWN IN THE LOWER TABLE.

Experiment ID	Mass of tared collection bottle (g)	Mass of collection bottle with solution (g)	Initial powder mass (g)	Measured flow rate (mL/d)	Initial pH	Final pH	Duration (hour)	Li (g/mL)	B (g/mL)	Na (g/mL)	Mg (g/mL)	Al (g/mL)	Si (g/mL)	Mo (g/mL)	Cs (g/mL)
MW-T_11-1A	24.603	54.56	0.110	9.984	7.10	8.68	72.00	6.022E-07	1.492E-06	1.875E-06	8.401E-07	2.972E-07	6.545E-06	3.101E-07	3.338E-07
MW-T_11-1B	24.713	54.58		9.956		8.72	144.00	5.982E-07	1.432E-06	1.795E-06	8.341E-07	2.942E-07	6.485E-06	3.051E-07	3.338E-07
MW-T_11-1C	24.565	54.49		9.975		8.69	216.00	5.962E-07	1.512E-06	1.705E-06	8.021E-07	3.012E-07	6.555E-06	3.081E-07	3.218E-07
MW-T_11-1D	24.669	54.11		9.813		8.70	288.00	5.872E-07	1.512E-06	1.765E-06	8.091E-07	2.952E-07	6.505E-06	3.071E-07	3.278E-07
MW-T_11-2A	24.585	54.41	0.107	9.942	7.10	8.71	72.00	6.125E-07	1.646E-06	1.931E-06	8.159E-07	3.033E-07	6.325E-06	3.215E-07	3.108E-07
MW-T_11-2B	24.674	54.48		9.934		8.73	144.00	6.075E-07	1.626E-06	1.891E-06	8.129E-07	3.123E-07	6.305E-06	3.145E-07	3.068E-07
MW-T_11-2C	24.560	54.13		9.857		8.70	216.00	6.015E-07	1.626E-06	1.911E-06	8.309E-07	3.073E-07	6.295E-06	3.145E-07	3.128E-07
MW-T_11-2D	24.701	54.09		9.796		8.69	288.00	5.955E-07	1.596E-06	1.971E-06	8.419E-07	3.073E-07	6.435E-06	3.155E-07	3.018E-07
MW-T_11-3A	24.740	54.56	0.104	9.939	7.10	8.73	72.00	5.887E-07	1.651E-06	1.955E-06	8.791E-07	3.203E-07	6.605E-06	3.096E-07	3.095E-07
MW-T_11-3B	24.691	54.63		9.978		8.70	144.00	5.827E-07	1.631E-06	1.885E-06	8.711E-07	3.143E-07	6.555E-06	3.046E-07	3.175E-07
MW-T_11-3C	24.709	54.69		9.993		8.72	216.00	5.457E-07	1.651E-06	1.945E-06	8.631E-07	3.123E-07	6.485E-06	3.136E-07	3.205E-07
MW-T_11-3D	24.685	54.09		9.802		8.73	288.00	5.427E-07	1.631E-06	1.955E-06	8.771E-07	3.123E-07	6.535E-06	3.276E-07	3.235E-07
MW-T_12-1A	24.623	54.55	0.501	9.975	7.10	8.78	72.00	3.031E-06	8.424E-06	1.090E-05	4.202E-06	2.932E-06	3.436E-05	1.470E-06	1.270E-06
MW-T_12-1B	24.734	54.70		9.987		8.76	144.00	3.021E-06	8.334E-06	1.080E-05	4.152E-06	2.902E-06	3.416E-05	1.520E-06	1.260E-06
MW-T_12-1C	24.605	54.52		9.972		8.77	216.00	3.071E-06	8.404E-06	1.080E-05	4.202E-06	3.002E-06	3.506E-05	1.460E-06	1.290E-06
MW-T_12-1D	24.644	54.13		9.829		8.76	288.00	2.961E-06	8.474E-06	1.090E-05	4.032E-06	2.902E-06	3.526E-05	1.550E-06	1.280E-06
MW-T_12-2A	24.645	54.56	0.503	9.972	7.10	8.77	72.00	3.141E-06	8.481E-06	1.070E-05	4.020E-06	2.980E-06	3.266E-05	1.620E-06	1.101E-06
MW-T_12-2B	24.604	54.59		9.996		8.75	144.00	3.011E-06	8.311E-06	1.100E-05	4.030E-06	2.950E-06	3.196E-05	1.550E-06	1.091E-06
MW-T_12-2C	24.712	54.65		9.979		8.78	216.00	3.101E-06	8.341E-06	1.100E-05	4.120E-06	2.930E-06	3.186E-05	1.550E-06	1.191E-06
MW-T_12-2D	24.637	54.58		9.981		8.77	288.00	3.141E-06	8.331E-06	1.090E-05	4.080E-06	2.990E-06	3.256E-05	1.540E-06	1.271E-06
MW-T_12-3A	24.628	54.56	0.497	9.977	7.10	8.78	72.00	3.030E-06	8.588E-06	1.050E-05	4.040E-06	2.740E-06	3.316E-05	1.560E-06	1.270E-06
MW-T_12-3B	24.698	54.65		9.984		8.76	144.00	3.020E-06	8.678E-06	1.020E-05	4.170E-06	2.710E-06	3.396E-05	1.540E-06	1.250E-06
MW-T_12-3C	24.750	54.71		9.986		8.76	216.00	3.000E-06	8.538E-06	1.040E-05	4.090E-06	2.800E-06	3.456E-05	1.590E-06	1.280E-06
MW-T_12-3D	24.627	53.98		9.783		8.79	288.00	3.040E-06	8.478E-06	1.050E-05	4.190E-06	2.900E-06	3.396E-05	1.580E-06	1.300E-06

ID	Li (g/mL)	B (g/mL)	Na (g/mL)	Mg (g/mL)	Al (g/mL)	Si (g/mL)	Mo (g/mL)	Cs (g/mL)
MW-T_11-1 (Average Blank)	1.20E-09	2.27E-09	4.67E-09	5.50E-11	2.12E-10	6.47E-08	1.09E-09	7.89E-10
MW-T_11-1 (Blank 1)	1.30E-09	2.69E-09	5.65E-09	1.10E-10	3.88E-10	6.47E-08	1.27E-09	8.51E-10
MW-T_11-1 (Blank 2)	1.09E-09	1.85E-09	3.69E-09	0.00E+00	3.61E-11	6.47E-08	9.09E-10	7.28E-10
MW-T_11-2 (Average Blank)	2.45E-09	6.45E-09	1.08E-08	2.88E-09	3.00E-10	6.47E-08	1.55E-09	1.81E-09
MW-T_11-2 (Blank 1)	2.58E-09	6.54E-09	1.07E-08	6.56E-10	1.43E-10	6.47E-08	1.72E-09	1.98E-09
MW-T_11-2 (Blank 2)	2.32E-09	6.37E-09	1.08E-08	5.10E-09	4.58E-10	6.47E-08	1.38E-09	1.64E-09
MW-T_11-3 (Average Blank)	7.33E-10	1.23E-09	4.90E-09	9.68E-11	3.30E-10	6.47E-08	6.35E-10	5.40E-10
MW-T_11-3 (Blank 1)	7.72E-10	1.56E-09	5.03E-09	1.83E-10	1.53E-10	6.47E-08	6.83E-10	5.77E-10
MW-T_11-3 (Blank 2)	6.93E-10	8.96E-10	4.77E-09	1.07E-11	5.06E-10	6.47E-08	5.87E-10	5.03E-10
MW-T_12-1 (Average Blank)	5.88E-10	4.08E-09	2.89E-09	1.78E-09	2.30E-09	6.47E-08	2.28E-10	3.30E-10
MW-T_12-1 (Blank 1)	7.60E-10	5.60E-10	3.57E-09	2.24E-09	3.33E-09	6.47E-08	2.53E-10	4.41E-10
MW-T_12-1 (Blank 2)	4.16E-10	7.60E-09	2.22E-09	1.32E-09	1.28E-09	6.47E-08	2.03E-10	2.19E-10
MW-T_12-2 (Average Blank)	8.55E-10	1.23E-09	3.75E-09	3.45E-10	4.31E-10	6.47E-08	4.62E-10	6.48E-10
MW-T_12-2 (Blank 1)	9.98E-10	1.54E-09	4.34E-09	4.81E-10	4.24E-10	6.47E-08	5.07E-10	7.38E-10
MW-T_12-2(Blank 2)	7.12E-10	9.14E-10	3.16E-09	2.10E-10	4.38E-10	6.47E-08	4.17E-10	5.58E-10
MW-T_12-3 (Average Blank)	2.18E-10	7.60E-09	1.19E-09	3.10E-10	3.56E-10	6.47E-08	2.65E-10	1.81E-10
MW-T_12-3(Blank 1)	2.63E-10	7.60E-09	1.45E-09	2.30E-10	5.48E-10	6.47E-08	2.75E-10	2.07E-10
MW-T_12-3 (Blank 2)	1.74E-10	7.60E-09	9.24E-10	3.90E-10	1.65E-10	6.47E-08	2.54E-10	1.55E-10

APPENDIX 11 RAW DATA OF EXPERIMENTS MW-T_13 AND MW-T_14. EXPERIMENTAL CONDITIONS ARE: Q = 250 ML/D, T = 90 ^{O}C. CONTROL-TEST DATA IS SHOWN IN THE LOWER TABLE.

Experiment ID	Mass of tared collection bottle (g)	Mass of collection bottle with solution (g)	Initial powder mass (g)	Measured flow rate (mL/d)	Initial pH	Final pH	Duration (hour)	Li (g/mL)	B (g/mL)	Na (g/mL)	Mg (g/mL)	Al (g/mL)	Si (g/mL)	Mo (g/mL)	Cs (g/mL)
MW-T_13-1A	24.839	50.14	0.098	242.9	7.12	8.20	2.50	3.005E-07	7.495E-07	1.026E-06	4.212E-07	4.671E-07	3.616E-06	1.428E-07	1.645E-07
MW-T_13-1B	24.483	76.55		249.9		8.22	5.00	3.045E-07	7.605E-07	1.048E-06	4.122E-07	4.561E-07	3.596E-06	1.418E-07	1.625E-07
MW-T_13-1C	24.608	101.61		246.4		8.21	7.50	3.075E-07	7.595E-07	1.028E-06	4.192E-07	4.561E-07	3.596E-06	1.448E-07	1.695E-07
MW-T_13-1D	24.596	128.05		248.3		8.24	10.00	3.125E-07	7.965E-07	1.048E-06	4.092E-07	4.601E-07	3.586E-06	1.488E-07	1.675E-07
MW-T_13-2A	24.606	50.24	0.099	246.1	7.12	8.23	2.50	3.164E-07	8.610E-07	1.085E-06	4.955E-07	3.702E-07	3.950E-06	1.398E-07	1.728E-07
MW-T_13-2B	24.362	75.42		245.1		8.22	5.00	3.174E-07	8.590E-07	1.119E-06	4.925E-07	3.912E-07	3.930E-06	1.418E-07	1.748E-07
MW-T_13-2C	24.649	101.62		246.3		8.21	7.50	3.184E-07	8.830E-07	1.099E-06	5.035E-07	3.902E-07	3.880E-06	1.398E-07	1.758E-07
MW-T_13-2D	24.424	128.42		249.6		8.25	10.00	3.224E-07	8.560E-07	1.086E-06	5.085E-07	3.822E-07	3.970E-06	1.468E-07	1.718E-07
MW-T_13-3A	24.574	50.12	0.139	245.2	7.12	8.19	2.50	2.859E-07	8.240E-07	1.140E-06	4.595E-07	4.060E-07	3.220E-06	1.469E-07	1.484E-07
MW-T_13-3B	24.606	76.65		249.8		8.21	5.00	2.799E-07	8.300E-07	1.007E-06	4.445E-07	4.110E-07	3.270E-06	1.499E-07	1.444E-07
MW-T_13-3C	24.530	101.34		245.8		8.23	7.50	2.829E-07	8.450E-07	1.005E-06	4.485E-07	4.110E-07	3.288E-06	1.459E-07	1.584E-07
MW-T_13-3D	24.500	126.83		245.6		8.23	10.00	2.779E-07	8.150E-07	1.004E-06	4.585E-07	4.160E-07	3.180E-06	1.439E-07	1.694E-07
MW-T_14-1A	24.418	50.01	0.473	245.7	7.12	8.23	2.50	1.425E-06	4.015E-06	5.198E-06	1.756E-06	1.405E-06	1.544E-05	4.867E-07	6.770E-07
MW-T_14-1B	24.475	75.64		245.6		8.23	5.00	1.445E-06	4.055E-06	5.138E-06	1.786E-06	1.405E-06	1.554E-05	4.837E-07	6.690E-07
MW-T_14-1C	24.435	99.50		240.2		8.24	7.50	1.465E-06	4.055E-06	4.998E-06	1.776E-06	1.395E-06	1.514E-05	4.867E-07	6.600E-07
MW-T_14-1D	24.462	128.50		249.7		8.25	10.00	1.485E-06	3.915E-06	4.998E-06	1.806E-06	1.425E-06	1.534E-05	4.907E-07	6.540E-07
MW-T_14-2A	24.700	50.05	0.517	243.4	7.12	8.22	2.50	1.530E-06	3.944E-06	5.186E-06	1.829E-06	1.265E-06	1.447E-05	5.338E-07	6.359E-07
MW-T_14-2B	24.634	75.93		246.2		8.23	5.00	1.540E-06	4.054E-06	5.106E-06	1.829E-06	1.305E-06	1.427E-05	5.318E-07	6.159E-07
MW-T_14-2C	24.674	102.33		248.5		8.23	7.50	1.590E-06	3.914E-06	5.036E-06	1.819E-06	1.475E-06	1.427E-05	5.378E-07	6.169E-07
MW-T_14-2D	24.631	125.51		242.1		8.25	10.00	1.570E-06	3.974E-06	5.116E-06	1.809E-06	1.495E-06	1.477E-05	5.158E-07	6.179E-07
MW-T_14-3A	24.591	49.77	0.528	241.7	7.12	8.23	2.50	1.563E-06	3.642E-06	4.736E-06	1.671E-06	1.360E-06	1.541E-05	5.278E-07	6.647E-07
MW-T_14-3B	24.667	76.06		246.7		8.23	5.00	1.543E-06	3.622E-06	4.726E-06	1.631E-06	1.400E-06	1.551E-05	5.298E-07	6.717E-07
MW-T_14-3C	24.584	101.49		246.1		8.25	7.50	1.553E-06	3.732E-06	4.776E-06	1.651E-06	1.400E-06	1.541E-05	5.238E-07	6.777E-07
MW-T_14-3D	24.633	128.17		248.5		8.24	10.00	1.553E-06	3.752E-06	4.756E-06	1.661E-06	1.410E-06	1.511E-05	5.188E-07	6.667E-07

ID	Li (g/mL)	B (g/mL)	Na (g/mL)	Mg (g/mL)	Al (g/mL)	Si (g/mL)	Mo (g/mL)	Cs (g/mL)
MW-T_13-1 (Average Blank)	2.53E-09	6.50E-09	2.78E-08	9.18E-09	1.05E-07	5.50E-09	8.45E-10	1.50E-09
MW-T_13-1 (Blank 1)	3.25E-09	8.00E-09	3.58E-08	1.21E-08	1.37E-07	1.70E-08	8.77E-10	1.94E-09
MW-T_13-1 (Blank 2)	1.82E-09	5.00E-09	1.98E-08	6.25E-09	7.31E-08	6.47E-08	8.12E-10	1.05E-09
MW-T_13-2 (Average Blank)	1.24E-08	5.10E-08	9.92E-08	7.15E-08	4.52E-08	4.20E-07	6.85E-09	8.83E-09
MW-T_13-2 (Blank 1)	4.12E-09	1.20E-08	5.30E-08	2.02E-08	6.72E-08	3.40E-08	3.54E-09	2.63E-09
MW-T_13-2 (Blank 2)	2.07E-08	9.00E-08	1.45E-07	1.23E-07	2.33E-08	8.05E-07	1.02E-08	1.50E-08
MW-T_13-3 (Average Blank)	3.93E-09	1.30E-08	8.96E-08	1.95E-08	5.30E-08	3.00E-08	2.87E-09	2.36E-09
MW-T_13-3 (Blank 1)	4.76E-09	1.60E-08	8.95E-08	2.06E-08	8.02E-08	2.90E-08	3.82E-09	2.79E-09
MW-T_13-3 (Blank 2)	3.10E-09	1.00E-08	8.97E-08	1.85E-08	2.57E-08	3.10E-08	1.92E-09	1.93E-09
MW-T_14-1 (Average Blank)	4.80E-09	1.50E-08	3.75E-08	2.57E-08	3.52E-08	3.60E-08	2.68E-09	2.98E-09
MW-T_14-1 (Blank 1)	5.95E-09	1.80E-08	4.15E-08	2.68E-08	4.15E-08	6.00E-08	3.43E-09	3.66E-09
MW-T_14-1 (Blank 2)	3.65E-09	1.20E-08	3.35E-08	2.46E-08	2.90E-08	1.20E-08	1.94E-09	2.30E-09
MW-T_14-2 (Average Blank)	9.96E-09	3.40E-08	9.63E-08	6.93E-08	9.46E-08	2.68E-07	3.79E-09	6.92E-09
MW-T_12-2 (Blank 1)	1.17E-08	4.10E-08	9.18E-08	8.13E-08	1.06E-07	3.43E-07	4.49E-09	8.10E-09
MW-T_12-2(Blank 2)	8.20E-09	2.70E-08	1.01E-07	5.73E-08	8.31E-08	1.93E-07	3.09E-09	5.75E-09
MW-T_14-3 (Average Blank)	2.81E-09	1.15E-08	4.61E-08	1.09E-08	9.63E-09	1.25E-08	8.84E-09	1.73E-09
MW-T_12-3(Blank 1)	3.47E-09	1.50E-08	7.18E-08	1.43E-08	1.24E-08	3.10E-08	1.04E-08	2.16E-09
MW-T_12-3 (Blank 2)	2.15E-09	8.00E-09	2.04E-08	7.61E-09	6.87E-09	6.47E-08	7.30E-09	1.31E-09

APPENDIX 12 RAW DATA OF EXPERIMENTS MW-T_15 AND MW-T_16. EXPERIMENTAL CONDITIONS ARE: Q = 125 mL/D, T = 90 °C. CONTROL-TEST DATA IS SHOWN IN THE LOWER TABLE.

Experiment ID	Mass of tared collection bottle (g)	Mass of collection bottle with solution (g)	Initial powder mass (g)	Measured flow rate (mL/d)	Initial pH	Final pH	Duration (hour)	Li (g/mL)	B (g/mL)	Na (g/mL)	Mg (g/mL)	Al (g/mL)	Si (g/mL)	Mo (g/mL)	Cs (g/mL)
MW-T_15-1A	24.632	49.69	0.104	120.3	7.04	8.17	5.00	6.62E-07	1.64E-06	2.08E-06	8.32E-07	8.28E-07	7.25E-06	2.48E-07	3.28E-07
MW-T_15-1B	24.491	75.87		123.3		8.18	10.00	6.49E-07	1.59E-06	2.10E-06	8.33E-07	8.41E-07	7.30E-06	2.54E-07	3.24E-07
MW-T_15-1C	24.520	100.40		121.4		8.18	15.00	6.47E-07	1.61E-06	2.07E-06	8.11E-07	8.36E-07	7.35E-06	2.51E-07	3.21E-07
MW-T_15-1D	24.341	127.92		124.3		8.19	20.00	6.38E-07	1.67E-06	2.14E-06	8.31E-07	8.44E-07	7.31E-06	2.52E-07	3.25E-07
MW-T_15-2A	24.532	50.07	0.120	122.6	7.04	8.14	5.00	6.50E-07	1.79E-06	2.28E-06	9.51E-07	7.78E-07	7.50E-06	2.39E-07	3.17E-07
MW-T_15-2B	24.390	76.60		125.3		8.14	10.00	6.56E-07	1.83E-06	2.26E-06	9.63E-07	7.57E-07	7.73E-06	2.31E-07	3.10E-07
MW-T_15-2C	24.371	100.75		122.2		8.20	15.00	6.59E-07	1.77E-06	2.27E-06	9.78E-07	7.58E-07	7.53E-06	2.41E-07	3.15E-07
MW-T_15-2D	24.818	126.07		121.5		8.21	20.00	6.53E-07	1.78E-06	2.23E-06	9.56E-07	7.48E-07	7.62E-06	2.42E-07	3.13E-07
MW-T_15-3A	24.401	50.07	0.102	123.2	7.04	8.18	5.00	6.08E-07	1.72E-06	2.18E-06	8.88E-07	7.60E-07	7.09E-06	2.48E-07	3.22E-07
MW-T_15-3B	24.861	75.94		122.6		8.21	10.00	6.12E-07	1.79E-06	2.13E-06	9.27E-07	7.85E-07	7.43E-06	2.57E-07	3.29E-07
MW-T_15-3C	24.633	100.38		121.2		8.21	15.00	6.07E-07	1.74E-06	2.16E-06	9.27E-07	7.62E-07	7.26E-06	2.58E-07	3.32E-07
MW-T_15-3D	24.412	128.08		124.4		8.20	20.00	5.97E-07	1.71E-06	2.18E-06	9.02E-07	7.75E-07	7.40E-06	2.47E-07	3.21E-07
MW-T_16-1A	24.711	50.48	0.520	123.7	7.04	8.20	5.00	3.06E-06	1.05E-07	1.11E-05	1.90E-06	1.71E-06	2.99E-05	1.74E-06	6.03E-07
MW-T_16-1B	24.532	75.37		122.0		8.22	10.00	3.08E-06	1.05E-07	1.13E-05	1.95E-06	1.75E-06	3.00E-05	1.75E-06	6.16E-07
MW-T_16-1C	24.890	101.70		122.9		8.21	15.00	3.01E-06	1.08E-07	1.09E-05	1.90E-06	1.74E-06	2.96E-05	1.73E-06	6.28E-07
MW-T_16-1D	24.616	127.03		122.9		8.24	20.00	3.03E-06	1.07E-07	1.17E-05	1.98E-06	1.85E-06	3.00E-05	1.75E-06	6.08E-07
MW-T_16-2A	24.545	50.36	0.502	123.9	7.04	8.22	5.00	3.03E-06	1.21E-07	1.20E-05	1.84E-06	2.00E-06	2.93E-05	1.87E-06	6.31E-07
MW-T_16-2B	24.617	75.62		122.4		8.21	10.00	3.10E-06	1.21E-07	1.20E-05	1.80E-06	1.95E-06	3.02E-05	1.90E-06	6.50E-07
MW-T_16-2C	24.898	100.77		121.4		8.21	15.00	3.00E-06	1.21E-07	1.23E-05	1.82E-06	1.97E-06	3.03E-05	1.91E-06	6.39E-07
MW-T_16-2D	24.216	128.47		125.1		8.22	20.00	3.12E-06	1.20E-07	1.21E-05	1.84E-06	1.97E-06	2.94E-05	1.93E-06	6.29E-07
MW-T_16-3A	24.571	50.36	0.506	123.8	7.04	8.19	5.00	2.76E-06	1.06E-07	1.18E-05	1.88E-06	1.92E-06	2.58E-05	1.90E-06	6.06E-07
MW-T_16-3B	24.356	75.86		123.6		8.22	10.00	2.80E-06	1.05E-07	1.18E-05	1.94E-06	1.86E-06	2.67E-05	1.91E-06	6.19E-07
MW-T_16-3C	24.299	101.42		123.4		8.21	15.00	2.86E-06	1.03E-07	1.23E-05	1.94E-06	1.84E-06	2.58E-05	1.95E-06	6.16E-07
MW-T_16-3D	24.446	127.86		124.1		8.21	20.00	2.84E-06	1.05E-07	1.21E-05	1.94E-06	1.92E-06	2.80E-05	1.95E-06	6.08E-07

ID	Li (g/mL)	B (g/mL)	Na (g/mL)	Mg (g/mL)	Al (g/mL)	Si (g/mL)	Mo (g/mL)	Cs (g/mL)
MW-T_15-1 (Average Blank)	2.53E-09	6.50E-09	2.78E-08	9.18E-09	1.05E-07	5.50E-09	8.45E-10	1.50E-09
MW-T_15-1 (Blank 1)	3.25E-09	8.00E-09	3.58E-08	1.21E-08	1.37E-07	1.70E-08	8.77E-10	1.94E-09
MW-T_15-1 (Blank 2)	1.82E-09	5.00E-09	1.98E-08	6.25E-09	7.31E-08	6.47E-08	8.12E-10	1.05E-09
MW-T_15-2 (Average Blank)	1.24E-08	5.10E-08	9.92E-08	7.15E-08	4.52E-08	4.20E-07	6.85E-09	8.83E-09
MW-T_15-2 (Blank 1)	4.12E-09	1.20E-08	5.30E-08	2.02E-08	6.72E-08	3.40E-08	3.54E-09	2.63E-09
MW-T_15-2 (Blank 2)	2.07E-08	9.00E-08	1.45E-07	1.23E-07	2.33E-08	8.05E-07	1.02E-08	1.50E-08
MW-T_15-3 (Average Blank)	3.93E-09	1.30E-08	8.96E-08	1.95E-08	5.30E-08	3.00E-08	2.87E-09	2.36E-09
MW-T_15-3 (Blank 1)	4.76E-09	1.60E-08	8.95E-08	2.06E-08	8.02E-08	2.90E-08	3.82E-09	2.79E-09
MW-T_15-3 (Blank 2)	3.10E-09	1.00E-08	8.97E-08	1.85E-08	2.57E-08	3.10E-08	1.92E-09	1.93E-09
MW-T_16-1 (Average Blank)	4.80E-09	1.50E-08	3.75E-08	2.57E-08	3.52E-08	3.60E-08	2.68E-09	2.98E-09
MW-T_16-1 (Blank 1)	5.95E-09	1.80E-08	4.15E-08	2.68E-08	4.15E-08	6.00E-08	3.43E-09	3.66E-09
MW-T_16-1 (Blank 2)	3.65E-09	1.20E-08	3.35E-08	2.46E-08	2.90E-08	1.20E-08	1.94E-09	2.30E-09
MW-T_16-2 (Average Blank)	9.96E-09	3.40E-08	9.63E-08	6.93E-08	9.46E-08	2.68E-07	3.79E-09	6.92E-09
MW-T_16-2 (Blank 1)	1.17E-08	4.10E-08	9.18E-08	8.13E-08	1.06E-07	3.43E-07	4.49E-09	8.10E-09
MW-T_16-2(Blank 2)	8.20E-09	2.70E-08	1.01E-07	5.73E-08	8.31E-08	1.93E-07	3.09E-09	5.75E-09
MW-T_16-3 (Average Blank)	2.81E-09	1.15E-08	4.61E-08	1.09E-08	9.63E-09	1.25E-08	8.84E-09	1.73E-09
MW-T_16-3(Blank 1)	3.47E-09	1.50E-08	7.18E-08	1.43E-08	1.24E-08	3.10E-08	1.04E-08	2.16E-09
MW-T_16-3 (Blank 2)	2.15E-09	8.00E-09	2.04E-08	7.61E-09	6.87E-09	6.47E-08	7.30E-09	1.31E-09

APPENDIX 13 RAW DATA OF EXPERIMENTS MW-T_17 AND MW-T_18. EXPERIMENTAL CONDITIONS ARE: Q = 75 ML/D, T = 90 ^{O}C. CONTROL-TEST DATA IS SHOWN IN THE LOWER TABLE.

Experiment ID	Mass of tared collection bottle (g)	Mass of collection bottle with solution (g)	Initial powder mass (g)	Measured flow rate (mL/d)	Initial pH	Final pH	Duration (hour)	Li (g/mL)	B (g/mL)	Na (g/mL)	Mg (g/mL)	Al (g/mL)	Si (g/mL)	Mo (g/mL)	Cs (g/mL)
MW-T_17-1A	24.628	49.56	0.119	74.8	7.26	8.41	8.00	9.66E-07	2.63E-07	3.11E-06	1.48E-06	1.34E-06	1.25E-05	5.00E-07	4.95E-07
MW-T_17-1B	24.623	73.02		72.6		8.39	16.00	9.63E-07	2.76E-07	3.19E-06	1.47E-06	1.35E-06	1.24E-05	4.96E-07	4.94E-07
MW-T_17-1C	24.671	99.47		74.8		8.40	24.00	9.43E-07	2.69E-07	3.11E-06	1.46E-06	1.33E-06	1.26E-05	4.96E-07	5.09E-07
MW-T_17-1D	24.643	125.18		75.4		8.40	32.00	9.55E-07	2.74E-07	3.16E-06	1.50E-06	1.35E-06	1.24E-05	4.86E-07	5.09E-07
MW-T_17-2A	24.677	49.58	0.100	74.7	7.26	8.41	8.00	9.38E-07	3.42E-07	3.61E-06	1.42E-06	1.24E-06	1.23E-05	5.14E-07	5.25E-07
MW-T_17-2B	24.631	73.76		73.7		8.41	16.00	9.30E-07	3.38E-07	3.64E-06	1.47E-06	1.20E-06	1.18E-05	4.98E-07	5.20E-07
MW-T_17-2C	24.567	99.27		74.7		8.42	24.00	9.57E-07	3.40E-07	3.57E-06	1.44E-06	1.18E-06	1.19E-05	5.05E-07	5.09E-07
MW-T_17-2D	24.605	122.74		73.6		8.42	32.00	9.59E-07	3.42E-07	3.60E-06	1.44E-06	1.21E-06	1.18E-05	4.99E-07	5.14E-07
MW-T_17-3A	24.691	49.36	0.131	74.0	7.26	8.38	8.00	9.71E-07	3.04E-07	3.59E-06	1.53E-06	1.26E-06	1.24E-05	4.53E-07	4.61E-07
MW-T_17-3B	24.592	73.39		73.2		8.41	16.00	1.00E-06	2.94E-07	3.57E-06	1.48E-06	1.28E-06	1.26E-05	4.66E-07	4.73E-07
MW-T_17-3C	24.672	99.67		75.0		8.43	24.00	9.67E-07	2.95E-07	3.58E-06	1.46E-06	1.29E-06	1.25E-05	4.63E-07	4.71E-07
MW-T_17-3D	24.679	122.55		73.4		8.43	32.00	9.72E-07	2.94E-07	3.62E-06	1.53E-06	1.27E-06	1.25E-05	4.59E-07	4.83E-07
MW-T_18-1A	24.752	49.89	0.540	75.4	7.26	8.43	8.00	7.50E-06	1.79E-05	2.38E-05	1.69E-06	2.18E-06	4.69E-05	3.53E-06	1.26E-06
MW-T_18-1B	24.604	73.20		72.9		8.45	16.00	7.45E-06	1.78E-05	2.29E-05	1.68E-06	2.20E-06	4.82E-05	3.46E-06	1.29E-06
MW-T_18-1C	24.646	99.45		74.8		8.43	24.00	7.49E-06	1.80E-05	2.33E-05	1.73E-06	2.22E-06	4.75E-05	3.50E-06	1.29E-06
MW-T_18-1D	24.671	125.07		75.3		8.45	32.00	7.45E-06	1.85E-05	2.36E-05	1.73E-06	2.24E-06	4.78E-05	3.58E-06	1.32E-06
MW-T_18-2A	24.627	49.69	0.550	75.2	7.26	8.42	8.00	7.11E-06	1.68E-05	2.13E-05	1.60E-06	2.20E-06	4.73E-05	3.66E-06	1.42E-06
MW-T_18-2B	24.645	73.05		72.6		8.41	16.00	7.11E-06	1.70E-05	2.09E-05	1.62E-06	2.23E-06	4.69E-05	3.73E-06	1.41E-06
MW-T_18-2C	24.623	98.82		74.2		8.44	24.00	7.21E-06	1.68E-05	2.13E-05	1.62E-06	2.22E-06	4.74E-05	3.72E-06	1.42E-06
MW-T_18-2D	24.671	123.74		74.3		8.45	32.00	7.26E-06	1.76E-05	2.16E-05	1.68E-06	2.13E-06	4.89E-05	3.83E-06	1.36E-06
MW-T_18-3A	24.723	49.72	0.540	75.0	7.26	8.41	8.00	7.30E-06	1.78E-05	2.37E-05	1.72E-06	2.14E-06	4.42E-05	3.70E-06	1.39E-06
MW-T_18-3B	24.646	73.25		72.9		8.44	16.00	7.51E-06	1.84E-05	2.29E-05	1.66E-06	2.06E-06	4.39E-05	3.68E-06	1.35E-06
MW-T_18-3C	24.515	97.02		72.5		8.42	24.00	7.48E-06	1.78E-05	2.33E-05	1.72E-06	2.14E-06	4.48E-05	3.78E-06	1.36E-06
MW-T_18-3D	24.601	123.67		74.3		8.43	32.00	7.49E-06	1.83E-05	2.35E-05	1.73E-06	2.17E-06	4.45E-05	3.68E-06	1.36E-06

ID	Li (g/mL)	B (g/mL)	Na (g/mL)	Mg (g/mL)	Al (g/mL)	Si (g/mL)	Mo (g/mL)	Cs (g/mL)
MW-T_17-1 (Average Blank)	2.53E-09	6.50E-09	2.78E-08	9.18E-09	1.05E-07	5.50E-09	8.45E-10	1.50E-09
MW-T_17-1 (Blank 1)	3.25E-09	8.00E-09	3.58E-08	1.21E-08	1.37E-07	1.70E-08	8.77E-10	1.94E-09
MW-T_17-1 (Blank 2)	1.82E-09	5.00E-09	1.98E-08	6.25E-09	7.31E-08	6.47E-08	8.12E-10	1.05E-09
MW-T_17-2 (Average Blank)	1.24E-08	5.10E-08	9.92E-08	7.15E-08	4.52E-08	4.20E-07	6.85E-09	8.83E-09
MW-T_17-2 (Blank 1)	4.12E-09	1.20E-08	5.30E-08	2.02E-08	6.72E-08	3.40E-08	3.54E-09	2.63E-09
MW-T_17-2 (Blank 2)	2.07E-08	9.00E-08	1.45E-07	1.23E-07	2.33E-08	8.05E-07	1.02E-08	1.50E-08
MW-T_17-3 (Average Blank)	3.93E-09	1.30E-08	8.96E-08	1.95E-08	5.30E-08	3.00E-08	2.87E-09	2.36E-09
MW-T_17-3 (Blank 1)	4.76E-09	1.60E-08	8.95E-08	2.06E-08	8.02E-08	2.90E-08	3.82E-09	2.79E-09
MW-T_17-3 (Blank 2)	3.10E-09	1.00E-08	8.97E-08	1.85E-08	2.57E-08	3.10E-08	1.92E-09	1.93E-09
MW-T_18-1 (Average Blank)	4.80E-09	1.50E-08	3.75E-08	2.57E-08	3.52E-08	3.60E-08	2.68E-09	2.98E-09
MW-T_18-1 (Blank 1)	5.95E-09	1.80E-08	4.15E-08	2.68E-08	4.15E-08	6.00E-08	3.43E-09	3.66E-09
MW-T_18-1 (Blank 2)	3.65E-09	1.20E-08	3.35E-08	2.46E-08	2.90E-08	1.20E-08	1.94E-09	2.30E-09
MW-T_18-2 (Average Blank)	9.96E-09	3.40E-08	9.63E-08	6.93E-08	9.46E-08	2.68E-07	3.79E-09	6.92E-09
MW-T_18-2 (Blank 1)	1.17E-08	4.10E-08	9.18E-08	8.13E-08	1.06E-07	3.43E-07	4.49E-09	8.10E-09
MW-T_18-2(Blank 2)	8.20E-09	2.70E-08	1.01E-07	5.73E-08	8.31E-08	1.93E-07	3.09E-09	5.75E-09
MW-T_18-3 (Average Blank)	2.81E-09	1.15E-08	4.61E-08	1.09E-08	9.63E-09	1.25E-08	8.84E-09	1.73E-09
MW-T_18-3(Blank 1)	3.47E-09	1.50E-08	7.18E-08	1.43E-08	1.24E-08	3.10E-08	1.04E-08	2.16E-09
MW-T_18-3 (Blank 2)	2.15E-09	8.00E-09	2.04E-08	7.61E-09	6.87E-09	6.47E-08	7.30E-09	1.31E-09

APPENDIX 14 RAW DATA OF EXPERIMENTS MW-T_19 AND MW-T_20. EXPERIMENTAL CONDITIONS ARE: Q = 50 mL/D, T = 90 ^{O}C. CONTROL-TEST DATA IS SHOWN IN THE LOWER TABLE.

Experiment ID	Mass of tared collection bottle (g)	Mass of collection bottle with solution (g)	Initial powder mass (g)	Measured flow rate (mL/d)	Initial pH	Final pH	Duration (hour)	Li (g/mL)	B (g/mL)	Na (g/mL)	Mg (g/mL)	Al (g/mL)	Si (g/mL)	Mo (g/mL)	Cs (g/mL)
MW-T_19-1A	24.153	73.22	0.128	49.1	7.06	8.24	24.00	1.62E-06	5.23E-06	6.58E-06	1.68E-06	1.59E-06	1.77E-05	8.42E-07	7.20E-07
MW-T_19-1B	24.193	122.49		49.1		8.21	48.00	1.67E-06	5.06E-06	6.50E-06	1.67E-06	1.65E-06	1.74E-05	8.21E-07	7.26E-07
MW-T_19-1C	24.155	173.86		49.9		8.23	72.00	1.62E-06	5.00E-06	6.34E-06	1.68E-06	1.65E-06	1.75E-05	8.44E-07	7.24E-07
MW-T_19-1D	24.186	220.11		49.0		8.23	96.00	1.64E-06	5.18E-06	6.26E-06	1.68E-06	1.61E-06	1.72E-05	8.11E-07	7.10E-07
MW-T_19-2A	24.150	73.35	0.116	49.2	7.06	8.21	24.00	1.69E-06	5.38E-06	7.22E-06	1.65E-06	1.44E-06	1.81E-05	8.86E-07	7.21E-07
MW-T_19-2B	24.224	122.26		49.0		8.24	48.00	1.65E-06	5.44E-06	7.19E-06	1.70E-06	1.42E-06	1.80E-05	8.98E-07	7.38E-07
MW-T_19-2C	24.228	173.03		49.6		8.23	72.00	1.63E-06	5.32E-06	7.12E-06	1.67E-06	1.50E-06	1.80E-05	9.19E-07	7.15E-07
MW-T_19-2D	24.201	222.04		49.5		8.24	96.00	1.66E-06	5.31E-06	7.29E-06	1.65E-06	1.45E-06	1.82E-05	8.97E-07	7.25E-07
MW-T_19-3A	24.193	73.87	0.118	49.7	7.06	8.25	24.00	1.53E-06	5.32E-06	7.11E-06	1.71E-06	1.54E-06	1.58E-05	9.22E-07	7.14E-07
MW-T_19-3B	24.148	120.79		48.3		8.23	48.00	1.52E-06	5.49E-06	7.28E-06	1.73E-06	1.58E-06	1.64E-05	9.06E-07	7.11E-07
MW-T_19-3C	24.181	172.86		49.6		8.24	72.00	1.57E-06	5.35E-06	7.11E-06	1.72E-06	1.56E-06	1.64E-05	8.94E-07	7.01E-07
MW-T_19-3D	24.205	221.97		49.4		8.26	96.00	1.55E-06	5.38E-06	7.12E-06	1.73E-06	1.58E-06	1.59E-05	9.20E-07	7.30E-07
MW-T_20-1A	24.538	73.54	0.502	49.0	7.06	8.28	24.00	1.60E-05	4.12E-05	4.76E-05	2.25E-06	2.08E-06	6.92E-05	6.88E-06	1.74E-06
MW-T_20-1B	24.645	124.45		49.9		8.26	48.00	1.58E-05	4.11E-05	4.76E-05	2.24E-06	2.04E-06	6.77E-05	7.22E-06	1.81E-06
MW-T_20-1C	24.658	173.69		49.7		8.27	72.00	1.57E-05	4.14E-05	4.90E-05	2.24E-06	2.09E-06	6.85E-05	7.08E-06	1.82E-06
MW-T_20-1D	24.473	224.19		49.9		8.26	96.00	1.60E-05	4.13E-05	4.86E-05	2.31E-06	2.12E-06	6.89E-05	7.00E-06	1.81E-06
MW-T_20-2A	24.635	73.94	0.516	49.3	7.06	8.26	24.00	1.42E-05	4.00E-05	4.36E-05	2.18E-06	2.12E-06	6.75E-05	7.07E-06	1.82E-06
MW-T_20-2B	24.692	123.00		49.2		8.24	48.00	1.44E-05	4.11E-05	4.43E-05	2.15E-06	2.11E-06	6.85E-05	6.99E-06	1.77E-06
MW-T_20-2C	24.603	173.29		49.6		8.26	72.00	1.48E-05	4.38E-05	4.47E-05	2.16E-06	2.14E-06	6.74E-05	6.94E-06	1.77E-06
MW-T_20-2D	24.612	218.05		48.4		8.27	96.00	1.47E-05	4.39E-05	4.49E-05	2.18E-06	2.08E-06	6.67E-05	7.11E-06	1.78E-06
MW-T_20-3A	24.646	74.28	0.520	49.6	7.06	8.24	24.00	1.56E-05	4.41E-05	4.89E-05	2.26E-06	2.09E-06	6.45E-05	6.62E-06	1.65E-06
MW-T_20-3B	24.676	121.98		48.7		8.29	48.00	1.60E-05	4.41E-05	4.82E-05	2.30E-06	2.12E-06	6.20E-05	6.62E-06	1.71E-06
MW-T_20-3C	24.644	170.60		48.7		8.27	72.00	1.55E-05	4.34E-05	4.73E-05	2.26E-06	2.13E-06	6.32E-05	6.51E-06	1.66E-06
MW-T_20-3D	24.588	222.52		49.5		8.27	96.00	1.61E-05	4.30E-05	4.73E-05	2.31E-06	2.16E-06	6.30E-05	6.58E-06	1.71E-06

ID	Li (g/mL)	B (g/mL)	Na (g/mL)	Mg (g/mL)	Al (g/mL)	Si (g/mL)	Mo (g/mL)	Cs (g/mL)
MW-T_19-1 (Average Blank)	2.53E-09	6.50E-09	2.78E-08	9.18E-09	1.05E-07	5.50E-09	8.45E-10	1.50E-09
MW-T_19-1 (Blank 1)	3.25E-09	8.00E-09	3.58E-08	1.21E-08	1.37E-07	1.70E-08	8.77E-10	1.94E-09
MW-T_19-1 (Blank 2)	1.82E-09	5.00E-09	1.98E-08	6.25E-09	7.31E-08	6.47E-08	8.12E-10	1.05E-09
MW-T_19-2 (Average Blank)	1.24E-08	5.10E-08	9.92E-08	7.15E-08	4.52E-08	4.20E-07	6.85E-09	8.83E-09
MW-T_19-2 (Blank 1)	4.12E-09	1.20E-08	5.30E-08	2.02E-08	6.72E-08	3.40E-08	3.54E-09	2.63E-09
MW-T_19-2 (Blank 2)	2.07E-08	9.00E-08	1.45E-07	1.23E-07	2.33E-08	8.05E-07	1.02E-08	1.50E-08
MW-T_19-3 (Average Blank)	3.93E-09	1.30E-08	8.96E-08	1.95E-08	5.30E-08	3.00E-08	2.87E-09	2.36E-09
MW-T_19-3 (Blank 1)	4.76E-09	1.60E-08	8.95E-08	2.06E-08	8.02E-08	2.90E-08	3.82E-09	2.79E-09
MW-T_19-3 (Blank 2)	3.10E-09	1.00E-08	8.97E-08	1.85E-08	2.57E-08	3.10E-08	1.92E-09	1.93E-09
MW-T_20-1 (Average Blank)	4.80E-09	1.50E-08	3.75E-08	2.57E-08	3.52E-08	3.60E-08	2.68E-09	2.98E-09
MW-T_20-1 (Blank 1)	5.95E-09	1.80E-08	4.15E-08	2.68E-08	4.15E-08	6.00E-08	3.43E-09	3.66E-09
MW-T_20-1 (Blank 2)	3.65E-09	1.20E-08	3.35E-08	2.46E-08	2.90E-08	1.20E-08	1.94E-09	2.30E-09
MW-T_20-2 (Average Blank)	9.96E-09	3.40E-08	9.63E-08	6.93E-08	9.46E-08	2.68E-07	3.79E-09	6.92E-09
MW-T_20-2 (Blank 1)	1.17E-08	4.10E-08	9.18E-08	8.13E-08	1.06E-07	3.43E-07	4.49E-09	8.10E-09
MW-T_20-2(Blank 2)	8.20E-09	2.70E-08	1.01E-07	5.73E-08	8.31E-08	1.93E-07	3.09E-09	5.75E-09
MW-T_20-3 (Average Blank)	2.81E-09	1.15E-08	4.61E-08	1.09E-08	9.63E-09	1.25E-08	8.84E-09	1.73E-09
MW-T_20-3(Blank 1)	3.47E-09	1.50E-08	7.18E-08	1.43E-08	1.24E-08	3.10E-08	1.04E-08	2.16E-09
MW-T_20-3 (Blank 2)	2.15E-09	8.00E-09	2.04E-08	7.61E-09	6.87E-09	6.47E-08	7.30E-09	1.31E-09

APPENDIX 15 RAW DATA OF EXPERIMENTS MW-T_21 AND MW-T_22. EXPERIMENTAL CONDITIONS ARE: Q = 25 mL/d, T = 90 ^{o}C. CONTROL-TEST DATA IS SHOWN IN THE LOWER TABLE.

Experiment ID	Mass of tared collection bottle (g)	Mass of collection bottle with solution (g)	Initial powder mass (g)	Measured flow rate (mL/d)	Initial pH	Final pH	Duration (hour)	Li (g/mL)	B (g/mL)	Na (g/mL)	Mg (g/mL)	Al (g/mL)	Si (g/mL)	Mo (g/mL)	Cs (g/mL)
MW-T_21-1A	24.431	73.87	0.104	24.721	7.18	8.41	48.00	3.440E-06	9.493E-06	1.381E-05	1.831E-06	1.922E-06	3.026E-05	1.661E-06	1.020E-06
MW-T_21-1B	24.427	123.60		24.792		8.39	96.00	3.400E-06	9.473E-06	1.411E-05	1.781E-06	1.932E-06	3.046E-05	1.621E-06	1.020E-06
MW-T_21-1C	24.393	172.59		24.699		8.42	144.00	3.400E-06	9.493E-06	1.391E-05	1.821E-06	1.952E-06	3.026E-05	1.621E-06	1.020E-06
MW-T_21-1D	24.562	223.54		24.872		8.41	192.00	3.460E-06	9.093E-06	1.381E-05	1.781E-06	1.872E-06	3.056E-05	1.601E-06	1.030E-06
MW-T_21-2A	24.451	72.77	0.106	24.161	7.18	8.38	48.00	3.170E-06	9.572E-06	1.361E-05	1.752E-06	1.771E-06	3.136E-05	1.541E-06	1.020E-06
MW-T_21-2B	24.602	119.73		23.781		8.40	96.00	3.160E-06	9.512E-06	1.351E-05	1.782E-06	1.771E-06	3.256E-05	1.521E-06	1.030E-06
MW-T_21-2C	24.418	167.53		23.852		8.41	144.00	3.160E-06	9.422E-06	1.391E-05	1.902E-06	1.781E-06	3.116E-05	1.501E-06	1.030E-06
MW-T_21-2D	24.423	214.61		23.773		8.39	192.00	3.190E-06	9.422E-06	1.361E-05	1.942E-06	1.791E-06	3.146E-05	1.521E-06	1.020E-06
MW-T_21-3A	24.532	72.12	0.111	23.795	7.18	8.37	48.00	3.420E-06	9.241E-06	1.261E-05	1.913E-06	1.891E-06	3.006E-05	1.590E-06	9.601E-07
MW-T_21-3B	24.479	119.56		23.771		8.39	96.00	3.440E-06	9.011E-06	1.261E-05	1.923E-06	1.941E-06	3.116E-05	1.590E-06	9.591E-07
MW-T_21-3C	24.398	167.01		23.769		8.42	144.00	3.350E-06	9.301E-06	1.281E-05	1.903E-06	1.961E-06	3.166E-05	1.630E-06	9.601E-07
MW-T_21-3D	24.413	214.53		23.765		8.42	192.00	3.370E-06	9.321E-06	1.311E-05	1.903E-06	1.941E-06	3.186E-05	1.640E-06	9.571E-07
MW-T_22-1A	24.621	74.40	0.515	24.890	7.18	8.43	48.00	3.260E-05	1.000E-04	1.230E-04	1.291E-06	3.866E-07	1.291E-04	1.310E-05	1.060E-05
MW-T_22-1B	24.512	124.16		24.912		8.42	96.00	3.330E-05	1.020E-04	1.270E-04	1.291E-06	3.926E-07	1.271E-04	1.320E-05	1.080E-05
MW-T_22-1C	24.604	174.09		24.915		8.41	144.00	3.450E-05	9.771E-05	1.230E-04	1.301E-06	3.946E-07	1.281E-04	1.330E-05	1.070E-05
MW-T_22-1D	24.483	223.87		24.923		8.44	192.00	3.450E-05	1.010E-04	1.250E-04	1.301E-06	3.876E-07	1.321E-04	1.300E-05	1.080E-05
MW-T_22-2A	24.441	74.10	0.502	24.827	7.18	8.41	48.00	3.600E-05	9.232E-05	1.270E-04	1.281E-06	3.739E-07	1.231E-04	1.390E-05	1.040E-05
MW-T_22-2B	24.509	123.71		24.801		8.43	96.00	3.580E-05	9.241E-05	1.250E-04	1.201E-06	3.809E-07	1.201E-04	1.400E-05	1.020E-05
MW-T_22-2C	24.437	168.40		23.993		8.42	144.00	3.680E-05	9.371E-05	1.250E-04	1.191E-06	3.779E-07	1.231E-04	1.430E-05	1.010E-05
MW-T_22-2D	24.463	214.80		23.792		8.43	192.00	3.700E-05	9.211E-05	1.270E-04	1.211E-06	3.699E-07	1.231E-04	1.440E-05	1.000E-05
MW-T_22-3A	24.518	72.52	0.506	24.001	7.18	8.44	48.00	3.600E-05	9.941E-05	1.120E-04	1.321E-06	3.929E-07	1.281E-04	1.420E-05	1.030E-05
MW-T_22-3B	24.472	120.25		23.945		8.41	96.00	3.640E-05	9.741E-05	1.150E-04	1.291E-06	3.929E-07	1.301E-04	1.400E-05	1.010E-05
MW-T_22-3C	24.449	167.74		23.882		8.43	144.00	3.570E-05	9.901E-05	1.150E-04	1.331E-06	3.969E-07	1.311E-04	1.430E-05	1.040E-05
MW-T_22-3D	24.587	217.41		24.103		8.46	192.00	3.550E-05	9.891E-05	1.160E-04	1.301E-06	3.859E-07	1.311E-04	1.450E-05	1.060E-05

ID	Li (g/mL)	B (g/mL)	Na (g/mL)	Mg (g/mL)	Al (g/mL)	Si (g/mL)	Mo (g/mL)	Cs (g/mL)
MW-T_21-1 (Average Blank)	4.71E-10	1.25E-08	6.19E-09	1.42E-09	2.30E-09	6.47E-08	8.51E-10	1.23E-10
MW-T_21-1 (Blank 1)	7.14E-10	1.60E-08	8.88E-09	1.76E-09	2.65E-09	6.47E-08	6.33E-10	1.41E-10
MW-T_21-1 (Blank 2)	2.28E-10	9.00E-09	3.50E-09	1.09E-09	1.96E-09	6.47E-08	1.07E-09	1.04E-10
MW-T_21-2 (Average Blank)	1.25E-10	1.20E-08	6.34E-09	2.18E-09	1.14E-08	6.47E-08	7.12E-10	9.90E-11
MW-T_21-2 (Blank 1)	1.25E-10	1.60E-08	8.21E-09	2.75E-09	1.49E-08	6.47E-08	4.30E-10	1.30E-10
MW-T_21-2 (Blank 2)	1.25E-10	8.00E-09	4.46E-09	1.62E-09	7.96E-09	6.47E-08	9.94E-10	6.80E-11
MW-T_21-3 (Average Blank)	1.25E-10	1.05E-08	1.23E-08	2.66E-09	1.09E-08	6.47E-08	4.81E-10	1.03E-10
MW-T_21-3 (Blank 1)	1.25E-10	1.30E-08	1.83E-08	2.66E-09	1.38E-08	6.47E-08	5.14E-10	9.30E-11
MW-T_21-3 (Blank 2)	1.25E-10	8.00E-09	6.32E-09	2.65E-09	8.06E-09	6.47E-08	4.47E-10	1.12E-10
MW-T_22-1 (Average Blank)	1.25E-10	8.50E-09	3.19E-09	1.09E-09	5.76E-10	6.47E-08	1.02E-09	4.75E-11
MW-T_22-1 (Blank 1)	1.25E-10	1.10E-08	3.47E-09	1.22E-09	5.65E-10	6.47E-08	1.32E-09	4.40E-11
MW-T_22-1 (Blank 2)	1.25E-10	6.00E-09	2.90E-09	9.66E-10	5.87E-10	6.47E-08	7.16E-10	5.10E-11
MW-T_22-2 (Average Blank)	1.25E-10	9.00E-09	2.82E-09	9.08E-10	2.85E-09	6.47E-08	5.77E-10	8.45E-11
MW-T_22-2 (Blank 1)	1.25E-10	1.10E-08	2.98E-09	8.81E-10	9.17E-10	6.47E-08	4.79E-10	4.50E-11
MW-T_22-2(Blank 2)	1.25E-10	7.00E-09	2.67E-09	9.35E-10	4.79E-09	6.47E-08	6.75E-10	1.24E-10
MW-T_22-3 (Average Blank)	1.80E-10	8.00E-09	4.85E-09	1.41E-09	9.17E-10	6.47E-08	1.20E-09	2.40E-10
MW-T_22-3(Blank 1)	2.34E-10	1.00E-08	5.44E-09	1.57E-09	8.20E-10	6.47E-08	1.22E-09	2.87E-10
MW-T_22-3 (Blank 2)	1.25E-10	6.00E-09	4.25E-09	1.24E-09	1.01E-09	6.47E-08	1.19E-09	1.93E-10

APPENDIX 16 RAW DATA OF EXPERIMENTS MW-T_23 AND MW-T_24. EXPERIMENTAL CONDITIONS ARE: Q = 10 mL/d, T = 90 °C. CONTROL-TEST DATA IS SHOWN IN THE LOWER TABLE.

Experiment ID	Mass of tared collection bottle (g)	Mass of collection bottle with solution (g)	Initial powder mass (g)	Measured flow rate (mL/d)	Initial pH	Final pH	Duration (hour)	Li (g/mL)	B (g/mL)	Na (g/mL)	Mg (g/mL)	Al (g/mL)	Si (g/mL)	Mo (g/mL)	Cs (g/mL)
MW-T_23-1A	24.192	53.70	0.107	9.837	7.11	8.35	72.00	1.500E-05	4.480E-05	5.451E-05	2.793E-06	2.368E-06	7.016E-05	7.300E-06	6.130E-06
MW-T_23-1B	24.218	81.59		9.562		8.37	144.00	1.500E-05	4.400E-05	5.571E-05	2.793E-06	2.338E-06	7.086E-05	7.360E-06	6.220E-06
MW-T_23-1C	24.278	113.50		9.913		8.39	216.00	1.560E-05	4.530E-05	5.611E-05	2.873E-06	2.328E-06	7.096E-05	7.220E-06	6.130E-06
MW-T_23-1D	24.151	142.54		9.866		8.38	288.00	1.590E-05	4.470E-05	5.471E-05	2.823E-06	2.328E-06	7.146E-05	7.230E-06	6.280E-06
MW-T_23-2A	24.197	52.08	0.109	9.293	7.11	8.37	72.00	1.700E-05	4.481E-05	5.531E-05	2.654E-06	2.154E-06	6.976E-05	7.840E-06	5.820E-06
MW-T_23-2B	24.232	80.37		9.356		8.38	144.00	1.680E-05	4.451E-05	5.541E-05	2.564E-06	2.224E-06	7.206E-05	7.850E-06	5.780E-06
MW-T_23-2C	24.109	107.55		9.271		8.36	216.00	1.650E-05	4.511E-05	5.511E-05	2.614E-06	2.194E-06	6.986E-05	7.610E-06	5.720E-06
MW-T_23-2D	24.116	135.28		9.264		8.38	288.00	1.650E-05	4.371E-05	5.551E-05	2.564E-06	2.204E-06	6.996E-05	7.550E-06	5.740E-06
MW-T_23-3A	24.186	53.15	0.100	9.653	7.11	8.41	72.00	1.630E-05	4.141E-05	5.384E-05	2.819E-06	2.375E-06	7.166E-05	7.561E-06	6.220E-06
MW-T_23-3B	24.208	81.69		9.581		8.36	144.00	1.650E-05	4.191E-05	5.244E-05	2.819E-06	2.315E-06	7.166E-05	7.591E-06	6.300E-06
MW-T_23-3C	24.255	110.41		9.573		8.37	216.00	1.640E-05	4.101E-05	5.374E-05	2.849E-06	2.385E-06	7.166E-05	7.601E-06	6.050E-06
MW-T_23-3D	24.162	137.21		9.421		8.37	288.00	1.700E-05	4.161E-05	5.314E-05	2.839E-06	2.355E-06	7.456E-05	7.781E-06	6.100E-06
MW-T_24-1A	24.166	53.64	0.509	9.823	7.11	8.48	72.00	8.670E-05	2.590E-04	2.740E-04	5.359E-06	7.287E-07	2.271E-04	3.070E-05	2.170E-05
MW-T_24-1B	24.126	82.95		9.804		8.47	144.00	8.550E-05	2.570E-04	2.780E-04	5.419E-06	7.527E-07	2.281E-04	3.020E-05	2.210E-05
MW-T_24-1C	24.229	113.09		9.873		8.51	216.00	8.600E-05	2.470E-04	2.740E-04	5.509E-06	7.417E-07	2.231E-04	2.970E-05	2.250E-05
MW-T_24-1D	24.139	141.56		9.785		8.52	288.00	8.770E-05	2.550E-04	2.690E-04	5.479E-06	7.507E-07	2.231E-04	2.980E-05	2.180E-05
MW-T_24-2A	24.265	54.03	0.499	9.921	7.11	8.47	72.00	8.530E-05	2.510E-04	2.890E-04	5.206E-06	7.223E-07	2.231E-04	2.830E-05	2.350E-05
MW-T_24-2B	24.214	81.23		9.503		8.49	144.00	8.380E-05	2.480E-04	2.860E-04	5.216E-06	7.223E-07	2.251E-04	2.810E-05	2.310E-05
MW-T_24-2C	24.135	109.59		9.495		8.50	216.00	8.570E-05	2.530E-04	2.940E-04	5.366E-06	7.233E-07	2.291E-04	2.880E-05	2.340E-05
MW-T_24-2D	24.133	134.97		9.236		8.53	288.00	8.630E-05	2.520E-04	2.860E-04	5.316E-06	7.283E-07	2.281E-04	2.870E-05	2.290E-05
MW-T_24-3A	24.230	53.52	0.503	9.764	7.11	8.48	72.00	8.300E-05	2.330E-04	2.940E-04	5.260E-06	7.180E-07	2.096E-04	3.020E-05	2.320E-05
MW-T_24-3B	24.193	81.18		9.497		8.47	144.00	8.080E-05	2.380E-04	2.920E-04	5.420E-06	7.200E-07	2.096E-04	3.040E-05	2.280E-05
MW-T_24-3C	24.098	109.59		9.499		8.51	216.00	8.300E-05	2.350E-04	2.890E-04	5.340E-06	7.090E-07	2.016E-04	2.980E-05	2.300E-05
MW-T_24-3D	24.151	136.65		9.375		8.52	288.00	8.200E-05	2.320E-04	2.920E-04	5.330E-06	7.300E-07	2.096E-04	3.100E-05	2.300E-05

ID	Li (g/mL)	B (g/mL)	Na (g/mL)	Mg (g/mL)	Al (g/mL)	Si (g/mL)	Mo (g/mL)	Cs (g/mL)
MW-T_23-1 (Average Blank)	9.26E-10	4.00E-09	1.43E-08	2.91E-09	1.76E-08	6.47E-08	3.04E-10	1.47E-10
MW-T_23-1 (Blank 1)	1.32E-09	5.00E-09	2.02E-08	2.97E-09	3.22E-08	6.47E-08	3.25E-10	1.72E-10
MW-T_23-1 (Blank 2)	5.37E-10	3.00E-09	8.35E-09	2.85E-09	3.06E-09	6.47E-08	2.82E-10	1.21E-10
MW-T_23-2 (Average Blank)	1.25E-10	5.00E-09	7.82E-09	4.06E-09	4.28E-09	6.47E-08	3.35E-10	1.46E-10
MW-T_23-2 (Blank 1)	1.25E-10	6.00E-09	8.23E-09	6.59E-09	5.98E-09	6.47E-08	4.54E-10	1.76E-10
MW-T_23-2 (Blank 2)	1.25E-10	4.00E-09	7.41E-09	1.53E-09	2.58E-09	6.47E-08	2.16E-10	1.16E-10
MW-T_23-3 (Average Blank)	1.25E-10	5.50E-09	3.98E-08	8.65E-09	5.47E-09	6.47E-08	8.19E-10	4.26E-10
MW-T_23-3 (Blank 1)	1.25E-10	5.00E-09	7.57E-09	3.73E-09	8.77E-09	6.47E-08	4.53E-10	3.01E-10
MW-T_23-3 (Blank 2)	1.25E-10	6.00E-09	7.20E-08	1.36E-08	2.16E-09	6.47E-08	1.18E-09	5.50E-10
MW-T_24-1 (Average Blank)	2.59E-09	9.00E-09	2.73E-08	9.12E-09	2.70E-09	6.47E-08	7.29E-10	6.29E-10
MW-T_24-1 (Blank 1)	1.25E-10	5.00E-09	2.40E-08	4.23E-09	3.95E-09	6.47E-08	4.72E-10	5.08E-10
MW-T_24-1 (Blank 2)	5.05E-09	1.30E-08	3.06E-08	1.40E-08	1.45E-09	1.06E-07	9.85E-10	7.50E-10
MW-T_24-2 (Average Blank)	1.25E-10	1.05E-08	9.91E-09	1.56E-08	3.33E-09	6.47E-08	9.06E-10	2.59E-10
MW-T_24-2 (Blank 1)	1.25E-10	1.60E-08	1.54E-08	2.93E-08	3.08E-09	6.20E-08	1.52E-09	3.07E-10
MW-T_24-2(Blank 2)	1.25E-10	5.00E-09	4.47E-09	1.96E-09	3.58E-09	6.47E-08	2.89E-10	2.11E-10
MW-T_24-3 (Average Blank)	2.08E-09	1.30E-08	1.87E-08	1.02E-08	3.05E-09	6.47E-07	1.95E-09	6.07E-10
MW-T_24-3(Blank 1)	5.70E-11	1.10E-08	1.28E-08	1.53E-08	2.44E-09	1.29E-07	1.46E-09	2.76E-10
MW-T_24-3 (Blank 2)	4.10E-09	1.50E-08	2.46E-08	5.15E-09	3.65E-09	6.47E-08	2.44E-09	9.37E-10

APPENDIX 17 STEADY-STATE PLOTS FOR EXPERIMENTS CONDUCTED AT OTHER VALUES OF PARAMETER Q/S IN DEIONISED WATER.

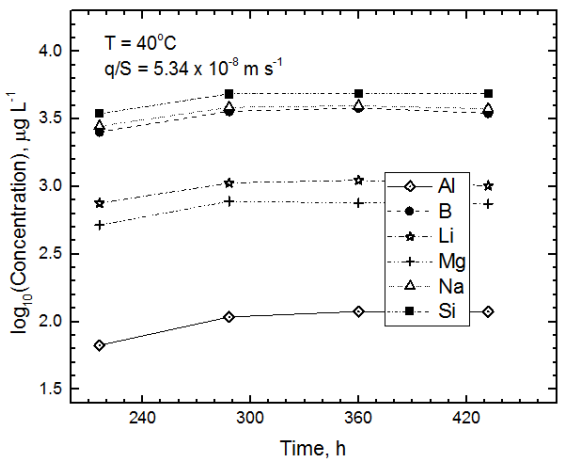

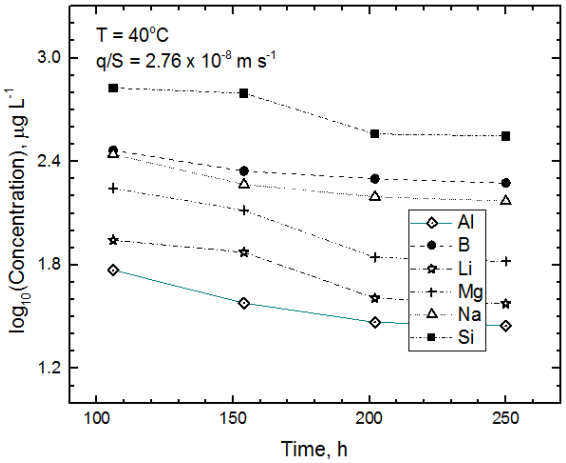

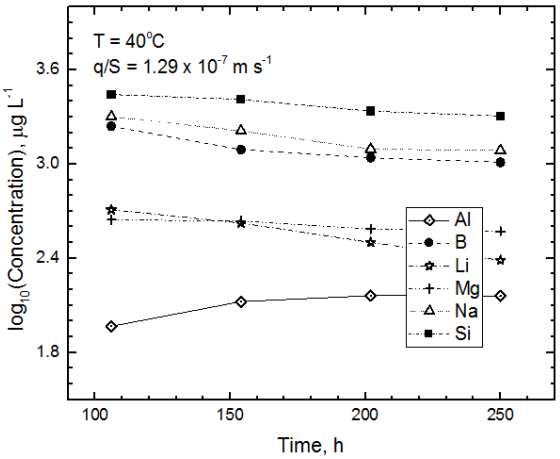

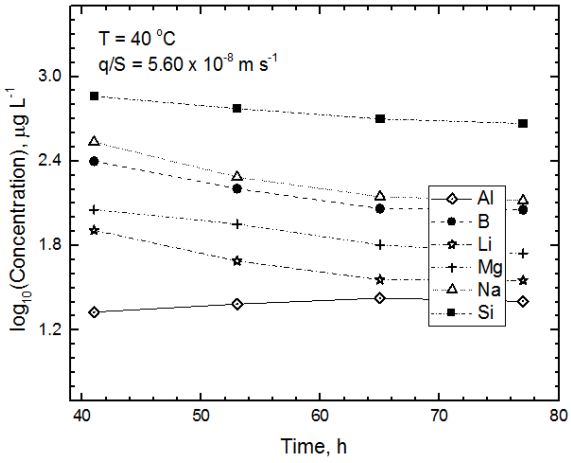

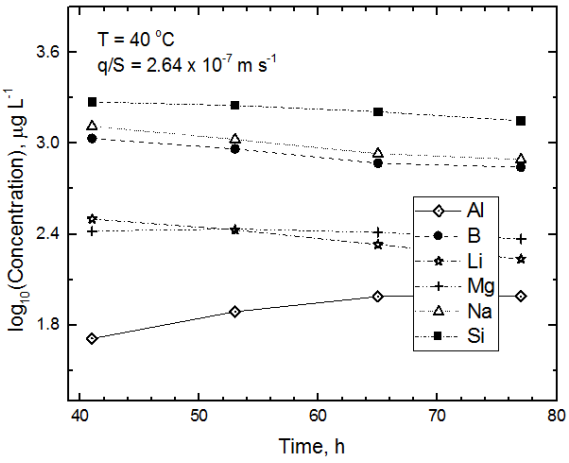
T = 40 °C
q/S = 2.64 x 10-7 m s-1
log10(Concentration), µg L-1
Time, h
Al
B
Li
Mg
Na
Si

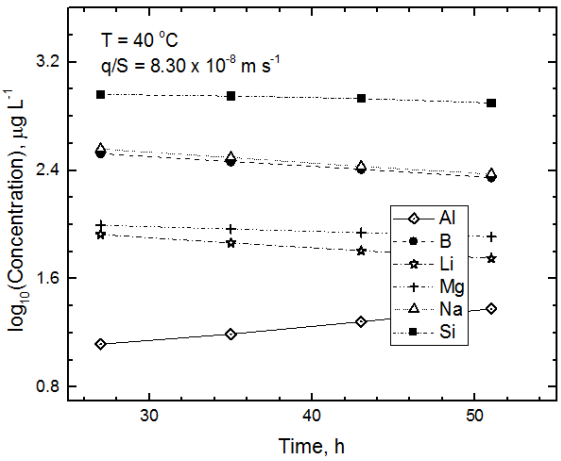
T = 40 °C
q/S = 8.30 x 10-8 m s-1
log10(Concentration), µg L-1
Time, h
Al
B
Li
Mg
Na
Si

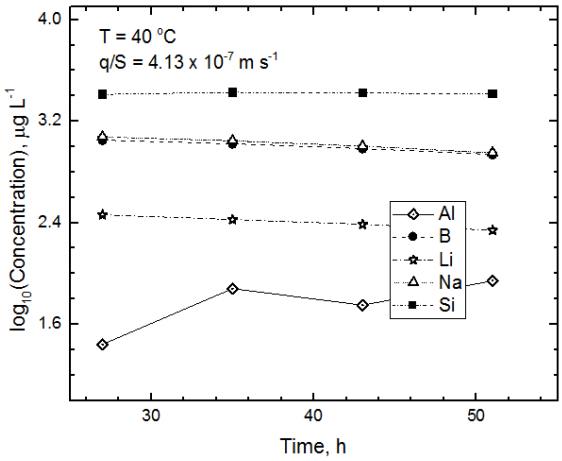
T = 40 °C
q/S = 4.13 x 10-7 m s-1
log10(Concentration), µg L-1
Time, h
Al
B
Li
Na
Si

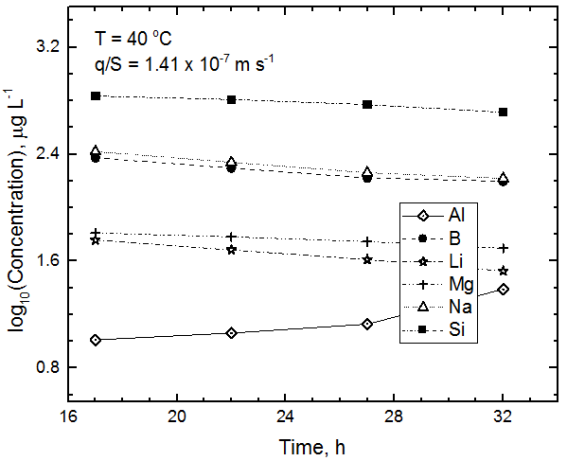
T = 40 °C
q/S = 1.41 x 10-7 m s-1
log10(Concentration), µg L-1
Time, h
Al
B
Li
Mg
Na
Si

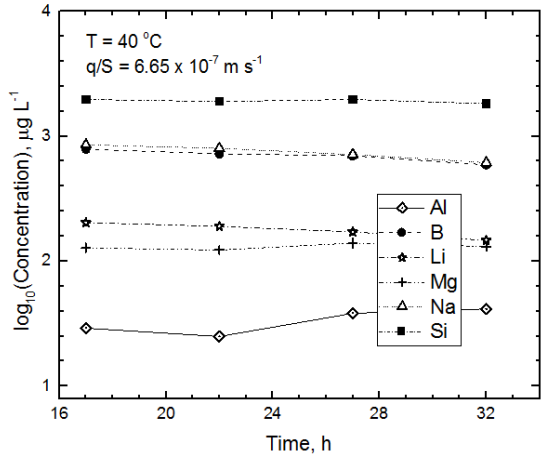
T = 40 °C
q/S = 6.65 x 10-7 m s-1
log10(Concentration), µg L-1
Time, h
Al
B
Li
Mg
Na
Si

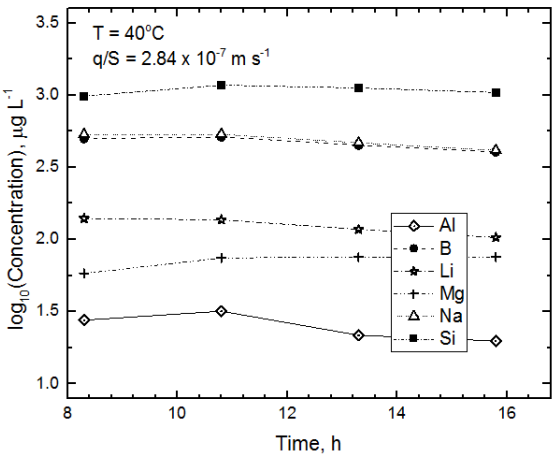
T = 40°C
q/S = 2.84 x 10-7 m s-1
log10(Concentration), µg L-1
Time, h
Al
B
Li
Mg
Na
Si

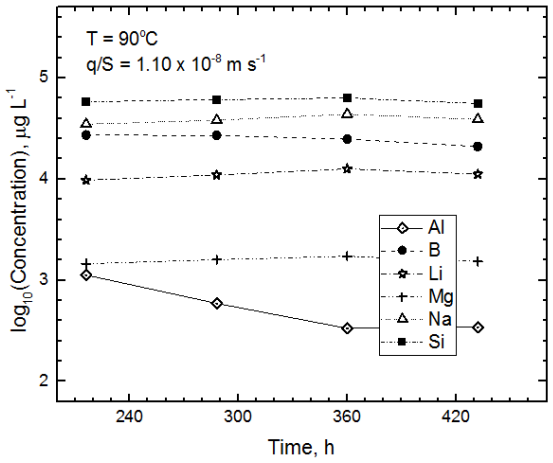
T = 90°C
q/S = 1.10 x 10-8 m s-1
log10(Concentration), µg L-1
Time, h
Al
B
Li
Mg
Na
Si

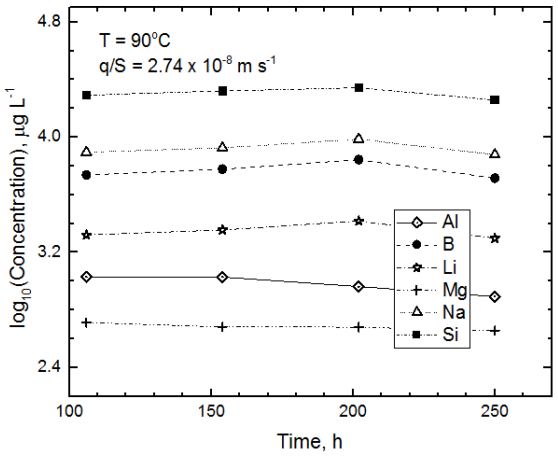
T = 90°C
q/S = 2.74 x 10-8 m s-1
log10(Concentration), µg L-1
Time, h
Al
B
Li
Mg
Na
Si

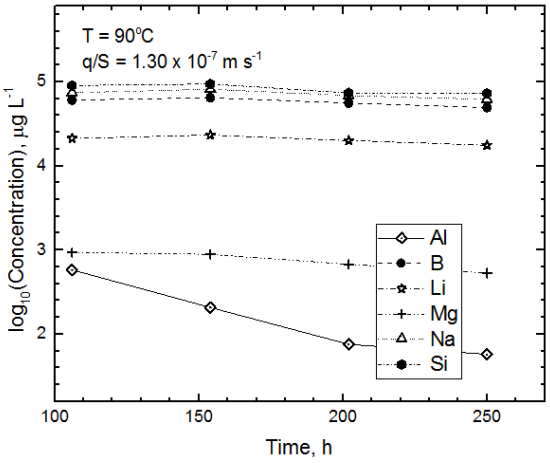
T = 90°C
q/S = 1.30 x 10-7 m s-1
log10(Concentration), µg L-1
Time, h
Al
B
Li
Mg
Na
Si

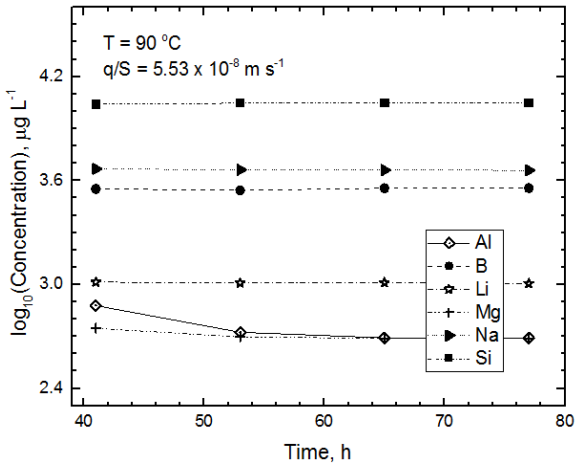
T = 90 °C
q/S = 5.53 x 10-8 m s-1
log10(Concentration), µg L-1
Time, h
Al
B
Li
Mg
Na
Si

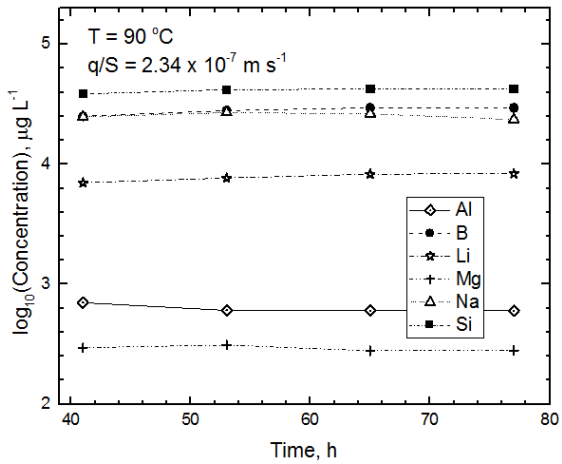
T = 90 °C
q/S = 2.34 x 10-7 m s-1
log10(Concentration), µg L-1
Time, h
Al
B
Li
Mg
Na
Si

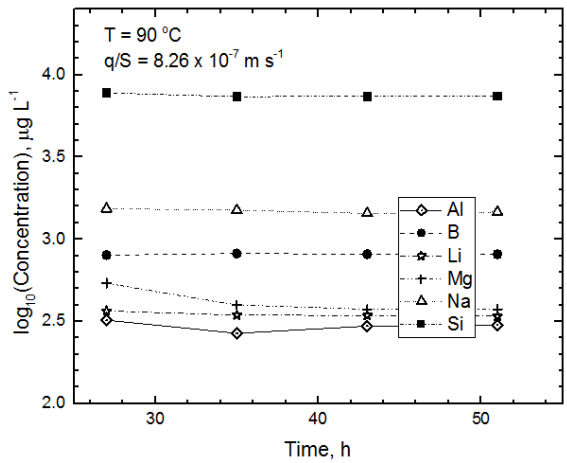
T = 90 °C
q/S = 8.26 x 10-7 m s-1
log10(Concentration), µg L-1
Time, h
Al
B
Li
Mg
Na
Si

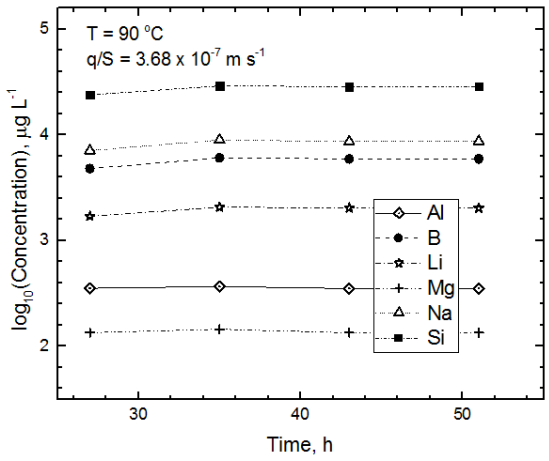
T = 90 °C
q/S = 3.68 x 10-7 m s-1
log10(Concentration), µg L-1
Time, h
Al
B
Li
Mg
Na
Si

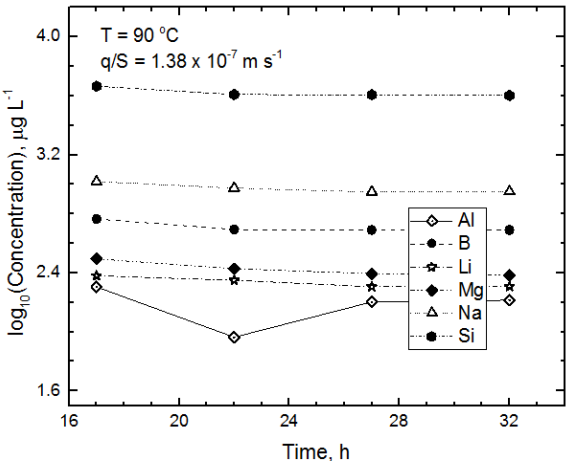
T = 90 °C
q/S = 1.38 x 10-7 m s-1
log10(Concentration), µg L-1
Time, h
Al
B
Li
Mg
Na
Si

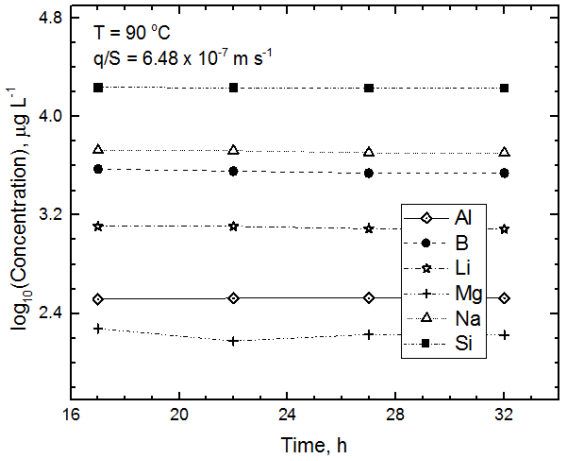
T = 90 °C
q/S = 6.48 x 10-7 m s-1
log10(Concentration), µg L-1
Time, h
Al
B
Li
Mg
Na
Si

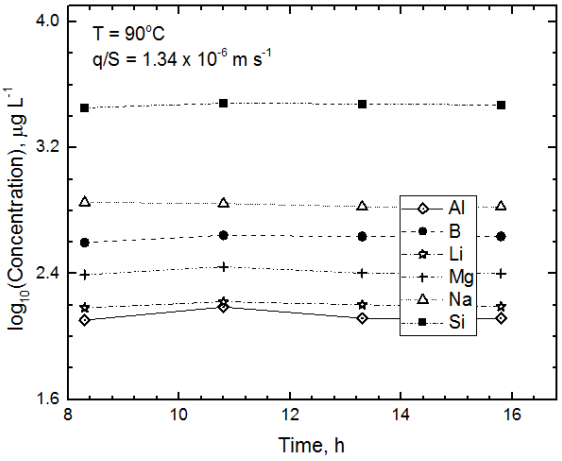
T = 90°C
q/S = 1.34 x 10-6 m s-1
log10(Concentration), µg L-1
Time, h
Al
B
Li
Mg
Na
Si

APPENDIX 18 DISSOLUTION RATES (IN G/M^2/D) FOR TRIPLICATE EXPERIMENTS MEASURED IN DEIONISED WATER AT 40 ^{O}C.

Experiment ID	Al	B	Cs	Li	Mg	Mo	Na	Si
MW-T_1-1	0.195	0.190	0.191	0.197	0.188	0.179	0.187	0.185
MW-T_1-2	0.180	0.195	0.192	0.187	0.196	0.186	0.197	0.194
MW-T_1-3	0.195	0.188	0.184	0.189	0.189	0.199	0.195	0.197
MW-T_2-1	0.083	0.161	0.167	0.156	0.143	0.172	0.159	0.145
MW-T_2-2	0.083	0.153	0.164	0.155	0.141	0.161	0.158	0.144
MW-T_2-3	0.083	0.145	0.158	0.154	0.145	0.159	0.160	0.137
MW-T_3-1	0.170	0.175	0.179	0.180	0.185	0.181	0.174	0.183
MW-T_3-2	0.173	0.176	0.173	0.182	0.181	0.175	0.189	0.182
MW-T_3-3	0.179	0.195	0.176	0.178	0.183	0.181	0.189	0.175
MW-T_4-1	0.051	0.145	0.147	0.145	0.118	0.155	0.134	0.122
MW-T_4-2	0.050	0.138	0.145	0.149	0.117	0.149	0.137	0.112
MW-T_4-3	0.052	0.137	0.140	0.144	0.116	0.152	0.137	0.120
MW-T_5-1	0.094	0.152	0.161	0.147	0.138	0.154	0.160	0.136
MW-T_5-2	0.096	0.151	0.154	0.144	0.150	0.172	0.150	0.147
MW-T_5-3	0.101	0.150	0.165	0.156	0.147	0.172	0.158	0.146
MW-T_6-1	0.030	0.099	0.122	0.119	0.076	0.157	0.119	0.078
MW-T_6-2	0.028	0.103	0.126	0.121	0.080	0.152	0.124	0.084
MW-T_6-3	0.029	0.098	0.127	0.120	0.081	0.150	0.117	0.084
MW-T_7-1	0.194	0.186	0.177	0.185	0.198	0.188	0.196	0.192
MW-T_7-2	0.196	0.195	0.182	0.184	0.183	0.188	0.198	0.184
MW-T_7-3	0.171	0.183	0.190	0.186	0.195	0.176	0.182	0.194
MW-T_8-1	0.075	0.150	0.148	0.144	0.134	0.156	0.146	0.134
MW-T_8-2	0.072	0.149	0.148	0.155	0.137	0.160	0.146	0.136
MW-T_8-3	0.069	0.151	0.163	0.148	0.137	0.161	0.149	0.144
MW-T_9-1	0.155	0.172	0.166	0.181	0.173	0.176	0.181	0.172
MW-T_9-2	0.143	0.175	0.170	0.161	0.163	0.166	0.175	0.170
MW-T_9-3	0.146	0.175	0.165	0.174	0.174	0.177	0.175	0.162
MW-T_10-1	0.041	0.132	0.127	0.134	0.101	0.131	0.131	0.104
MW-T_10-2	0.039	0.126	0.124	0.124	0.099	0.129	0.131	0.098
MW-T_10-3	0.040	0.129	0.124	0.126	0.094	0.139	0.128	0.098
MW-T_11-1	0.058	0.135	0.141	0.140	0.140	0.154	0.133	0.132
MW-T_11-2	0.062	0.137	0.144	0.135	0.142	0.153	0.132	0.127
MW-T_11-3	0.060	0.139	0.144	0.142	0.138	0.161	0.131	0.131
MW-T_12-1	0.122	0.158	0.119	0.155	0.157	0.170	0.162	0.147
MW-T_12-2	0.124	0.160	0.123	0.159	0.150	0.168	0.167	0.149
MW-T_12-3	0.126	0.162	0.124	0.160	0.143	0.169	0.166	0.151

APPENDIX 19 DISSOLUTION RATES (IN G/M^2/D) FOR TRIPLICATE EXPERIMENTS MEASURED IN DEIONISED WATER AT 90 ^{O}C.

Experiment ID	Al	B	Cs	Li	Mg	Mo	Na	Si
MW-T_13-1	1.824	1.782	1.921	1.848	1.809	1.911	1.788	1.871
MW-T_13-2	1.805	1.819	1.893	1.813	1.792	1.779	1.833	1.848
MW-T_13-3	1.741	1.799	1.856	1.829	1.919	1.830	1.809	1.741
MW-T_14-1	1.434	1.779	1.599	2.019	1.549	1.377	1.803	1.627
MW-T_14-2	1.456	1.763	1.538	1.86	1.556	1.336	1.809	1.604
MW-T_14-3	1.340	1.828	1.543	1.881	1.485	1.367	1.938	1.629
MW-T_15-1	1.749	1.824	1.775	1.892	1.864	1.491	1.794	1.836
MW-T_15-2	1.730	1.809	1.768	1.748	1.750	1.508	1.811	1.813
MW-T_15-3	1.771	1.827	1.767	1.910	1.756	1.531	1.885	1.811
MW-T_16-1	0.984	2.209	0.744	1.906	0.836	2.458	2.179	1.547
MW-T_16-2	0.952	1.850	0.732	1.940	0.809	2.535	2.227	1.523
MW-T_16-3	0.944	2.241	0.762	1.824	0.851	2.477	2.254	1.610
MW-T_17-1	1.641	1.750	1.621	1.567	1.753	1.709	1.732	1.789
MW-T_17-2	1.705	1.640	1.646	1.617	1.685	1.757	1.693	1.790
MW-T_17-3	1.724	1.800	1.503	1.676	1.722	1.724	1.675	1.731
MW-T_18-1	0.658	2.571	0.947	2.800	0.428	2.936	2.536	1.545
MW-T_18-2	0.650	2.301	0.957	2.697	0.440	2.913	2.443	1.453
MW-T_18-3	0.672	2.418	0.979	2.783	0.434	2.821	2.581	1.472
MW-T_19-1	1.346	2.148	1.447	1.743	1.264	1.995	2.260	1.569
MW-T_19-2	1.324	1.992	1.511	1.676	1.235	1.950	2.189	1.551
MW-T_19-3	1.290	2.100	1.452	1.801	1.281	2.055	2.151	1.620
MW-T_20-1	0.433	3.896	0.878	3.888	0.395	3.626	3.467	1.415
MW-T_20-2	0.425	4.038	0.855	3.940	0.391	3.565	3.618	1.420
MW-T_20-3	0.432	3.766	0.781	3.812	0.384	3.789	3.415	1.455
MW-T_21-1	0.843	2.015	1.087	1.898	0.750	1.966	2.324	1.560
MW-T_21-2	0.926	1.950	1.107	1.971	0.743	2.003	2.264	1.560
MW-T_21-3	0.901	1.945	1.106	1.891	0.760	1.821	2.312	1.470
MW-T_22-1	0.039	4.471	0.513	4.463	0.115	3.683	4.367	1.350
MW-T_22-2	0.041	4.370	0.479	4.484	0.109	3.700	4.652	1.385
MW-T_22-3	0.040	4.569	0.484	4.403	0.115	3.657	4.631	1.375
MW-T_23-1	0.448	3.966	0.717	3.798	0.434	3.734	3.973	1.438
MW-T_23-2	0.458	3.762	0.711	3.876	0.486	3.694	3.726	1.443
MW-T_23-3	0.444	3.642	0.771	3.906	0.460	3.942	3.881	1.469
MW-T_24-1	0.031	4.531	0.155	4.271	0.186	3.045	4.344	0.910
MW-T_24-2	0.030	4.463	0.168	4.016	0.183	3.258	4.076	0.979
MW-T_24-3	0.029	4.536	0.163	4.403	0.195	3.087	4.27	0.931

APPENDIX 20 PROPAGATION OF UNCERTAINTIES FOR RATES MEASURED IN DEIONISED WATER AT 40 AND 90 ^{o}C. THE MEAN VALUES OF FLOW RATE (Q), SURFACE AREA (S), AND NORMALISED CONCENTRATION (C) CAN BE FOUND IN TABLES 3.1, 3.2 AND 3.3, RESPECTIVELY.

Table 9.1: Uncertainties in the rates calculated based on Si release in deionised water. Note that the uncertainty in the analysed mass fraction of Si is 0.0014899 (from Appendix 4).

Experiment ID	q (m/s3) Uncertainty	S (m2) Uncertainty	C of Si (g/m3) Uncertainty	(dNR/dC)^2 *Qc^2	(dNR/dF)^2* QF^2	(dNR/dS)^2* QS^2	(dNR/df)^2* Qf^2	QNR^2	QNR (g/(m2s))	QNR (g/(m2d))
MW-T_1	1.1905E-11	5.94678E-05	0.027266314	7.873E-14	2.67374E-16	2.44605E-14	1.98124E-15	1.05E-13	3.04102E-07	0.026274
MW-T_2	1.8297E-11	0.000105293	0.093234329	7.5667E-14	1.76523E-16	9.6262E-16	5.87324E-16	7.74E-14	1.85353E-07	0.016014
MW-T_3	6.8965E-12	6.45372E-05	0.046713382	6.6782E-14	2.82781E-16	1.44968E-14	1.04869E-15	8.26E-14	2.61795E-07	0.022619
MW-T_4	8.9266E-12	6.75663E-05	0.126179778	1.961E-14	1.27637E-16	3.06775E-16	4.5443E-16	2.05E-14	1.22918E-07	0.01062
MW-T_5	9.8901E-12	2.08157E-05	0.062626987	4.8248E-14	8.71462E-16	1.24389E-15	7.95291E-16	5.12E-14	1.86879E-07	0.016146
MW-T_6	9.8886E-12	2.45685E-05	0.223037296	3.5761E-14	2.96889E-16	2.63848E-17	2.98477E-16	3.64E-14	1.2814E-07	0.011071
MW-T_7	6.2453E-12	1.71264E-05	0.02720103	4.6603E-14	1.85979E-15	3.45174E-14	2.21729E-15	8.52E-14	2.74357E-07	0.023704
MW-T_8	9.5003E-12	1.4158E-05	0.134007611	4.2391E-14	1.80787E-15	4.21093E-16	8.84827E-16	4.55E-14	2.06088E-07	0.017806
MW-T_9	6.7439E-12	9.00798E-06	0.017242566	3.5296E-15	3.90023E-15	3.06512E-15	7.42687E-16	1.12E-14	1.02334E-07	0.008842
MW-T_10	7.6835E-12	1.71247E-05	0.099652051	6.2933E-15	2.61308E-15	3.39031E-16	4.93219E-16	9.74E-15	9.6738E-08	0.008358
MW-T_11	3.7516E-13	1.01891E-05	0.123820962	4.1682E-14	4.92097E-17	2.66742E-15	4.86611E-16	4.49E-14	1.87753E-07	0.016222
MW-T_12	3.4544E-13	1.0445E-05	0.437580137	1.8231E-14	5.04328E-17	8.44021E-17	3.20783E-16	1.87E-14	1.34403E-07	0.011612
MW-T_13	1.9546E-11	0.000318332	0.218804747	3.9212E-12	3.77135E-14	2.74709E-11	8.94965E-14	3.15E-11	5.60331E-06	0.484126
MW-T_14	3.1583E-11	0.00039865	0.896113907	2.8445E-12	7.3777E-14	1.45993E-12	6.19375E-14	4.44E-12	2.09586E-06	0.181082
MW-T_15	1.4778E-11	0.000132892	0.331270638	2.3015E-12	4.05958E-14	2.68269E-12	4.70415E-14	5.07E-12	2.23344E-06	0.192969
MW-T_16	8.8976E-12	0.00012963	0.056637221	2.9646E-15	1.24064E-14	8.90757E-14	3.61353E-14	1.41E-13	3.74861E-07	0.032388
MW-T_17	6.4841E-12	0.000212777	0.642220527	2.9135E-12	2.58279E-14	6.00205E-12	4.74769E-14	8.99E-12	2.96302E-06	0.256005
MW-T_18	6.2025E-12	7.84344E-05	2.378287829	1.8043E-12	1.85882E-14	2.37396E-14	2.98606E-14	1.88E-12	1.27663E-06	0.110301
MW-T_19	3.5406E-12	8.68659E-05	1.105774322	3.0681E-12	1.28935E-14	8.80552E-13	4.40216E-14	4.01E-12	1.99541E-06	0.172403
MW-T_20	6.6956E-12	0.000129963	3.653424559	2.2182E-12	3.66024E-14	8.29414E-14	3.35121E-14	2.37E-12	1.42251E-06	0.122905
MW-T_21	6.3787E-12	3.9819E-05	0.993755036	1.6045E-12	1.73718E-13	2.8228E-13	4.74638E-14	2.11E-12	1.25E-06	0.108
MW-T_22	3.3985E-11	6.91918E-05	9.204952748	3.1093E-12	5.78419E-12	2.8386E-14	3.63891E-14	8.96E-12	2.80853E-06	0.242657
MW-T_23	2.9946E-12	5.79113E-05	6.452986861	9.1879E-12	4.14173E-13	9.76462E-13	7.252E-14	1.07E-11	2.91253E-06	0.251643
MW-T_24	2.1915E-12	6.22353E-05	4.34391234	1.1557E-13	2.66916E-14	5.94942E-15	9.56174E-15	1.58E-13	3.90516E-07	0.033741

Table 9.2: Uncertainties in the rates calculated based on B release in deionised water. Note that the uncertainty in the analysed mass fraction of B is 0.0003510 (from Appendix 4).

Experiment ID	q (m/s3) Uncertainty	S (m2) Uncertainty	C of B (g/m3) Uncertainty	(dNR/dC)^ 2*Qc^2	(dNR/dF)^2* QF^2	(dNR/dS)^ 2*QS^2	(dNR/df)^2 *Qf^2	QNR^2	QNR (g/(m2s))	QNR (g/(m2d))
MW-T_1	1.1905E-11	5.93556E-05	0.013612842	3.716E-13	6.32034E-16	5.809E-14	9.3519E-15	4.397E-13	6.18E-07	0.0533992
MW-T_2	1.8297E-11	0.000105553	0.044491389	2.033E-13	6.11586E-16	3.254E-15	3.9116E-15	2.11E-13	3.775E-07	0.0326198
MW-T_3	6.8965E-12	6.44347E-05	0.016038044	9.382E-14	5.70476E-16	2.453E-14	3.5261E-15	1.224E-13	3.453E-07	0.029835
MW-T_4	8.9266E-12	6.77028E-05	0.042648344	4.144E-14	3.14782E-16	7.454E-16	2.1799E-15	4.468E-14	1.812E-07	0.0156566
MW-T_5	9.8901E-12	2.07864E-05	0.011094249	2.155E-14	1.78818E-15	2.336E-15	2.9664E-15	2.864E-14	1.568E-07	0.0135485
MW-T_6	9.8886E-12	2.42558E-05	0.067826316	4.281E-14	8.42061E-16	6.788E-17	1.5667E-15	4.529E-14	1.722E-07	0.0148744
MW-T_7	6.2453E-12	1.71253E-05	0.015264931	3.044E-13	2.87069E-15	5.368E-14	6.8333E-15	3.678E-13	5.284E-07	0.0456566
MW-T_8	9.5003E-12	1.41395E-05	0.055030665	1.441E-13	8.32932E-15	1.937E-15	8.0829E-15	1.624E-13	3.846E-07	0.0332285
MW-T_9	6.7439E-12	9.01821E-06	0.012979034	4.705E-14	1.03294E-14	7.194E-15	3.4474E-15	6.802E-14	2.239E-07	0.0193474
MW-T_10	7.6835E-12	1.70692E-05	0.087105685	1.296E-13	1.27088E-14	1.653E-15	4.7867E-15	1.487E-13	3.258E-07	0.0281478
MW-T_11	3.7516E-13	1.01931E-05	0.031295456	4.658E-14	5.96022E-17	3.918E-15	1.4149E-15	5.198E-14	2.043E-07	0.0176547
MW-T_12	3.4544E-13	1.07362E-05	0.068844509	7.88E-15	3.27797E-16	7.115E-16	5.1035E-15	1.402E-14	1.183E-07	0.0102191
MW-T_13	1.9546E-11	0.000318402	0.01676118	3.675E-13	1.43444E-14	1.034E-11	6.1605E-14	1.078E-11	3.28E-06	0.2834274
MW-T_14	3.1583E-11	0.000398099	0.162032715	4.306E-12	6.71059E-14	1.33E-12	1.0325E-13	5.806E-12	2.012E-06	0.1738695
MW-T_15	1.4778E-11	0.00013371	0.045745514	8.476E-13	1.13461E-14	7.485E-13	2.3775E-14	1.631E-12	1.239E-06	0.1070151
MW-T_16	8.8976E-12	0.000129885	0.20416706	7.249E-13	9.60482E-15	7.152E-14	5.2788E-14	8.588E-13	8.987E-07	0.0776476
MW-T_17	6.4841E-12	0.000212777	0.065050188	6.077E-13	5.63913E-15	1.291E-12	1.8626E-14	1.923E-12	1.379E-06	0.1191332
MW-T_18	6.2025E-12	7.84344E-05	0.24489406	3.203E-13	1.46103E-14	1.854E-14	4.2532E-14	3.96E-13	6.197E-07	0.053545
MW-T_19	3.5406E-12	8.74089E-05	0.288579225	6.857E-12	2.41925E-14	1.707E-12	1.5242E-13	8.741E-12	2.658E-06	0.2296692
MW-T_20	6.6956E-12	0.000135438	2.39779576	1.721E-11	3.3199E-13	8.364E-13	5.3944E-13	1.892E-11	4.138E-06	0.3575648
MW-T_21	6.3787E-12	3.35126E-05	0.074789846	1.081E-13	2.82545E-13	3.519E-13	1.413E-13	8.838E-13	9.317E-07	0.0804981
MW-T_22	6.2981E-12	0.000123568	4.974939809	2.874E-11	1.34751E-12	1.329E-12	7.0825E-13	3.212E-11	4.993E-06	0.4313587
MW-T_23	2.9946E-12	5.05632E-05	1.679798334	2.008E-11	1.54253E-12	3.527E-12	5.0644E-13	2.566E-11	4.227E-06	0.3651924
MW-T_24	2.1915E-12	5.6291E-05	8.608471141	1.277E-11	1.08917E-12	3.737E-13	7.2813E-13	1.497E-11	3.64E-06	0.3145163

Table 9.3: Uncertainties in the rates calculated based on Na release in deionised water. Note that the uncertainty in the analysed mass fraction of Na is 0.0004267 (from Appendix 4).

Experiment ID	q (m/s3) Uncertainty	S (m2) Uncertainty	C of Na (g/m3) Uncertainty	(dNR/dC)^2 *Qc^2	(dNR/dF)^ 2*QF^2	(dNR/dS)^2 *QS^2	(dNR/df)^2 *Qf^2	QNR^2	QNR (g/(m2s))	QNR (g/(m2d))
MW-T_1	1.19052E-11	5.9351E-05	0.013218071	1.85192E-13	5.151E-16	4.6999E-14	1.067E-14	2.43378E-13	4.841E-07	0.0418288
MW-T_2	1.82973E-11	0.00010555	0.041307217	1.29026E-13	4.553E-16	2.4083E-15	4.084E-15	1.35974E-13	2.959E-07	0.0255625
MW-T_3	6.89647E-12	6.451E-05	0.014577298	5.68476E-14	4.758E-16	2.0122E-14	4.071E-15	8.15173E-14	2.744E-07	0.0237123
MW-T_4	8.92663E-12	6.7859E-05	0.067718926	8.17695E-14	2.431E-16	5.7747E-16	2.375E-15	8.49652E-14	2.307E-07	0.0199316
MW-T_5	9.89011E-12	2.076E-05	0.010564035	1.08388E-14	1.388E-15	1.7972E-15	3.225E-15	1.72485E-14	1.303E-07	0.0112603
MW-T_6	9.88865E-12	2.4689E-05	0.079622106	3.96751E-14	6.293E-16	5.2007E-17	1.642E-15	4.19985E-14	1.666E-07	0.0143915
MW-T_7	6.24527E-12	1.7128E-05	0.008645238	5.41614E-14	3.341E-15	6.1821E-14	1.11E-14	1.30426E-13	3.527E-07	0.0304738
MW-T_8	9.50034E-12	1.4138E-05	0.089743591	2.84806E-13	7.73E-15	1.8027E-15	1.061E-14	3.04952E-13	4.931E-07	0.0426077
MW-T_9	6.74393E-12	9.0179E-06	0.021290773	8.59618E-14	1.012E-14	7.1207E-15	4.816E-15	1.08015E-13	2.861E-07	0.0247214
MW-T_10	7.68345E-12	1.7073E-05	0.125830747	1.0821E-13	1.107E-14	1.4401E-15	5.887E-15	1.26606E-13	3.474E-07	0.0300153
MW-T_11	3.75159E-13	1.0198E-05	0.032690889	3.47102E-14	6.053E-17	3.3954E-15	1.729E-15	3.98952E-14	1.792E-07	0.0154824
MW-T_12	3.45436E-13	1.0686E-05	0.137514408	3.75168E-14	2.589E-16	5.5825E-16	5.697E-15	4.40309E-14	1.725E-07	0.0149033
MW-T_13	1.95457E-11	0.00031855	0.02346291	6.17597E-13	2.471E-14	1.796E-11	1.632E-13	1.87653E-11	4.331E-06	0.3742129
MW-T_14	3.15834E-11	0.00039878	0.286758322	6.25532E-12	7.936E-14	1.5496E-12	1.83E-13	8.06727E-12	2.545E-06	0.2198755
MW-T_15	1.47782E-11	0.00013292	0.082922464	2.73703E-12	2.525E-14	1.6553E-12	8.102E-14	4.49858E-12	1.99E-06	0.1719451
MW-T_16	8.89761E-12	0.0001317	0.440818337	2.04808E-12	1.37E-14	1.0357E-13	1.133E-13	2.27866E-12	1.506E-06	0.1301605
MW-T_17	6.48412E-12	0.00021278	0.113297711	9.44183E-13	1.235E-14	2.8542E-12	6.314E-14	3.87383E-12	1.967E-06	0.1699897
MW-T_18	6.20252E-12	7.8434E-05	0.576721254	1.1631E-12	2.062E-14	2.646E-14	9.307E-14	1.30325E-12	1.121E-06	0.096896
MW-T_19	3.54058E-12	8.7409E-05	0.384132045	5.62344E-12	2.697E-14	1.8717E-12	2.564E-13	7.77849E-12	2.697E-06	0.2330199
MW-T_20	6.69564E-12	0.00013544	1.984033399	8.07631E-12	1.669E-13	4.4473E-13	4.466E-13	9.13462E-12	2.84E-06	0.2453551
MW-T_21	6.37866E-12	3.3513E-05	0.477695507	3.56289E-12	3.753E-13	4.6376E-13	2.867E-13	4.68864E-12	2.003E-06	0.1730823
MW-T_22	6.29807E-12	0.00012357	6.764254604	3.26452E-11	1.365E-12	1.3504E-12	1.099E-12	3.64593E-11	5.48E-06	0.4734708
MW-T_23	2.99463E-12	5.0563E-05	1.041067947	2.79702E-12	2.818E-12	6.3408E-12	1.299E-12	1.32544E-11	3.497E-06	0.3021215
MW-T_24	2.19145E-12	5.6291E-05	7.481727359	6.64097E-12	7.763E-13	2.7066E-13	7.745E-13	8.46239E-12	2.766E-06	0.2389711

Table 9.4: Uncertainties in the rates calculated based on Li release in deionised water. Note that the uncertainty in the analysed mass fraction of Li is 0.0001257 (from Appendix 4).

Experiment ID	q (m/s3) Uncertainty	S (m2) Uncertainty	C of Li (g/m3) Uncertainty	(dNR/dC)^ 2*Qc^2	(dNR/dF)^ 2*QF^2	(dNR/dS)^ 2*QS^2	(dNR/df)^ 2*Qf^2	QNR^2	QNR (g/(m2s))	QNR (g/(m2d))
MW-T_1	1.1905E-11	5.9356E-05	0.002976854	1.5085E-13	3.653E-16	3.359E-14	5.42E-13	7.26817E-13	8.5029E-07	0.073465
MW-T_2	1.8297E-11	0.00010558	0.017552659	2.1541E-13	3.904E-16	2.056E-15	2.475E-13	4.65367E-13	6.7218E-07	0.058077
MW-T_3	6.8965E-12	6.4457E-05	0.002745407	2.5523E-14	2.973E-16	1.29E-14	1.858E-13	2.24551E-13	4.6705E-07	0.040354
MW-T_4	8.9266E-12	6.7887E-05	0.014763143	6.9835E-14	1.806E-16	4.293E-16	1.254E-13	1.95803E-13	4.2335E-07	0.036577
MW-T_5	9.8901E-12	2.0766E-05	0.002660133	8.8436E-15	1.001E-15	1.304E-15	1.663E-13	1.77432E-13	4.172E-07	0.036046
MW-T_6	9.8886E-12	2.4387E-05	0.021019448	2.8105E-14	4.842E-16	3.914E-17	8.991E-14	1.18533E-13	3.4241E-07	0.029584
MW-T_7	6.2453E-12	1.7126E-05	0.003878881	1.4894E-13	2.58E-15	4.792E-14	6.116E-13	8.11067E-13	8.3004E-07	0.071715
MW-T_8	9.5003E-12	1.4147E-05	0.023247511	1.9431E-13	6.275E-15	1.461E-15	6.108E-13	8.12857E-13	8.8229E-07	0.07623
MW-T_9	6.7439E-12	9.0114E-06	0.004292268	4.579E-14	8.196E-15	5.907E-15	2.842E-13	3.44077E-13	5.2065E-07	0.044984
MW-T_10	7.6835E-12	1.7077E-05	0.03161734	1.0632E-13	9.592E-15	1.249E-15	3.627E-13	4.79906E-13	6.7264E-07	0.058116
MW-T_11	3.7516E-13	1.0197E-05	0.010807021	3.7617E-14	6.061E-17	3.36E-15	1.216E-13	1.62644E-13	3.9277E-07	0.033935
MW-T_12	3.4544E-13	1.0687E-05	0.068117498	1.6909E-13	2.462E-16	5.292E-16	3.836E-13	5.53519E-13	7.0565E-07	0.060968
MW-T_13	1.9546E-11	0.00031839	0.012468021	3.351E-12	1.733E-14	1.243E-11	8.045E-12	2.38439E-11	4.853E-06	0.419297
MW-T_14	3.1583E-11	0.00039841	0.08479378	4.2917E-12	7.196E-14	1.411E-12	1.187E-11	1.76441E-11	4.1719E-06	0.360449
MW-T_15	1.4778E-11	0.00013315	0.018592528	1.4049E-12	1.757E-14	1.153E-12	4.005E-12	6.58094E-12	2.5472E-06	0.22008
MW-T_16	8.8976E-12	0.00013089	0.073357941	7.6675E-13	1.039E-14	7.746E-14	6.106E-12	6.96046E-12	2.6368E-06	0.22782
MW-T_17	6.4841E-12	0.00021278	0.030825731	9.2174E-13	8.756E-15	2.068E-12	3.251E-12	6.24943E-12	2.4967E-06	0.215717
MW-T_18	6.2025E-12	7.8434E-05	0.093201134	4.3922E-13	1.495E-14	1.905E-14	4.761E-12	5.23467E-12	2.2869E-06	0.197592
MW-T_19	3.5406E-12	8.7409E-05	0.087436235	3.977E-12	1.742E-14	1.214E-12	1.181E-11	1.7023E-11	4.108E-06	0.354934
MW-T_20	6.6956E-12	0.00013544	0.4737591	8.6089E-12	2.247E-13	5.645E-13	3.959E-11	4.89868E-11	6.9713E-06	0.602322
MW-T_21	6.3787E-12	3.3513E-05	0.17101087	4.6115E-12	3.506E-13	4.367E-13	1.908E-11	2.44812E-11	4.9011E-06	0.423454
MW-T_22	6.2981E-12	0.00012357	2.010050535	3.5688E-11	1.48E-12	1.459E-12	8.461E-11	1.23232E-10	1.0996E-05	0.950057
MW-T_23	2.9946E-12	5.0563E-05	0.738945341	2.1041E-11	3.027E-12	6.818E-12	9.899E-11	1.29873E-10	1.1183E-05	0.96619
MW-T_24	2.1915E-12	5.6291E-05	1.909214619	5.242E-12	1.084E-12	3.772E-13	7.652E-11	8.32182E-11	9.0795E-06	0.78447

Table 9.5: Uncertainties in the rates calculated based on Mg release in deionised water. Note that the uncertainty in the analysed mass fraction of Mg is 0.0001836 (from Appendix 4).

Experiment ID	q (m/s3) Uncertainty	S (m2) Uncertainty	C of Mg (g/m3) Uncertainty	(dNR/dC)^ 2*Qc^2	(dNR/dF)^ 2*QF^2	(dNR/dS)^ 2*QS^2	(dNR/df)^ 2*Qf^2	QNR^2	QNR (g/(m2s))	QNR (g/(m2d))
MW-T_1	1.19052E-11	5.9394E-05	0.003025452	4.769E-14	1.419E-16	1.31E-14	1.838E-13	2.44717E-13	4.94E-07	0.042696
MW-T_2	1.82973E-11	0.00010549	0.001515622	4.964E-16	4.366E-17	2.474E-16	2.602E-14	2.68064E-14	1.63E-07	0.014066
MW-T_3	6.89647E-12	6.4489E-05	0.006511534	5.11E-14	1.499E-16	7.683E-15	9.62E-14	1.55134E-13	3.92E-07	0.033899
MW-T_4	8.92663E-12	6.7717E-05	0.010627155	8.387E-15	3.482E-17	8.478E-17	2.16E-14	3.0107E-14	1.72E-07	0.01484
MW-T_5	9.89011E-12	2.0745E-05	0.004704977	1.046E-14	5.758E-16	8.025E-16	8.922E-14	1.01057E-13	3.17E-07	0.027415
MW-T_6	9.88865E-12	2.4675E-05	0.006963499	9.353E-16	1.009E-16	9.436E-18	1.82E-14	1.9242E-14	1.38E-07	0.011959
MW-T_7	6.24527E-12	1.7133E-05	0.006737305	1.558E-13	2.3E-15	4.399E-14	4.885E-13	6.90539E-13	8E-07	0.069108
MW-T_8	9.50034E-12	1.4155E-05	0.018099209	4.564E-14	2.506E-15	5.835E-16	2.122E-13	2.6092E-13	5.09E-07	0.044008
MW-T_9	6.74393E-12	9.0233E-06	0.008538427	8.231E-14	7.161E-15	5.564E-15	2.325E-13	3.27529E-13	5.17E-07	0.044669
MW-T_10	7.68345E-12	1.713E-05	0.010111106	4.977E-15	3.872E-15	5.035E-16	1.266E-13	1.35978E-13	3.67E-07	0.031684
MW-T_11	3.75159E-13	1.0198E-05	0.015364437	2.913E-14	6.767E-17	3.559E-15	1.121E-13	1.44879E-13	3.76E-07	0.03251
MW-T_12	3.45436E-13	1.0404E-05	0.048721804	1.4E-14	7.886E-17	1.256E-16	8.317E-14	9.73754E-14	3.1E-07	0.026825
MW-T_13	1.95457E-11	0.00031868	0.011616908	5.722E-13	1.757E-14	1.231E-11	6.917E-12	1.98152E-11	4.45E-06	0.384101
MW-T_14	3.15834E-11	0.00039822	0.027969237	3.829E-13	2.588E-15	5.542E-14	4.087E-13	8.49592E-13	8.72E-07	0.075372
MW-T_15	1.47782E-11	0.00013318	0.022236401	8.529E-13	1.002E-14	6.547E-13	1.979E-12	3.49675E-12	1.86E-06	0.160419
MW-T_16	8.89761E-12	0.00012875	0.014893589	1.255E-14	6.767E-17	5.052E-16	3.609E-14	4.92114E-14	2.2E-07	0.019014
MW-T_17	6.48412E-12	0.00021278	0.035886082	4.99E-13	4.422E-15	1.157E-12	1.585E-12	3.24581E-12	1.79E-06	0.154372
MW-T_18	6.20252E-12	7.8434E-05	0.013158811	3.564E-15	2.444E-17	3.457E-17	7.528E-15	1.11513E-14	1.04E-07	0.009026
MW-T_19	3.54058E-12	8.7409E-05	0.045105213	3.98E-13	1.627E-15	1.122E-13	9.514E-13	1.46313E-12	1.2E-06	0.103952
MW-T_20	6.69564E-12	0.00013544	0.018806855	3.527E-15	1.073E-16	2.842E-16	1.768E-14	2.16003E-14	1.47E-07	0.012662
MW-T_21	6.37866E-12	3.3513E-05	0.044920446	1.193E-13	5.965E-15	7.697E-15	2.822E-13	4.15158E-13	6.4E-07	0.055297
MW-T_22	6.29807E-12	0.00012357	0.054044949	1.083E-14	7.232E-16	6.037E-16	3.73E-14	4.94579E-14	2.17E-07	0.018739
MW-T_23	2.99463E-12	5.0563E-05	0.132036432	2.434E-13	2.175E-14	4.929E-14	6.324E-13	9.468E-13	9.53E-07	0.082322
MW-T_24	2.19145E-12	5.6291E-05	0.130624025	8.639E-15	1.691E-15	5.75E-16	1.054E-13	1.16327E-13	3.39E-07	0.029319

Table 9.6: Uncertainties in the rates calculated based on Al release in deionised water. Note that the uncertainty in the analysed mass fraction of Al is 0.0001540 (from Appendix 4).

Experiment ID	q (m/s3) Uncertainty	S (m2) Uncertainty	C of Al (g/m3) Uncertainty	(dNR/dC) ^2*Qc^2	(dNR/dF)^ 2*QF^2	(dNR/dS)^ 2*QS^2	(dNR/df)^ 2*Qf^2	QNR^2	QNR (g/(m2s))	QNR (g/(m2d))
MW-T_1	1.19052E-11	5.9457E-05	0.000169917	1.963E-16	5.795E-19	8.402E-17	2.157E-15	2.43784E-15	4.67146E-08	0.004036
MW-T_2	1.82973E-11	0.00010564	0.002126501	1.336E-15	8.247E-18	4.382E-17	8.414E-15	9.80173E-15	9.78937E-08	0.008458
MW-T_3	6.89647E-12	6.4447E-05	0.00131845	2.852E-15	8.127E-18	8.041E-16	1.843E-14	2.20899E-14	1.40427E-07	0.012133
MW-T_4	8.92663E-12	6.7333E-05	0.0061772	3.772E-15	3.249E-18	7.818E-18	3.689E-15	7.47196E-15	8.52572E-08	0.007366
MW-T_5	9.89011E-12	2.0757E-05	0.001017596	1.54E-15	2.346E-17	4.53E-17	9.233E-15	1.08421E-14	9.97261E-08	0.008616
MW-T_6	9.88865E-12	2.4329E-05	0.002481976	1.727E-16	1.232E-17	1.353E-18	4.844E-15	5.03048E-15	6.65883E-08	0.005753
MW-T_7	6.24527E-12	1.7131E-05	0.001874416	2.028E-14	2.663E-16	4.681E-15	9.524E-14	1.20472E-13	3.44295E-07	0.029747
MW-T_8	9.50034E-12	1.417E-05	0.007908929	1.35E-14	3.506E-16	8.32E-17	5.53E-14	6.92337E-14	2.55108E-07	0.022041
MW-T_9	6.74393E-12	8.9847E-06	0.002423002	9.374E-15	1.19E-15	9.708E-16	7.485E-14	8.63881E-14	2.84131E-07	0.024549
MW-T_10	7.68345E-12	1.7168E-05	0.010929623	6.094E-15	5.615E-16	7.376E-17	3.383E-14	4.05636E-14	1.97578E-07	0.017071
MW-T_11	3.75159E-13	1.022E-05	0.003878674	2.875E-15	3.777E-18	2.248E-16	1.293E-14	1.60362E-14	1.22643E-07	0.010596
MW-T_12	3.45436E-13	1.0383E-05	0.012272391	1.739E-15	4.891E-18	4.377E-18	5.339E-15	7.08747E-15	8.09498E-08	0.006994
MW-T_13	1.95457E-11	0.00031868	0.005070522	1.594E-13	6.98E-15	4.703E-12	4.837E-12	9.70577E-12	3.10428E-06	0.26821
MW-T_14	3.15834E-11	0.00039851	0.007102793	1.46E-14	3.667E-15	7.615E-14	1.026E-12	1.12023E-12	1.05704E-06	0.091328
MW-T_15	1.47782E-11	0.00013335	0.006595454	8E-14	4.816E-15	3.138E-13	1.73E-12	2.12889E-12	1.42263E-06	0.122915
MW-T_16	8.89761E-12	0.00012906	0.019606803	2.729E-14	3.842E-16	2.68E-15	3.481E-13	3.78494E-13	6.15091E-07	0.053144
MW-T_17	6.48412E-12	0.00021278	0.028751993	5.143E-13	3.322E-15	7.618E-13	1.909E-12	3.18891E-12	1.78499E-06	0.154223
MW-T_18	6.20252E-12	7.8434E-05	0.024052234	1.533E-14	2.277E-16	3.182E-16	1.269E-13	1.42791E-13	3.77443E-07	0.032611
MW-T_19	3.54058E-12	8.6866E-05	0.049114215	5.147E-13	2.878E-15	1.902E-13	3.016E-12	3.72419E-12	1.89359E-06	0.163606
MW-T_20	6.69564E-12	0.00012996	0.038821027	2.185E-14	6.211E-16	1.542E-15	1.98E-13	2.22008E-13	4.70149E-07	0.040621
MW-T_21	6.37866E-12	3.9819E-05	0.073587894	3.67E-13	3.116E-14	5.498E-14	2.752E-12	3.20496E-12	1.78022E-06	0.153811
MW-T_22	6.29807E-12	6.9192E-05	0.014270625	1.352E-15	1.165E-16	3.563E-17	1.264E-14	1.4145E-14	9.77104E-08	0.008442
MW-T_23	2.99463E-12	5.7911E-05	0.042542417	2.464E-14	3.654E-15	9.931E-15	2.227E-13	2.60897E-13	4.62681E-07	0.039976
MW-T_24	2.19145E-12	6.2235E-05	0.005403143	2.309E-17	9.407E-17	3.257E-17	1.62E-14	1.63523E-14	1.20781E-07	0.010435

Table 9.7: Uncertainties in the rates calculated based on Cs release in deionised water. Note that the uncertainty in the analysed mass fraction of Cs is 0.0000638 (from Appendix 4).

Experiment ID	q (m/s3) Uncertainty	S (m2) Uncertainty	C of Cs (g/m3) Uncertainty	(dNR/dC)^ 2*Qc^2	(dNR/dF)^ 2*QF^2	(dNR/dS)^ 2*QS^2	(dNR/df)^ 2*Qf^2	QNR^2	QNR (g/(m2s))	QNR (g/(m2d))
MW-T_1	1.1905E-11	5.93556E-05	0.000861284	4.084E-14	1.841E-14	1.692E-12	4.573E-12	6.32356E-12	2.5E-06	0.216278
MW-T_2	1.8297E-11	0.000105553	0.002655528	3.205E-14	1.781E-14	9.476E-14	1.913E-12	2.05722E-12	1.43E-06	0.123355
MW-T_3	6.8965E-12	6.44347E-05	0.000853804	1.051E-14	1.661E-14	7.144E-13	1.724E-12	2.46564E-12	1.54E-06	0.133211
MW-T_4	8.9266E-12	6.77028E-05	0.003264834	9.861E-15	9.167E-15	2.171E-14	1.066E-12	1.1066E-12	1.05E-06	0.090409
MW-T_5	9.8901E-12	2.07864E-05	0.003230783	8.214E-14	5.207E-14	6.803E-14	1.45E-12	1.6527E-12	1.28E-06	0.110319
MW-T_6	9.8886E-12	2.42558E-05	0.002957314	2.795E-15	2.452E-14	1.977E-15	7.661E-13	7.95362E-13	8.87E-07	0.076659
MW-T_7	6.2453E-12	1.71253E-05	0.001026493	6.526E-14	8.36E-14	1.563E-12	3.341E-12	5.05329E-12	2.07E-06	0.179032
MW-T_8	9.5003E-12	1.41395E-05	0.002503067	8.961E-15	2.426E-13	5.642E-14	3.952E-12	4.26012E-12	2.02E-06	0.174306
MW-T_9	6.7439E-12	9.01821E-06	0.003613363	9.078E-14	3.008E-13	2.095E-13	1.686E-12	2.28674E-12	1.35E-06	0.116385
MW-T_10	7.6835E-12	1.70692E-05	0.020007286	1.6E-13	3.701E-13	4.813E-14	2.34E-12	2.91869E-12	1.66E-06	0.143335
MW-T_11	3.7516E-13	1.01931E-05	0.006020687	5.943E-14	1.736E-15	1.141E-13	6.918E-13	8.67097E-13	8.69E-07	0.075059
MW-T_12	3.4544E-13	1.07362E-05	0.036344509	8.8E-14	9.546E-15	2.072E-14	2.495E-12	2.61364E-12	1.6E-06	0.138307
MW-T_13	1.9546E-11	0.000318402	0.010387879	4.113E-12	4.08E-13	2.941E-10	3.196E-11	3.30629E-10	1.82E-05	1.569333
MW-T_14	3.1583E-11	0.000398099	0.025219237	2.649E-12	1.909E-12	3.782E-11	5.356E-11	9.59431E-11	9.77E-06	0.843702
MW-T_15	1.4778E-11	0.00013371	0.014236401	2.893E-12	3.227E-13	2.129E-11	1.233E-11	3.68404E-11	6.06E-06	0.523481
MW-T_16	8.8976E-12	0.000129885	0.008398	3.432E-14	2.732E-13	2.034E-12	2.738E-11	2.97261E-11	5.45E-06	0.470866
MW-T_17	6.4841E-12	0.000212777	0.025386082	2.619E-12	1.604E-13	3.672E-11	9.663E-12	4.91582E-11	7.01E-06	0.605547
MW-T_18	6.2025E-12	7.84344E-05	0.007994832	1.165E-14	4.156E-13	5.272E-13	2.206E-11	2.30185E-11	4.78E-06	0.412926
MW-T_19	3.5406E-12	8.74089E-05	0.044665824	3.504E-12	6.881E-13	4.855E-11	7.907E-11	1.31804E-10	1.15E-05	0.991655
MW-T_20	6.6956E-12	0.000135438	0.014049849	2.029E-14	9.443E-12	2.379E-11	2.798E-10	3.13094E-10	1.76E-05	1.523308
MW-T_21	6.3787E-12	3.35126E-05	0.037420446	8.164E-13	8.037E-12	1.001E-11	7.33E-11	9.21615E-11	9.54E-06	0.824103
MW-T_22	6.2981E-12	0.000123568	0.049044949	7.759E-14	3.833E-11	3.781E-11	3.674E-10	4.43629E-10	2.1E-05	1.81839
MW-T_23	2.9946E-12	5.05632E-05	0.077036432	6.331E-13	4.388E-11	1.003E-10	2.627E-10	4.07547E-10	2.02E-05	1.742506
MW-T_24	2.1915E-12	5.6291E-05	0.074183418	2.708E-14	3.098E-11	1.063E-11	3.777E-10	4.19365E-10	2.04E-05	1.76528

Table 9.8: Uncertainties in the rates calculated based on Mo release in deionised water. Note that the uncertainty in the analysed mass fraction of Mo is 0.0000632 (from Appendix 4).

Experiment ID	q (m/s3) Uncertainty	S (m2) Uncertainty	C of Mo (g/m3) Uncertainty	(dNR/dC)^ 2*Qc^2	(dNR/dF)^ 2*QF^2	(dNR/dS)^ 2*QS^2	(dNR/df)^ 2*Qf^2	QNR^2	QNR (g/(m2s))	QNR (g/(m2d))
MW-T_1	1.19052E-11	5.9356E-05	0.000834112	4.679E-14	1.622E-14	1.491E-12	5.967E-11	6.12282E-11	7.79E-06	0.67283
MW-T_2	1.82973E-11	0.00010555	0.004943297	4.171E-14	1.57E-14	8.352E-14	2.496E-11	2.51008E-11	4.99E-06	0.431141
MW-T_3	6.89647E-12	6.4435E-05	0.001538044	2.325E-14	1.464E-14	6.297E-13	2.25E-11	2.31674E-11	4.73E-06	0.408332
MW-T_4	8.92663E-12	6.7703E-05	0.008248808	4.865E-14	8.08E-15	1.913E-14	1.391E-11	1.39857E-11	3.72E-06	0.321523
MW-T_5	9.89011E-12	2.0786E-05	0.003306663	8.406E-14	4.59E-14	5.996E-14	1.893E-11	1.91186E-11	4.33E-06	0.373705
MW-T_6	9.88865E-12	2.4256E-05	0.018695117	8.01E-14	2.161E-14	1.742E-15	9.997E-12	1.01008E-11	3.16E-06	0.273329
MW-T_7	6.24527E-12	1.7125E-05	0.001774615	7.733E-14	7.368E-14	1.378E-12	4.36E-11	4.5132E-11	6.21E-06	0.536136
MW-T_8	9.50034E-12	1.414E-05	0.020030665	4.865E-13	2.138E-13	4.973E-14	5.158E-11	5.23268E-11	7.07E-06	0.611018
MW-T_9	6.74393E-12	9.0182E-06	0.003236211	6.539E-14	2.651E-13	1.847E-13	2.2E-11	2.25132E-11	4.18E-06	0.361214
MW-T_10	7.68345E-12	1.7069E-05	0.021257286	1.511E-13	3.262E-13	4.242E-14	3.054E-11	3.10636E-11	5.39E-06	0.465928
MW-T_11	3.75159E-13	1.0193E-05	0.004192879	2.27E-14	1.53E-15	1.006E-13	9.028E-12	9.15317E-12	2.84E-06	0.24528
MW-T_12	3.45436E-13	1.0736E-05	0.035594509	7.994E-14	8.414E-15	1.826E-14	3.257E-11	3.26718E-11	5.65E-06	0.488243
MW-T_13	1.95457E-11	0.0003184	0.009637879	3.292E-12	3.596E-13	2.593E-10	4.171E-10	6.79975E-10	2.6E-05	2.250623
MW-T_14	3.15834E-11	0.0003981	0.023969237	2.311E-12	1.682E-12	3.334E-11	6.99E-10	7.36348E-10	2.71E-05	2.339679
MW-T_15	1.47782E-11	0.00013371	0.011736401	1.631E-12	2.845E-13	1.877E-11	1.61E-10	1.81635E-10	1.34E-05	1.161608
MW-T_16	8.89761E-12	0.00012989	0.008148	2.842E-14	2.408E-13	1.793E-12	3.574E-10	3.59433E-10	1.89E-05	1.637187
MW-T_17	6.48412E-12	0.00021278	0.022886082	2.166E-12	1.414E-13	3.236E-11	1.261E-10	1.60768E-10	1.27E-05	1.095447
MW-T_18	6.20252E-12	7.8434E-05	0.006494832	7.902E-15	3.663E-13	4.647E-13	2.879E-10	2.8878E-10	1.69E-05	1.463067
MW-T_19	3.54058E-12	8.7409E-05	0.042165824	2.731E-12	6.065E-13	4.279E-11	1.032E-09	1.07797E-09	3.28E-05	2.836065
MW-T_20	6.69564E-12	0.00013544	0.013670233	1.739E-14	8.323E-12	2.097E-11	3.652E-09	3.68129E-09	6.05E-05	5.226996
MW-T_21	6.37866E-12	3.3513E-05	0.019920446	1.58E-13	7.084E-12	8.822E-12	9.566E-10	9.72636E-10	3.1E-05	2.67665
MW-T_22	6.29807E-12	0.00012357	0.046544949	6.624E-14	3.378E-11	3.332E-11	4.795E-09	4.862E-09	6.96E-05	6.017192
MW-T_23	2.99463E-12	5.0563E-05	0.059536432	3.865E-13	3.867E-11	8.842E-11	3.429E-09	3.55605E-09	5.96E-05	5.150549
MW-T_24	2.19145E-12	5.6291E-05	0.064183418	2.016E-14	2.731E-11	9.37E-12	4.929E-09	4.96611E-09	7.01E-05	6.055018

APPENDIX 21 RAW DATA OF EXPERIMENTS GW_1 AND GW_7. EXPERIMENTAL CONDITIONS ARE: Q = 250 ML/D, T = 40 ^{O}C. CONTROL-TEST DATA IS SHOWN IN THE LOWER TABLE.

Experiment ID	Mass of tared collection bottle (g)	Mass of collection bottle with solution (g)	Initial powder mass (g)	Measured flow rate (mL/d)	Final pH	Duration (hour)	Li (g/mL)	B (g/mL)	Na (g/mL)	Mg (g/mL)	Al (g/mL)	Si (g/mL)	Mo (g/mL)	Cs (g/mL)	Ca (g/mL)
GW_1-1A	24.190	49.930	0.519	247.1	6.84	2.50	1.260E-07	4.294E-07	4.272E-04	3.768E-04	4.335E-07	8.835E-06	1.056E-07	1.443E-07	1.706E-03
GW_1-1B	24.122	49.893	0.519	247.4	6.87	5.00	1.193E-07	3.687E-07	3.927E-04	3.768E-04	2.004E-07	8.737E-06	1.074E-07	1.313E-07	1.731E-03
GW_1-1C	24.099	50.047	0.519	249.1	6.82	7.50	9.434E-08	3.293E-07	3.355E-03	3.769E-04	2.545E-07	9.112E-06	9.339E-08	7.428E-08	1.714E-03
GW_1-1D	24.303	50.063	0.519	247.3	6.86	10.00	8.155E-08	9.838E-08	3.342E-04	3.769E-04	2.645E-07	9.045E-06	8.851E-08	9.306E-08	1.587E-03
GW_1-2A	24.121	49.986	0.501	248.3	6.79	2.50	1.101E-07	3.152E-07	5.692E-02	3.421E-04	3.304E-08	8.328E-06	8.820E-08	1.276E-07	6.945E-04
GW_1-2B	24.180	50.097	0.501	248.8	6.85	5.00	1.471E-07	2.923E-07	9.215E-04	3.425E-04	6.428E-08	9.252E-06	7.368E-08	1.056E-07	6.562E-04
GW_1-2C	24.244	49.994	0.501	247.2	6.83	7.50	1.303E-07	3.430E-07	4.203E-03	3.423E-04	5.433E-08	7.924E-06	7.900E-08	9.385E-08	6.614E-04
GW_1-2D	24.124	50.009	0.501	248.5	6.88	10.00	1.259E-07	3.798E-07	4.359E-02	3.420E-04	5.333E-08	7.853E-06	8.056E-08	1.270E-07	6.790E-04
GW_1-3A	24.110	49.818	0.512	246.8	6.82	2.50	1.273E-07	3.014E-07	4.600E-02	3.368E-04	3.026E-07	7.363E-06	8.909E-08	1.408E-07	6.914E-04
GW_1-3B	24.272	49.991	0.512	246.9	6.77	5.00	1.125E-07	4.318E-07	4.767E-04	3.364E-04	3.738E-07	7.083E-06	1.211E-07	1.358E-07	7.055E-04
GW_1-3C	24.279	50.185	0.512	248.7	6.84	7.50	1.436E-07	4.113E-07	4.910E-02	3.365E-04	3.631E-07	7.158E-06	1.053E-07	1.179E-07	7.188E-04
GW_1-3D	24.287	50.027	0.512	247.1	6.92	10.00	1.193E-07	5.331E-07	8.201E-04	3.369E-04	3.432E-07	8.602E-06	9.268E-08	1.313E-07	7.260E-04
GW_7-1A	24.132	49.955	0.513	247.9	6.61	2.50	2.389E-07	2.340E-07	4.300E-02	2.706E-04	1.372E-07	9.186E-06	1.169E-07	1.450E-07	2.005E-03
GW_7-1B	24.020	49.864	0.513	248.1	6.52	5.00	2.269E-07	2.529E-07	4.280E-03	2.792E-04	1.273E-07	9.566E-06	6.881E-08	8.596E-08	2.005E-03
GW_7-1C	24.028	49.841	0.513	247.8	6.66	7.50	2.402E-07	2.389E-07	4.364E-02	2.506E-04	1.343E-07	9.526E-06	6.232E-08	7.044E-08	2.072E-03
GW_7-1D	24.292	50.052	0.513	247.3	6.59	10.00	2.250E-07	1.802E-07	6.211E-02	2.600E-04	1.649E-07	9.532E-06	5.457E-08	9.224E-08	2.070E-03
GW_7-2A	24.315	50.138	0.502	247.9	6.63	2.50	7.946E-08	4.182E-07	8.917E-04	2.734E-04	1.698E-07	7.278E-06	1.487E-07	1.826E-07	2.777E-04
GW_7-2B	24.160	49.993	0.502	248.0	6.50	5.00	7.935E-08	4.857E-07	7.228E-03	2.744E-04	2.390E-07	7.778E-06	1.208E-07	1.369E-07	1.609E-04
GW_7-2C	24.176	50.072	0.502	248.6	6.54	7.50	6.669E-08	4.523E-07	5.096E-03	2.725E-04	2.458E-07	7.778E-06	1.018E-07	1.013E-07	1.275E-04
GW_7-2D	23.996	49.767	0.502	247.4	6.61	10.00	7.128E-08	6.802E-07	4.718E-03	2.733E-04	2.457E-07	7.778E-06	1.131E-07	9.327E-08	2.801E-04
GW_7-3A	24.179	49.919	0.513	247.1	6.55	2.50	2.517E-08	2.369E-07	9.329E-04	2.831E-04	2.326E-07	9.125E-06	8.917E-08	1.023E-07	2.112E-03
GW_7-3B	24.192	49.921	0.513	247.0	6.62	5.00	4.487E-08	2.216E-07	1.189E-03	2.835E-04	1.430E-07	9.493E-06	8.735E-08	9.820E-08	2.240E-03
GW_7-3C	24.253	50.034	0.513	247.5	6.60	7.50	3.807E-08	1.537E-07	4.161E-03	2.945E-04	1.530E-07	9.070E-06	7.657E-08	8.300E-08	1.250E-03
GW_7-3D	24.230	50.022	0.513	247.6	6.59	10.00	4.831E-08	1.282E-07	8.166E-04	2.938E-04	1.440E-07	9.451E-06	6.970E-08	7.079E-08	1.266E-03

ID	Li (g/mL)	B (g/mL)	Na (g/mL)	Mg (g/mL)	Al (g/mL)	Si (g/mL)	Mo (g/mL)	Cs (g/mL)	Ca (g/mL)
GW_1-1 (Average Blank)	2.56E-09	1.89E-08	2.30E-02	3.51E-04	1.16E-07	7.16E-06	1.83E-09	2.87E-09	1.98E-03
GW_1-1 (Blank 1)	2.58E-09	3.77E-08	4.18E-02	3.70E-04	5.03E-08	6.85E-06	1.79E-09	2.82E-09	1.96E-03
GW_1-1 (Blank 2)	2.54E-09	0.00E+00	4.23E-03	3.32E-04	1.81E-07	7.47E-06	1.87E-09	2.91E-09	1.99E-03
GW_1-2 (Average Blank)	2.29E-09	2.02E-08	6.00E-04	3.43E-04	4.67E-08	6.92E-06	1.11E-09	2.19E-09	7.80E-04
GW_1-2 (Blank 1)	2.30E-09	4.04E-08	6.03E-04	3.43E-04	4.26E-08	6.03E-06	1.13E-09	2.22E-09	7.86E-04
GW_1-2 (Blank 2)	2.28E-09	0.00E+00	5.98E-04	3.44E-04	5.08E-08	7.80E-06	1.10E-09	2.17E-09	7.74E-04
GW_1-3 (Average Blank)	4.33E-09	1.82E-08	5.93E-04	3.36E-04	6.25E-08	7.39E-06	2.46E-09	3.72E-09	7.72E-04
GW_1-3 (Blank 1)	4.28E-09	3.65E-08	5.94E-04	3.26E-04	6.18E-08	6.92E-06	2.43E-09	3.77E-09	7.70E-04
GW_1-3 (Blank 2)	4.38E-09	0.00E+00	5.92E-04	3.46E-04	6.33E-08	7.87E-06	2.48E-09	3.66E-09	7.75E-04
GW_7-1 (Average Blank)	6.25E-09	0.00E+00	1.43E-02	2.05E-04	7.02E-08	7.79E-06	4.51E-09	9.49E-09	1.94E-03
GW_7-1 (Blank 1)	6.09E-09	0.00E+00	2.43E-02	2.07E-04	6.94E-08	7.51E-06	4.49E-09	9.28E-09	1.96E-03
GW_7-1 (Blank 2)	6.42E-09	0.00E+00	4.31E-03	2.02E-04	7.11E-08	8.08E-06	4.53E-09	9.71E-09	1.92E-03
GW_7-2 (Average Blank)	7.45E-09	1.23E-08	7.35E-04	3.34E-04	4.25E-08	7.21E-06	4.64E-09	1.14E-08	7.11E-04
GW_7-2 (Blank 1)	7.72E-09	2.45E-08	6.49E-04	3.48E-04	3.71E-08	6.60E-06	4.83E-09	1.16E-08	7.06E-04
GW_7-2 (Blank 2)	7.19E-09	0.00E+00	8.20E-04	3.21E-04	4.79E-08	7.83E-06	4.45E-09	1.11E-08	7.16E-04
GW_7-3 (Average Blank)	1.63E-08	8.31E-09	3.99E-03	2.85E-04	6.47E-08	7.86E-06	1.01E-08	1.55E-08	1.82E-03
GW_7-3 (Blank 1)	1.60E-08	1.66E-08	3.86E-03	2.72E-04	6.66E-08	7.63E-06	9.89E-09	1.49E-08	1.74E-03
GW_7-3 (Blank 2)	1.66E-08	0.00E+00	4.12E-03	2.98E-04	6.28E-08	8.09E-06	1.03E-08	1.62E-08	1.90E-03

APPENDIX 22 RAW DATA OF EXPERIMENTS GW_2 AND GW_8. EXPERIMENTAL CONDITIONS ARE: Q = 125 ML/D, T = 40 °C. CONTROL-TEST DATA IS SHOWN IN THE LOWER TABLE.

Experiment ID	Mass of tared collection bottle (g)	Mass of collection bottle with solution (g)	Initial powder mass (g)	Measured flow rate (mL/d)	Final pH	Duration (hour)	Li (g/mL)	B (g/mL)	Na (g/mL)	Mg (g/mL)	Al (g/mL)	Si (g/mL)	Mo (g/mL)	Cs (g/mL)	Ca (g/mL)
GW_2-1A	24.224	49.849	0.505	123.0	6.81	5.00	2.58E-07	4.87E-07	1.13E-02	1.60E-04	6.24E-08	1.17E-05	1.69E-07	1.73E-07	1.73E-03
GW_2-1B	24.066	49.670	0.505	122.9	6.92	10.00	3.28E-07	5.42E-07	6.66E-03	1.61E-04	2.89E-07	1.17E-05	1.83E-07	1.86E-07	1.73E-03
GW_2-1C	24.085	49.920	0.505	124.0	6.88	15.00	2.10E-07	4.22E-07	1.13E-02	1.60E-04	7.58E-08	1.21E-05	8.40E-08	9.05E-08	1.74E-03
GW_2-1D	24.204	50.021	0.505	123.9	6.76	20.00	1.70E-07	5.44E-07	8.75E-03	1.60E-04	7.06E-08	1.17E-05	7.31E-08	7.55E-08	1.70E-03
GW_2-2A	24.195	50.237	0.512	125.0	6.84	5.00	2.60E-07	6.01E-07	8.23E-04	4.01E-04	2.65E-07	9.52E-06	1.68E-07	1.88E-07	5.88E-04
GW_2-2B	24.226	50.247	0.512	124.9	6.72	10.00	1.16E-07	5.81E-07	7.25E-04	4.00E-04	9.02E-08	9.65E-06	1.16E-07	1.21E-07	5.72E-04
GW_2-2C	24.235	50.256	0.512	124.9	6.78	15.00	1.95E-07	5.15E-07	8.14E-04	4.00E-04	1.24E-07	9.53E-06	8.15E-08	8.07E-08	5.65E-04
GW_2-2D	24.264	50.264	0.512	124.8	6.83	20.00	1.63E-07	4.71E-07	7.11E-04	4.01E-04	7.88E-08	9.55E-06	6.73E-08	6.77E-08	5.68E-04
GW_2-3A	24.201	49.930	0.501	123.5	6.77	5.00	1.00E-07	4.54E-07	6.97E-02	4.24E-04	5.14E-07	1.11E-05	8.31E-08	9.49E-08	5.58E-04
GW_2-3B	24.183	49.871	0.501	123.3	6.82	10.00	1.13E-07	4.56E-07	7.03E-04	4.23E-04	3.79E-07	1.11E-05	8.35E-08	9.77E-08	5.67E-04
GW_2-3C	24.225	50.183	0.501	124.6	6.81	15.00	1.89E-07	4.11E-07	7.14E-04	4.23E-04	4.96E-07	1.05E-05	6.93E-08	7.09E-08	5.71E-04
GW_2-3D	24.282	50.199	0.501	124.4	6.82	20.00	1.78E-07	4.20E-07	7.28E-04	4.22E-04	5.17E-07	1.13E-05	6.80E-08	7.29E-08	5.76E-04
GW_8-1A	24.056	49.785	0.511	123.5	6.59	5.00	1.26E-07	3.95E-07	4.31E-03	1.48E-04	6.32E-07	9.99E-06	1.56E-07	1.76E-07	1.75E-03
GW_8-1B	24.054	49.804	0.511	123.6	6.58	10.00	1.33E-07	4.27E-07	9.30E-03	1.47E-04	6.69E-07	9.72E-06	1.64E-07	1.80E-07	1.79E-03
GW_8-1C	24.190	50.023	0.511	124.0	6.50	15.00	1.44E-07	2.05E-07	9.36E-03	1.49E-04	8.06E-08	9.28E-06	6.73E-08	7.10E-08	1.80E-03
GW_8-1D	24.191	50.045	0.511	124.1	6.61	20.00	1.35E-07	2.87E-07	1.16E-02	1.49E-04	1.65E-07	9.53E-06	6.27E-08	6.70E-08	1.85E-03
GW_8-2A	24.099	50.120	0.506	124.9	6.58	5.00	1.08E-07	2.37E-07	4.97E-02	3.86E-04	7.72E-08	1.14E-05	1.25E-07	1.40E-07	5.70E-04
GW_8-2B	24.092	50.113	0.506	124.9	6.62	10.00	1.10E-07	2.58E-07	5.05E-02	3.88E-04	6.76E-08	1.19E-05	1.26E-07	1.41E-07	5.63E-04
GW_8-2C	24.224	50.078	0.506	124.1	6.55	15.00	1.12E-07	3.89E-07	9.01E-03	3.85E-04	8.29E-08	1.10E-05	6.44E-08	6.58E-08	5.64E-04
GW_8-2D	24.129	50.004	0.506	124.2	6.53	20.00	1.45E-07	3.68E-07	9.01E-03	3.85E-04	1.67E-07	1.11E-05	6.20E-08	6.44E-08	5.68E-04
GW_8-3A	24.190	49.794	0.500	122.9	6.50	5.00	2.34E-07	6.79E-07	1.20E-02	1.60E-04	8.71E-08	9.97E-06	1.54E-07	1.75E-07	1.78E-03
GW_8-3B	24.080	49.705	0.500	123.0	6.51	10.00	2.25E-07	6.78E-07	9.72E-03	1.58E-04	9.35E-08	9.73E-06	1.58E-07	1.84E-07	1.39E-03
GW_8-3C	24.211	50.044	0.500	124.0	6.56	15.00	2.33E-07	7.39E-07	1.20E-02	1.59E-04	1.83E-07	1.06E-05	2.04E-07	2.13E-07	1.26E-03
GW_8-3D	24.105	49.938	0.500	124.0	6.58	20.00	2.17E-07	5.59E-07	1.18E-02	1.59E-04	1.00E-07	1.02E-05	9.78E-08	1.01E-07	1.25E-03

ID	Li (g/mL)	B (g/mL)	Na (g/mL)	Mg (g/mL)	Al (g/mL)	Si (g/mL)	Mo (g/mL)	Cs (g/mL)	Ca (g/mL)
GW_2-1 (Average Blank)	3.83E-09	0.00E+00	1.05E-02	1.59E-04	4.55E-08	9.08E-06	3.18E-09	1.94E-09	1.78E-03
GW_2-1 (Blank 1)	3.87E-09	0.00E+00	1.03E-02	1.47E-04	4.48E-08	8.96E-06	3.26E-09	2.00E-09	1.74E-03
GW_2-1 (Blank 2)	3.79E-09	0.00E+00	1.07E-02	1.70E-04	4.61E-08	9.20E-06	3.10E-09	1.88E-09	1.81E-03
GW_2-2 (Average Blank)	4.88E-09	0.00E+00	9.02E-04	4.00E-04	7.61E-08	9.06E-06	3.63E-09	2.44E-09	6.15E-04
GW_2-2 (Blank 1)	4.97E-09	0.00E+00	8.07E-04	4.12E-04	8.22E-08	8.75E-06	3.51E-09	2.54E-09	6.12E-04
GW_2-2 (Blank 2)	4.79E-09	0.00E+00	9.97E-04	3.88E-04	6.99E-08	9.36E-06	3.75E-09	2.35E-09	6.18E-04
GW_2-3 (Average Blank)	4.02E-09	0.00E+00	7.42E-04	4.24E-04	5.39E-08	9.72E-06	2.56E-09	1.94E-09	5.92E-04
GW_2-3 (Blank 1)	4.09E-09	0.00E+00	7.48E-04	4.36E-04	5.11E-08	9.80E-06	2.63E-09	1.90E-09	6.15E-04
GW_2-3 (Blank 2)	3.94E-09	0.00E+00	7.36E-04	4.12E-04	5.67E-08	9.64E-06	2.49E-09	1.98E-09	5.68E-04
GW_8-1 (Average Blank)	3.16E-08	6.06E-08	1.06E-02	1.48E-04	8.65E-08	8.50E-06	1.68E-08	1.77E-08	1.76E-03
GW_8-1 (Blank 1)	1.07E-09	0.00E+00	1.04E-02	1.44E-04	3.81E-08	8.35E-06	2.25E-09	5.94E-10	1.75E-03
GW_8-1 (Blank 2)	6.22E-08	1.21E-07	1.07E-02	1.52E-04	1.35E-07	8.64E-06	3.13E-08	3.47E-08	1.77E-03
GW_8-2 (Average Blank)	1.30E-09	0.00E+00	8.41E-04	3.88E-04	5.05E-08	9.56E-06	1.41E-09	5.72E-10	5.82E-04
GW_8-2 (Blank 1)	1.27E-09	0.00E+00	7.82E-04	3.86E-04	4.65E-08	9.16E-06	1.28E-09	5.32E-10	5.67E-04
GW_8-2 (Blank 2)	1.34E-09	0.00E+00	8.99E-04	3.89E-04	5.45E-08	9.95E-06	1.55E-09	6.13E-10	5.97E-04
GW_8-3 (Average Blank)	7.50E-10	0.00E+00	9.49E-03	1.57E-04	5.11E-08	8.83E-06	2.35E-09	2.46E-10	1.72E-03
GW_8-3 (Blank 1)	7.32E-10	0.00E+00	1.06E-02	1.55E-04	4.04E-08	8.68E-06	2.28E-09	2.29E-10	1.73E-03
GW_8-3 (Blank 2)	7.68E-10	0.00E+00	8.36E-03	1.58E-04	6.19E-08	8.98E-06	2.42E-09	2.62E-10	1.71E-03

APPENDIX 23 RAW DATA OF EXPERIMENTS GW_3 AND GW_9. EXPERIMENTAL CONDITIONS ARE: Q = 75 ML/D, T = 40 ^{O}C. CONTROL-TEST DATA IS SHOWN IN THE LOWER TABLE.

Experiment ID	Mass of tared collection bottle (g)	Mass of collection bottle with solution (g)	Initial powder mass (g)	Measured flow rate (mL/d)	Final pH	Duration (hour)	Li (g/mL)	B (g/mL)	Na (g/mL)	Mg (g/mL)	Al (g/mL)	Si (g/mL)	Mo (g/mL)	Cs (g/mL)	Ca (g/mL)
GW_3-1A	24.064	48.697	0.500	73.9	6.90	8.00	2.43E-07	5.43E-07	9.60E-03	1.46E-04	7.84E-08	1.51E-05	9.83E-08	1.08E-07	1.73E-03
GW_3-1B	24.085	48.685	0.500	73.8	6.83	16.00	2.42E-07	5.62E-07	9.32E-03	1.46E-04	7.88E-08	1.45E-05	1.02E-07	1.10E-07	1.75E-03
GW_3-1C	24.151	48.784	0.500	73.9	6.77	24.00	2.24E-07	5.69E-07	1.16E-02	1.47E-04	7.12E-08	9.15E-06	1.03E-07	1.01E-07	1.72E-03
GW_3-1D	24.204	48.804	0.500	73.8	6.81	32.00	2.23E-07	5.65E-07	9.23E-03	1.46E-04	7.14E-08	9.83E-06	1.02E-07	1.03E-07	1.69E-03
GW_3-2A	24.136	49.136	0.504	75.0	6.84	8.00	3.06E-07	6.67E-07	7.13E-04	4.10E-04	9.26E-08	1.12E-05	1.03E-07	1.04E-07	5.11E-04
GW_3-2B	24.131	49.098	0.504	74.9	6.81	16.00	3.05E-07	6.53E-07	6.90E-02	4.11E-04	9.68E-08	1.13E-05	1.02E-07	1.05E-07	5.05E-04
GW_3-2C	24.167	49.167	0.504	75.0	6.79	24.00	1.93E-07	4.94E-07	7.15E-04	4.12E-04	8.66E-08	2.08E-05	8.68E-08	8.52E-08	5.66E-04
GW_3-2D	24.082	49.082	0.504	75.0	6.87	32.00	1.90E-07	4.82E-07	3.15E-03	4.11E-04	8.60E-08	2.02E-05	8.76E-08	9.55E-08	5.65E-04
GW_3-3A	24.006	48.339	0.513	73.0	6.75	8.00	2.84E-07	5.55E-07	6.79E-04	3.88E-04	2.30E-07	1.16E-05	9.45E-08	1.09E-07	5.00E-04
GW_3-3B	24.214	48.481	0.513	72.8	6.79	16.00	2.70E-07	5.31E-07	6.91E-04	3.89E-04	1.74E-07	1.19E-05	8.91E-08	1.04E-07	5.26E-04
GW_3-3C	24.190	48.223	0.513	72.1	6.91	24.00	2.28E-07	6.39E-07	7.24E-04	3.88E-04	1.69E-07	1.08E-05	9.97E-08	9.75E-08	5.29E-04
GW_3-3D	24.234	48.267	0.513	72.1	6.74	32.00	2.29E-07	6.54E-07	7.21E-04	3.88E-04	1.77E-07	1.08E-05	1.02E-07	9.57E-08	5.27E-04
GW_9-1A	24.257	48.824	0.508	73.7	6.55	8.00	2.52E-07	5.68E-07	9.55E-03	1.51E-04	9.54E-08	1.27E-05	1.05E-07	1.13E-07	1.78E-03
GW_9-1B	24.108	48.708	0.508	73.8	6.52	16.00	2.53E-07	5.76E-07	6.97E-03	1.52E-04	8.17E-08	1.29E-05	1.07E-07	1.12E-07	1.82E-03
GW_9-1C	24.237	48.870	0.508	73.9	6.60	24.00	1.81E-07	4.27E-07	1.23E-02	1.51E-04	1.41E-07	1.28E-05	8.14E-08	8.36E-08	1.87E-03
GW_9-1D	24.241	48.841	0.508	73.8	6.56	32.00	1.79E-07	4.26E-07	6.99E-03	1.51E-04	8.39E-08	1.29E-05	8.14E-08	8.08E-08	1.85E-03
GW_9-2A	24.270	49.270	0.507	75.0	6.53	8.00	2.82E-07	5.99E-07	9.98E-04	3.98E-04	9.80E-08	1.58E-05	9.72E-08	1.10E-07	3.99E-04
GW_9-2B	24.248	49.215	0.507	74.9	6.55	16.00	2.64E-07	5.47E-07	6.67E-02	3.97E-04	8.89E-08	1.60E-05	9.08E-08	1.05E-07	3.75E-04
GW_9-2C	24.054	49.021	0.507	74.9	6.59	24.00	2.05E-07	5.86E-07	7.22E-02	3.97E-04	9.40E-08	1.63E-05	8.93E-08	9.12E-08	3.89E-04
GW_9-2D	24.217	49.150	0.507	74.8	6.62	32.00	2.91E-07	9.20E-07	7.18E-04	3.97E-04	2.08E-07	1.62E-05	1.13E-07	1.30E-07	3.61E-04
GW_9-3A	24.089	48.289	0.506	72.6	6.57	8.00	2.61E-07	5.58E-07	1.38E-03	1.52E-04	9.62E-08	1.17E-05	1.06E-07	1.14E-07	1.53E-03
GW_9-3B	24.165	48.365	0.506	72.6	6.53	16.00	2.62E-07	5.73E-07	2.13E-03	1.53E-04	8.13E-08	1.21E-05	1.09E-07	1.14E-07	1.62E-03
GW_9-3C	24.080	48.480	0.506	73.2	6.51	24.00	2.24E-07	5.55E-07	1.12E-03	1.53E-04	8.40E-08	1.16E-05	1.03E-07	1.03E-07	1.57E-03
GW_9-3D	24.109	48.542	0.506	73.3	6.54	32.00	2.25E-07	5.64E-07	1.25E-02	1.53E-04	7.79E-08	1.20E-05	1.04E-07	1.03E-07	1.77E-03

ID	Li (g/mL)	B (g/mL)	Na (g/mL)	Mg (g/mL)	Al (g/mL)	Si (g/mL)	Mo (g/mL)	Cs (g/mL)	Ca (g/mL)
GW_3-1 (Average Blank)	1.33E-09	0.00E+00	7.55E-03	1.44E-04	7.98E-08	9.61E-06	3.11E-09	3.94E-10	1.76E-03
GW_3-1 (Blank 1)	1.57E-09	0.00E+00	4.33E-03	1.36E-04	8.99E-08	9.34E-06	4.01E-09	5.14E-10	1.70E-03
GW_3-1 (Blank 2)	1.08E-09	0.00E+00	1.08E-02	1.53E-04	6.96E-08	9.89E-06	2.21E-09	2.74E-10	1.82E-03
GW_3-2 (Average Blank)	1.06E-09	0.00E+00	6.51E-04	4.09E-04	1.54E-07	1.07E-05	1.56E-09	3.48E-10	5.75E-04
GW_3-2 (Blank 1)	1.40E-09	0.00E+00	6.29E-04	3.97E-04	1.68E-07	1.07E-05	1.97E-09	4.96E-10	5.64E-04
GW_3-2 (Blank 2)	7.32E-10	0.00E+00	6.73E-04	4.20E-04	1.40E-07	1.07E-05	1.15E-09	1.99E-10	5.86E-04
GW_3-3 (Average Blank)	1.76E-08	0.00E+00	6.25E-04	3.87E-04	5.73E-08	1.17E-05	8.52E-09	8.96E-09	5.36E-04
GW_3-3 (Blank 1)	3.41E-08	0.00E+00	6.18E-04	3.72E-04	6.16E-08	1.10E-05	1.48E-08	1.76E-08	5.14E-04
GW_3-3 (Blank 2)	1.11E-09	0.00E+00	6.32E-04	4.01E-04	5.30E-08	1.25E-05	2.24E-09	3.42E-10	5.59E-04
GW_9-1 (Average Blank)	1.34E-09	0.00E+00	8.58E-03	1.49E-04	3.84E-08	1.09E-05	2.98E-09	4.71E-10	1.77E-03
GW_9-1 (Blank 1)	1.37E-09	0.00E+00	6.34E-03	1.44E-04	3.61E-08	1.11E-05	3.76E-09	5.33E-10	1.76E-03
GW_9-1 (Blank 2)	1.31E-09	0.00E+00	1.08E-02	1.53E-04	4.07E-08	1.07E-05	2.19E-09	4.09E-10	1.79E-03
GW_9-2 (Average Blank)	1.51E-09	0.00E+00	6.31E-04	3.95E-04	4.33E-08	1.31E-05	3.31E-09	5.29E-10	5.50E-04
GW_9-2 (Blank 1)	1.87E-09	0.00E+00	6.18E-04	3.81E-04	4.35E-08	1.30E-05	4.01E-09	6.91E-10	5.34E-04
GW_9-2 (Blank 2)	1.15E-09	0.00E+00	6.44E-04	4.09E-04	4.31E-08	1.32E-05	2.61E-09	3.66E-10	5.67E-04
GW_9-3 (Average Blank)	1.44E-09	0.00E+00	7.65E-03	1.51E-04	6.43E-08	1.02E-05	3.70E-09	5.32E-10	1.78E-03
GW_9-3 (Blank 1)	1.50E-09	0.00E+00	6.45E-03	1.46E-04	3.45E-08	1.02E-05	4.79E-09	6.49E-10	1.76E-03
GW_9-3 (Blank 2)	1.38E-09	0.00E+00	8.86E-03	1.56E-04	9.42E-08	1.02E-05	2.61E-09	4.14E-10	1.81E-03

APPENDIX 24 RAW DATA OF EXPERIMENTS GW_4 AND GW_10. EXPERIMENTAL CONDITIONS ARE: Q = 50 mL/D, T = 40 °C. CONTROL-TEST DATA IS SHOWN IN THE LOWER TABLE.

Experiment ID	Mass of tared collection bottle (g)	Mass of collection bottle with solution (g)	Initial powder mass (g)	Measured flow rate (mL/d)	Final pH	Duration (hour)	Li (g/mL)	B (g/mL)	Na (g/mL)	Mg (g/mL)	Al (g/mL)	Si (g/mL)	Mo (g/mL)	Cs (g/mL)	Ca (g/mL)
GW_4-1A	24.349	72.469	0.501	48.1	6.78	24.00	3.981E-07	1.089E-06	4.242E-02	1.291E-04	2.629E-07	4.358E-06	2.340E-07	2.800E-07	1.536E-03
GW_4-1B	24.212	72.572	0.501	48.4	6.84	48.00	4.113E-07	1.129E-06	4.323E-02	1.249E-04	5.819E-08	4.405E-06	2.491E-07	2.892E-07	1.526E-03
GW_4-1C	24.285	73.255	0.501	49.0	6.72	72.00	3.723E-07	1.078E-06	4.171E-02	1.282E-04	5.941E-08	4.397E-06	2.397E-07	2.626E-07	1.535E-03
GW_4-1D	24.158	72.988	0.501	48.8	6.77	96.00	3.709E-07	1.094E-06	4.158E-03	1.259E-04	6.343E-08	4.571E-06	2.386E-07	2.576E-07	1.538E-03
GW_4-2A	24.205	73.755	0.503	49.6	6.83	24.00	3.018E-07	7.844E-07	8.295E-04	3.628E-04	1.768E-07	4.619E-06	1.493E-07	1.724E-07	5.771E-04
GW_4-2B	24.217	73.297	0.503	49.1	6.77	48.00	3.229E-07	8.713E-07	7.608E-04	3.613E-04	1.228E-07	4.586E-06	1.774E-07	1.916E-07	5.457E-04
GW_4-2C	24.242	73.472	0.503	49.2	6.79	72.00	1.888E-07	5.648E-07	6.575E-04	3.625E-04	3.540E-07	4.794E-06	1.050E-07	1.182E-07	5.656E-04
GW_4-2D	24.251	73.721	0.503	49.5	6.81	96.00	1.873E-07	5.544E-07	6.411E-04	3.616E-04	3.978E-08	4.894E-06	1.000E-07	1.150E-07	5.511E-04
GW_4-3A	24.253	71.643	0.500	47.4	6.74	24.00	3.572E-07	1.023E-06	6.251E-04	3.409E-04	1.668E-07	3.649E-06	1.775E-07	2.181E-07	5.408E-04
GW_4-3B	24.335	71.905	0.500	47.6	6.72	48.00	2.568E-07	6.700E-07	6.425E-04	3.426E-04	3.306E-08	3.664E-06	1.292E-07	1.534E-07	5.367E-04
GW_4-3C	24.292	71.812	0.500	47.5	6.75	72.00	1.896E-07	5.623E-07	6.334E-04	3.430E-04	4.394E-08	3.633E-06	1.065E-07	1.148E-07	5.416E-04
GW_4-3D	24.296	71.956	0.500	47.7	6.72	96.00	1.923E-07	5.813E-07	6.500E-04	3.406E-04	6.462E-08	3.825E-06	1.081E-07	1.206E-07	5.405E-04
GW_10-1A	24.253	73.413	0.509	49.2	6.57	24.00	4.440E-07	1.201E-06	4.169E-03	1.293E-04	2.780E-08	3.857E-06	2.720E-07	3.013E-07	1.515E-03
GW_10-1B	24.281	73.261	0.509	49.0	6.53	48.00	4.308E-07	1.171E-06	4.148E-03	1.275E-04	1.754E-08	3.833E-06	2.671E-07	2.945E-07	1.531E-03
GW_10-1C	24.234	73.434	0.509	49.2	6.58	72.00	4.099E-07	1.217E-06	4.224E-03	1.316E-04	1.050E-08	3.940E-06	2.715E-07	2.939E-07	1.567E-03
GW_10-1D	24.089	73.069	0.509	49.0	6.51	96.00	3.969E-07	1.172E-06	4.067E-03	1.257E-04	1.104E-08	3.940E-06	2.635E-07	2.808E-07	1.529E-03
GW_10-2A	24.203	73.053	0.510	48.9	6.55	24.00	4.384E-07	1.158E-06	6.461E-02	3.659E-04	2.137E-07	3.928E-06	2.174E-07	2.595E-07	3.897E-04
GW_10-2B	24.156	73.066	0.510	48.9	6.54	48.00	2.874E-07	6.801E-07	6.254E-02	3.633E-04	2.340E-08	3.951E-06	1.364E-07	1.647E-07	3.779E-04
GW_10-2C	24.188	73.258	0.510	49.1	6.57	72.00	1.851E-07	5.697E-07	1.343E-02	3.607E-04	2.928E-08	3.945E-06	1.042E-07	1.190E-07	3.819E-04
GW_10-2D	24.333	73.543	0.510	49.2	6.55	96.00	1.898E-07	5.843E-07	2.432E-02	3.630E-04	2.010E-08	3.903E-06	1.078E-07	1.191E-07	3.931E-04
GW_10-3A	24.158	72.848	0.506	48.7	6.52	24.00	4.845E-07	1.356E-06	4.076E-03	1.277E-04	3.388E-08	4.493E-06	3.082E-07	3.487E-07	1.758E-03
GW_10-3B	24.213	73.043	0.506	48.8	6.55	48.00	4.864E-07	1.369E-06	4.135E-03	1.275E-04	2.236E-08	4.459E-06	3.103E-07	3.500E-07	1.676E-03
GW_10-3C	24.220	73.200	0.506	49.0	6.53	72.00	4.762E-07	1.438E-06	4.130E-03	1.280E-04	1.712E-07	4.420E-06	3.093E-07	3.555E-07	1.596E-03
GW_10-3D	24.251	73.171	0.506	48.9	6.57	96.00	4.297E-07	1.262E-06	4.055E-03	1.288E-04	2.222E-08	4.432E-06	2.855E-07	3.126E-07	1.598E-03

ID	Li (g/mL)	B (g/mL)	Na (g/mL)	Mg (g/mL)	Al (g/mL)	Si (g/mL)	Mo (g/mL)	Cs (g/mL)	Ca (g/mL)
GW_4-1 (Average Blank)	7.69E-09	3.34E-08	4.37E-03	1.26E-04	4.23E-09	1.94E-06	6.29E-09	5.69E-09	1.55E-03
GW_4-1 (Blank 1)	8.10E-09	3.95E-08	4.38E-03	1.23E-04	0.00E+00	2.01E-06	6.74E-09	6.01E-09	1.54E-03
GW_4-1 (Blank 2)	7.29E-09	2.73E-08	4.35E-03	1.29E-04	8.46E-09	1.87E-06	5.84E-09	5.37E-09	1.57E-03
GW_4-2 (Average Blank)	1.02E-09	2.69E-08	7.79E-04	3.59E-04	0.00E+00	1.36E-06	1.41E-09	7.84E-10	5.93E-04
GW_4-2 (Blank 1)	1.54E-09	2.87E-08	8.76E-04	3.50E-04	0.00E+00	8.32E-07	1.83E-09	1.07E-09	6.00E-04
GW_4-2 (Blank 2)	5.03E-10	2.50E-08	6.82E-04	3.68E-04	0.00E+00	1.88E-06	9.93E-10	4.98E-10	5.86E-04
GW_4-3 (Average Blank)	1.03E-11	2.18E-08	6.39E-04	3.39E-04	8.97E-11	1.40E-06	1.30E-09	1.44E-10	5.43E-04
GW_4-3 (Blank 1)	2.05E-11	2.22E-08	6.35E-04	3.27E-04	0.00E+00	9.97E-07	1.42E-09	1.51E-10	5.35E-04
GW_4-3 (Blank 2)	0.00E+00	2.13E-08	6.43E-04	3.51E-04	1.79E-10	1.81E-06	1.18E-09	1.37E-10	5.50E-04
GW_10-1 (Average Blank)	7.40E-09	2.83E-08	4.27E-03	1.25E-04	0.00E+00	1.66E-06	6.18E-09	5.62E-09	1.51E-03
GW_10-1 (Blank 1)	7.24E-09	2.89E-08	4.31E-03	1.23E-04	0.00E+00	1.86E-06	6.04E-09	5.49E-09	1.49E-03
GW_10-1 (Blank 2)	7.57E-09	2.77E-08	4.23E-03	1.28E-04	0.00E+00	1.47E-06	6.31E-09	5.75E-09	1.53E-03
GW_10-2 (Average Blank)	1.31E-07	4.63E-07	8.27E-04	3.49E-04	0.00E+00	2.00E-06	6.40E-08	9.02E-08	5.93E-04
GW_10-2 (Blank 1)	3.08E-10	2.15E-08	7.73E-04	3.41E-04	0.00E+00	1.90E-06	1.53E-09	1.80E-09	5.65E-04
GW_10-2 (Blank 2)	2.62E-07	9.04E-07	8.80E-04	3.57E-04	0.00E+00	2.10E-06	1.26E-07	1.79E-07	6.21E-04
GW_10-3 (Average Blank)	1.14E-08	4.07E-08	4.49E-03	1.36E-04	7.46E-08	1.68E-06	8.93E-09	8.59E-09	1.65E-03
GW_10-3 (Blank 1)	9.51E-09	3.53E-08	4.34E-03	1.26E-04	0.00E+00	1.61E-06	7.32E-09	7.09E-09	1.53E-03
GW_10-3 (Blank 2)	1.32E-08	4.61E-08	4.65E-03	1.47E-04	1.49E-07	1.76E-06	1.05E-08	1.01E-08	1.77E-03

APPENDIX 25 RAW DATA OF EXPERIMENTS GW_5 AND GW_11. EXPERIMENTAL CONDITIONS ARE: Q = 25 ML/D, T = 40 ^{O}C. CONTROL-TEST DATA IS SHOWN IN THE LOWER TABLE.

Experiment ID	Mass of tared collection bottle (g)	Mass of collection bottle with solution (g)	Initial powder mass (g)	Measured flow rate (mL/d)	Final pH	Duration (hour)	Li (g/mL)	B (g/mL)	Na (g/mL)	Mg (g/mL)	Al (g/mL)	Si (g/mL)	Mo (g/mL)	Cs (g/mL)	Ca (g/mL)
GW_5-1A	24.167	74.027	0.503	24.9	6.73	48.00	4.24E-07	1.19E-06	4.09E-03	1.25E-04	7.81E-09	4.05E-06	2.68E-07	3.06E-07	1.43E-03
GW_5-1B	24.228	74.048	0.503	24.9	6.76	96.00	4.28E-07	1.20E-06	4.05E-03	1.25E-04	8.13E-09	3.94E-06	2.76E-07	3.16E-07	1.42E-03
GW_5-1C	24.259	74.039	0.503	24.9	6.78	144.00	3.59E-07	1.06E-06	4.14E-03	1.24E-04	5.26E-09	3.99E-06	2.43E-07	2.64E-07	1.38E-03
GW_5-1D	24.220	74.080	0.503	24.9	6.71	192.00	3.57E-07	1.06E-06	4.09E-03	1.24E-04	7.44E-09	3.76E-06	2.44E-07	2.62E-07	1.40E-03
GW_5-2A	24.250	74.210	0.507	25.0	6.77	48.00	3.69E-07	9.85E-07	6.31E-03	3.55E-04	2.38E-08	4.20E-06	1.93E-07	2.09E-07	5.40E-04
GW_5-2B	24.274	74.214	0.507	25.0	6.74	96.00	3.62E-07	9.63E-07	6.27E-03	3.54E-04	2.65E-08	3.73E-06	1.96E-07	2.05E-07	5.43E-04
GW_5-2C	24.235	74.135	0.507	25.0	6.71	144.00	2.64E-07	8.57E-07	6.64E-03	3.56E-04	2.99E-08	3.23E-06	1.49E-07	1.59E-07	5.40E-04
GW_5-2D	24.295	74.115	0.507	24.9	6.79	192.00	2.51E-07	9.32E-07	6.16E-02	3.55E-04	3.25E-08	3.32E-06	1.43E-07	1.51E-07	5.35E-04
GW_5-3A	24.208	71.988	0.496	23.9	6.75	48.00	3.20E-07	8.80E-07	6.48E-02	3.52E-04	2.55E-08	4.68E-06	1.70E-07	2.02E-07	5.22E-04
GW_5-3B	24.412	72.252	0.496	23.9	6.74	96.00	3.19E-07	8.69E-07	6.25E-04	3.51E-04	2.04E-08	5.23E-06	1.71E-07	1.96E-07	5.25E-04
GW_5-3C	24.263	70.683	0.496	23.2	6.72	144.00	3.06E-07	9.08E-07	2.72E-03	3.51E-04	1.73E-08	4.79E-06	2.01E-07	2.16E-07	5.26E-04
GW_5-3D	24.232	70.712	0.496	23.2	6.74	192.00	3.31E-07	9.65E-07	3.10E-03	3.50E-04	1.50E-08	5.00E-06	2.17E-07	2.35E-07	5.29E-04
GW_11-1A	24.183	74.123	0.504	25.0	6.53	48.00	4.60E-07	1.26E-06	4.03E-03	1.25E-04	8.83E-08	3.21E-06	3.02E-07	3.47E-07	1.49E-03
GW_11-1B	24.270	74.170	0.504	25.0	6.55	96.00	4.69E-07	1.30E-06	4.00E-03	1.24E-04	9.12E-08	3.48E-06	3.08E-07	3.49E-07	1.53E-03
GW_11-1C	24.296	74.056	0.504	24.9	6.51	144.00	3.91E-07	1.15E-06	4.05E-03	1.23E-04	9.50E-08	3.63E-06	2.71E-07	2.99E-07	1.54E-03
GW_11-1D	24.230	73.890	0.504	24.8	6.58	192.00	3.93E-07	1.13E-06	3.93E-03	1.25E-04	4.35E-08	3.82E-06	2.70E-07	2.98E-07	1.57E-03
GW_11-2A	24.275	71.375	0.500	23.6	6.54	48.00	3.58E-07	9.34E-07	5.20E-02	3.49E-04	2.84E-08	2.67E-06	1.89E-07	2.20E-07	5.51E-04
GW_11-2B	24.222	71.062	0.500	23.4	6.52	96.00	3.58E-07	9.50E-07	5.39E-02	3.45E-04	2.12E-08	2.56E-06	1.92E-07	2.13E-07	5.56E-04
GW_11-2C	24.262	72.002	0.500	23.9	6.56	144.00	2.58E-07	7.34E-07	4.14E-02	3.46E-04	2.69E-08	2.12E-06	1.45E-07	1.63E-07	5.45E-04
GW_11-2D	24.176	72.196	0.500	24.0	6.54	192.00	2.53E-07	7.30E-07	5.23E-02	3.46E-04	7.57E-08	2.36E-06	1.44E-07	1.56E-07	5.43E-04
GW_11-3A	24.158	72.918	0.498	24.4	6.56	48.00	5.32E-07	1.33E-06	3.98E-03	1.22E-04	6.81E-08	3.61E-06	3.24E-07	3.40E-07	1.23E-03
GW_11-3B	24.352	73.432	0.498	24.5	6.56	96.00	5.35E-07	1.34E-06	4.05E-03	1.23E-04	8.88E-08	3.70E-06	3.39E-07	3.51E-07	1.28E-03
GW_11-3C	24.076	72.516	0.498	24.2	6.55	144.00	4.43E-07	1.19E-06	4.17E-03	1.24E-04	7.49E-08	3.28E-06	2.94E-07	3.05E-07	1.32E-03
GW_11-3D	24.153	72.733	0.498	24.3	6.51	192.00	4.29E-07	1.16E-06	4.06E-03	1.23E-04	9.85E-08	3.32E-06	2.86E-07	2.91E-07	1.58E-03

ID	Li (g/mL)	B (g/mL)	Na (g/mL)	Mg (g/mL)	Al (g/mL)	Si (g/mL)	Mo (g/mL)	Cs (g/mL)	Ca (g/mL)
GW_5-1 (Average Blank)	2.92E-08	1.03E-07	3.99E-03	1.20E-04	2.93E-08	0.00E+00	2.27E-08	2.19E-08	1.45E-03
GW_5-1 (Blank 1)	2.93E-08	1.06E-07	3.95E-03	1.18E-04	3.01E-08	1.26E-06	2.28E-08	2.21E-08	1.41E-03
GW_5-1 (Blank 2)	2.91E-08	1.00E-07	4.02E-03	1.23E-04	2.84E-08	1.31E-06	2.26E-08	2.17E-08	1.48E-03
GW_5-2 (Average Blank)	3.65E-10	2.39E-08	6.23E-04	3.52E-04	0.00E+00	1.99E-06	2.38E-09	4.34E-10	5.44E-04
GW_5-2 (Blank 1)	3.88E-10	2.50E-08	6.09E-04	3.40E-04	0.00E+00	1.75E-06	2.34E-09	4.30E-10	5.36E-04
GW_5-2 (Blank 2)	3.42E-10	2.27E-08	6.36E-04	3.63E-04	0.00E+00	2.22E-06	2.42E-09	4.38E-10	5.53E-04
GW_5-3 (Average Blank)	0.00E+00	2.41E-08	6.14E-04	3.47E-04	2.29E-09	9.88E-07	2.73E-09	1.97E-10	5.29E-04
GW_5-3 (Blank 1)	0.00E+00	2.50E-08	6.03E-04	3.39E-04	3.66E-09	1.13E-06	2.71E-09	1.56E-10	5.26E-04
GW_5-3 (Blank 2)	4.24E-12	2.32E-08	6.26E-04	3.54E-04	9.30E-10	8.48E-07	2.76E-09	2.38E-10	5.32E-04
GW_11-1 (Average Blank)	2.68E-08	9.13E-08	3.90E-03	1.19E-04	2.95E-08	0.00E+00	1.94E-08	2.05E-08	1.42E-03
GW_11-1 (Blank 1)	1.72E-08	6.07E-08	3.89E-03	1.18E-04	2.22E-08	8.82E-07	1.43E-08	1.31E-08	1.42E-03
GW_11-1 (Blank 2)	3.64E-08	1.22E-07	3.90E-03	1.20E-04	3.68E-08	9.17E-07	2.46E-08	2.80E-08	1.41E-03
GW_11-2 (Average Blank)	3.55E-09	3.28E-08	6.61E-04	3.44E-04	2.07E-08	1.14E-06	5.05E-09	2.52E-09	5.82E-04
GW_11-2 (Blank 1)	3.38E-09	3.21E-08	6.11E-04	3.43E-04	2.07E-08	1.14E-06	4.92E-09	2.40E-09	5.98E-04
GW_11-2 (Blank 2)	3.73E-09	3.35E-08	7.12E-04	3.45E-04	2.07E-08	1.14E-06	5.17E-09	2.64E-09	5.67E-04
GW_11-3 (Average Blank)	7.79E-08	2.51E-07	3.93E-03	1.19E-04	9.87E-08	0.00E+00	4.81E-08	5.86E-08	1.58E-03
GW_11-3 (Blank 1)	1.33E-07	4.26E-07	3.92E-03	1.18E-04	1.63E-07	1.27E-06	7.75E-08	1.00E-07	1.73E-03
GW_11-3 (Blank 2)	2.31E-08	7.57E-08	3.94E-03	1.19E-04	3.42E-08	1.13E-06	1.86E-08	1.68E-08	1.44E-03

APPENDIX 26 RAW DATA OF EXPERIMENTS GW_6 AND GW_12. EXPERIMENTAL CONDITIONS ARE: Q = 10 mL/D, T = 40 °C. CONTROL-TEST DATA IS SHOWN IN THE LOWER TABLE.

Experiment ID	Mass of tared collection bottle (g)	Mass of collection bottle with solution (g)	Initial powder mass (g)	Measured flow rate (mL/d)	Final pH	Duration (hour)	Li (g/mL)	B (g/mL)	Na (g/mL)	Mg (g/mL)	Al (g/mL)	Si (g/mL)	Mo (g/mL)	Cs (g/mL)	Ca (g/mL)
GW_6-1A	24.159	53.619	0.507	9.8	6.75	72.00	9.77E-07	2.66E-06	1.32E-02	1.18E-04	1.74E-08	5.67E-06	9.14E-07	1.01E-06	1.48E-03
GW_6-1B	24.221	53.651	0.507	9.8	6.71	144.00	6.73E-07	1.99E-06	4.04E-02	1.38E-04	1.74E-08	5.93E-06	4.97E-07	5.26E-07	1.52E-03
GW_6-1C	24.116	53.876	0.507	9.9	6.74	216.00	4.61E-07	1.37E-06	4.01E-02	1.38E-04	1.19E-09	5.64E-06	3.42E-07	3.71E-07	1.52E-03
GW_6-1D	24.157	53.737	0.507	9.9	6.68	288.00	4.61E-07	1.37E-06	3.99E-02	1.37E-04	1.23E-09	5.68E-06	3.45E-07	3.68E-07	1.53E-03
GW_6-2A	24.185	54.125	0.506	10.0	6.72	72.00	4.76E-07	1.34E-06	5.60E-03	2.93E-04	1.05E-08	4.74E-06	2.71E-07	2.86E-07	5.11E-04
GW_6-2B	24.090	53.880	0.506	9.9	6.74	144.00	4.81E-07	1.33E-06	8.54E-04	2.89E-04	1.08E-08	4.38E-06	2.76E-07	2.94E-07	5.12E-04
GW_6-2C	24.224	54.134	0.506	10.0	6.75	216.00	3.35E-07	1.02E-06	5.25E-03	2.88E-04	3.66E-09	3.86E-06	2.07E-07	2.14E-07	4.92E-04
GW_6-2D	24.186	54.156	0.506	10.0	6.77	288.00	3.50E-07	1.08E-06	5.51E-03	2.89E-04	5.02E-09	4.16E-06	2.18E-07	2.25E-07	5.14E-04
GW_6-3A	24.126	52.356	0.504	9.4	6.73	72.00	4.60E-07	1.28E-06	5.45E-03	3.83E-04	1.46E-08	5.57E-06	2.64E-07	2.82E-07	4.68E-04
GW_6-3B	24.085	52.645	0.504	9.5	6.75	144.00	4.61E-07	1.31E-06	5.37E-03	3.77E-04	1.49E-08	5.28E-06	2.68E-07	2.87E-07	4.58E-04
GW_6-3C	24.210	52.830	0.504	9.5	6.71	216.00	3.81E-07	1.14E-06	5.22E-03	3.65E-04	4.97E-08	5.41E-06	2.30E-07	2.46E-07	4.67E-04
GW_6-3D	24.246	52.656	0.504	9.5	6.74	288.00	4.12E-07	1.19E-06	5.39E-03	3.83E-04	4.86E-08	5.45E-06	2.45E-07	2.72E-07	4.64E-04
GW_12-1A	24.241	53.731	0.503	9.8	6.51	72.00	7.20E-07	2.14E-06	3.93E-03	1.36E-04	9.32E-09	5.65E-06	5.30E-07	5.69E-07	1.46E-03
GW_12-1B	24.194	53.624	0.503	9.8	6.54	144.00	7.50E-07	2.23E-06	4.05E-03	1.41E-04	8.82E-09	6.33E-06	5.59E-07	5.83E-07	1.53E-03
GW_12-1C	24.285	53.805	0.503	9.8	6.56	216.00	4.01E-07	1.22E-06	3.88E-03	1.36E-04	9.23E-09	4.75E-06	3.05E-07	3.17E-07	1.51E-03
GW_12-1D	24.204	53.814	0.503	9.9	6.52	288.00	4.15E-07	1.27E-06	4.03E-03	1.41E-04	7.82E-09	4.99E-06	3.17E-07	3.38E-07	1.55E-03
GW_12-2A	24.155	53.345	0.504	9.7	6.49	72.00	5.29E-07	1.51E-06	5.28E-03	2.74E-04	9.02E-08	5.91E-06	3.09E-07	3.40E-07	4.89E-04
GW_12-2B	24.276	53.226	0.504	9.7	6.55	144.00	5.18E-07	1.49E-06	5.25E-03	2.78E-04	7.02E-08	6.54E-06	3.18E-07	3.32E-07	4.84E-04
GW_12-2C	24.127	53.467	0.504	9.8	6.53	216.00	4.51E-07	1.36E-06	5.43E-03	2.94E-04	8.17E-08	5.86E-06	2.81E-07	3.08E-07	5.14E-04
GW_12-2D	24.112	53.602	0.504	9.8	6.55	288.00	4.32E-07	1.30E-06	5.39E-03	2.84E-04	8.99E-08	5.62E-06	2.75E-07	2.86E-07	4.99E-04
GW_12-3A	24.136	53.566	0.505	9.8	6.59	72.00	8.13E-07	2.38E-06	5.94E-02	1.38E-04	5.14E-09	4.12E-06	6.06E-07	6.40E-07	1.49E-03
GW_12-3B	24.189	53.709	0.505	9.8	6.51	144.00	8.28E-07	2.45E-06	5.88E-02	1.43E-04	6.18E-09	4.10E-06	6.35E-07	6.66E-07	1.32E-03
GW_12-3C	24.246	53.706	0.505	9.8	6.52	216.00	6.53E-07	1.96E-06	5.85E-02	1.36E-04	7.54E-09	3.36E-06	4.98E-07	5.22E-07	1.41E-03
GW_12-3D	24.110	53.360	0.505	9.8	6.52	288.00	6.57E-07	1.93E-06	5.87E-02	1.37E-04	6.22E-09	3.27E-06	5.09E-07	5.34E-07	1.51E-03

ID	Li (g/mL)	B (g/mL)	Na (g/mL)	Mg (g/mL)	Al (g/mL)	Si (g/mL)	Mo (g/mL)	Cs (g/mL)	Ca (g/mL)
GW_6-1 (Average Blank)	2.26E-10	4.22E-09	4.03E-03	1.38E-04	3.05E-09	8.19E-07	2.88E-09	3.76E-10	1.54E-03
GW_6-1 (Blank 1)	2.41E-10	5.79E-09	3.99E-03	1.32E-04	0.00E+00	8.44E-07	2.93E-09	3.79E-10	1.50E-03
GW_6-1 (Blank 2)	2.11E-10	2.65E-09	4.07E-03	1.43E-04	6.09E-09	7.94E-07	2.82E-09	3.73E-10	1.59E-03
GW_6-2 (Average Blank)	8.29E-10	2.42E-08	5.49E-04	2.82E-04	2.58E-08	1.71E-06	3.68E-09	7.32E-10	5.14E-04
GW_6-2 (Blank 1)	8.32E-10	2.54E-08	5.36E-04	2.70E-04	0.00E+00	1.46E-06	3.70E-09	7.42E-10	5.03E-04
GW_6-2 (Blank 2)	8.25E-10	2.31E-08	5.62E-04	2.93E-04	5.16E-08	1.97E-06	3.67E-09	7.21E-10	5.24E-04
GW_6-3 (Average Blank)	3.50E-10	2.15E-08	5.23E-04	3.53E-04	0.00E+00	1.10E-06	2.73E-09	3.98E-10	4.74E-04
GW_6-3 (Blank 1)	3.68E-10	2.27E-08	5.21E-04	3.50E-04	0.00E+00	9.94E-07	2.69E-09	3.72E-10	4.66E-04
GW_6-3 (Blank 2)	3.33E-10	2.04E-08	5.25E-04	3.56E-04	0.00E+00	1.20E-06	2.77E-09	4.25E-10	4.83E-04
GW_12-1 (Average Blank)	9.23E-11	2.53E-09	4.05E-03	1.38E-04	6.05E-10	2.34E-07	3.09E-09	2.36E-10	1.52E-03
GW_12-1 (Blank 1)	6.48E-11	3.14E-09	4.05E-03	1.35E-04	1.21E-09	2.88E-07	3.17E-09	2.60E-10	1.50E-03
GW_12-1 (Blank 2)	1.20E-10	1.92E-09	4.06E-03	1.40E-04	0.00E+00	1.80E-07	3.02E-09	2.12E-10	1.54E-03
GW_12-2 (Average Blank)	6.62E-10	2.20E-08	5.20E-04	2.56E-04	7.17E-08	2.32E-06	5.47E-09	6.12E-10	4.21E-04
GW_12-2 (Blank 1)	7.01E-10	2.31E-08	5.21E-04	2.56E-04	6.74E-08	2.05E-06	5.45E-09	6.14E-10	4.23E-04
GW_12-2 (Blank 2)	6.22E-10	2.09E-08	5.19E-04	2.55E-04	7.60E-08	2.59E-06	5.48E-09	6.10E-10	4.18E-04
GW_12-3 (Average Blank)	1.16E-10	4.07E-09	4.04E-03	1.37E-04	0.00E+00	2.68E-07	1.93E-09	3.17E-10	1.53E-03
GW_12-3 (Blank 1)	1.75E-10	6.21E-09	4.05E-03	1.36E-04	0.00E+00	3.45E-07	1.95E-09	3.68E-10	1.52E-03
GW_12-3 (Blank 2)	5.60E-11	1.92E-09	4.03E-03	1.38E-04	0.00E+00	1.92E-07	1.92E-09	2.67E-10	1.54E-03

APPENDIX 27 STEADY-STATE PLOTS FOR EXPERIMENTS CONDUCTED AT OTHER VALUES OF PARAMETER Q/S IN SIMULANT GROUNDWATERS.

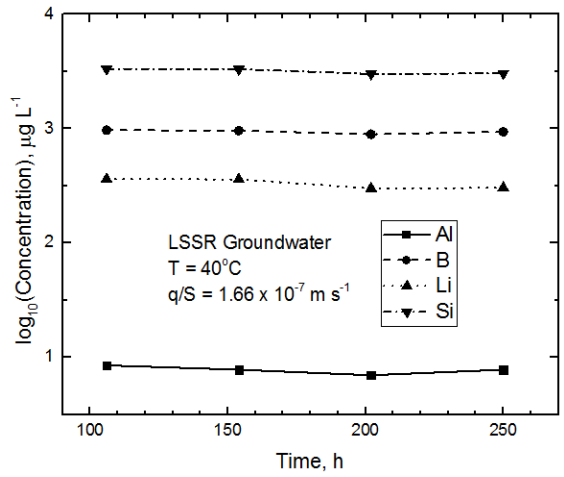

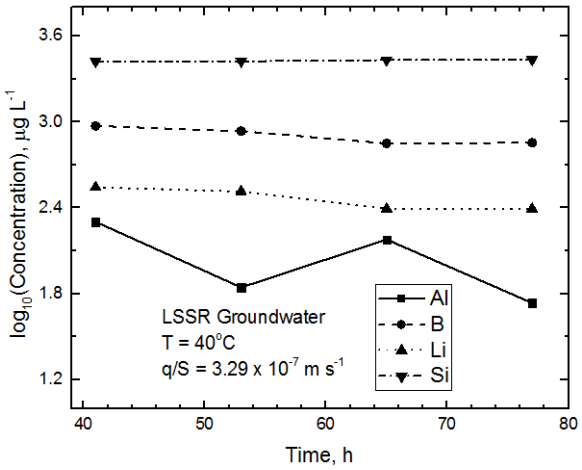

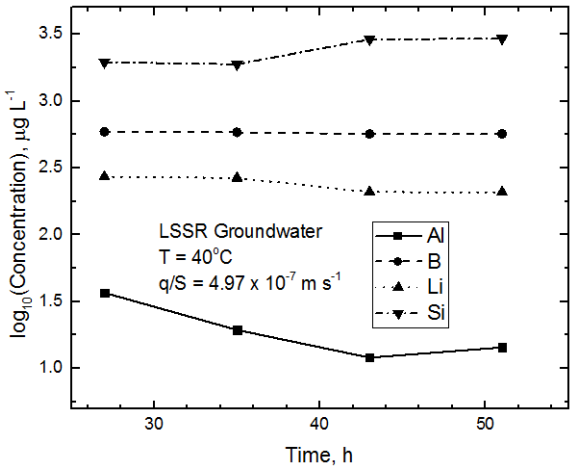

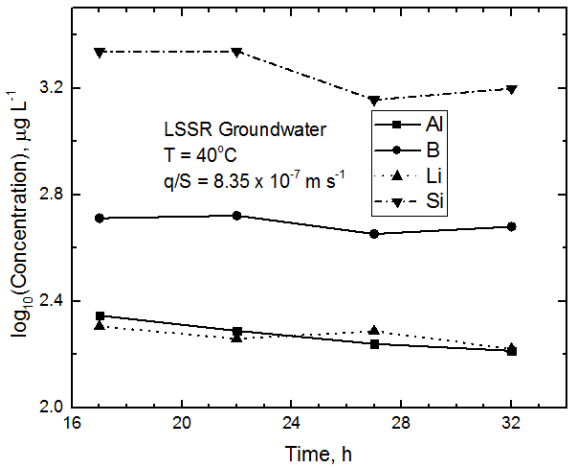

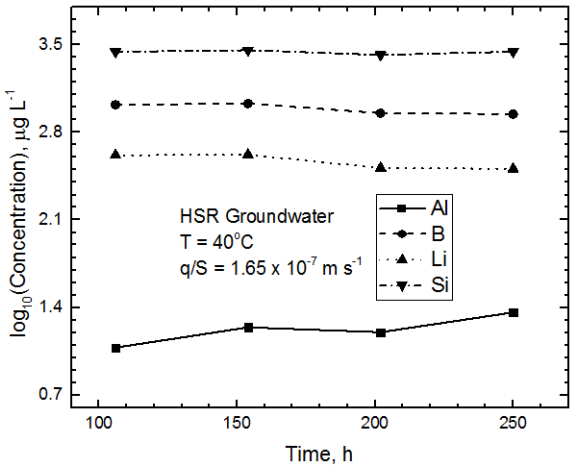
HSR Groundwater
T = 40°C
q/S = 1.65 x 10⁻⁷ m s⁻¹
Al
B
Li
Si
log10(Concentration), µg L⁻¹
Time, h

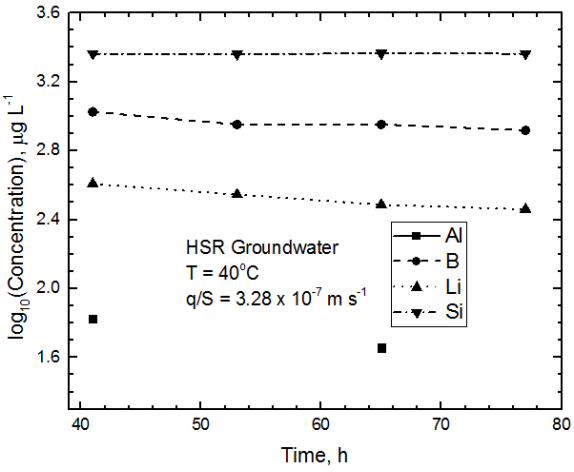
HSR Groundwater
T = 40°C
q/S = 3.28 x 10⁻⁷ m s⁻¹
Al
B
Li
Si
log10(Concentration), µg L⁻¹
Time, h

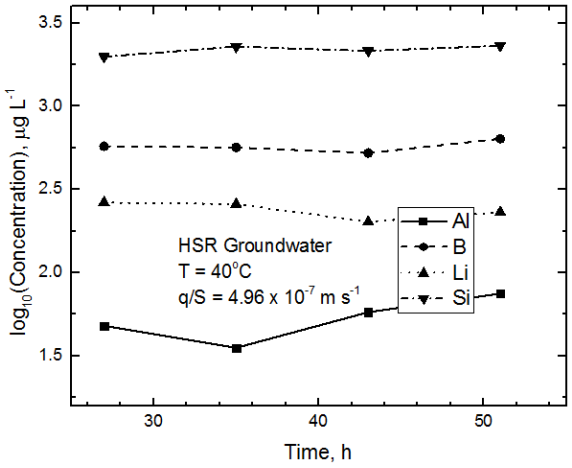
HSR Groundwater
T = 40°C
q/S = 4.96 x 10⁻⁷ m s⁻¹
Al
B
Li
Si
log10(Concentration), µg L⁻¹
Time, h

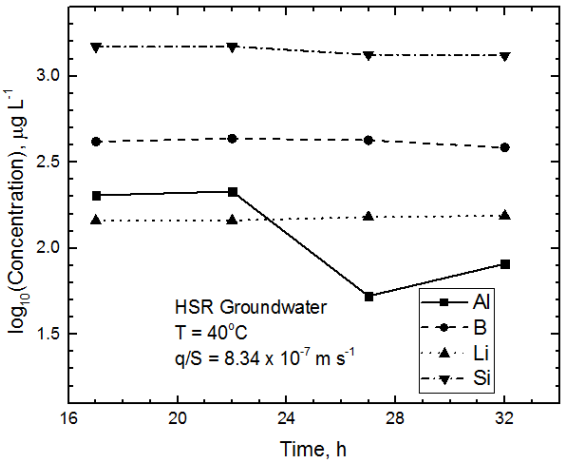
HSR Groundwater
T = 40°C
q/S = 8.34 x 10⁻⁷ m s⁻¹
Al
B
Li
Si
log10(Concentration), µg L⁻¹
Time, h

APPENDIX 28 DISSOLUTION RATES (IN G/M^2/D) FOR TRIPLICATE EXPERIMENTS MEASURED IN SIMULANT GROUNDWATERS.

Experiment ID	Li	B	Al	Si	Mo	Cs
GW_1-1	0.152	0.154	0.211	0.227	0.302	0.336
GW_1-2	0.193	0.173	0.006	0.189	0.257	0.361
GW_1-3	0.182	0.217	0.351	0.020	0.315	0.404
GW_2-1	0.180	0.137	0.049	0.180	0.198	0.207
GW_2-2	0.135	0.148	0.040	0.033	0.167	0.178
GW_2-3	0.108	0.121	0.268	0.084	0.119	0.133
GW_3-1	0.106	0.093	-0.002	0.100	0.095	0.102
GW_3-2	0.114	0.096	-0.024	0.207	0.091	0.094
GW_3-3	0.103	0.094	0.047	-0.018	0.081	0.086
GW_4-1	0.114	0.116	0.026	0.065	0.149	0.169
GW_4-2	0.076	0.073	0.044	0.089	0.084	0.095
GW_4-3	0.073	0.073	0.019	0.058	0.080	0.094
GW_5-1	0.056	0.057	-0.003	0.052	0.076	0.086
GW_5-2	0.048	0.050	0.004	0.022	0.054	0.058
GW_5-3	0.047	0.047	0.002	0.050	0.058	0.066
GW_6-1	0.039	0.040	0.000	0.026	0.066	0.072
GW_6-2	0.025	0.026	-0.001	0.014	0.031	0.033
GW_6-3	0.025	0.026	0.002	0.022	0.031	0.033
GW_7-1	0.339	0.123	0.088	0.215	0.225	0.281
GW_7-2	0.102	0.275	0.231	0.058	0.376	0.378
GW_7-3	0.034	0.095	0.128	0.184	0.222	0.230
GW_8-1	0.077	0.073	0.186	0.074	0.152	0.168
GW_8-2	0.090	0.086	0.030	0.118	0.150	0.165
GW_8-3	0.173	0.184	0.041	0.086	0.244	0.271
GW_9-1	0.097	0.081	0.023	0.075	0.086	0.092
GW_9-2	0.119	0.110	0.030	0.117	0.091	0.105
GW_9-3	0.108	0.091	0.008	0.064	0.096	0.102
GW_10-1	0.124	0.126	0.004	0.058	0.166	0.181
GW_10-2	0.043	0.031	0.018	0.050	0.049	0.047
GW_10-3	0.137	0.143	-0.003	0.072	0.186	0.211
GW_11-1	0.062	0.062	0.006	0.047	0.087	0.098
GW_11-2	0.045	0.043	0.002	0.016	0.050	0.058
GW_11-3	0.062	0.055	-0.002	0.046	0.084	0.084
GW_12-1	0.035	0.038	0.000	0.027	0.054	0.058
GW_12-2	0.029	0.030	0.001	0.019	0.037	0.040
GW_12-3	0.045	0.048	0.000	0.018	0.071	0.075

APPENDIX 29 PROPAGATION OF UNCERTAINTIES FOR RATES MEASURED IN SIMULANT GROUNDWATERS. THE MEAN VALUES OF FLOW RATE (Q), SURFACE AREA (S), AND NORMALISED CONCENTRATION (C) CAN BE FOUND IN TABLES 4.1 AND 4.2, RESPECTIVELY.

Table 9.9: Uncertainties in the rates calculated based on Si release in simulant groundwaters. Note that the uncertainty in the analysed mass fraction of Si is 0.0014899 (from Appendix 4).

Experiment ID	q(m/s3) Uncertainty	S (m2) Uncertaint	C of Li (g/m3)	(dNR/dC)^2* Qc^2	(dNR/dF)^2* QF^2	(dNR/dS)^2* QS^2	(dNR/df)^2* Qf^2	QNR^2	QNR (g/(m2s))	QNR (g/(m2d))
GW_1	1.02357E-11	0.00015381	0.673055	1.22971E-12	3.55081E-17	8.97505E-16	1.25336E-15	1.23189E-12	1.00645E-06	0.043479
GW_2	8.659E-12	9.7374E-05	1.705012	1.77885E-12	5.46767E-17	1.6744E-16	5.70877E-16	1.77964E-12	1.28609E-06	0.055559
GW_3	1.43902E-11	0.00011668	4.409788	4.42904E-12	4.06655E-16	2.29325E-16	5.39198E-16	4.43022E-12	1.98136E-06	0.042797
GW_4	1.06866E-11	2.3126E-05	0.572572	2.92363E-14	2.40524E-16	4.81345E-18	2.87927E-16	2.97695E-14	1.71862E-07	0.007424
GW_5	9.15156E-12	9.6937E-05	1.335992	4.11251E-14	2.39272E-16	2.92713E-17	9.97035E-17	4.14934E-14	2.01137E-07	0.008689
GW_6	2.92409E-12	2.5627E-05	1.22266	5.37299E-15	3.74848E-17	4.88231E-19	2.40993E-17	5.43506E-15	7.30531E-08	0.003156
GW_7	5.18385E-12	0.0001051	0.654834	9.65101E-13	1.18902E-17	4.65186E-16	1.38742E-15	9.66966E-13	9.80244E-07	0.042347
GW_8	6.23644E-12	9.3863E-05	0.469158	1.45165E-13	4.08572E-17	1.35044E-16	4.96233E-16	1.45838E-13	3.54785E-07	0.015327
GW_9	1.1487E-11	1.6938E-05	0.684498	9.79003E-14	1.75589E-16	3.77042E-18	4.2396E-16	9.85036E-14	3.08332E-07	0.01332
GW_10	1.67158E-12	3.6996E-05	0.425233	1.58978E-14	4.80759E-18	8.64246E-18	2.0657E-16	1.61178E-14	1.2684E-07	0.005479
GW_11	7.04583E-12	5.1672E-05	1.29594	3.78319E-14	1.15384E-16	6.31825E-18	7.52208E-17	3.80288E-14	1.94042E-07	0.008383
GW_12	7.13862E-13	1.9944E-05	0.967993	3.44002E-15	3.22199E-18	3.23607E-19	2.66887E-17	3.47025E-15	5.80529E-08	0.002508

Table 9.10: Uncertainties in the rates calculated based on B release in simulant groundwaters. Note that the uncertainty in the analysed mass fraction of B is 0.0003510 (from Appendix 4).

Experiment ID	q(m/s3) Uncertainty	S (m2) Uncertainty	C of Li (g/m3)	(dNR/dC)^2* Qc^2	(dNR/dF)^2* QF^2	(dNR/dS)^2* QS^2	(dNR/df)^ 2*Qf^2	QNR^2	QNR (g/(m2s))	QNR (g/(m2d))
GW_1	1.0236E-11	0.0001539	0.101609	6.11952E-13	5.91114E-17	1.41636E-15	1.175E-15	6.14603E-13	6.48566E-07	0.028018
GW_2	8.659E-12	9.3851E-05	0.065261	4.45132E-14	1.14345E-16	2.98997E-16	6.542E-16	4.55807E-14	2.12186E-07	0.009166
GW_3	1.439E-11	0.00011327	0.072479	1.94447E-14	3.51439E-16	2.10982E-16	3.166E-16	2.03237E-14	1.41687E-07	0.006121
GW_4	1.0687E-11	2.7404E-05	0.243548	1.01047E-13	4.01377E-16	1.09607E-17	2.767E-16	1.01736E-13	3.10614E-07	0.013419
GW_5	9.1516E-12	9.2934E-05	0.081994	3.44475E-15	3.88896E-16	4.30885E-17	9.427E-17	3.971E-15	5.93495E-08	0.002564
GW_6	2.9241E-12	2.0747E-05	0.385052	1.35819E-14	9.18434E-17	7.89021E-19	3.41E-17	1.37086E-14	9.81872E-08	0.004242
GW_7	5.1838E-12	0.00010958	0.173039	1.44761E-12	1.33938E-17	5.88342E-16	9.568E-16	1.44917E-12	1.10284E-06	0.047643
GW_8	6.2364E-12	9.559E-05	0.228966	5.63157E-13	6.08156E-17	2.19771E-16	4.638E-16	5.63902E-13	7.3567E-07	0.031781
GW_9	1.1487E-11	1.7105E-05	0.094111	6.63802E-14	2.22914E-16	4.78862E-18	3.159E-16	6.69238E-14	1.84272E-07	0.007961
GW_10	1.6716E-12	4.0485E-05	0.556636	5.27942E-13	1.57929E-17	2.96549E-17	3.572E-16	5.28345E-13	7.0505E-07	0.030458
GW_11	7.0458E-12	5.1585E-05	0.158505	1.03801E-14	2.79758E-16	1.4423E-17	1.018E-16	1.07761E-14	1.03215E-07	0.004459
GW_12	7.1386E-13	1.5748E-05	0.436459	1.25715E-14	1.10814E-17	7.21795E-19	5.38E-17	1.26371E-14	1.11657E-07	0.004824

Table 9.11: Uncertainties in the rates calculated based on Li release in simulant groundwaters. Note that the uncertainty in the analysed mass fraction of Li is 0.0001257 (from Appendix 4).

Experiment ID	q(m/s3) Uncertainty	S (m2) Uncertaint	C of Li (g/m3)	(dNR/dC)^2* Qc^2	(dNR/dF)^2* QF^2	(dNR/dS)^2* QS^2	(dNR/df)^2* Qf^2	QNR^2	QNR (g/(m2s))	QNR (g/(m2d))
GW_1	1.02357E-11	0.0001539	0.0191374	1.22888E-13	5.45917E-17	1.30034E-15	3.59142E-15	1.27834E-13	3.41632E-07	0.014759
GW_2	8.659E-12	9.385E-05	0.0584678	4.58571E-13	1.18112E-16	3.20224E-16	2.33244E-15	4.61341E-13	5.20813E-07	0.022499
GW_3	1.43902E-11	0.0001133	0.0242734	1.81345E-14	4.22524E-16	2.74406E-16	1.3709E-15	2.02023E-14	1.354E-07	0.005849
GW_4	1.06866E-11	2.74E-05	0.0802426	8.43766E-14	4.00079E-16	1.09108E-17	9.19149E-16	8.57067E-14	2.81907E-07	0.012178
GW_5	9.15156E-12	9.293E-05	0.0393935	4.81717E-15	3.44391E-16	4.05566E-17	2.95088E-16	5.4972E-15	7.3823E-08	0.003189
GW_6	2.92409E-12	2.075E-05	0.1328126	1.28589E-14	8.64682E-17	7.39635E-19	1.05831E-16	1.30519E-14	9.31732E-08	0.004025
GW_7	5.18385E-12	0.0001096	0.1072992	3.51408E-12	1.28627E-17	5.40528E-16	2.92949E-15	3.51756E-12	1.87147E-06	0.080847
GW_8	6.23644E-12	9.559E-05	0.0681405	3.62075E-13	5.30132E-17	2.12646E-16	1.49002E-15	3.63831E-13	6.00208E-07	0.025929
GW_9	1.1487E-11	1.711E-05	0.024657	2.66018E-14	3.11512E-16	6.17454E-18	1.36274E-15	2.82822E-14	1.40042E-07	0.00605
GW_10	1.67158E-12	4.048E-05	0.1699617	3.78519E-13	1.64694E-17	2.97086E-17	1.2116E-15	3.79777E-13	5.90357E-07	0.025503
GW_11	7.04583E-12	5.158E-05	0.0587736	1.06103E-14	3.12476E-16	1.5681E-17	3.68441E-16	1.13069E-14	1.06104E-07	0.004584
GW_12	7.13862E-13	1.575E-05	0.1438777	1.01551E-14	9.63467E-18	6.24614E-19	1.54739E-16	1.03201E-14	1.01297E-07	0.004376

Table 9.12: Uncertainties in the rates calculated based on Al release in simulant groundwaters. Note that the uncertainty in the analysed mass fraction of Al is 0.0001540 (from Appendix 4).

Experiment ID	q(m/s3) Uncertainty	S (m2) Uncertai	C of Li (g/m3)	(dNR/dC)^2* Qc^2	(dNR/dF)^2* QF^2	(dNR/dS)^2* QS^2	(dNR/df)^2* Qf^2	QNR^2	QNR (g/(m2s))	QNR (g/(m2d))
GW_1	1.02357E-11	0.000154	0.152759	4.87402E-12	6.20979E-17	1.55734E-15	1.64551E-15	4.87729E-12	2.2005E-06	0.095062
GW_2	8.659E-12	9.74E-05	0.219235	2.62615E-12	9.19985E-17	2.44735E-16	6.35649E-16	2.62712E-12	1.5988E-06	0.069067
GW_3	1.43902E-11	0.000117	0.099345	1.88855E-13	2.16984E-18	1.78149E-18	3.25586E-18	1.88862E-13	4.3081E-07	0.003722
GW_4	1.06866E-11	2.31E-05	0.071582	7.40663E-14	6.41192E-17	1.14193E-18	4.85739E-17	7.41801E-14	2.0588E-07	0.008894
GW_5	9.15156E-12	9.69E-05	0.026695	1.49386E-15	1.34287E-19	1.64878E-20	4.24939E-20	1.49405E-15	3.863E-08	0.000417
GW_6	2.92409E-12	2.56E-05	0.026785	2.67266E-16	1.06314E-20	1.40358E-22	5.26756E-21	2.67282E-16	1.5365E-08	0.000133
GW_7	5.18385E-12	0.000105	0.066938	9.54194E-13	1.06457E-17	4.36974E-16	9.84332E-16	9.55626E-13	9.672E-07	0.041783
GW_8	6.23644E-12	9.39E-05	0.180281	2.58885E-12	7.4439E-17	1.5126E-16	4.23562E-16	2.5895E-12	1.3103E-06	0.056605
GW_9	1.1487E-11	1.69E-05	0.037921	4.05599E-14	9.15017E-18	2.36022E-19	1.95322E-17	4.05888E-14	1.6473E-07	0.007116
GW_10	1.67158E-12	3.7E-05	0.064633	4.62481E-14	2.39872E-19	2.41853E-19	4.49302E-18	4.62531E-14	1.8464E-07	0.003988
GW_11	7.04583E-12	5.17E-05	0.03943	3.31985E-15	3.69933E-19	2.34452E-20	2.12852E-19	3.32046E-15	5.6812E-08	0.000614
GW_12	7.13862E-13	1.99E-05	0.004983	9.96269E-18	8.68991E-22	1.49261E-22	8.93129E-21	9.97264E-18	2.8746E-09	0.000124

Table 9.13: Uncertainties in the rates calculated based on Cs release in simulant groundwaters. Note that the uncertainty in the analysed mass fraction of Cs is 0.0000638 (from Appendix 4).

Experiment ID	q(m/s3) Uncertainty	S (m2) Uncertainty	C of Li (g/m3)	(dNR/dC)^2* Qc^2	(dNR/dF)^2* QF^2	(dNR/dS)^2* QS^2	(dNR/df)^2* Qf^2	QNR^2	QNR (g/(m2s))	QNR (g/(m2d))
GW_1	1.02357E-11	0.0001539	0.016542	3.29562E-13	1.85677E-16	4.67305E-15	6.71922E-14	4.01613E-13	6.1935E-07	0.026756
GW_2	8.659E-12	9.3851E-05	0.02752	3.28316E-13	2.09931E-16	4.2597E-16	1.61173E-14	3.45069E-13	4.81613E-07	0.020806
GW_3	1.43902E-11	0.00011327	0.00694	5.01877E-15	2.70065E-16	1.66474E-16	4.33151E-15	9.78682E-15	9.85282E-08	0.004256
GW_4	1.06866E-11	2.7404E-05	0.069394	2.16026E-13	5.96126E-16	1.63226E-17	7.1561E-15	2.23795E-13	4.67247E-07	0.020185
GW_5	9.15156E-12	9.2934E-05	0.048449	2.6249E-14	5.6051E-16	6.38774E-17	2.42176E-15	2.92952E-14	1.70533E-07	0.007367
GW_6	2.92409E-12	2.0747E-05	0.177414	8.84188E-14	1.82261E-16	1.51424E-18	1.11589E-15	8.97184E-14	2.36517E-07	0.010218
GW_7	5.18385E-12	0.00010958	0.024997	8.19238E-13	3.95046E-17	1.60883E-15	4.57383E-14	8.66624E-13	8.55157E-07	0.036943
GW_8	6.23644E-12	9.559E-05	0.038618	6.54382E-13	2.31592E-16	5.83107E-16	2.15465E-14	6.76743E-13	6.72287E-07	0.029043
GW_9	1.1487E-11	1.7105E-05	0.010301	1.79214E-14	2.10277E-16	4.26395E-18	4.89507E-15	2.3031E-14	1.34822E-07	0.005824
GW_10	1.67158E-12	4.0485E-05	0.13761	8.60408E-13	2.69663E-17	5.05568E-17	1.06296E-14	8.71115E-13	9.12472E-07	0.039419
GW_11	7.04583E-12	5.1585E-05	0.059758	3.94263E-14	5.05781E-16	2.57733E-17	3.15399E-15	4.31118E-14	2.07461E-07	0.008962
GW_12	7.13862E-13	1.5748E-05	0.145725	3.81312E-14	1.98315E-17	1.28898E-18	1.66602E-15	3.98183E-14	1.97576E-07	0.008535

Table 9.14: Uncertainties in the rates calculated based on Mo release in simulant groundwaters. Note that the uncertainty in the analysed mass fraction of Mo is 0.0000632 (from Appendix 4).

Experiment ID	q(m/s3) Uncertainty	S (m2) Uncertainty	C of Li (g/m3)	(dNR/dC)^2* Qc^2	(dNR/dF)^2* QF^2	(dNR/dS)^2* QS^2	(dNR/df)^2* Qf^2	QNR^2	QNR (g/(m2s))	QNR (g/(m2d))
GW_1	1.02357E-11	0.000153902	0.012885	2.61591E-13	1.37615E-16	3.29374E-15	9.00652E-13	1.16567E-12	1.06872E-06	0.046168
GW_2	8.659E-12	9.38514E-05	0.027509	3.93485E-13	2.03446E-16	4.17057E-16	3.00048E-13	6.94153E-13	7.48539E-07	0.032337
GW_3	1.43902E-11	0.000113267	0.008004	7.52833E-15	2.81668E-16	1.68121E-16	8.31635E-14	9.11416E-14	3.01815E-07	0.013038
GW_4	1.06866E-11	2.74036E-05	0.061897	1.99318E-13	5.03858E-16	1.39848E-17	1.16434E-13	3.1627E-13	5.59636E-07	0.024176
GW_5	9.15156E-12	9.29338E-05	0.041558	2.17538E-14	5.19322E-16	5.79065E-17	4.17548E-14	6.40858E-14	2.52963E-07	0.010928
GW_6	2.92409E-12	2.07469E-05	0.160882	8.11738E-14	1.75004E-16	1.45872E-18	2.04541E-14	1.01804E-13	2.70288E-07	0.011676
GW_7	5.18385E-12	0.000109577	0.027882	9.91466E-13	3.68478E-17	1.51553E-15	8.17487E-13	1.81051E-12	1.33022E-06	0.057466
GW_8	6.23644E-12	9.55896E-05	0.034665	6.39894E-13	2.02315E-16	5.31333E-16	3.72864E-13	1.01349E-12	9.28363E-07	0.040105
GW_9	1.1487E-11	1.71054E-05	0.010376	1.38414E-14	1.9555E-16	4.03021E-18	8.79058E-14	1.01947E-13	3.18792E-07	0.013772
GW_10	1.67158E-12	4.04846E-05	0.117226	7.03988E-13	2.49666E-17	4.77929E-17	1.89522E-13	8.93582E-13	9.36346E-07	0.04045
GW_11	7.04583E-12	5.15849E-05	0.059665	4.44588E-14	4.81458E-16	2.4787E-17	5.76722E-14	1.02637E-13	3.20152E-07	0.013831
GW_12	7.13862E-13	1.57482E-05	0.142416	4.11604E-14	2.00562E-17	1.28693E-18	3.16301E-14	7.28119E-14	2.67164E-07	0.011541

APPENDIX 30 COMPUTER CODES USED IN ESTIMATING THE TIME TAKEN FOR THE WASTE GLASS TO DISSOLVE AT EACH DISSOLUTION STAGE.

```
function Time = timeestimation(Rate, Diameter, Height, Mass)
global rate1 rate2 rate3 ratio D H mass
rate1 = Rate(1); %g/m2/d
rate2 = Rate(2); % g/m2/d
rate3 = Rate(3); %g/m2/d
D = Diameter; % m
H = Height; % m
mass = Mass; % g
ratio = [1,1000,10];%%Time ratio
ratio = ratio/sum(ratio);
total_surface_area = 0.5*pi*D*(D + 2*H);
timeguess = mass/(total_surface_area*rate1);
Time = fzero(@(T)desolve(T),timeguess)/365.25*ratio;

function res = desolve(T)
global rate1 rate2 rate3 ratio D H mass

mass1 = mass;

% stage1
D1 = D; H1 = H;
total_surface_area = 0.5*pi*D1*(D1 + 2*H1);
diss_rate1 = rate1*total_surface_area;
mass2 = mass1 - diss_rate1*ratio(1)*T;

% stage2
D2 = D1*(mass2/mass1)^(1/3);
H2 = H1*(mass2/mass1)^(1/3);
total_surface_area = 0.5*pi*D2*(D2 + 2*H2);
diss_rate2 = rate2*total_surface_area;
mass3 = mass2 - diss_rate2*ratio(2)*T;

% stage3
D3 = D2*(mass3/mass2)^(1/3);
H3 = H2*(mass3/mass2)^(1/3);
total_surface_area = 0.5*pi*D3*(D3 + 2*H3);
diss_rate3 = rate3*total_surface_area;
res = mass3 - diss_rate3*ratio(3)*T;
```

APPENDIX 31 CONTENTS OF ATTACHED CD.

The attached CD contains GoldSim model files of all the four scenarios (i.e. disposal options) investigated in Chapter 6. All the four models contain fewer than 500 numerical elements.

The GoldSim files can be accessed by installing GoldSim Contaminant Transport on a computer. Any version of the GoldSim licence can be used to open the files, including the GoldSim Academic licence, since the models contain fewer than 500 elements. GoldSim Academic is offered at no cost and can be requested from GoldSim Technology Group LLC.

The models can be run by simply pressing F5 on the computer keyboard, and can be returned back to edit mode by pressing F4. The models can be navigated both in edit and result modes.